DOUBLE STATOR SWITCHED RELUCTANCE MACHINE WITH MUTUAL COUPLED WINDINGS

YANG LU

A thesis submitted for the degree of

Doctor of Philosophy

SEPTEMBER 1, 2018

NEWCASTLE UNIVERSITY

Abstract

This thesis describes the development of a four-phase double-stator switched-reluctance motor (DSSRM) with mutually coupled windings. This machine, which has a topology that combines features of both the mutually coupled and double-stator switched-reluctance motor, will be shown to have the potential to offer improved torque productivity under the same ohmic loss limitation; though experimental mechanical and thermal confirmation remains to be completed.

It is widely thought that the electrification of vehicle traction will be an essential element in the automotive industry in the next decade. An eventual sales ban on diesel and petrol vehicles has recently been reported to be planned by several industrial countries. Even disregarding these political declarations, which could only be considered as expectation rather than strict policy, the spread of hybrid powertrain technology and the continuous fall of Li-ion battery prices will effectively motivate an increasing number of automotive manufacturers to participate in this revolution. Since the cost of rare-earth materials is expected to continuously rise and the mining of these resources has left an enormous impact on the environment, the development of a high-performance SRM as an alternative to a permanent magnet synchronous machine (PMSM) is worthy and necessary.

In addition to the enhancement of electromagnetic performance, this thesis discusses the mechanical properties and rotor structure of the DSSRM. The rotor support, which holds the rotor segments together, should be strictly of non-conducting material to prevent significant eddy current loss. Since most materials struggle to offer a compatible stiffness to steel, methods have been investigated to meet the challenge of designing a rotor support able to endure the centrifugal force of rotor segments during high-speed spinning. Thermal issues pose another challenge for this prototype but simulations indicate that the DSSRM could have better cooling capability than the conventional SRM configuration.

A prototype was built and compared with a 12/16 segmental-rotor SRM, previously developed at Newcastle University. The results indicated that the prototype machine gave a promising torque performance with a relatively low copper loss.

Table of Contents

List of Figures

List of Table

Acknowledgment

I would like to appreciate a number of people who have assisted me in preparation for this thesis.

Firstly, James Widmer, Richard Martin and Barrie Mecrow: their tireless support helped me grow from a person who nearly knows nothing about this research area.

I would also thanks to Chris Manning, John Smith, Alan Wheatley and other technicians in the mechanical workshop who helped me built up the prototype.

Also, without the assistant from Gordon Marshall and James Richardson, my experiment test would not be so easily prepared.

I would like to thank Ruchao Pupadubsin, Andy Steven, Mohamed Mohamed and the rest of the Newcastle University electrical machines team for their generous sharing of knowledge and experience.

Finally, I would also thank my parents and friends, their love and support helped me get through all the difficulties during these years.

List of Acronyms

AC	Alternative Current
CAD	Computer Aided Design
DC	Direct Current
EDM	Electrical Discharge Machining
EMF	Electromotive Force
FE	Finite Element
IEEE	Institute of Electrical and Electronics Engineers
IPM	Interior Permanent Magnet
MMF	Magnetomotive Force
NdFeB	Neodymium Iron Boron
PEEK	Polyether Ether Ketone
PWM	Pulse Width Modulation
RMS	Root Mean Square
SRM	Switched Reluctance Machine
VA	Volt Ampere

Chapter 1. Introduction

This doctoral thesis describes the development of a novel SRM topology, which is designed to provide high performance in terms of torque per unit copper loss. The motivation and contribution of this research is provided in this chapter, along with a brief outline of the thesis structure.

1.1 Background Knowledge

With increasing concerns surrounding global warming and air pollution, the electrification of the automotive industry is becoming an unstoppable trend; thus it can be predicted that electric machines will replace internal combustion engines within a few decades. Amongst all types of electric machines, the SRM with its unique features is considered to be a potential candidate for future vehicle propulsion.

1.1.1 The Electrified Propulsion of Automotive Industry

Electrification is forecast to be the most important development in the automotive industry over the next decade and could be realised along four technical routes:

- Hybrid electric vehicle (HEV): The HEV is powered by an internal combustion engine (ICE), as with a conventional vehicle, but is also equipped with an electric motor that assists propulsion. This type of powertrain has advantages in terms of fuel-efficiency and propulsion power because the electric motor possesses regeneration features and prevents low-efficiency operation conditions manifesting in the ICE. For example, the fuel economy of the hybrid Toyota Camry is 52.9% higher than the regular engine version (see Figure 1-1). Toyota HEVs have already achieved commercial success in the automotive market (the model Toyota Prius reached total sales of more than two million between 2011 and 2016 [1]). Moreover, increasingly stringent emissions policies are also driving other leading manufacturers to enhance fuel economy. In addition, the European Union has set a target to limit passenger car CO_2 emissions to 95 g/km by the year 2021, which is equivalent to a fuel consumption of 4.1 l/100 km of petrol or 3.6 l/100 km of diesel [2]. Consequently, European car manufacturers, such as Volvo and Jaguar Land Rover, whose technology previously centred on the diesel engine, have quickly responded to this policy by stating aims to exclusively produce hybrid or electric cars from 2020 onwards [3, 4]. Unlike the complicated powertrain technology used by Japanese manufacturers, the hybrid system of European car makers depends on the 48-V integrated starter generator (ISG), which is only fractionally more

expensive and requires less redesign effort than the conventional ICE platform [5, 6]. As a result, 48 V mild-hybrid concepts could be widely accepted by the automotive industry in the coming years.

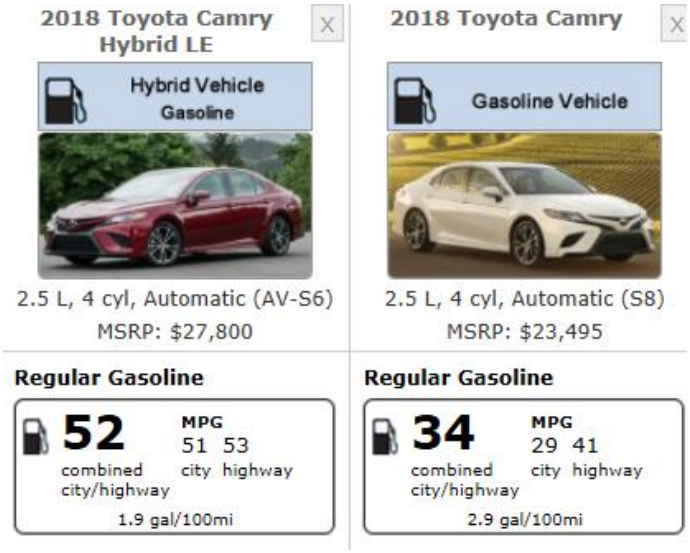

Figure 1-1 A comparison of the fuel consumption of hybrid and conventional ICE vehicles [7]

- Battery electric vehicle (BEV): The BEV is currently the most successful zero-emissions vehicle on the market; according to [8], sales have increased by 51% over the last two years (from 740,000 in 2016 to 1.1 million in 2017). Even excluding the impact of subsidies, the BEV has already become competitive in the luxury car market [9] (see Figure 1-2)

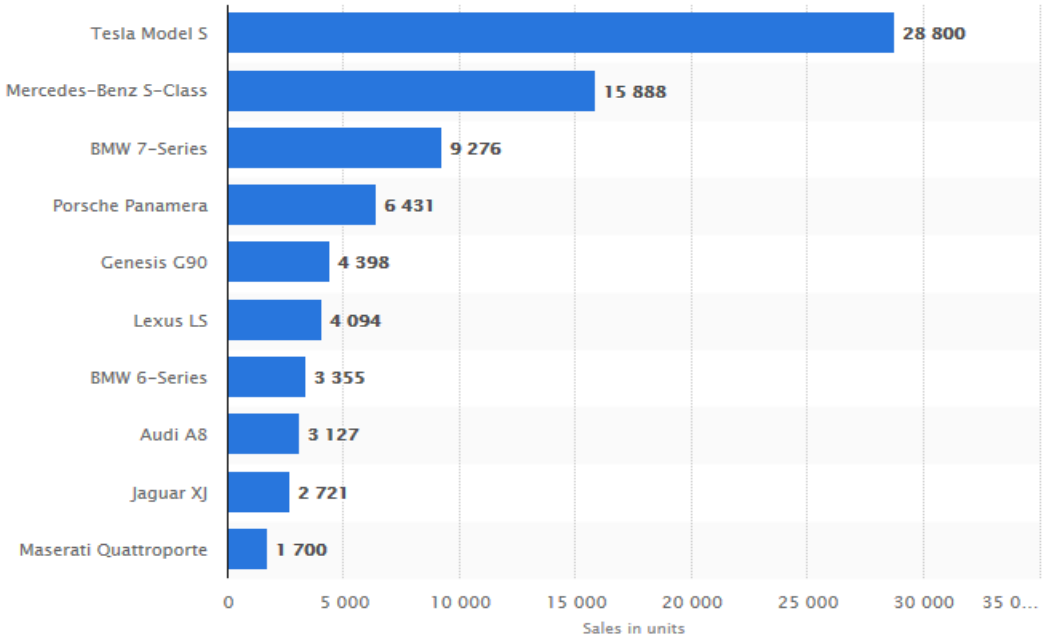

Figure 1-2 Sales of large luxury cars in the US in 2017, showing that the BEV (Tesla Model S) already dominates the market [9]

Moreover, due to an increase in global production, the cost of battery packs has been in steady decline over the past eight years [10, 11]. In 2010, when the first mass-produced BEV model – the Nissan Leaf – was launched, the price of the battery was circa USD 1,000 per kilowatt hour (kWh). However, nowadays, the cost of a battery for the Tesla Model 3 and Chevrolet Bolt is USD 190/kWh and USD 205/kWh, respectively [11]. It is almost certain that the price will drop to below USD 100/kWh by 2025 and according to [11], the eventual price could fall to USD 73/kWh by 2030 (see Figure 1-3). Since the battery pack makes up the largest proportion of the manufacturing costs of the BEV, a decrease in battery cost should guarantee a significant increase in the global market share of BEVs.

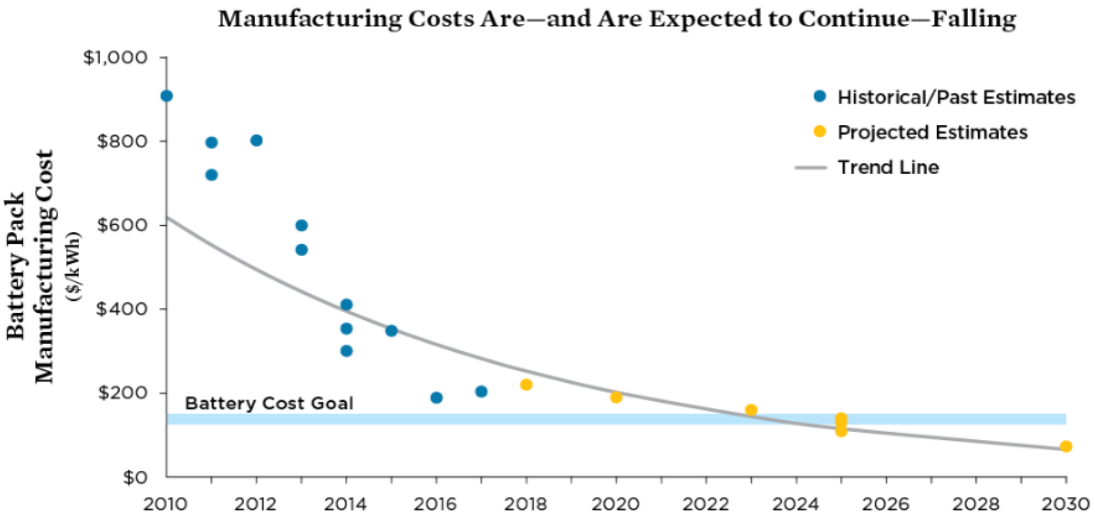

Figure 1-3 The price trend of battery packs in the electric vehicle (EV) industry [11]

- Plug-in hybrid electric vehicle (PHEV): The PHEV combines features of the HEV and BEV. Its battery is relatively small compared to a BEV and is designed to supply a pure-electricity range of between 30 km and 80 km. Consequently, the PHEV could behave as a BEV in urban commuting, with advantages such as zero-emissions and excellent economy, but without the range anxiety or the high cost of a large battery pack. Although its market share is lower than the BEV and HEV (with global sales of 386,000 in 2017 [8]), the PHEV is predicted to be a mainstream EV type in the next decade.
- Fuel-cell vehicle (FCV): the FCV is a type of serial-hybrid vehicle which uses a hydrogen-oxygen fuel cell unit rather than an ICE to supply electrical power [12]. Since its refill time is similar to a conventional diesel or petrol car, the FCV could effectively eliminate the range anxiety often experienced by BEV owners. As such, the FCV would otherwise have been the ideal alternative to ICE vehicles, if disadvantages such as the high price of the fuel cell unit did not exist. Furthermore, even if the manufacturing

costs could be managed in the future, the relatively low production efficiency of hydrogen and difficulties with hydrogen transportation could represent further challenges [13, 14].

1.1.2 The Rising Demand for Magnet-Free Electric Machines

The market size of the automotive industry was circa 79.02 million in 2017 and is set to continually expand due to economic development in China and India [15]. According to [16], prohibitions on conventional ICE vehicles will come into effect in all major industrial nations between 2025 and 2040. Thus, around 100 million electric motors will be required annually in the automotive industry following the electric revolution. Nowadays, the high-performance electric machine for vehicle propulsion is dominated by PMSMs that use a rare-earth material, generally neodymium iron boron (NdFeB)[17, 18]. With concerns of limited mining capability of this rare resource, the price of NdFeB has steadily increased in recent years, with further expansion expected [19, 20]. As can be seen from Figure 1-4, the price of NdFeB is set to reach USD 148,444/metric tonne in 2025, which is almost ten times the price it was in 2009 (USD 15,208/metric tonne). Moreover, an abnormal price surge between 2011 and 2012 indicates that the supply of rare-earth materials is vulnerable to market manipulation. Assuming each PMSM would require circa 1.5kg NdFeB[21], then it can be estimated that the automotive industry, as a whole, would have to spend a minimum USD 17.5 billion annually securing supplies of NdFeB in order to install PMSMs in vehicles.

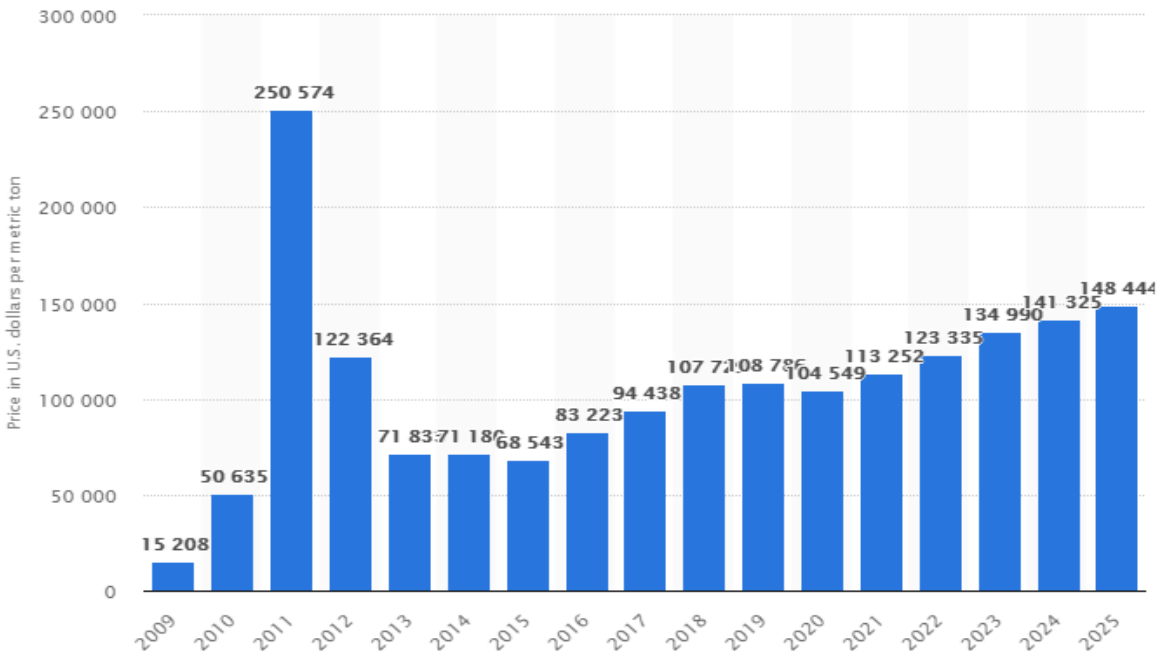

Figure 1-4 The price trend of NdFeB from 2009 to 2025 [20].

In addition to the financial costs, this massive use of rare-earth materials could leave a severe impact on the environment [22]. According to several reports[23, 24], the mining and recycling of rare-earth oxides has already undermined the local ecosystem in East Asia. This issue is discussed in [22] where the environmental impact of the NdFeB lifecycle is compared with other conventional materials used in PMSM manufacture (see Figure 1-5)

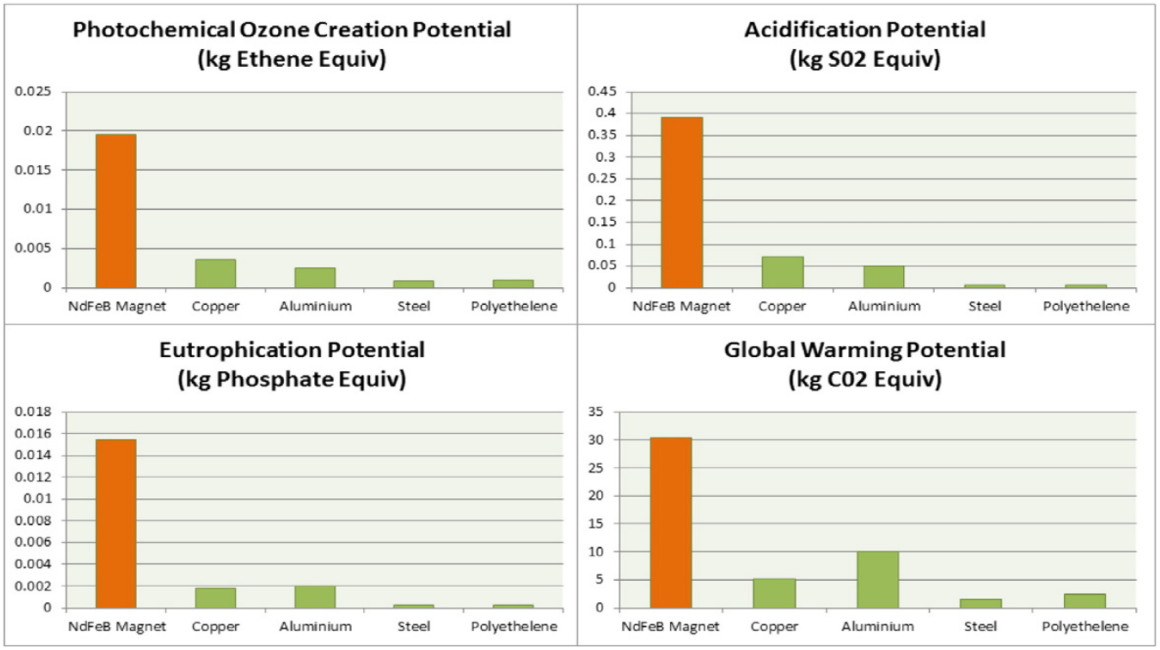

Figure 1-5 NdFeB potentially has a much higher environmental impact than other materials [22]

Furthermore, the utilisation of permanent magnets could have other limitations that need to be considered:

- The ever-present magnetic field of the permanent magnet could produce an undesirable loss in some scenarios. For example, the electric machine in a 48V mild hybrid system(ISG) could be directly connected to the engine shaft. When the vehicle is cruising on a highway with the ISG in idle mode, this could generate a loss via the rotational magnetic field and cogging torque. For the more sophisticated hybrid system, this condition could be avoided by introducing a clutch into the powertrain to allow for the decoupling of the electric motor and the engine [25]. However, even in the standard operation scenario, the permanent magnet would require a relatively large Volt-Ampere (VA) requirement to extend the speed range. As a result, the high-efficiency advantage of PMSM may be lost at high speed.
- The magnetism of a permanent-magnet material is not really 'permanent'. Its degradation could occur if heat or the external field is not appropriately controlled. Unfortunately, the electric motor in a hybrid vehicle is exposed to a relatively high ambient temperature and often operates under a heavy load. Thus, the PMSM must be carefully designed to maintain a low rotor temperature.

1.1.3 The Advantages and Disadvantages of the Switched-Reluctance Machine for Automotive Traction Applications

The development of a magnet-free electric machine for vehicle traction is worthy and necessary. The potential candidates, such as the induction machine (IM), switched-reluctance machine (SRM), synchronous-reluctance machine, and wound-rotor-synchronous machine have been analysed and compared in several papers [21, 22, 26, 27]. With consideration to torque density and efficiency, only the IM and SRM are widely accepted with the potential to be introduced into the vehicle traction market.

The IM has already achieved initial success in the EV market: Tesla, Inc., one of the most successful EV manufacturers whose name is a reference to the inventor of the IM, has vastly increased its production of powered BEVs since 2012[28], with annual sales figures reaching 100,000 in 2017 [29]. Interestingly, the SRM may also be evident soon amongst its production of BEVs; Elon Musk (the current CEO of Tesla, Inc) states that the twin-motor version Tesla Model 3 will be equipped with both an IM and SRM on the front and rear of the vehicle, individually [30].

The SRM is a type of reluctance machine with salient structure in both stator and rotor. Compared with the PMSM (which currently dominates the EV traction market) and the IM, the SRM possesses several advantages:

1) Low manufacturing costs: the low cost is guaranteed by the rotor structure. Without a permanent magnet and, instead, copper or aluminium in the rotor, an SRM could represent reduced material costs compared to the PMSM and IM.
2) Minimal cooling requirement: due to the absence of a permanent magnet material, the SRM is free from the demagnetisation problem associated with the PM machine. Thus, the SRM should naturally be able to endure higher temperatures than the PMSM. Moreover, since there is neither winding on the rotor nor significant end-winding on the stator, the cooling of the SRM should be significantly easier than with the IM.
3) Robust structure: the geometry of the rotor in the SRM is relatively simple, with neither magnets or windings; therefore, the rotor of the SRM tends to survive at higher rotation speeds than other electric machines.
4) Fault tolerance: this is an inherent feature of the SRM, since each of its phases is electrically and magnetically isolated. Thus, if a failure occurs in one phase, other phases should still operate undisturbed.

A specific comparison between these three machine types has been frequently discussed [22, 27, 31], and the results of one such study [22] are presented in TABLE 1-1 below.

TABLE 1-1 COMPARISON BETWEEN DIFFERENT MACHINE TYPE IN AUTOMOTIVE TRACTION APPLICATION [22]

	PMSM	**IM**	**SRM**
Power	**80kW**	**50kW**	**75Kw**
Peak Efficiency	**98%**	**96%**	**97%**
Active Material cost	**$223**	**$144**	**$118**
Drive VA Rating	**>twice that of the power**	**Small**	**>twice that of the power**
Torque Ripple	**Low**	**Low**	**Large**

Among the potential candidates for electric propulsion, the SRM can provide reasonable performance and efficiency while maintaining the lowest cost – however, there are still certain disadvantages that prevent the SRM from being widely accepted:

1) Performance: although the SRM could perform comparably within the magnet-free electric motor family, its torque density still struggles compared with mainstream PMSMs, which dominate the EV market.
2) Torque ripple: the SRM is known for its relatively large torque ripple. The effort to eliminate this issue mainly depends on sophisticated control algorithms.
3) Acoustic noise and vibration: noise, vibration and harshness (NVH) is a critical performance measure in the automotive industry. Noise and vibration in SRMs mainly occur on the stator teeth due to the rapidly varying electromagnetic force in the radial direction.
4) High apparent power requirement: The apparent power requirement of the SRM is relatively large, especially when compared with the induction machine. This increases the cost of the drive which somewhat counteracts any advantages of low manufacturing costs.

To address these disadvantages, researchers have already developed several possible novel designs which include, but are not restricted to, the segmental-rotor SRM, double-stator SRM and the mutually coupled SRM.

The segmental rotor SRM was firstly introduced by Mecrow et al. in 2003 [32] and was identified as having a 40% higher torque capability than the conventional SRM. However, this motor type suffers cross-saturation effects which can limit torque performance under highly saturated conditions. Moreover, the large inductance requires a higher VA from the drive than the conventional SRM

The double-stator SRM was initially a development of the segmental-rotor SRM with an additional stator inside the machine geometry [33]. This type of design is claimed to effectively enhance torque density and reduce vibration. Moreover, the double-stator structure was proven compatible with the flux loop in the conventional SRM in 2015 [34].

The mutually coupled SRM is a conventional SRM which can utilise the mutual coupling effects in torque production [35]. Unlike the fully pitched SRM, this machine should use both self and mutual inductance together and be equipped with single-tooth winding.

1.2 Objective and Contribution to the Knowledge

The objective of this project is to develop a novel SRM tropology with higher torque per unit copper loss. During this process several contributions have been made to the knowledge, and are listed as follows:

- An investigation of the impact of phase number upon the torque production has been made and a conclusion is created: most common three-phase SRMs have an advantage when the airgap reluctance has a dominate role in the magnetic path. In contrast, the higher phase number designs make better use of the iron path, which makes them more competitive when the machine is operating under saturated conditions (Chapter 3);
- An analytical model has been developed to make a fair comparison between three-phase and four-phase SRMs. It reveals that the four-phase machine tends to provide higher torque per unit copper loss when the machine design has a large split ratio (rotor radius to stator radius) or the machine is operating in the saturated condition (Chapter 3);
- To effectively analyse the four-phase configurations, an improved static flux-linkage vs current analysis was developed to replace the transient finite element analysis which is relatively time consuming but used to be necessary when evaluating torque performance of an SRM with two or more phase conducting simultaneously (Chapter 4);
- An analysis that reveals that mutual coupled winding arrangements enhance the performance of four-phase SRMs and that such a machine should have a larger splitting ratio. A 16/12 SRM with mutually coupled winding has been developed using this concept, verified by showing it surpasses the performance of Chiba's 18/12 SRM (widely accepted to be one of the best-optimised SRM ever published so far) during 2D transient FEA (Chapter 4);
- The examination of higher rotor pole number concepts suggests this would improve the torque in the linear region, but it is difficult to provide improvement during saturated conditions. Modification of the stator pole tip shows an improvement of performance when saturated (Chapter 4);
- Development of novel rotor structures which exhibit good mechanical strength without producing significant eddy current loss (Chapter 5, 6).
- Development of a 16/12 mutual coupled double stator SRM prototype that provides very high torque per unit copper loss. The prototype is verified by comparison with a 12/16 segmental rotor SRM that is developed with the same objective, using both 2D FEA and experimental test (Chapter 5, 6).

Published Work:

Y. Lu and J. D. Widmer, "Development of a straight pole four-phase double-stator switched reluctance machine," *The Journal of Engineering,* vol. 2019, pp. 3997-4002, 2019.

1.3 Thesis Structure

The structure of this thesis consists of the following components:

Chapter 2. Literature Review - this chapter introduces the background knowledge of the SRM and analyses and evaluates several technologies relating to this project.

Chapter 3. Comparison between Three-Phase SRM and Four-Phase SRM - this section discusses the effects of increasing the number of phases. In the beginning, the investigation included a selection of phases ranging from three to six. The results of both 2D finite element method (FEM) and analytical equations indicate that the SRM with the higher phase number would provide higher overall torque production in certain circumstances.

Further comparison focuses on the three-phase and four-phase configurations by analysing the flux-linkage-current curves. The results suggest that the four-phase SRM performs best with a different geometric design to that of the three-phase SRM.

Chapter 4. The Development of Four-Phase SRM Design – following the conclusion from Chapter 3, the proposed SRM was developed, based on the four-phase SRM. The coil arrangements and pole number combinations were evaluated and simulation results based on the 2D FEM are provided.

The feasibility and suitability of the double-stator structure was investigated via an analytical method. Subsequently, a proposed four-phase double-stator SRM was developed and compared with other SRMs.

Chapter 5. Multi-Physical Challenges and Prototype Development – this chapter investigates the mechanical and thermal issues of the proposed machine. Various rotor structures and materials, which would provide sufficient robustness without sacrificing too much electromagnetic performance, were compared. Thermal analysis was conducted to ensure that the cooling performance of the proposed machine design would not be inferior to that of a conventional SRM.

Chapter 6. Construction and Test Results - This chapter describes the final design modifications and the construction process, in detail. Experimental results are presented.

Chapter 7. Conclusion and Future Work - this chapter concludes with the advantages of the proposed double-stator SRM, showing its potential for automotive traction applications, and suggests areas which require further development.

Chapter 2. Literature Review

This chapter review of published researches that relate to the thesis objective. Commencing with the history and general background knowledge of SRMs (see Section 2.1 and Section 2.2 respectively), the discussion of modern SRM designs is divided into four categories:

- A review of the conventional SRM (Section 2.3), including some classic analysis that attempts to establish a research guide in the early 1990s, up to the latest published results, which seek to deliver equivalent performance modern PMSMs in the automotive industry. This review ensures the baseline of a high-performance conventional SRM and concludes a generalised design concept that inspired the analysis in Chapter 3.
- A review of segmental rotor SRM design (Section 2.4), demonstrates both the pros and cons of this machine type, which is considered to be a significant milestone of SRM development and inspired the invention of the double stator SRM.
- A review of the double stator SRM design and development which is based on the segmental rotor SRM. It suggests that a double stator SRM, based on a conventional SRM, needs to be developed (Section 2.5).
- A review of the work undertaken to improve the performance of SRMs by using the mutual coupling effects (Section 2.6). This review provides ideas for developing the winding configuration of this project.

2.1 Switched Reluctance Machine History

The history of the switched-reluctance machine possibly dates back to the nineteenth century. According to Miller [36], the earliest record for the application of this technology was a locomotive propulsion system built by Davison for the railway between Glasgow and Edinburgh in 1838. Moreover, the original research for the reluctance machine began in 1824 [37]; however, the modern switched-reluctance machine research is believed to have been started in the late 1960s, after the development of modern power electronics [38].

2.2 Fundamental Principles and Torque Evaluation Methods

Unlike permanent-magnet or induction machines, which are mainly driven by the Lorentz force, the switched-reluctance machine rotates via a tendency towards seeking minimum reluctance [36, 37]. The typical structure of a conventional SRM has salient geometry in both stator and rotor, while its winding is often single-toothed on the stator pole. Consequently, an analysis of torque performance is complicated due to its highly nonlinear electromagnetic performance [39].

In general, the torque of the SRM is calculated as the differential of the co-energy with respect to angle[40]. Using a simple equation, the relation could be described as:

$$T(\theta, i) = \frac{\partial W(\theta,i)}{\partial \theta} \quad (2\text{-}1)$$

The co-energy $W$is represented by the area below the magnetisation curve; thus, it could be described as the integral of the flux linkage ψ in terms of the phase current, i:

$$\mathrm{W} = \int \psi \, di \quad (2\text{-}2)$$

Since the inductance will be increased steadily from the minimum value at the unaligned position to the maximum value at the aligned position, ideally, the corresponding phase will be conducting during this period. Consequently, the mean static torque could be evaluated from the magnetisation curves at these two positions

The electromagnetic characteristics which present in the magnetisation curve can be acquired via three principal methods [39, 41]:

1) The experimental method – test-based methods can provide the most accurate result, but can only be utilised after the machine is completed. In [42-46], some possible methods are outlined for analysing the magnetisation curve, including measuring the flux directly, measuring inductance directly and measuring the flux linkage indirectly. The first two, however, are direct methods and contain inherently critical disadvantages which have led to them never having been widely implemented. Specifically, to measure flux directly, a sophisticated (and likely expensive) sensor must be installed inside the machine during the assembly process. Whilst measuring the inductance directly, a high-frequency AC signal must be injected into the DC excitation current. Thus, in order to cover the range of operation conditions, taking the necessary measurements is relatively time-consuming, as the process must be repeated, beginning with the low excitation current all the way up to the maximum current, incrementally.

   The indirect flux linkage measurement is based on the voltage equation:

$$V = Ri + \frac{d\psi}{dt} \quad (2\text{-}3)$$

   Where V, R, and i represent the voltage, resistance and current of the excited phase. Then the flux linkage ψ can be calculated from the integration:

$$\psi = \int V - Ri \, dt \quad (2\text{-}4)$$

   The calculation of the above integration can be divided into the following methods:

a) Analogue integration – in this case, the integration calculation is fulfilled by using an operational amplifier circuit technique. As a result, the preparative work is relatively time-consuming, and the measurement accuracy will highly depend on the quality of the components.

b) Digital integration – this can eliminate the problems found in the analogue method, as the sampled data is amenable to being smoothed and processed by computer. Moreover, preparations for this method are simple: only a current sensor, voltage sensor, oscilloscope and digital power supply are required.

2) Finite element method (FEM) – the FEM is commonly utilised in contemporary machine-design tasks, as it can provide a high level of accuracy during the simulation process and is widely accessible through a variety of commercial software [47, 48].

In this PhD programme, the Infolytica MagNet is intensively used for electromagnetic FEA (Finite Element Analysis). As can be seen from Appendix 1, Visual Basic scripting is used to produce the motor geometry in this software. The triangular elements of the finite element model are automatically generated in each user-defined component and can be limited to a maximum size. The airgap is the critical area in the FEA, thus it is divided into four layers, by independently setting the mesh size of the airgap components(the tutorial of MagNet suggest the airbox for transient with motion FEA should divide into stator virtual air, stator air, rotor air, and rotor virtual air). This can improve the accuracy of the results.

Compared to the full 3D-model analysis, 2D FEM is widely accepted, absorbing just 15% of the time required by the former [49]. Taking vector potential A as an example, 2D analysis can effectively reduce the complexity of the governing equation relevant to the calculation. To be specific, the flux density can be expressed as $B = curl\ A$ and the current density as $J = curl\ H$. Normally, the relation between A and J is represented as $curl\left(\frac{1}{\mu_0\mu_r} curl\ A\right) = J$, which could be a relatively complicated structure after expansion. But in the two-dimensional environment, only A_z and J_z exist and no variation occurs in the z direction, thus the expression of J could be simplified as such:

$$\frac{\partial}{\partial x}\left(\frac{1}{\mu_0\mu_r}\frac{\partial A_z}{\partial x}\right) + \frac{\partial}{\partial y}\left(\frac{1}{\mu_0\mu_r}\frac{\partial A_z}{\partial y}\right) = -J_z \quad (2\text{-}5)$$

The 2D FEM, however, is undoubtedly less accurate than 3D FEM and experimental test, due to the absence of the following effects:

a) End-winding flux - the conductor that surrounds the stack end produces magnetic flux which is not considered in the 2D analysis. This effect is believed to be the primary source of error between the 3D and 2D FEM [47, 49]. Notably, the flux linkage in the 3D FEM analysis and test results should be higher than that of the 2D FEM. However, since the SRM will often operate under saturated conditions, this extra flux from the end- winding effect would be suppressed near the aligned position, and only effectively reinforces the flux around the unaligned position. As a result, the co-energy, and hence the torque capability, is overrated by the 2D FEM.

b) Axial fringing – this effect represents the phenomenon of flux fringing between the end of the stator and rotor stacks. According to [47, 49], axial fringing could become more apparent when the rotor pole nears its aligned position. However, since the SRM is presumed to be deeply saturated at this position, the axial fringing effect exerts less influence than end-winding flux.

3) An analytical method, known as the 'lumped parameter' method (see Figure 2-1) which considers the magnetic circuit in a similar manner to that of an electric circuit[39, 41, 50, 51].

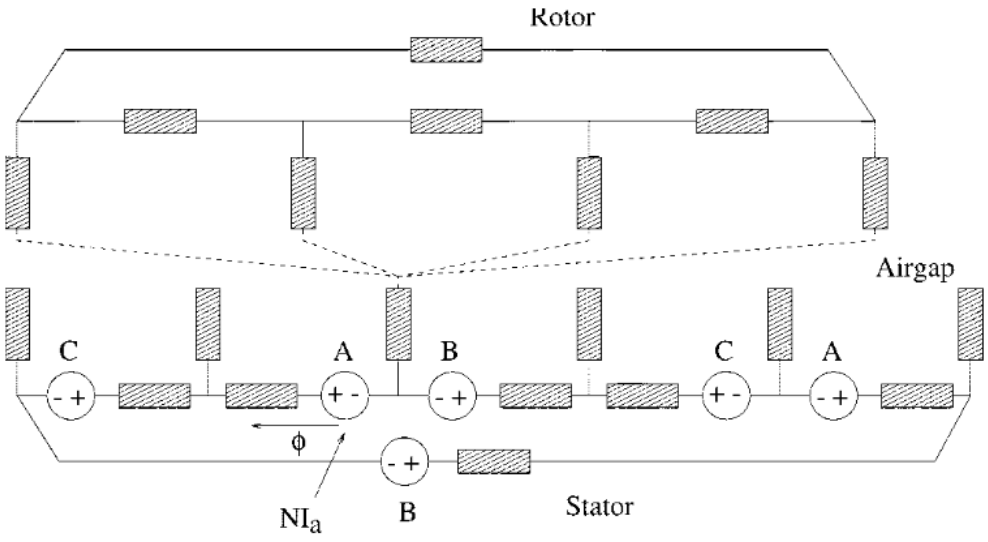

Figure 2-1 An example of a lumped parameter model [51]

With proper settings for the fringing effects in the modelling and using iterative techniques in the processing, this analytical method can also achieve a level of accuracy approaching that of 2D FEM [50]. The major advantage of this method is its economy of time: a magnetisation curve can be calculated in a few seconds, which is much more

efficient than the 2D FEM. Although the calculation speed of the analytical method is reasonably fast, the modelling and code work is relatively time-consuming.

2.3 Performance Improvement of Conventional Switched Reluctance Machines

Since the torque capability of the SRM is generally lower than that of the PMSM, a number of authors have focused their investigations on performance improvement. Moreover, the conventional SRM, as the most fundamental configuration, has attracted attention for decades [27, 31, 52].

Some of the early discussions on this topic, published during the 1990s, could still provide inspiration and instruction. In [53], a systematic analysis is made with the objective of torque maximisation, providing a range of recommended relationships for the various features, such as tooth width/tooth pitch, split ratio (rotor diameter/stator diameter), and back core-to-tooth width ratio. This article offers a valuable template for analysing nonlinear and highly coupled parameters.

Michaelides [54, 55] introduced a simple modification of winding direction that effectively increases torque capability: an individual phase should be oriented in opposition to its adjacent phase. Consequently, a short-flux path is generated when these two phases are energised simultaneously (see Figure 2-2). To take full advantage of this winding arrangement, Michaelides suggests developing a five- or even seven-phase SRM, which will allow two or three phases to be conducting concurrently. This idea was rejected due to the cost of a multitude of components in the converter; but this winding design is widely accepted and applied to most three-phase SRMs, nowadays.

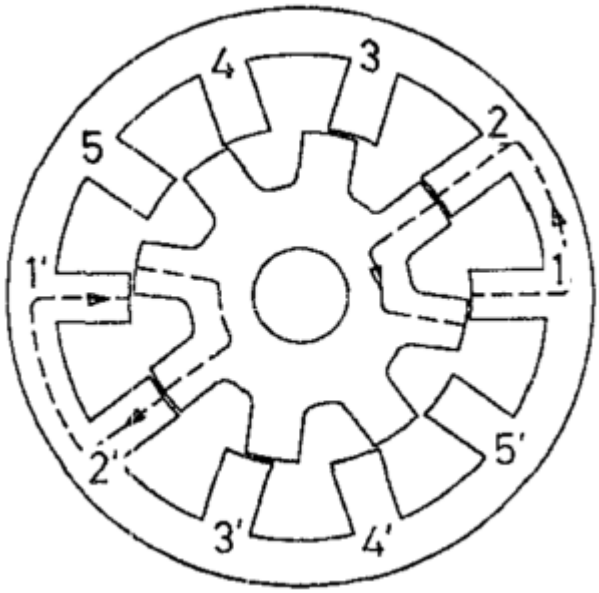

Figure 2-2 Short flux paths are generated where oppositely polarised phases run adjacent to one another [55]

A similar idea for the short-flux path design was proposed by Hendershot [56], where a 12/10 three-phase SRM was developed to reduce core loss and yoke reluctance. A detailed diagram is shown in Figure 2-3, in which the stator demonstrates an uneven pole architecture. Each phase consists of two adjacent poles with opposite polarity to create a short-flux path; however, the uneven design of the stator pole leads to wasted slot area, which results in an undesirable increase in copper loss.

Further development of the short-flux path concept is the E-core SRM[57, 58]. As can be seen from Figure 2-4, this SRM configuration has only two phases, and two isolated E-shaped cores make up the complete stator. Compared to the conventional design, this E-core SRM could benefit from low manufacturing costs and low core losses. Nevertheless, as a two-phase SRM, the application of the E-core is quite limited, and could also produce acoustic noise issues because of the lack of stiffness in the core back.

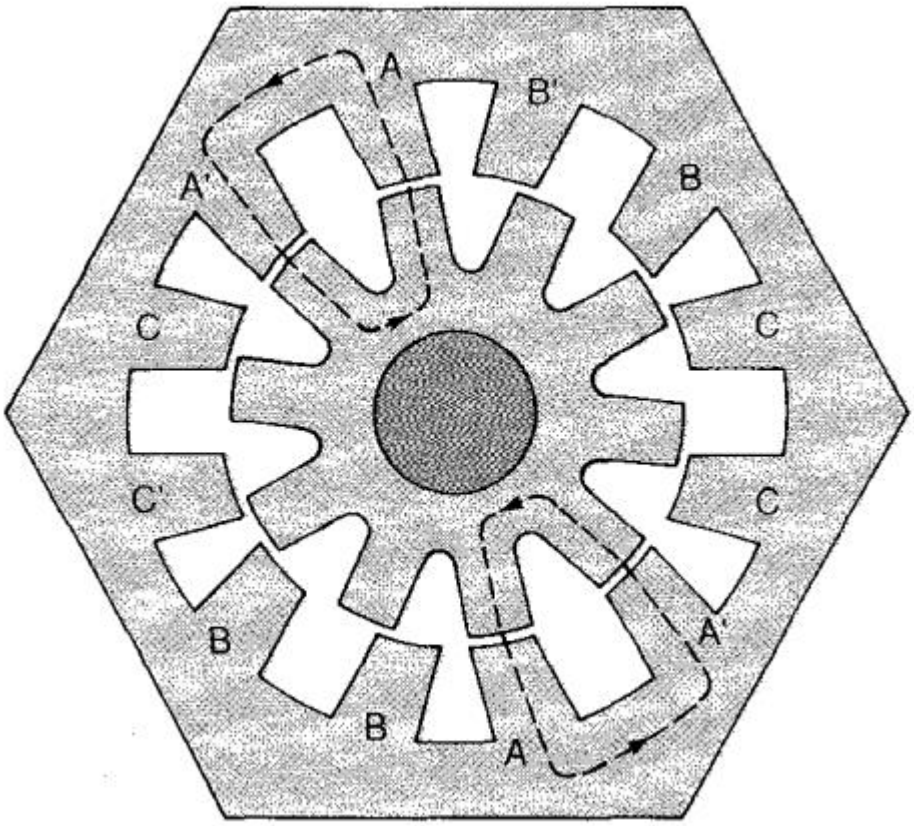

Figure 2-3 Cross section of a 12/10 three-phase SRM with short-flux-path design [54]

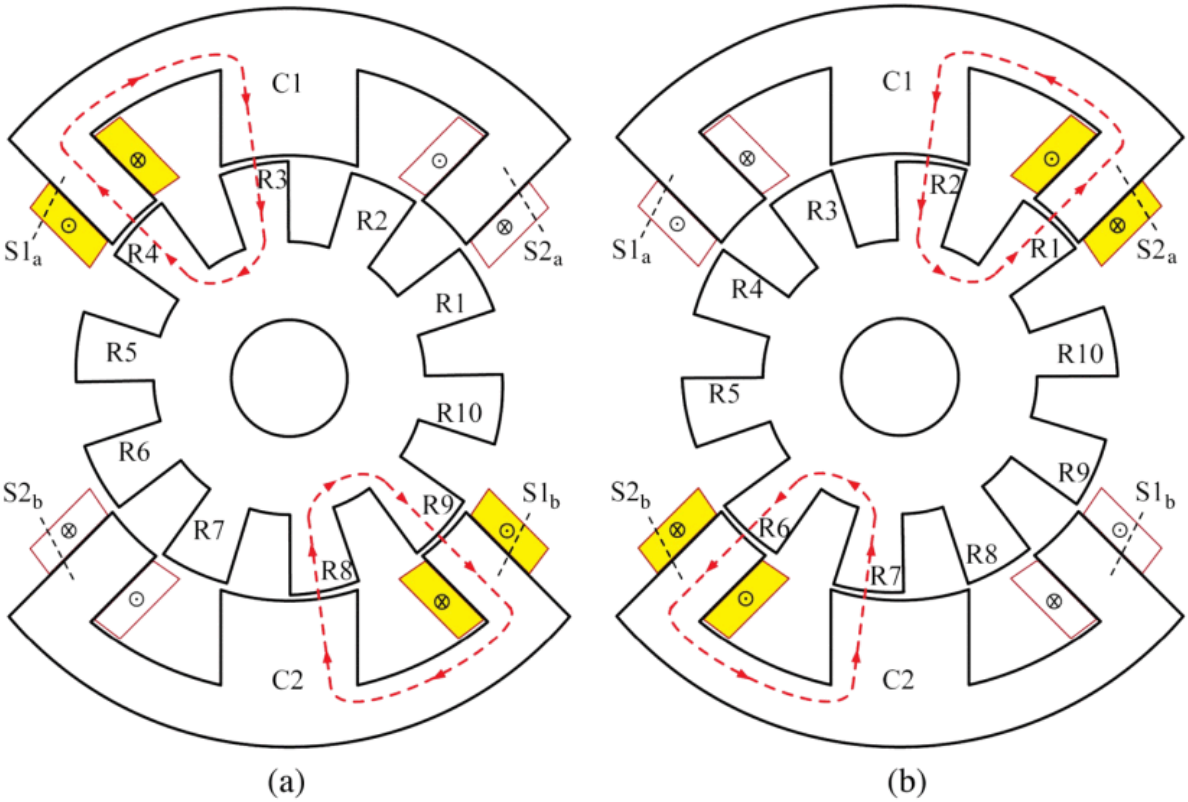

Figure 2-4 Flux path of an E-core SRM [57]

Higher pole numbers are popular in contemporary SRM design[59, 60]; most three-phase SRMs are now designed as 12/8 pole combinations rather than the fundamental 6/4. The origin of this logic is uncertain but the advantages are widely accepted as being the short-flux path and thinner coreback. Moreover, Chiba [61, 62] made comparisons of various pole combinations (including 6/4, 8/6, 12/8, 16/12) and stated that an increase in pole number could lead to an improvement in torque capability. As can be seen from Figure 2-5, the subjects of his comparison were restricted to the same total axial length (stack length + end-winding length). Thus, the conclusions have been affected by the differences in stack length.

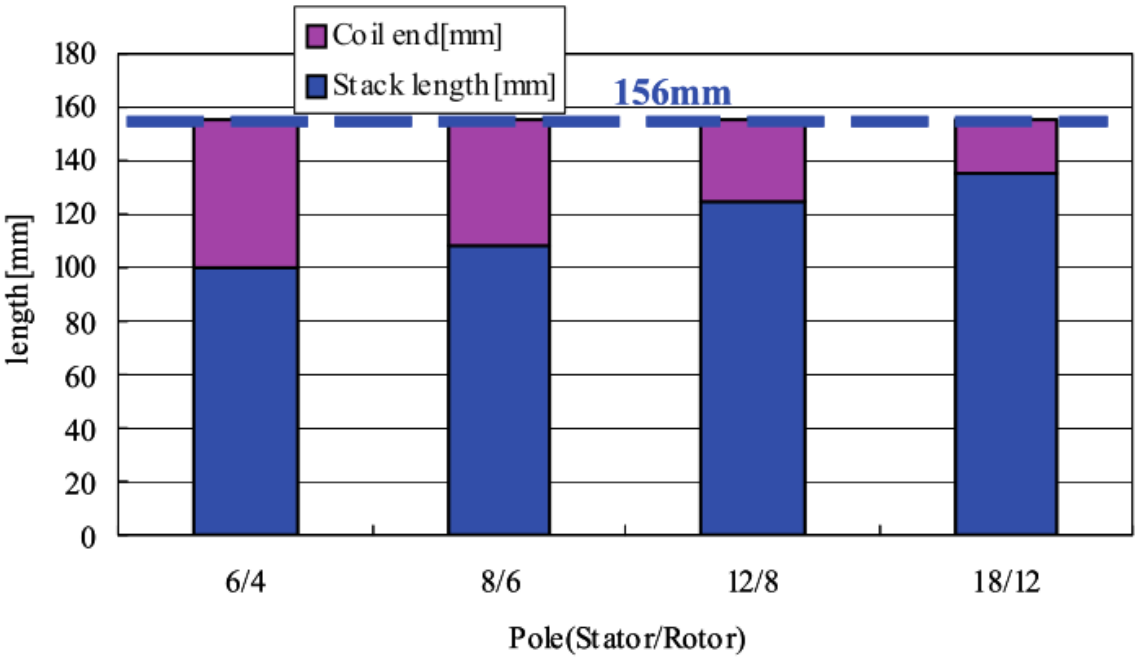

Figure 2-5 The variations in stack length and end winding length for different pole combinations [61]

Based on the above work, Chiba eventually developed a three-phase 18/12 SRM capable of providing torque performance comparable to the PMSM now incorporated into the second-generation Toyota Prius [60, 63-65]. It is possible this study proposed one of the best conventional SRM designs so far developed[26, 52], with a torque density of up to 45 Nm/L and a rated efficiency of up to 92%. This said, however, the current density of this SRM was approximately 32 A/mm^2 (with a fill factor of 0.57), which could represent a challenge, even for a state-of-the-art cooling system.

An SRM with a higher number of rotor than stator poles has also attracted some attention and prototypes have been explored [66-68]. According to [31], these SRMs could offer numerous

advantages, such as higher torque capability, lower torque ripple, and lower material costs over a conventional design (6/4 SRM and 8/6 SRM). However, the simulation and experimental results in [66-68] were found to exhibit a relatively low current density. Considering these machines have a narrow-pole configuration, a decline in performance could be expected during saturation conditions.

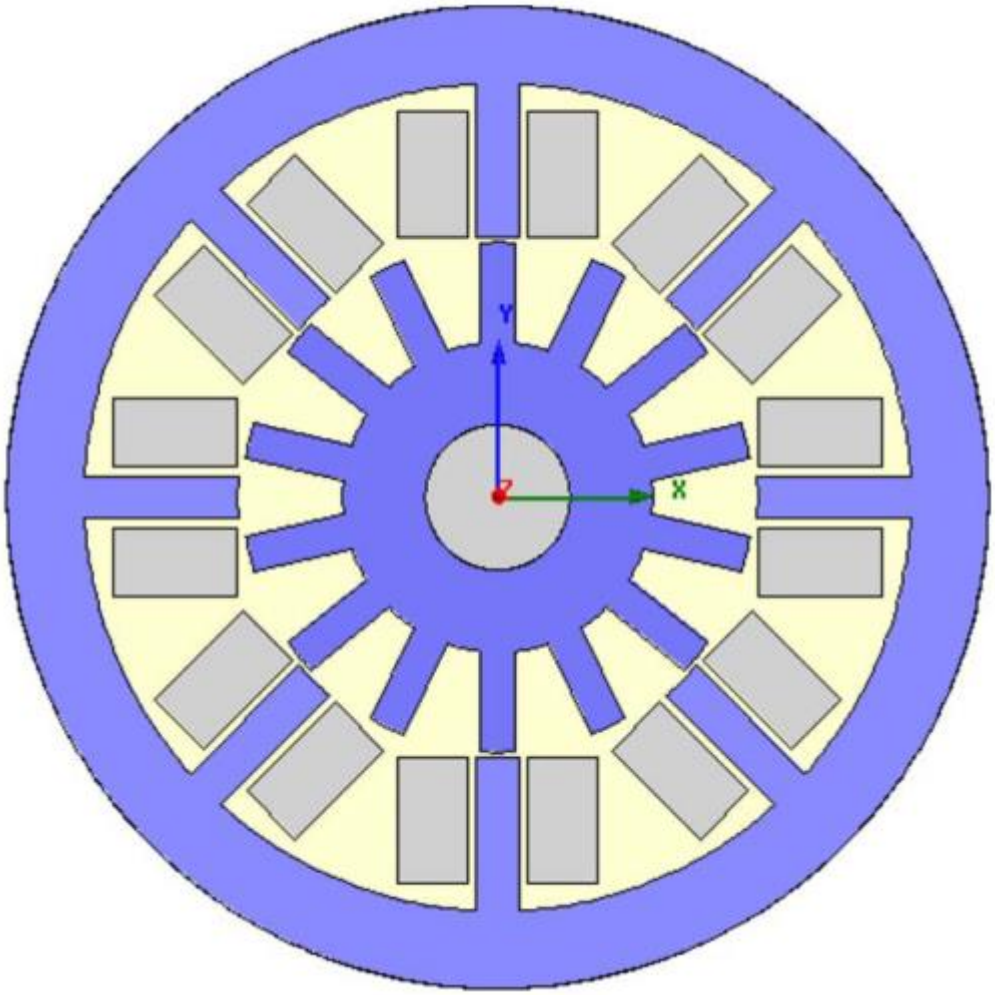

Figure 2-6 Cross section of an 8/14 SRM [67]

Instead of enhancing torque capability, the development of a high-speed SRM is another means of achieving the desired performance for vehicle traction[69, 70]. In [70], a high-speed SRM prototype is presented with a maximum speed of 50,000 rpm. The proposed machine is claimed to offer a compatible power density to that of the PMSM used in the third-generation Toyota Prius. Nevertheless, the extremely high speed could give rise to unexpected engineering challenges relating to the rotor design, of both mechanical and thermal properties.

2.4 Segmental Rotor Switched Reluctance Machines

The segmental-rotor SRM is a novel structure which could provide higher torque capacity than a conventional design. The first attempt at utilising a segmental-rotor design is believed to have been made by Horst who filed a patent for a two-phase SRM with unidirectional operation [71]. However, the version of the segmental-rotor SRM investigated in this study was devised by Mecrow[32, 72, 73]. In general, the pole arc-to-pole pitch ratio of a conventional SRM should be restricted to no more than 0.5 – otherwise, the unaligned inductance will not be maintained at a low level; however, in the segmental-rotor SRM, the pole arc-to-pitch ratio could near 0.7 without sacrificing the inductance ratio between the aligned and unaligned positions (see Figure 2-7). As a result, the torque capability of the segmental-rotor SRM could be as much as 40% higher than a conventional SRM with the same volume and copper loss.[72]

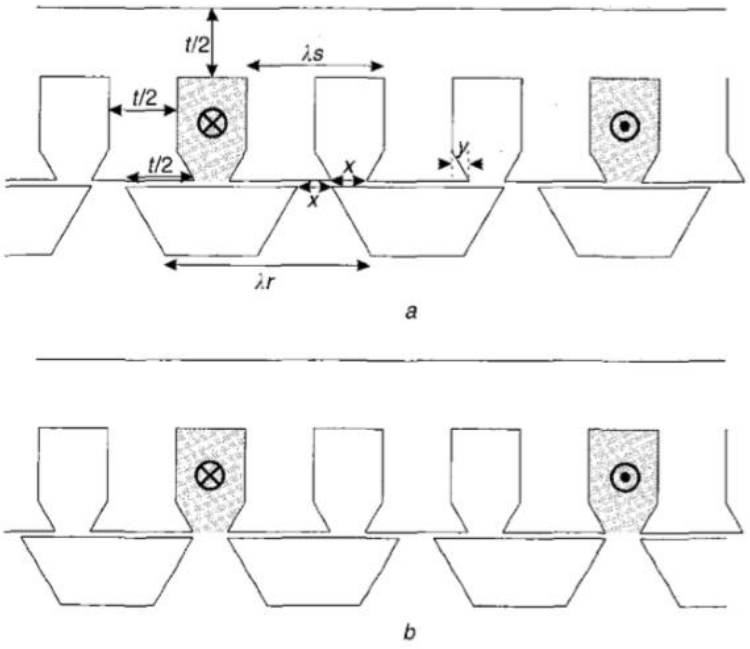

Figure 2-7 A rectilinear model of the segmental-rotor SRM: *a* = aligned position; *b* = *unaligned* position [72]

Based on the original structure, which had a fully-pitched winding design, a single-tooth winding version was developed in [74]. This variant can be seen from Figure 2-8, where both copper loss and electromagnetic performance are reduced compared to the fully-pitched segmental-rotor SRM. Nevertheless, a detailed comparison reveals that the single-tooth segmental SRM could deliver the same torque at a similar copper loss as the fully pitched version, whilst reducing the copper material usage by 29% [74]. Numerous authors have been working on further developing Mecrow's design [75-78] but significant improvements have not yet been made.

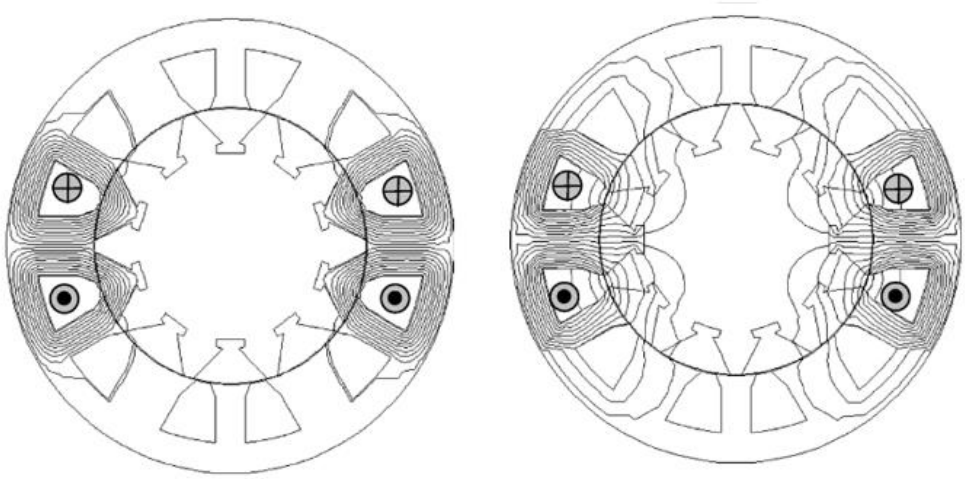

Figure 2-8 Magnetic flux plot for the single-tooth segmental SRM [73]. Left: aligned position. Right: unaligned position

Since the segmental SRM has a significantly better torque capability than the conventional SRM, the development for vehicle traction was considered in [79] where an 80kw segmental SRM is proposed to compare with the PMSM from Nissan Leaf.

However, any advantages of the segmental SRM are overshadowed by the following disadvantages:

- The energy conversion loop of the segmental SRM is considered to be worse than the conventional SRM, as the flux linkage is relatively large at the unaligned position and, therefore, would consume a higher VA rating from the drive.
- The advantage of performance could be undermined under high magnetic saturation - for instance, the magnetisation curve at the unaligned position would be steeper at the aligned position, causing the energy conversion loop to deteriorate (see Figure 2-9).

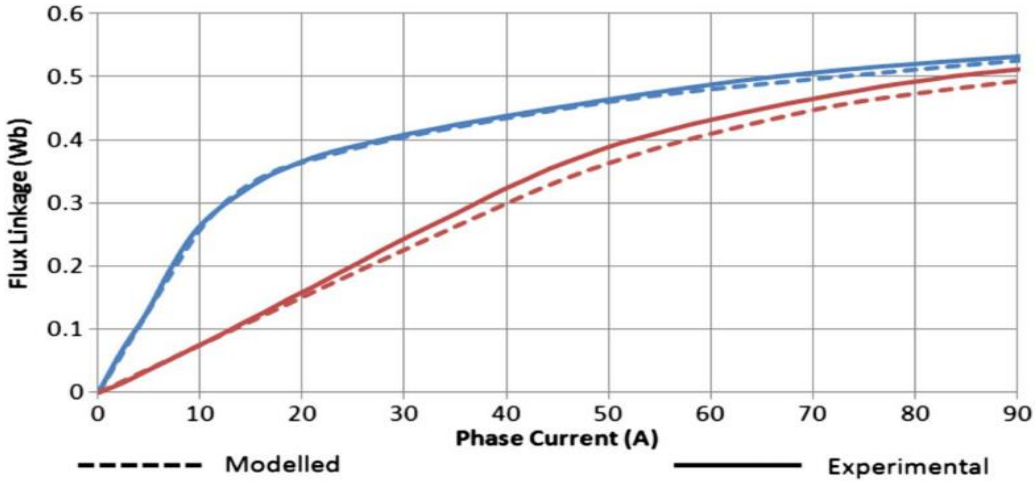

Figure 2-9 Magnetisation curve of an SRSRM [80]

- Cross-saturation can occur during phase interaction as one stator pole will temporarily carry flux from two adjacent phases, giving rise to local saturation, which could reduce the average torque expected.

2.5 Double Stator Switched Reluctance Machines

The double-stator SRM (DSSRM) has been researched extensively in recent years [81-83], The configuration of this machine was developed by Abbasian [33, 83](see Figure 2-10) and is actually a segmental-rotor SRM (SRSRM) with an extra inner stator providing higher torque capability. In [33], the development of this novel structure is described as having stemmed from an analysis of the surface force at the airgap using the Maxwell stress tensor method [84]: the author claimed that the flux density in the tangential direction is critical to the motional force, while the flux density in the normal direction would merely be a sign of poor utilisation of energy conversion. As can be seen from Figure 2-10, Abbasian believed that the flux path in the DSSM could effectively suppress the flux density in the normal direction and, therefore, enhance the efficiency of the energy conversion.

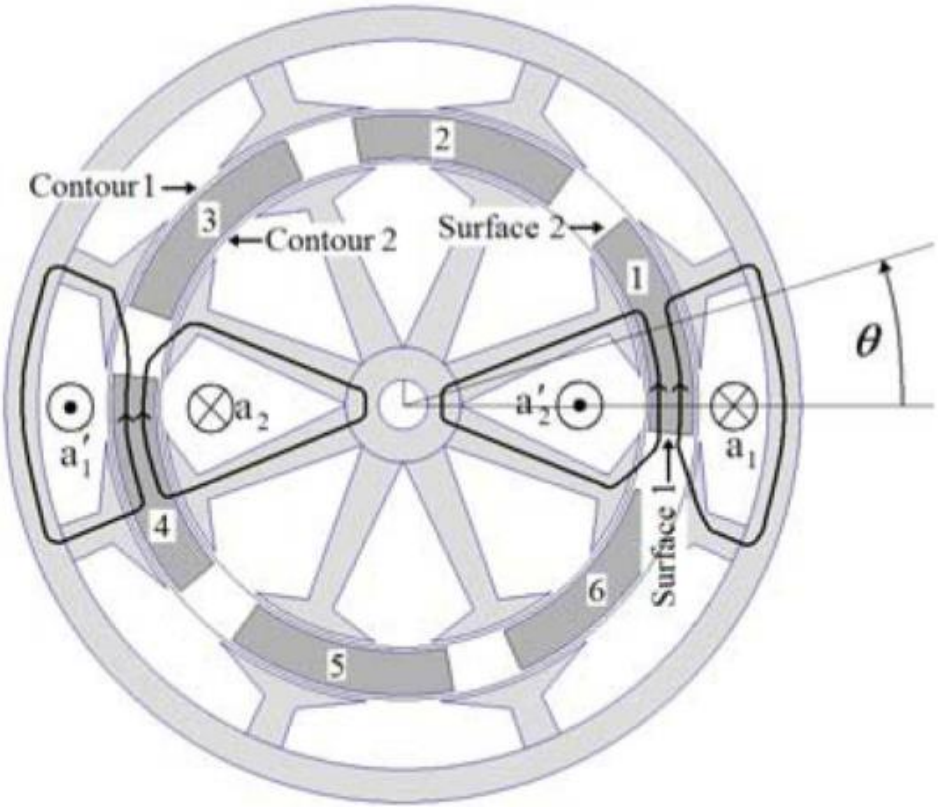

Figure 2-10 the cross-section of a DSSRM [33]

An analysis of transient force distribution would not necessarily ensure better overall performance as the airgap flux density variation is highly nonlinear in the SRM. However, only considering arrangement of the inner stator, which effectively improves the utilisation of

volume, a considerable torque density enhancement could still be expected from the DSSRM. According to [26, 85], the DSSRM can provide a torque density of 43.5 Nm/L as a liquid-cooling machine. On the other hand, although the performance of the DSSRM is highly praised in [86], the airgap force distribution analysis in that paper does not indicate the necessity of reducing the normal flux density. Consequently, although the ratio between normal and tangential flux density can affect the local force distribution in transient position, the high torque density of the DSSRM should be mainly attributed to the inherent flux path from the segmental-rotor configuration and the better utilisation of motor volume by the introduction of an inner stator.

Since the DSSRM possesses the inherent characteristics of the SRSRM, there is no doubt that the disadvantages of the SRSRM are also present in the DSSRM; moreover, the cross-saturation issues of the DSSRM not only occurr at the stator pole during phase interaction but also in the rotor segment, since the flux path is shared between both the inner and outer windings. According to [86], although the DSSRM can potentially provide a higher torque density than the SR-SRM due to a more compact configuration, other than that, its copper usage and average loss do not reveal clear superiority over the SRSRM when restricted to the same torque production.

A different configuration for a DSSRM is revealed in [34, 87, 88] with the flux path more similar to a conventional SRM than the SRSRM (see Figure 2-11); however, the purpose of this design is described as eliminating the radial force on the rotor – torque capability analysis and design optimisation for torque production are not examined in these works. A similar configuration is reported in [89] (see Figure 2-12), where a yokeless SRM is said to have been developed from the concept of the C-core SRM [90]

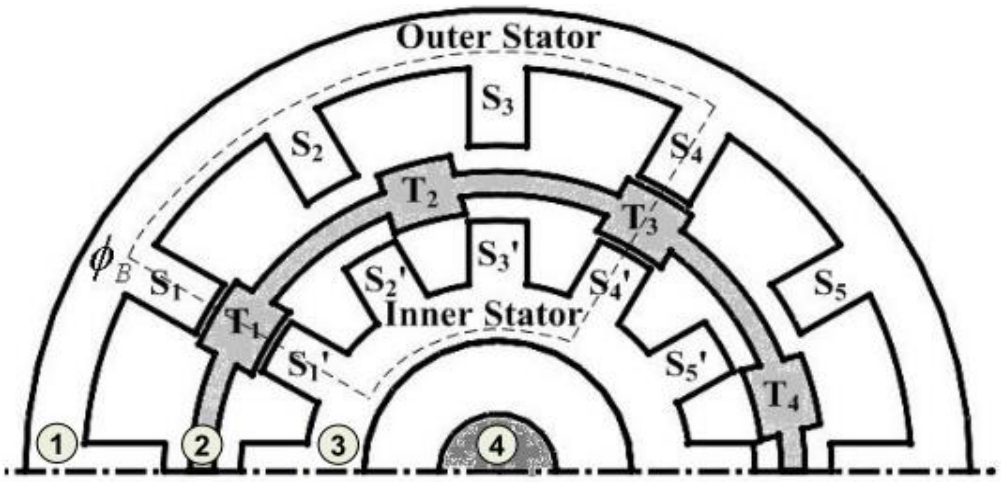

Figure 2-11 Cross section of a double-stator conventional SRM [87]

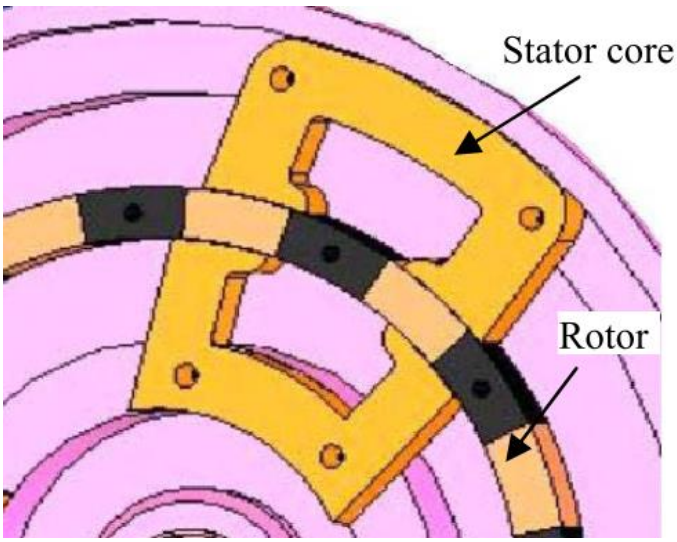

Figure 2-12 Structure of the yokeless SRM [89]

As a novel high-performance machine, the thermal analysis of DSSRM is investigated in[91]. Figure 2-13 shows that the prototype is a water-cooling DSSRM with a water jacket in both outer stator and inner stator. Since the cooling jacket for the inner stator is relatively small, the maximum temperature of inner winding is finally found 16℃ higher than the outer winding while the machine is energised with a current density of 10A/mm^2.

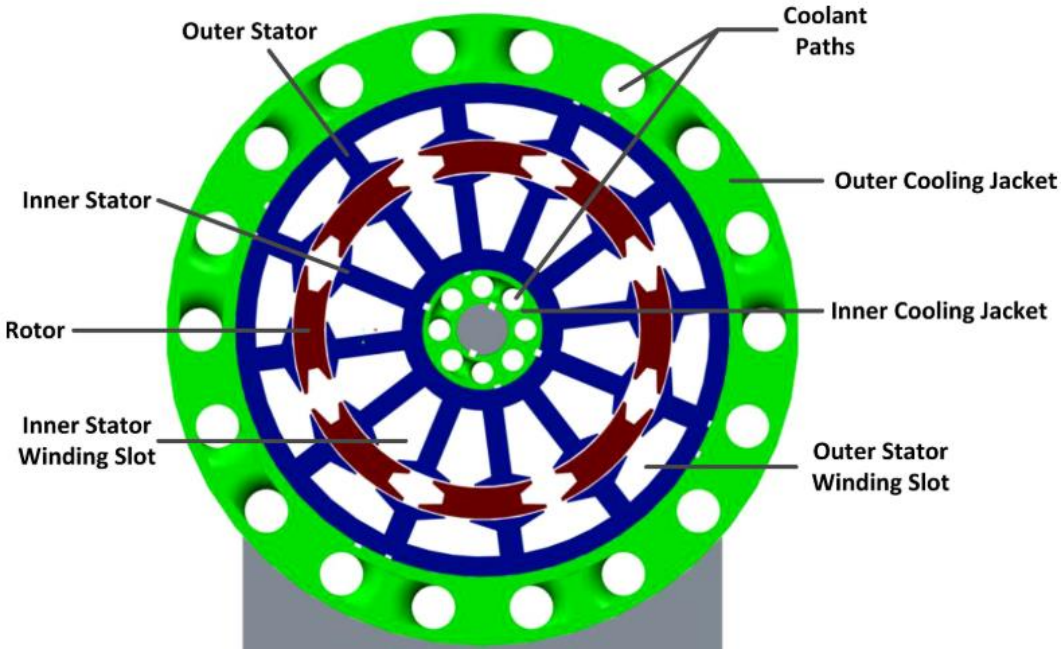

Figure 2-13 Cooling system of a DSSRM [91]

Furthermore, the rotor of the DSSRM is undoubtedly less robust than that of the conventional SRM, due to its segmental structure, and the use of metallic material in the rotor supporter is not recommended if a large eddy-current loss is to be avoided. Since most composite materials

could hardly provide a stiffness comparable to stainless steel, a considerable engineering challenge remains with regard to this application. It is also surprising to notice that discussions and analyses of the DSSRM rotor's mechanical properties in recent studies have not come close to resolving this challenge.

2.6 Development of Mutual Coupled Switched Reluctance Machines

Unlike conventional SRMs which are mainly driven by a variation in self-inductance, the mutually coupled SRM (MCSRM) is able to utilise mutual inductance for torque production. The first MCSRM, which was introduced by Mecrow [92], is a fully pitched SRM(see Figure 2-14). During normal operational conditions, this fully pitched SRM should energise at least two phases, simultaneously; its excitation methods, including the two-phase unipolar, two-phase bipolar, three-phase bipolar and sinusoidal are compared in [92, 93]. With unipolar excitation, the fully pitched SRM is reported to produce maximum average torque, which is about 25% higher than the conventional SRM[92]; however, the fully pitched winding leads to relatively large end-winding which could compromise its torque-to-volume advantage over the conventional SRM.

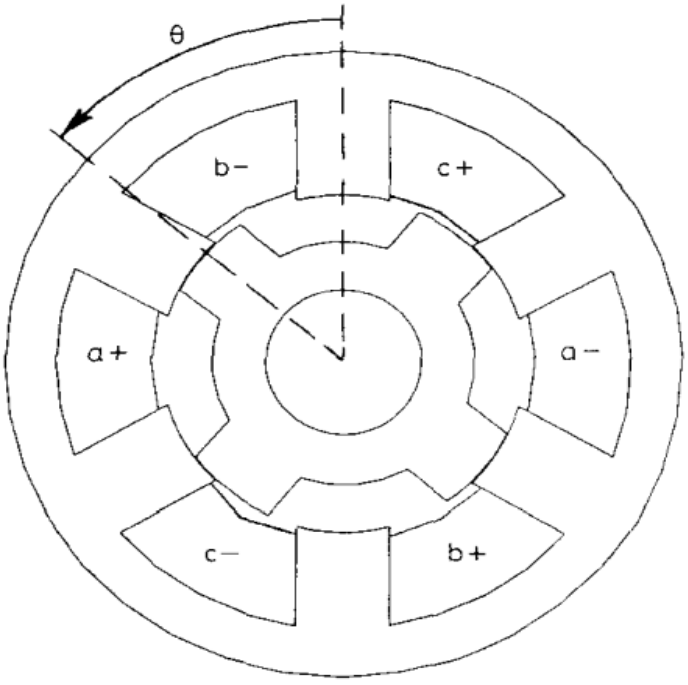

Figure 2-14 The structure and winding configuration of a fully pitched SRM [92]

In addition, mutual coupling effects also exist in the conventional single-tooth SRM and were analysed in [94-97], but, in most cases, the mutual inductance is neglible compared to the self-inductance in the torque production. In [98], an MCSRM with single-tooth winding and bipolar

excitation were introduced. Figure 2-15 shows that the winding arrangement is different from the conventional SRM: the two coils in the same phase are opposite one another. According to [35, 99, 100], the single-tooth MCSRM not only provides higher torque density than the conventional SRM but also eliminates the drawbacks of the fully pitched SRM.

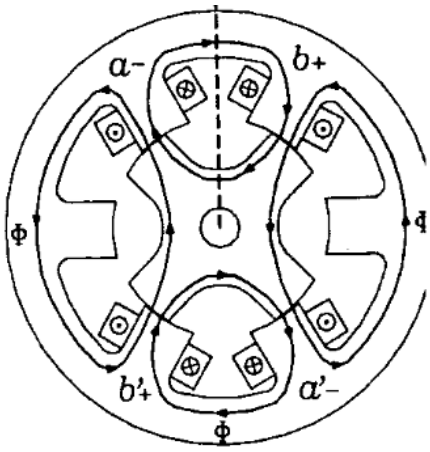

Figure 2-15 The flux path and coil arrangement of a single-tooth MCSRM [98]

However, in an odd number phase SRM (such as a three-phase), the opposing winding arrangement will have difficulty in maintaining a continuous pattern unless a bipolar excitation is avialable. The even-number phase SRM (such as a four-phase) could have an innate advantage to prevent this awkward situation. Widmer et al. in [101] compared a variety of winding configurations for a six-phase 12/10 SRM and revealed that the opposing winding arrangement (see Figure 2-16) found in the single-tooth MCSRM provide the best torque capability and lowest number of torque ripples. A larger prototype of this six-phase SRM has been developed for hybrid-truck traction, with a torque density of 61 Nm/L at a current density of 20 A/mm^2.

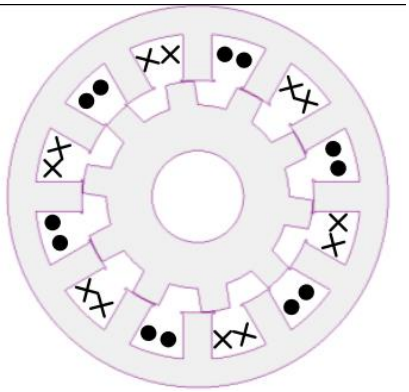

Figure 2-16 Opposing coil arrangement for the 12/10 six-phase SRM, equivalent to a six-phase MCSRM[101]

2.7 Conclusion

A variety of methods for improving the performance of SRMs have been explored.

Those studies which have assessed the conventional SRM and deemed it valid can be essentially divided into two categories: use of the short-flux path design to reduce Magnetic Motive Force (MMF) consumption in the iron core (to reduce reluctance and, thereby, increase the energy conversion in each stroke); an increase in the number of strokes per revolution with proper pole combinations.

The MCSRM appears to be a conventional SRM with a novel winding arrangement. Unlike the initial design which is also known as a fully pitched SRM, several studies present the MCSRM as a single-tooth winding, eliminating the drawbacks of enormous end-winding. In addition, some research indicates that an even phase-number configuration should be more suitable for the MCSRM.

The SRSRM is proposed as a potential novel SRM for torque improvement; however, its disadvantages, such as large unaligned inductance and cross-saturation issues, would raise the cost of the converter (greater volt–ampere and bipolar excitation) and undermine its performance under highly saturated conditions.

The DSSRM can be considered as a descendant of the SRSRM, while its inner stator is able to further enhance torque density. On the other hand, it also inherits all the disadvantages of the SRSRM. It is worth noting that the double-stator structure can also be implemented in conjunction with the conventional SRM, which could hints at a way to avoid the aforementioned drawbacks and could also be a means of enhancing the performance of the conventional SRM. Additionally, the rotor segments of the present DSSRM are mainly supported by stainless steel, which very likely leads to large eddy current loss and thermal issues (see Section 5.1.2).

Chapter 3. Comparison between Three-Phase SRM and Four-Phase SRM

Chapter 2 describes several methods for developing high-performance SRMs. It shows that the segmental rotor SRM does not necessarily provide higher torque than conventional SRM in some scenario (i.e. when the workload is relatively large). Most double stator SRMs, which have attracted attention in recent years, are based on the magnetic circuit from segmental rotor SRM. There are therefore concerns surrounding developing a double stator SRM magnetic circuit from conventional SRMs.

Recently published work on conventional SRM designs reveals a preference for high pole number topologies. Compared to multiple of the of standard 6/4 combination, such as 12/8 or 18/12, the discussions of higher phase number conditions is insufficient, as the same benefits may be achievable with the three phase multiples above.

The aim of Chapter 3 is to conduct a study of the impact of increasing phase number upon torque production. An analytical method is used to generate an estimation equation to predict the performance of SRMs with different phase number when only airgap reluctance is considered. The result is verified using static 2D finite element analysis, and suggests the SRM with higher phase number could outperform the three-phase SRM when the iron core occupies a large portion of the reluctance in the magnetic path.

Further analytical analysis is undertaken for comparison between three-phase and four-phase SRMs. By using a simplified model, it concludes that the four-phase candidate would perform better than its 3-phase competitor under a range of conditions. The conclusion is then verified and confirmed by 2D transient finite element analysis.

3.1 The Behaviours of Higher Phase Number SRMs regarding Torque Performance

Over the decades, the three-phase electric motor has dominated industry applications. Unlike other AC motors, the SRM has a unique inverter whose phases are isolated from each other. As such, the SRM has the freedom to be constructed with a higher phase number. The question is whether is it worth designing such an SRM, since it could lead to extra cost owing to the greater number of electronic power devices in the drive system.

A high phase number often means a high pole number which would provide the following advantages:

1. Increasing the pole number will reduce the width of each pole. As a result, the stator yoke width requirement will be reduced as well, giving more space for the rotor and the winding.
2. A narrow stator pole will decrease the length of the end-winding, reducing the winding resistance and overall axial length.

Meanwhile, the high pole number design could suffer several disadvantages:

1. Increasing the pole number would increase the commutation frequency, which would lead to a rise of core loss.
2. If higher phase number is considered, the inverter could require either more power electronic components or a complicated deisgn topology, which will eventually increase the system cost.

3.1.1 Developing the Torque Equation with the Assumption of Airgap-only Reluctance

In the first instance, the analysis used a model that only gave consideration to the airgap reluctance. Figure 3-1 shows a typical flux linkage-vs-current curve for an SRM in this situation:

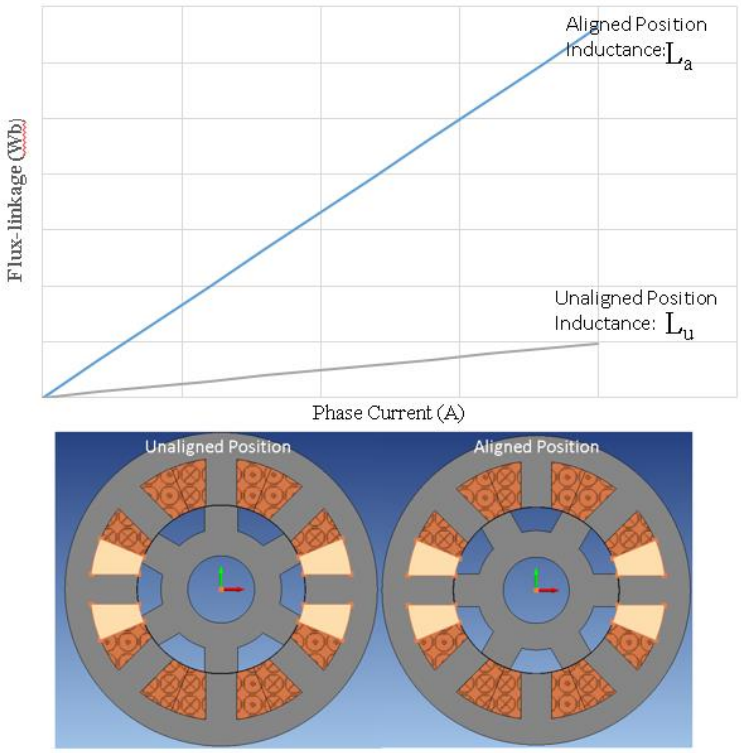

Figure 3-1 A basic flux-linkage vs current curve for the unaligned position and aligned position of SRM (linear condition) and the section figure of a typical 6/4 SRM at these two positions

It is easy to derive the co-energy which contributes to the mechanical output from the magnetisation curve at the unaligned and aligned positions:

$$W = \frac{(L_a - L_u)I^2}{2} = \frac{L_a}{2}\left(1 - \frac{L_u}{L_a}\right)I^2 \quad (3\text{-}1)$$

L_a is the inductance for the aligned position and L_u is the inductance for the unaligned position. Since only airgap reluctance is being considered at this stage, L_a can be deduced as follows:

$$L_a = \frac{N^2}{\mathcal{R}} \quad (3\text{-}2)$$

In the above equation, N is the number of turns and $\mathcal{R}$ is the magnetic reluctance. The reluctance can be further disassembled into l, μ, and A which represent the flux-path length, permeability and section area, respectively:

$$\mathcal{R} = \frac{l}{\mu A} \quad (3\text{-}3)$$

For the aligned position, the airgap reluctance can be derived from the airgap length g, permeability μ_0, bore diameter D, stator pole arc β_s, and stack length L:

$$\mathcal{R} = \frac{2g}{\mu_0 D \beta_s L} \quad (3\text{-}4)$$

In [36], the average torque of the SRM was determined from the energy conversion loop and the number of strokes per revolution:

$$T = \frac{mN_r}{2\pi} W \quad (3\text{-}5)$$

Combining the above equations; the average torque can be represented by the following equation:

$$T = \frac{\mu_0}{8\pi g} mN_r DL\beta_s N^2 I^2 k_l k_p \quad (3\text{-}6)$$

k_l and k_p are coefficients which are introduced to represent respectively $(1 - \frac{L_u}{La})$ and the phase interaction coefficient (the ratio between the average torque and superposition of the single-phase torque). A rough comparison can be made, based on this equation. In order to make this comparison between the different phase numbers fair, each machine is defined as having the same D, L, N and g; while β_s and I are inversely proportional to the phase number.

It can also be easily seen that La will show an inversely proportional relation to the phase number. On the other hand, L_u would not be that straightforward since the flux at this position is complicated [50]. The Figure 3-2 shows a typical example of flux distribution at the

unaligned position. As can be seen here, the flux path is dominated by a 'fringing effect', which is mentioned in [51].

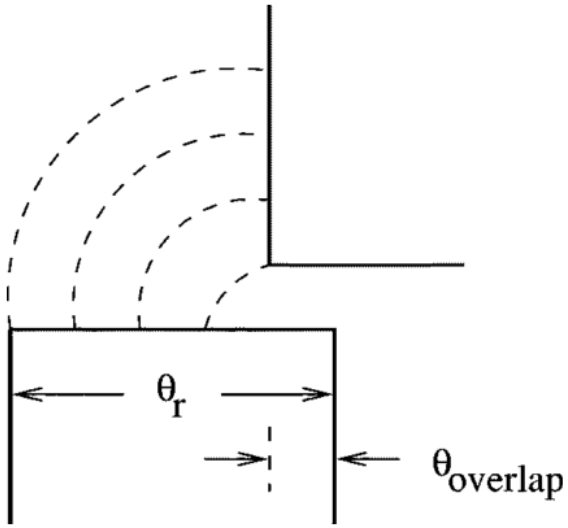

Figure 3-2 The example of fringing effects which describe the flux path from the face of one pole to the side of another pole[51]

In these circumstances, both the cross section and length of the 'fringing' flux path keep a linear relation to the stator pole width, which equals to $D\beta_s$. Consequently, the unaligned inductance L_u will remain at a similar level when just increasing the phase number during this comparison (this analysis could be less accurate when the change in phase number is large).

Taking a three-phase 6/4 SRM as standard, if it is assumed that the inductance ratio of this SRM is between 5 and 10, the range of $k_l$would be between 0.8 to 0.9. Its rival, a four-phase 8/6 SRM (with the same airgap length g, permeanbility μ_0, bore diameter D, stator pole arc β_s, and stack length L) would have a k_l range of approximately 0.7333 to 0.8666.

Thus, it can be derived that the torque (only airgap reluctance is considered at this stage)from the 8/6 SRM must be circa 0.773 to 0.813 of the 6/4 SRM. Similarly, it can be inferred that, as the number of phases increases, the torque will experience a decrease at this very condition(see Figure 3-3). Therefore, if the permeability of lamination steel is assumed to be infinite, the justification provided for considering an SRM with a higher phase number is insufficient.

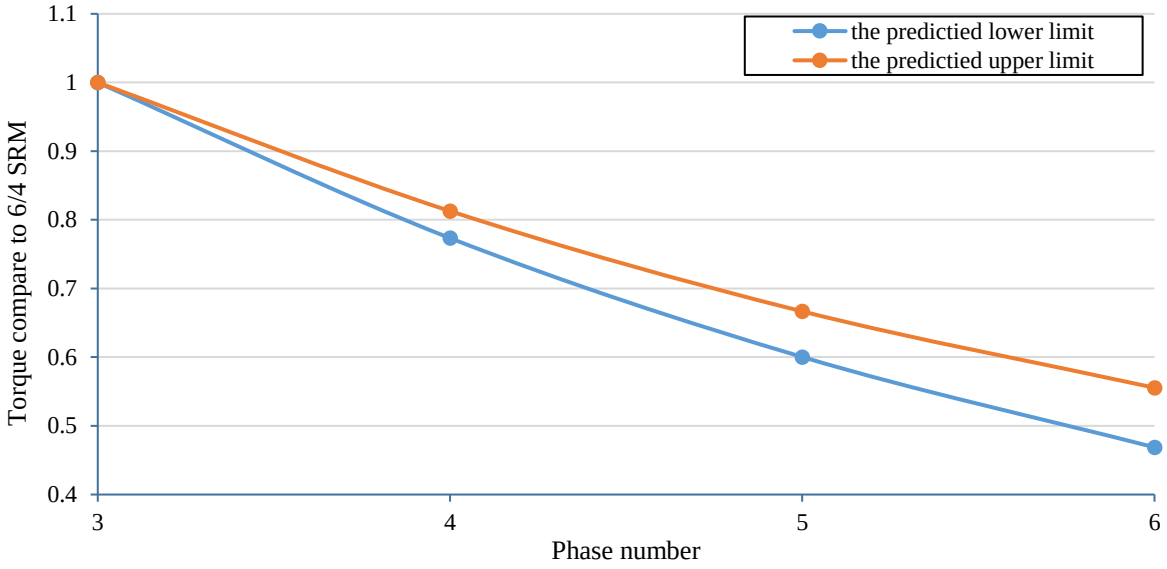

Figure 3-3 Torque production compared to the three-phase SRM using the analytical method (only considering airgap reluctance)

3.1.2 Verification using the 2D Finite Element Method and Considering the Nonlinear Condition

The 2D Finite Element Method (FEM) is a commonly used analysis for studying the electromagnetic characteristics of an electric motor. Since this method can provide a much more reliable estimate than the analytical method, it was used to verify the conclusions from the previous analysis and was utilised in further investigations.

As can be seen from Figure 3-4, four SRM models were created in Infolytica MagNet. To follow the setting of the analytical analysis in Section 3.1.1, parameters, such as the outer diameter, airgap, stator yoke, turns number, rotor diameter and rotor yoke, were kept equal in all the models. Meanwhile, the stator- and rotor-pole arcs were identical for the same motor, while being inversely proportional to the phase number in different models. Thus, the maximum current will also be set to inversely proportional to the phase number, to keep the same current density and copper loss in those models.

In order to ensure the accuracy, the default maximum element size of the mesh is limited to 1mm (based on author's experience, further reducing the mesh size won't improve the solving accuracy, and the software automatically applies a much smaller mesh in essential areas, such as the air-gap). And since the investigation is focused on the average torque in the ideal condition, the simulation assumes to current control (equivalent to the condition when the motor operates at low speed or has a large DC voltage reserve).

These 2D FEM results (based on the average torque under current control during a full electric cycle) confirmed the trend which is predicted in the previous analysis was accurate – a comparison is shown in Figure 3-5.

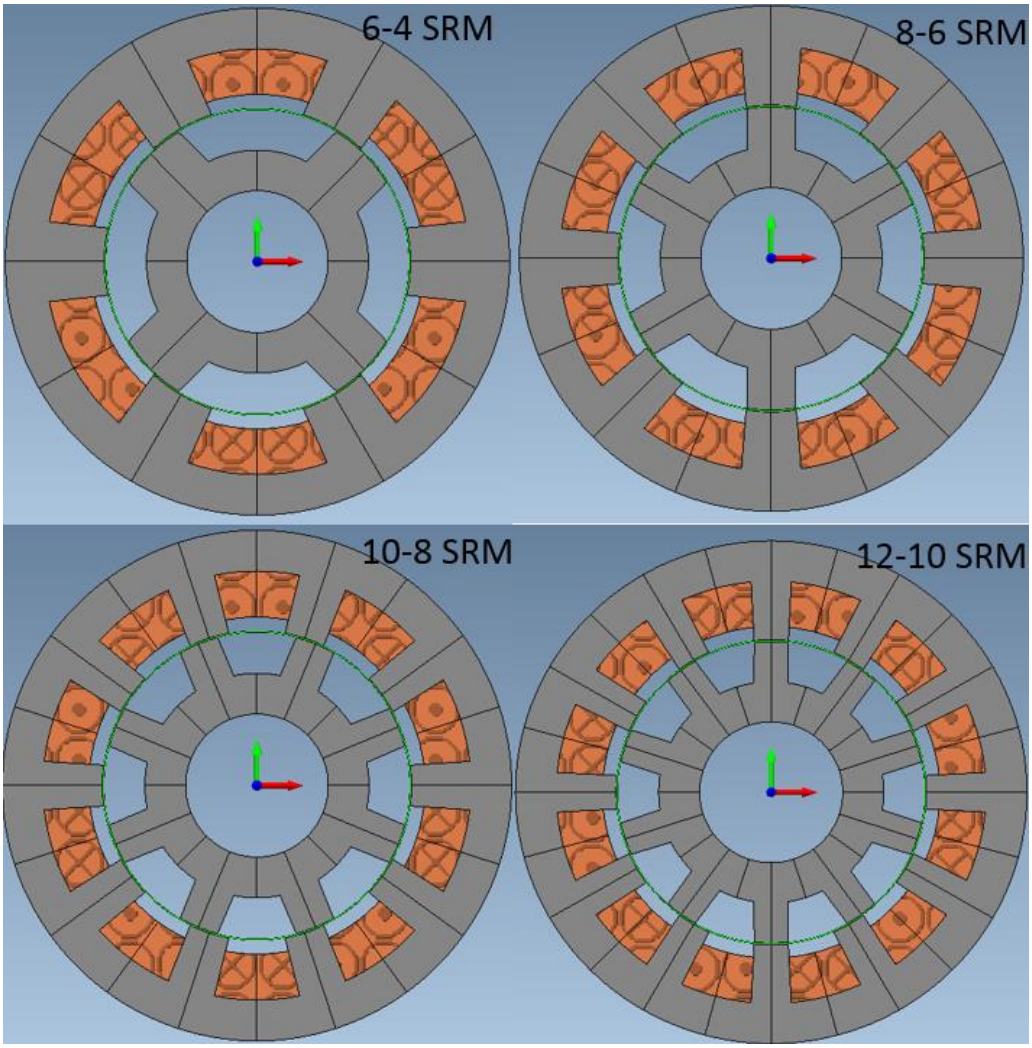

Figure 3-4 The 2D FE models for the 6/4 (three-phase), 8/6 (four-phase), 10/8 (five-phase), and 12/10 (six-phase) SRMs

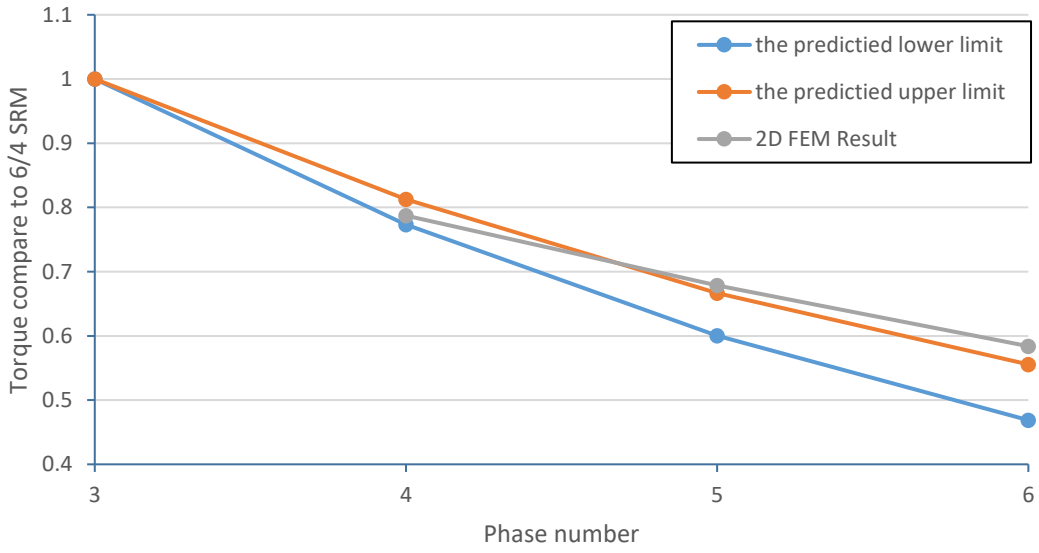

Figure 3-5 A comparison of the 2D FEM and analytical method results

The conditions in the previous analysis, where only airgap reluctance is important, do not exist in reality; therefore, the reluctance of the lamination component needed to be introduced into the investigation. Firstly, the lamination material in the simulation was set to constant permeability to simulate the conditions when the SRM is operating within the linear region. The results can be seen from the TABLE 3-1; , which shows that, under these circumstances, the torque drops while an increase in phase number is mitigated. And k_p is used to demonstrate the ratio between average torque and the superposition of single phase torque.

TABLE 3-1 THE 2D FEM RESULTS (LINEAR PERMEABILITY IN LAMINATION STEEL) FOR THE 6/4, 8/6, 10/8 AND 12/10 SRMS

Linear Permeability	6/4SRM	8/6SRM	10/8SRM	12/10SRM	Unit
Average torque	111.68	101.21	108.66	97.28	Nm
Average torque single phase	70.66	46.88	34.04	25.57	Nm
k_p	1.05	1.07	1.27	1.26	

It was presumed that, although a lower number of phases in the absence of magnetic reluctance in the laminationsd, any advantage would be lost when lamination steel was introduced into the magnetic circuit. To prove this, a new group of comparisons was made by applying modifications to the geometry to allocate more reluctance into the lamination steel component

rather than the airgap. In actuality, this condition was able to be verified by reducing the airgap length of the 6/4 and 8/6 SRMs from 3 mm to 2 mm; the results from the 2D FEM are shown in TABLE 3-2.

TABLE 3-2 THE 2D FEM RESULTS (LINEAR PERMEABILITY AND REDUCED AIRGAP) FOR THE 6/4 AND 8/6 SRMS

linear	6/4SRM	8/6SRM
Average torque	162.7	184.4

A similar result was achieved by decreasing the permeability in the lamination material. Saturation is a common cause of lowered permeability and it is not an unusual scenario for an SRM to be operating in a deeply saturated region.

Subsequently, by setting the lamination material to M270-35A steel (the B-H curve is shown in Figure 3-6), a new comparison was obtained, which factored in the saturation effect (see TABLE 3-3).

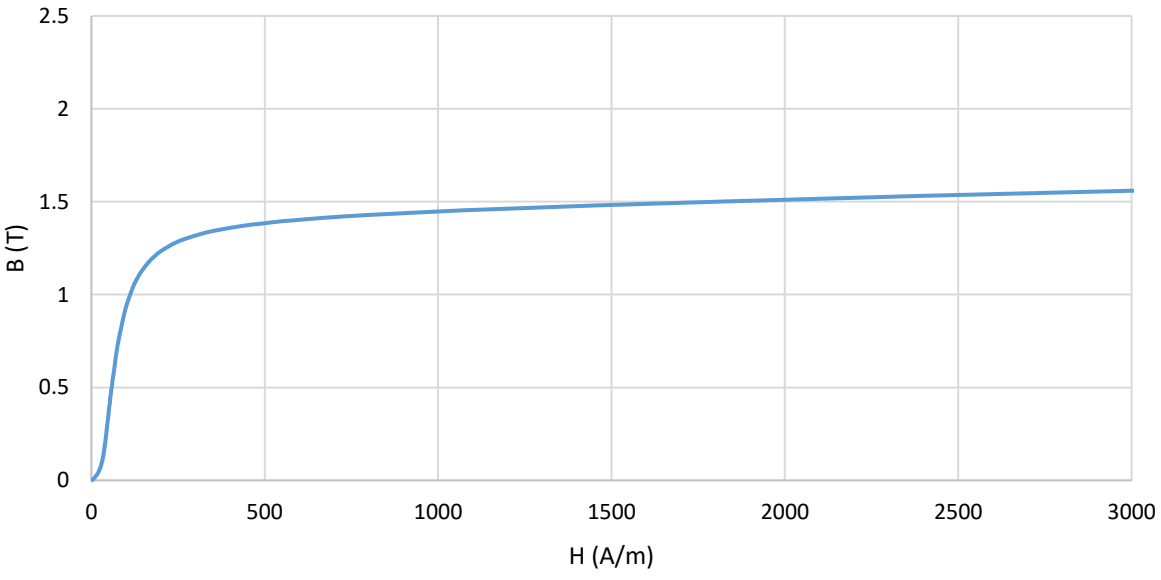

Figure 3-6 The B-H curve of M270-35A

With these SRMs running in a saturated region, it is clear that the four-phase SRM, with more phases, delivered more torque than the three-phase SRM. There is an explanation, as seen in Figure 3-7 whereby the magnetic path shortens as the phase number increases.

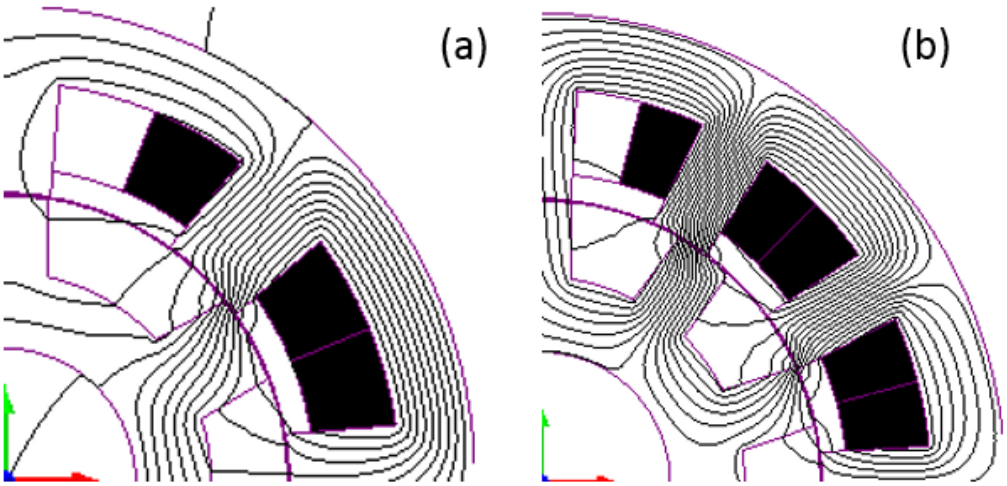

Figure 3-7 Flux-path plots during the phase interaction period: (a) a three-phase 6/4 SRM and (b) a four-phase 8/6 SRM

3.1.3 The influence of Phase Interaction

It is worth noting that the k_p in the 10/8 and 12/10 SRMs were higher than in the 6/4 and 8/6 SRMs. A higher k_p, whilst not guaranteeing a higher torque, might indicate that the machine would benefit more from phase interaction. This effect, described by Michaelides in [55], is due to the short flux path that is generated when two phases are energised simultaneously.

Moreover, when discussing phase interaction, there are two effects that cannot be ignored: cross-saturation and mutual coupling. Cross-saturation is an adverse effect created when the flux from one coil will not cross another coil but, instead, shares part of its flux path, increasing the local saturation. This effect is commonly found in SRMs and causes a significant decrease in the k_p (see Table 3) whose value in the 6/4 and 8/6 SRMs was shown below, indicating that the overall torque was lower than the superposition of the single-phase torque.

TABLE 3-3 THE 2D FEM RESULTS (NONLINEAR PERMEABILITY) FOR THE 6/4, 8/6, 10/8 AND 12/10 SRMS

Nonlinear	6/4SRM	8/6SRM	10/8SRM	12/10SRM	Unit
Average torque	60.66	64.96	69.21	66.31	Nm
Average torque single phase	42.48	33.57	26.90	21.68	Nm
k_p	0.95	0.96	1.02	1.01	

On the other hand, mutual coupling as another phase interaction effect can play a supporting role in torque production. In this case, the flux from one coil travels through another coil and, therefore, they reinforce one another. The mutual coupling effect is commonly seen in a mutually coupled SRM, which produces opposing flux within a single phase (see Figure 3-8). In conducting only a single phase, the SRM with the opposing coil follows a unique flux path, with a shorter magnetic circuit length and more poles carrying the flux, but at the cost of higher airgap reluctance. As a result, the SRM with the opposing coil is in an inferior position when only conducting a single phase. However, in a four-phase SRM, there are always two phases carrying current at any given moment (if the conduction angle reaches 180°). Due to the positive effects of phase interaction, the overall torque of the SRM with the opposing coil could be higher than that of the conventional SRM. As can be seen from TABLE 3-4, the SRM with an opposing coil would produce higher average torque than the original. Also, the average torque is significantly larger than the superposition of the torque from each single phase.

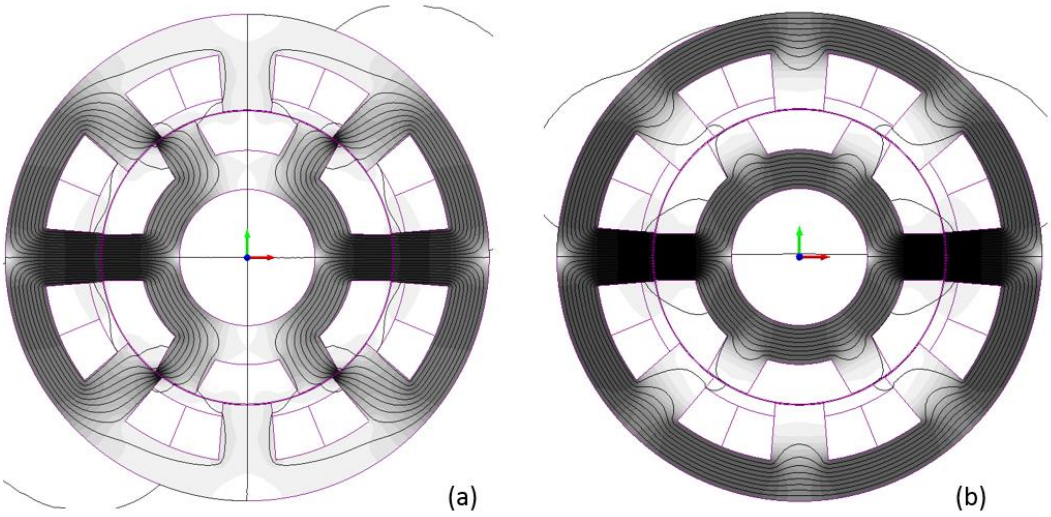

Figure 3-8 The flux path plots of a four-phase 8/6 SRM with differing coil arrangements: (a) opposing coils and (b) reinforced coil (the most common)

TABLE 3-4 THE 2D FEM RESULTS (NONLINEAR PERMEABILITY) FOR THE 8/6 SRM WITH DIFFERENT COIL ARRANGEMENT

Nonlinear	8/6SRM opposing coil	8/6SRM	Unit
Average torque	68.99	64.96	Nm
Average torque single phase	25.52	33.57	Nm
k_p	1.35	0.97	

3.2 Comparison between the 3-Phase SRM and 4-Phase SRM

The above comparisons only examine the situation for a particular motor size and geometry; a more general analysis should be required to provide a more objective conclusion. Moreover, it is unusual to consider the five-phase and six-phase SRMs as options, since too many phases would not only lead to a rise of iron loss (the hysteresis loss is proportional to the frequency and the eddy current is proportional to the square of the frequency) but also require too many electronic power components (increasing the cost and complexity of the drive). In reality, therefore, the four-phase SRM is more likely to be the appropriate option.

3.2.1 Analytical Method in the Linear Region

Taking the previous 2D FEM results as an example, Figure 3-9 shows the Ψ-I (flux-linkage vs phase current) curve comparison of the 6/4 and 8/6 SRM models. At this stage, both machines are operating in the linear region. The slope of the Ψ-I curve is the inductance, so the slope of L1a represents the inductance of the three-phase SRM at the aligned position, while L2u represents the inductance of the four-phase SRM at the unaligned position. To simplify the analysis, both 6/4 and 8/6 machines are assumed to have the same current density. Therefore, the current of the 8/6 SRM is set to 75% of that in the 6/4 SRM (since the slot area is inversely proportional to the phase number, when the split ratio and utilisation factor is fixed).

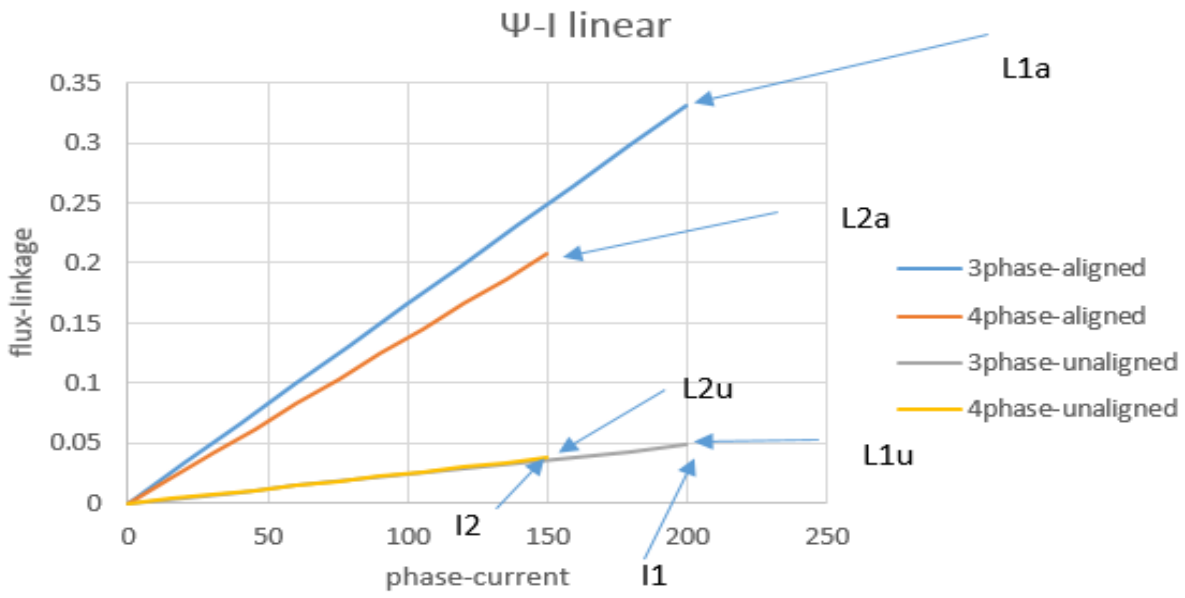

Figure 3-9 The flux linkage-vs-current curve for the 6/4 and 8/6 SRMs

The co-energy from each SRM can thus be derived:

$$W1 = \frac{1}{2}(L_{1a} - L_{1u})I_1^2 \quad (3\text{-}7)$$

$$W2 = \frac{1}{2}(L_{2a} - L_{2u})I_2^2 \quad (3\text{-}8)$$

From the equation$T=\frac{mN_r}{2\pi}W$ (3-5), it can be seen that the strokes per revolution of the four-phase SRM is 24 - twice that of the three-phase SRM. Then if the four-phase SRM is to provide more torque than its three-phase competitor, the co-energy of each stroke should satisfy the following condition ($W_2 \geq 0.5W_1$):

$$(L_{2a} - L_{2u})I_2^2 \geq \frac{1}{2}(L_{1a} - L_{1u})I_1^2 \quad (3\text{-}9)$$

Since $I_2 = \frac{3}{4}I_1$ (to maintain equal current density and copper loss)and $L_{2u} \approx L_{1u}$, then the above relationship could be further developed into:

$$L_{2a} \geq \frac{8}{9}L_{1a} + \frac{1}{9}L_{1u} \quad (3\text{-}10)$$

The ratio between the L_{1a} and L_{1u} is known as the inductance ratio, which is one of the critical parameters in SRM design. A reasonable SRM design should have a large inductance ratio (ideally more than 10) [36, 37], and, based on evidence from previous experiments and publications, a range from 6 to 12 should cover most situation(see Figure 3-10)

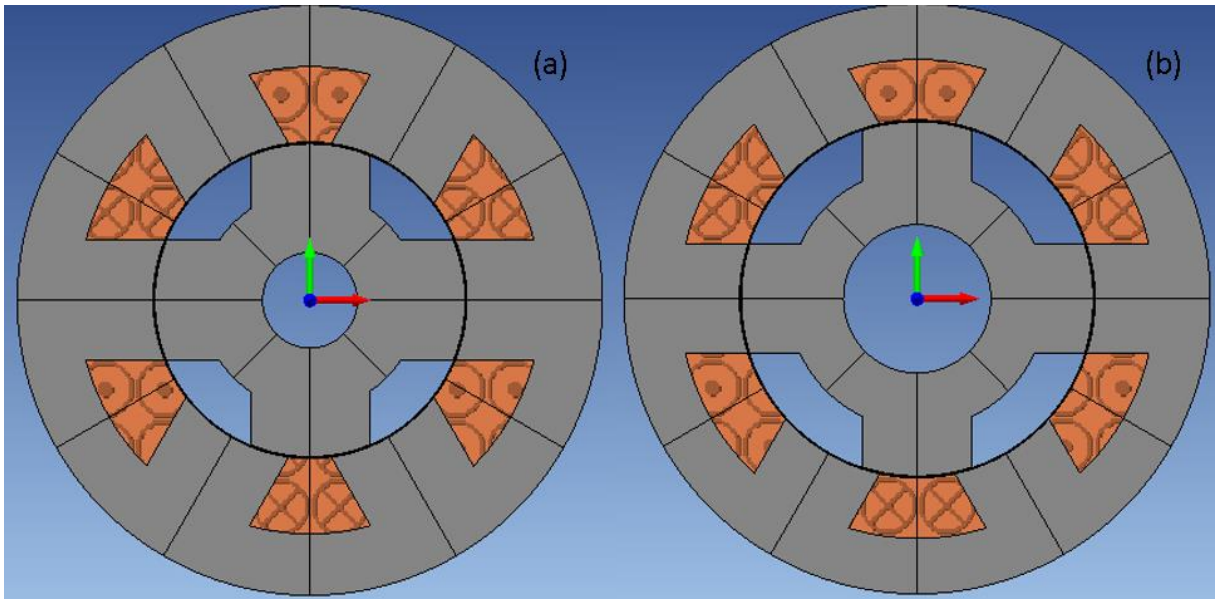

Figure 3-10 example of SRMs with different inductance ratio (a) inductance ratio=6, (b) inductance ratio=10.

Defining the inductance ratio as letter b and taking the equation $L_{1a} = bL_{1u}$, the formula can be rewritten as such:

$$L_{2a} \geq \frac{\left(8+\frac{1}{b}\right)}{9} L_{1a} \quad (3\text{-}11)$$

Taking $b = 6$ as an example, the 8/6 SRM will provide more torque if $L_{2a} \geq 0.9074 L_{1a}$. Moreover, if the steel in the magnetic circuit is assumed to have a uniform cross section, then the pole width of the 8/6 SRM is approximately $\frac{\sqrt{3}}{2}$ times that of the 6/4 SRM. Also, it is well known that inductance can be calculated using the following equation:

$$L = \frac{N^2}{\mathcal{R}} = \frac{N^2}{\frac{l}{\mu A}} \quad (3\text{-}12)$$

Where N is the number of winding turns per phase, $\mathcal{R}$ is the reluctance of the object in the magnetic circuit, l is the length of the object, μ is the permeability, and A is the cross-section area. Assuming the 6/4 and 8/6 SRMs have the same stator pole-to-stator pitch ratio, then it is simple to deduce that $L_{2a} \approx 0.75 L_{1a}$. This assumption is straightforward, but the current density under this condition is expected to be lower in the 8/6 SRM; however, it is unfair to make a comparison with the 6/4 SRM since the copper loss would be distinctly different in both machines, nor is it a proper design for an 8/6 SRM due to its potentially poor magnetic utility.

Alternatively, keeping the split ratio but changing the pole-to-pitch ratio in the 8/6 SRM could help to make a fair and straightforward comparison. In this scenario, following the same split ratio means keeping the same stator sector area, which consists of the slot area for winding and the core area for lamination. In addition, the stator area can be divided evenly by phase number, then, for each section, the 8/6 SRM will have 75% less area compared to the sections in the 6/4 SRM. Now the space allocated to the winding area is 25% less than that of the 6/4 SRM and, since the phase current is 25% less than the 6/4 SRM too, the 8/6 SRM will share the same current density as its competitor. As can be seen from the equationCopper $\text{Loss} = I^2R = I^2\rho\frac{l}{A} = IJ\rho l$(3-13), the copper loss is proportional to the phase current I, current density J, conductivity ρ, and conductor length l. Thus, the copper loss for the 8/6 SRM will equal the 6/4 SRM under this condition.

$$\text{Copper Loss} = I^2R = I^2\rho\frac{l}{A} = IJ\rho l \quad (3\text{-}13)$$

Furthermore, regarding the magnetic circuit, the ratio $\frac{3}{4}$ in the sector area was roughly equivalent to the ratio $\frac{\sqrt{3}}{2}$ in the width of the flux path. As such, it was derived that $L_{2a} \approx 0.866L_{1a} < 0.9074L_{1a}$. This result indicates that the four-phase SRM would produce slightly less average torque than the three-phase SRM in the linear region. It is not an unexpected result since a similar conclusion was confirmed by both the torque equation and the 2D FEM in section 3.1.

3.2.2 Analytical Method in the Nonlinear Region

Unlike other types of electric machine, the SRM often works in a magnetic saturation scenario. As such, it was more important to analyse the behaviour of the SRM at a highly saturated operating point. Also, there is a simplification method that is widely used to convert the nonlinear magnetisation curve into a semi-linear model [37, 50, 102].

As can be seen from Figure 3-11, the nonlinear energy conversion loop can be divided into linear and nonlinear regions. The nonlinear region represents the area where the phase current is beyond I_s and, in this area, flux linkage curves between the aligned and unaligned positions become a pair of parallel lines.

Several new parameters are introduced to help analyse this semi-linear energy conversion loop. On the horizontal axis, I_1, I_2 and I_s represents three critical phase current value: I_1 is the peak phase current of the 6/4 SRM, I_2 is the peak phase current of the 8/6 SRM(approximately 75% of the I_1); I_s is an assumed value that defines the boundary of linear semi-linear region. Also, it can be identified that the I_s is the same for both machines via the following equation:

$$B = \frac{Li}{AN} \quad (3\text{-}14)$$

In the above, B is the flux density and merely defines the parameters for determining the saturation point of the lamination steel. Regarding the remaining elements in the equation, L is the inductance, i is the current, A is the cross section area, and N is the number of turns. From the equation$La= \frac{N^2}{\mathcal{R}}$ (3-2) and equation$\mathcal{R}=$□μA□ (3-3), it could be calculated that the inductance L was proportional to the cross section area A. Moreover, the turn number of both machines was kept equal, since the peak current was set to be inversely proportional to the phase number. Therefore, the flux-density B would be proportional only to the current i in this scenario.

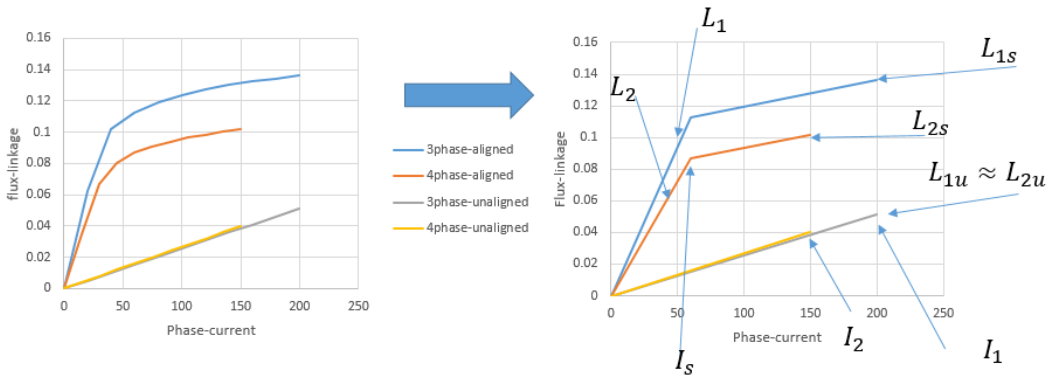

Figure 3-11 The nonlinear flux linkage-vs-current curve for the three-phase and four-phase SRMs (left) and the simplified nonlinear model (right)

A group of inductance measures were introduced to describe the coordinates of several unique points:

- L_1 and L_2 were the aligned inductance at the linear region for the 6/4 and 8/6 SRMs, respectively. These two inductance values were used to describe the aligned flux linkage curve in the linear area.
- L_{1u} and L_{2u} were the unaligned inductance for the 6/4 and 8/6 SRMs and, according to the analysis in Section 3.1.1, their values were similar to one another. In most cases, the value was assumed to remain the same from the beginning to the highly saturated condition.
- And finally, L_{1s} and L_{2s} were the aligned inductance for the 6/4 and 8/6 SRMs, corresponding to I_1 and I_2, respectively.

The overall co-energy value for this conversion loop of the 6/4 SRM could be calculated thusly:

$$W_1 = \frac{1}{2}(L_1 I_s - L_u I_s) I_s + (L_1 I_s - L_u I_s)(I_1 - I_s) \quad (3\text{-}15)$$

And, similarly, below is the expression for the 8/6 SRM:

$$W_2 = \frac{1}{2}(L_2 I_s - L_u I_s) I_s + (L_2 I_s - L_u I_s)(I_2 - I_s) \quad (3\text{-}16)$$

Using equation$T=mN_r 2\pi W$ (3-5), the number of strokes per revolution for the 8/6 was twice that of the 6/4 SRM, meaning the 8/6 and 6/4 SRMs could produce the same amount of average torque, as long as W_2 were to reach 50 % of the value of W_1.

Since $I_2 = \frac{3}{4} I_1$, it could be concluded that the 8/6 SRM would produce more torque than the 6/4 SRM, if the following relation were satisfied:

$$L_2 \geq \frac{\frac{L_1 I_1 I_S}{2} - \frac{L_1 I_S^2}{4} + \frac{L_u I_1 I_S}{4} - \frac{L_u I_S^2}{4}}{I_S\left(\frac{3}{4} I_1 - \frac{I_S}{2}\right)} \quad (3\text{-}17)$$

To analyse this complex expression, two new variables were introduced:

1. k: indicated the relation $I_s = kI_1$ which represented the ratio of I_s to I_1. This parameter described the saturation level of the 6/4 SRM. When $k \leq 1$, it meant the SRM was operating in the saturation condition.
2. b: indicated the relation $L_1 = bL_u$ which represented the inductance ratio between L_1 andL_u. This parameter described the inductance ratio between the unaligned and aligned positions in the 6/4 SRM.

Then the equation $L2 \geq \frac{\frac{L_1 I_1 I_S}{2} - \frac{L_1 I_S^2}{4} + \frac{L_u I_1 I_S}{4} - \frac{L_u I_S^2}{4}}{I_S\left(\frac{3}{4} I_1 - \frac{I_S}{2}\right)}$ (3-17) could be transformed into the following expression:

$$L_2 \geq \frac{L_1\left(\frac{k}{2} - \frac{k^2}{4} + \frac{k}{4b} - \frac{k^2}{4b}\right)}{\frac{3}{4}k - \frac{k^2}{2}} \quad (3\text{-}18)$$

From the section 3.2.1, it could be assumed that both the 8/6 and 6/4 SRMs had the same stator pole-to-stator pitch ratio. As such, it was simple to calculate that $L_2 \approx 0.75L_1$ and the above equation could be further developed into:

$$\frac{\left(\frac{k}{2} - \frac{k^2}{4} + \frac{k}{4b} - \frac{k^2}{4b}\right)}{\frac{3}{4}k - \frac{k^2}{2}} \leq 0.75 \quad (3\text{-}19)$$

Consequently, there was inequality between the two elements describing the balance of the torque comparison for the 6/4 and 8/6 SRMs. For example, assuming $b = 5$ (in most cases b is between 5and 12), this indicated that the 8/6 SRM would produce more torque, with $k < 0.744$. The curve in Figure 3-12 was generated to show this relation:

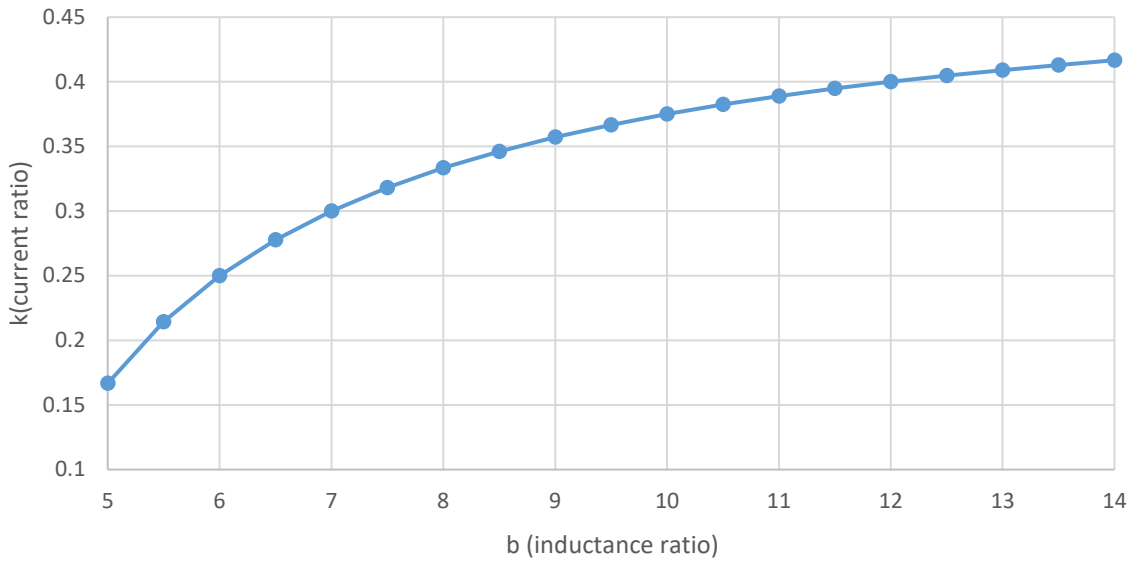

Figure 3-12 The *k* vs *b* curve describing the boundary for the 8/6 SRM to deliver higher torque

From the above figure, if the selected combination of *b* and *k* sits at a position beneath the curve, it means the 8/6 SRM should provide better torque performance under this condition.

3.2.3 2D Finite Element Simulation Results

The analytical results were verified using the 2D FEM. As can be seen from Figure 3-13, the 2D models of the 6/4 and 8/6 SRMs were generated in MagNet. In this figure, the two models are drawn with the same stator diameter, the same airgap length, same turn number and the same pole-to-pitch ratio in the stator. Moreover, the cross section in the flux path is assumed to be uniform: the stator and rotor poles share the same width, which also equals twice that of the stator and rotor yoke widths.

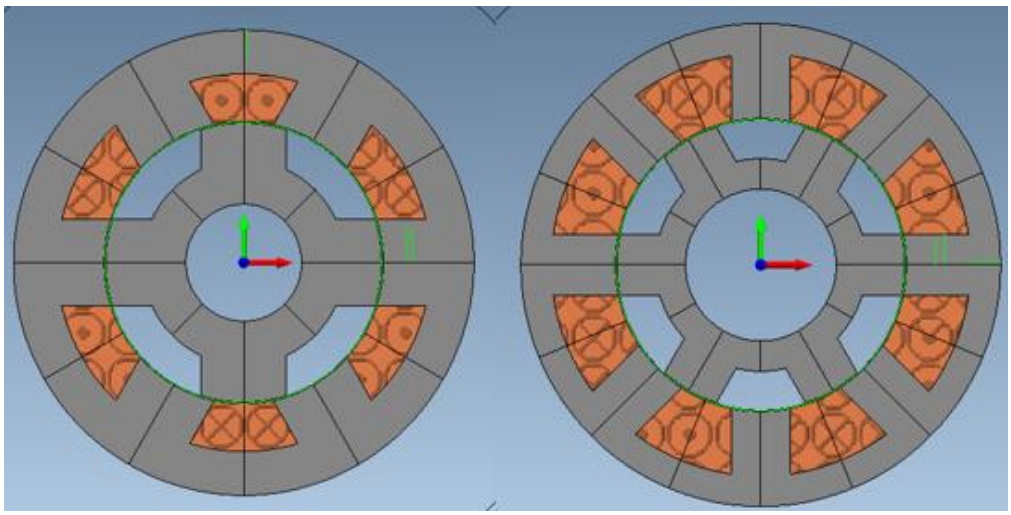

Figure 3-13 2D FE models for 6/4 SRM and 8/6 SRM

As was mentioned in section 3.2.2, the inductance ratio b and saturation ratio k were the critical values affecting the comparison between the 6/4 and 8/6 SRMs. The saturation ratio was clearly related to the phase current if the turn number was fixed. The inductance ratio is linked to a more complicated scenario. For instance, the split ratio (rotor outer diameter-to-stator outer diameter) and the utilisation factor (stator pole pitch-to-stator pitch) all have been involved in the inductance ratio.

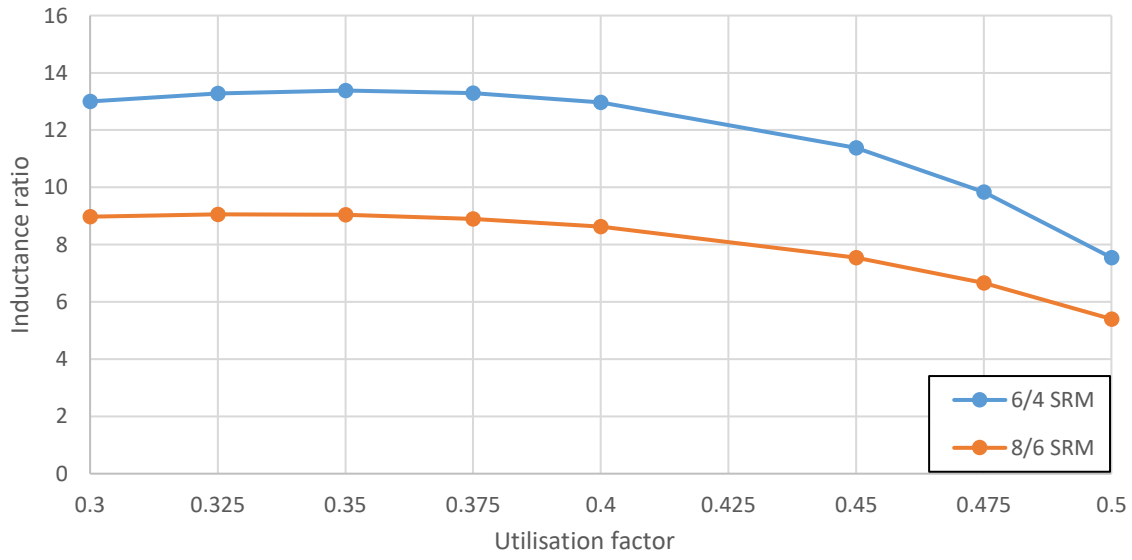

Figure 3-14 The 2D FEM results for inductance ratio against different utilisation factors

As can be seen from the Figure 3-14, the inductance ratio in both the 6/4 and 8/6 SRMs shows a falling tendency as the utilisation factor increases. This result indicates that the inductance ratio does not have a linear relation to the utilisation factor. To be specific, the inductance ratio

stays at virtually the same level until the utilisation factor reaches 0.4. This reveals that the unaligned inductance is constant when the utilisation factor is under 0.4.

Once the utilisation factor exceeds 0.4, the inductance ratio begins to decrease. This phenomenon is due to the large level of unwanted inductance at the unaligned position, which is caused by a narrow airgap at this point.

Although increasing the width of the poles could lower the value of *b* (the inductance ratio) in some conditions, the torque capability does not demonstrate a simple linear relation to it (see Figure 3-15).

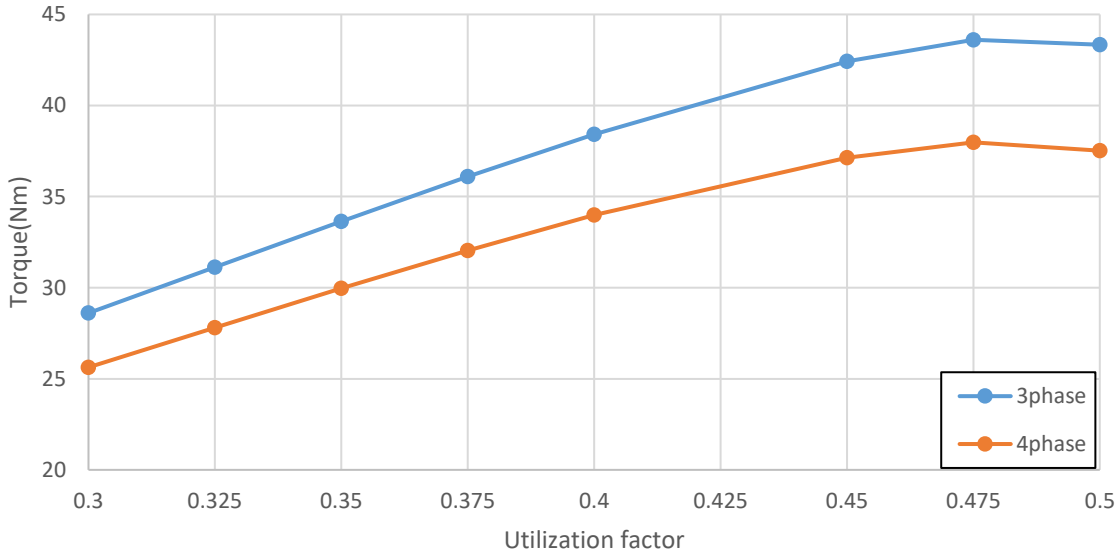

Figure 3-15 2D FEM results for torque against different utilisation factors

As can be seen from Figure 3-15, the torque from both SRM models is nearly proportional to the utilisation factor until the factor reaches circa 0.475. Furthermore, it seems that the four-phase SRM performs less favourably than the three-phase SRM with respect to torque capability. However, it does not mean the previous analytical method was incorrect. There is indeed a reason that could explain that difference. As in the last analysis, the flux path was assumed to be uniform. In this condition, the stator and rotor poles have the same width, which also equals twice that of the stator and rotor yokes. However, as in the more realistic 2D FEM models, the flux density could not spread evenly, even if the machine is designed to produce a uniform flux path. Moreover, the phase interaction effects were considered in the 2D FEM and it was apparent that the uniform flux path was not the optimal design during the phase interaction period. Since the phase interaction periods of four-Phase SRM is 50% longer than

the three-Phase SRM, there is no doubt the 2D FEM result of the four-Phase SRM will be slightly worse than the preivious analysis.

Also, the 2D FEM results did not prove that the three-phase SRM could outperform the four-phase SRM regarding torque capability, since this comparison was not limited to the same copper loss (see Figure 3-16)

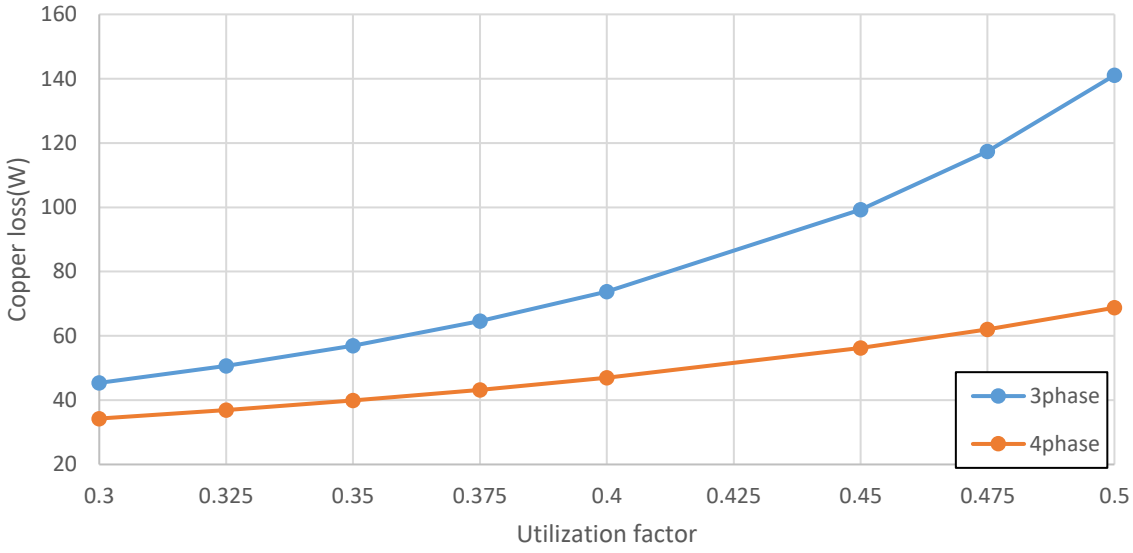

Figure 3-16 2D FEM results for torque against different utilisation factors

The curves in Figure 3-16 indicate that the three-phase SRM would require almost twice as much copper as that of the four-phase SRM. Substituting the copper loss in the torque data, a torque-per-unit copper loss figure is obtained (see Figure 3-17)

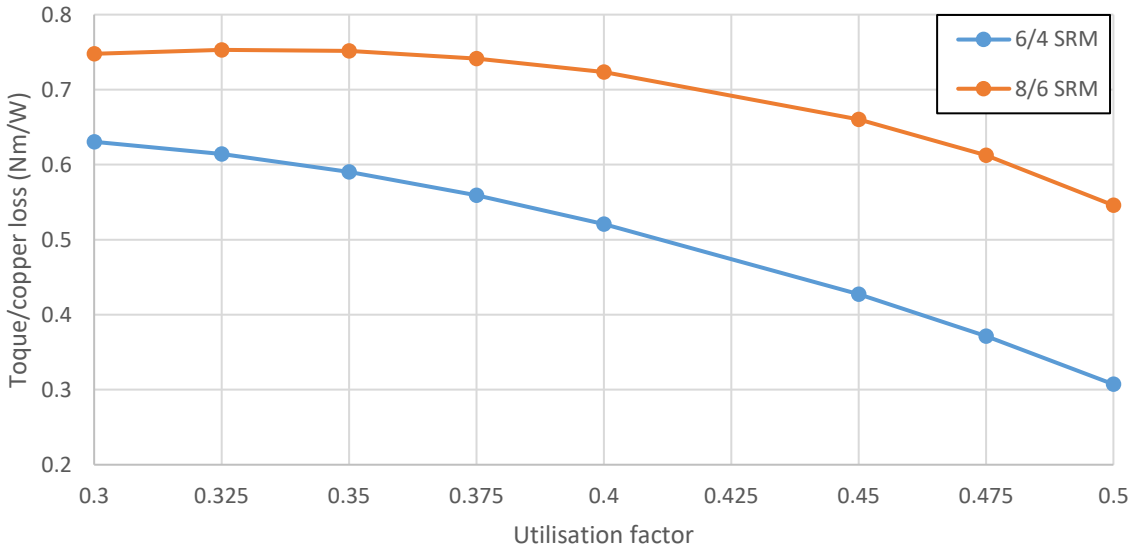

Figure 3-17 2D FEM results for torque-per-unit copper loss under different utilisation factors

As can be seen from the Figure 3-17, the 8/6 SRM has considerable advantages over the 6/4 SRM when it comes to torque-per-unit copper loss. It indicates that neither the 8/6 nor the 6/4 SRM take the absolutely advantage in this comparison. Although the above comparison would not be entirely fair, its data could be processed to illustrate the relationship between the inductance and torque ratios (see Figure 3-18)

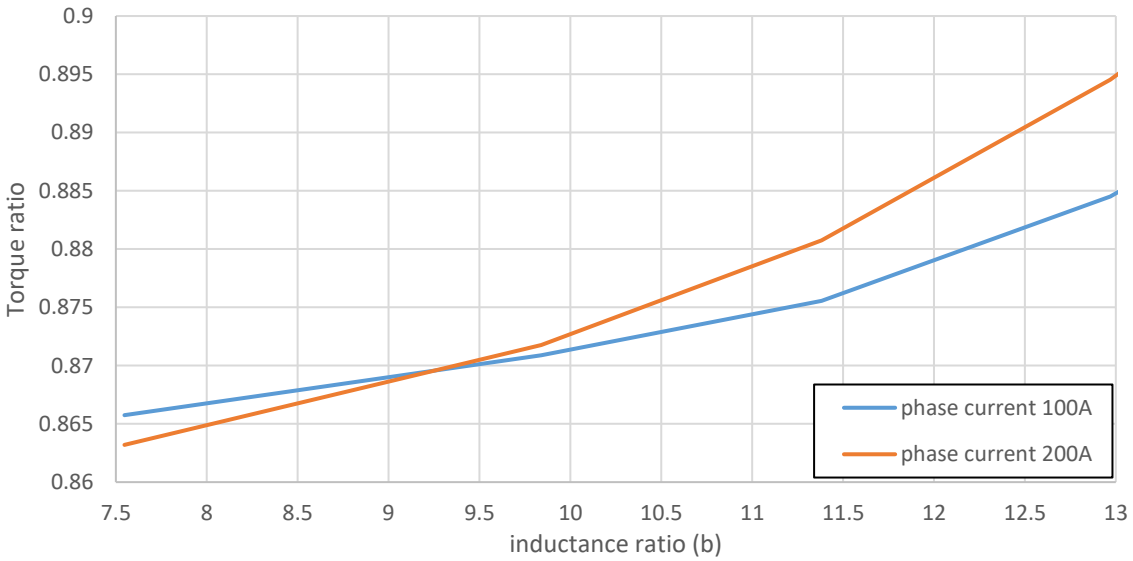

Figure 3-18 2D FEM results for the torque ratio against different inductance ratios

The vertical axis in Figure 3-18 represents the torque ratio (Torque of 8/6 SRM divide by the torque of 6/4 SRM), which describes the result from the torque of the 8/6 SRM divided by the torque of the 6/4. Moreover, there are two curves in Figure 3-18 representing the data from two different current levels. Specifically, the upper orange curve is the data for the 200-A phase current in the 6/4 SRM (150 A for 8/6 SRM), and the lower blue curve is for the 100-A phase current. The higher phase current indicates more saturation and therefore has a lower current ratio k. The overall results revealed that the small inductance and current ratios were in favour of the four-phase SRM design, in line with expectations from the analysis.

3.2.4 Correction for Copper Loss

In the above comparison, there is a considerably larger gap in copper loss between both models. Thus, correction of the previous model was required to generate a proper environment for simulation and analysis. A possible method for maintaining the copper loss in both models was to keep the same current density and make the slot area inversely proportional to the phase number. Examples of stator sections from both models are shown in Figure 3-19.

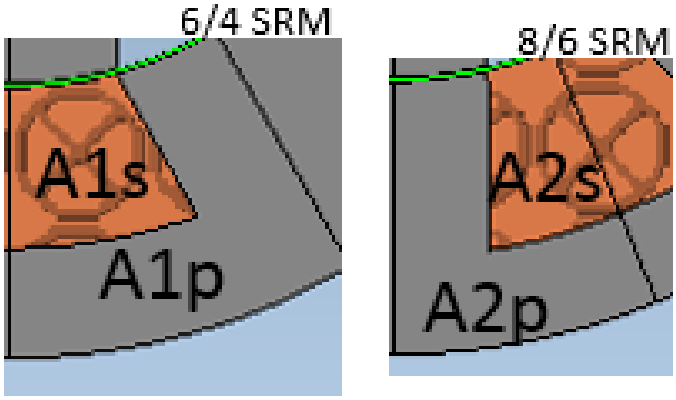

Figure 3-19 Stator sections of the 6/4 and 8/6 SRMs

Assuming the entire area of the 6/4 SRM stator section is equal to A1, it is given by:

$$A_1 = A_{1s} + A_{1p} \quad (3\text{-}20)$$

As can be seen from Figure 3-19, A_{1s} is the section area of the slot in the 6/4 SRM and A_{1p} is the section area of iron core in the 6/4 SRM.

As with the 8/6 SRM, its stator section area A2 can be given by:

$$A_2 = A_{2s} + A_{2p} \quad (3\text{-}21)$$

Where A_{2s} is the section area of the slot in the 8/6 SRM and A_{2p} is the section area of iron core in the 8/6 SRM.

The rotor and stator radii were exactly the same in both models, indicating that A_2 is equal to $\frac{3}{4}A_1$. Also, since the slot area is inversely proportional to the phase number, A_{2s} must be equal to $\frac{3}{4}A_{1s}$. Thus, the relation between A_{1p} and A_{2p} can be deduced as:

$$A_{2p} = \frac{3}{4}A_{1p} \quad (3\text{-}22)$$

Using basic geometric knowledge, the two-dimensional area is known to be proportional to the square of the one-dimensional length. Thus, the pole width of the 6/4 SRM (W_{p1}) and the pole width of the 8/6 SRM (W_{p2}) would obey the following relation:

$$W_{p2} = \frac{\sqrt{3}}{2}W_{p1} \quad (3\text{-}23)$$

It is simple to find that $L_2 \approx 0.866L_1$ at this condition, and thus the equation $k(2 - \frac{k^2}{4} + \frac{k}{4b} - \frac{k^2}{4b})(\frac{3}{4}k - \frac{k^2}{2}) \leq 0.75$ (3-19) could be revised as thus:

$$\frac{\left(\frac{k}{2}-\frac{k^2}{4}+\frac{kb}{4}-\frac{k^2 b}{4}\right)}{\frac{3}{4}k-\frac{k^2}{2}} \leq 0.866 \qquad (3\text{-}24)$$

As a result, it was possible to transform the data from Figure 3-12, the results are presented in Figure 3-20:

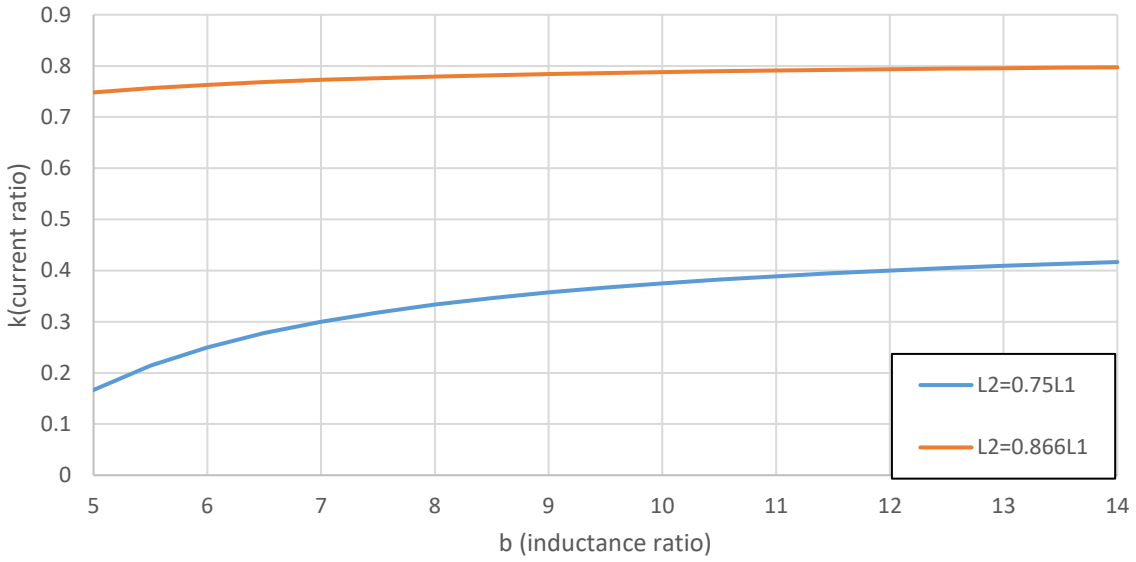

Figure 3-20 The *k* vs *b* curve describing the boundary for the 8/6 SRM to deliver higher torque

The blue curve in Figure 3-20 represents the data for the revised inductance relation (L2= 0.866 L1). Compared with the orange curve, which is precisely the curve from Figure 3-19(and represents the inductance relation L2=0.75 L1), the blue curve shows a similar steady trend. Meanwhile, the area beneath the blue curve is significantly larger than that under the orange curve. This result indicates that the four-phase SRM exhibits an advantage in this particular comparison. In other words, after the correction to maintain the same level of copper loss in both models, the 8/6 SRM model was very likely to offer better torque capacity.

Also, it should be noted that the analytical model did not carefully consider the changes that occurred in the unaligned inductance when the pole width increased in the 8/6 SRM. To some extent, if the utilisation factor were to increase, further enhancement of the pole width would no longer benefit the torque capacity as the clearance between the stator and rotor poles deteriorates at the unaligned position.

In addition, as can be seen in Figure 3-14 to Figure 3-17, the utilisation factor would have had a similar influence on the results, affecting such aspects as the inductance ratio, torque production and copper loss in both the 8/6 and 6/4 SRMs. Therefore, in reality, the suggested utilisation factor for both the 8/6 and 6/4 SRMs was a similar value. Moreover, this indicated that the method that merely extends the width of the stator pole would be insufficient for maintaining the level of copper loss.

There were two possible solutions that could be taken into consideration: the first was to keep the original geometry and phase current but increase the turns-number (from 20 to 25); the second was to raise the split ratio (from 0.6 to 0.68). These two methods were able to increase copper loss and the 2D FEM results are presented in Figure 3-21.

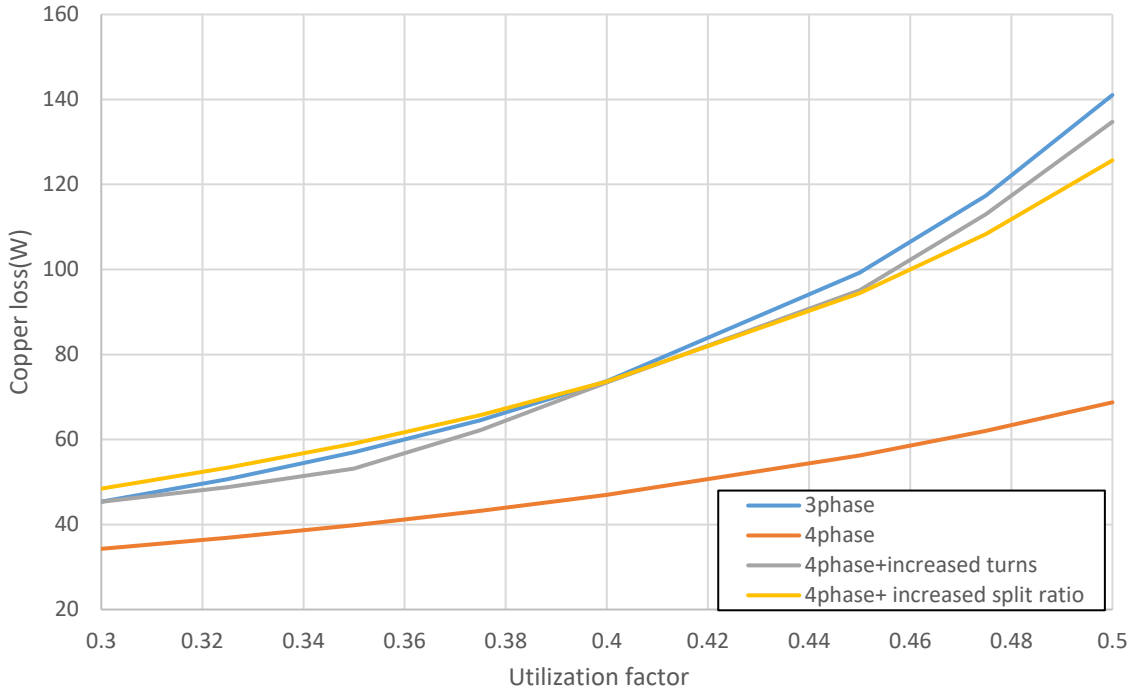

Figure 3-21 2D FEM results for torque against different utilisation factors

Compared to the data from the original four-phase 8/6 SRM model, the copper loss in these two methods increased significantly to match that of the three-phase 6/4 SRM model – the corresponding torque data is shown in Figure 3-22.

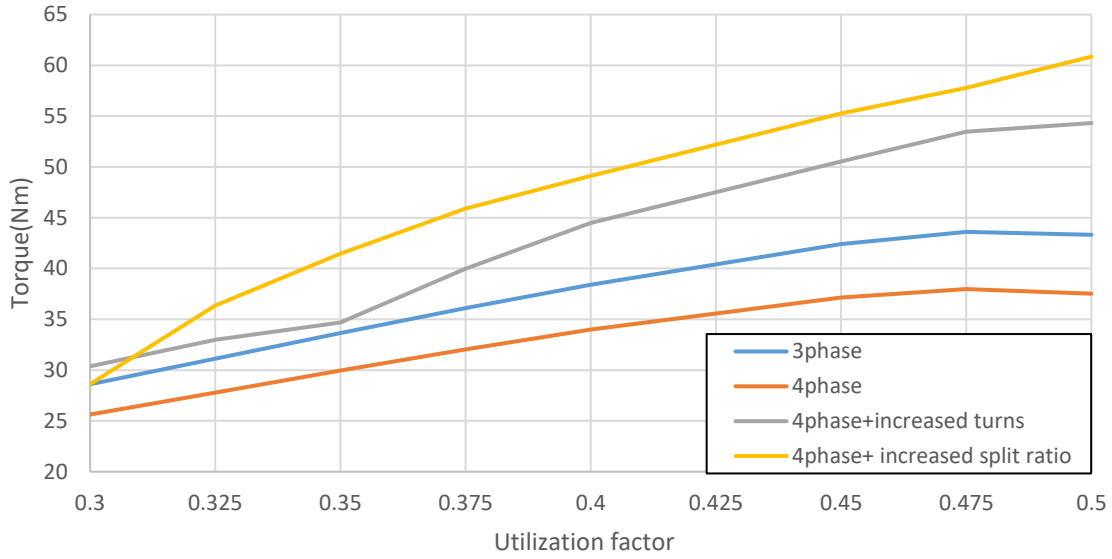

Figure 3-22 2D FEM results for torque against different utilisation factors

As can be seen from Figure 3-22, there is a considerable enhancement in torque capability. Specifically, by increasing the turn number, the four-phase SRM model not only notably outperforms its original but also delivers higher torque than the three-phase SRM model. Moreover, another method with an increased split ratio (yellow curve) performs even better, with a torque 40% higher than that of the three-phase SRM model. The results revealed that the four-phase SRM might display better torque performance than the three-phase SRM if the same copper loss were maintained.

This conclusion was double checked using an inverse process: reducing the copper loss of the original three-phase SRM model to match that of the original four-phase SRM. This process was undertaken by reducing the turn number-per-phase or the split ratio, and the corresponding results are shown in Figure 3-23.

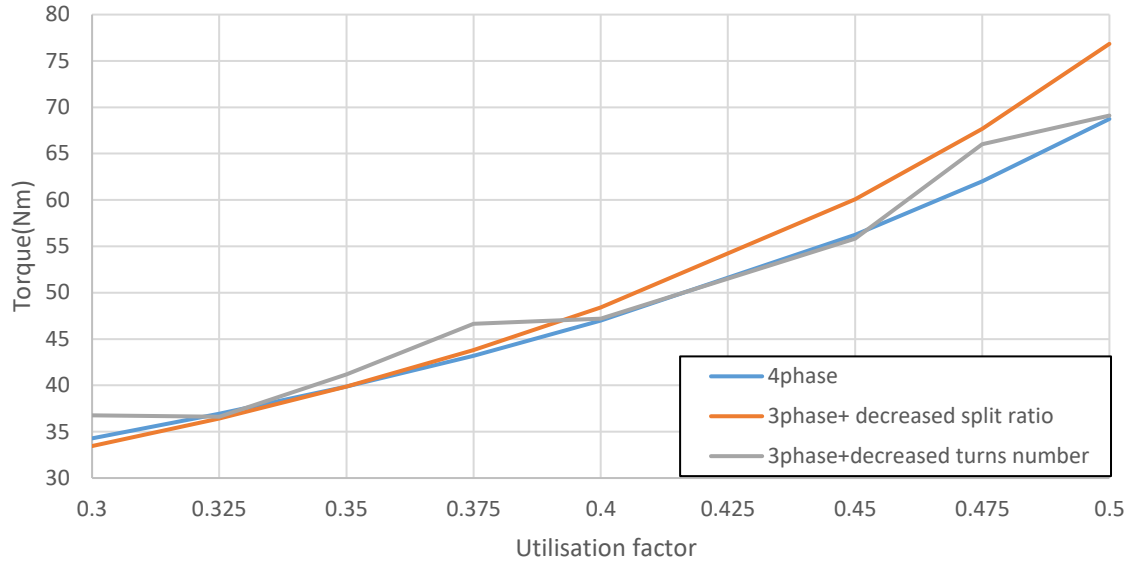

Figure 3-23 2D FEM results for torque against different utilisation factors

By decreasing the turn number (from 20 to 15) or the split ratio (from 0.6 to 0.53), the copper loss of the three-phase models was reduced significantly. The exact copper loss was still higher than the four-phase model, but the difference was minimised to less than 11%. The torque performance was also reduced, as expected (see Figure 3-24): these two derivatives from the original three-phase model all delivered significantly lower torque than the four-phase model.

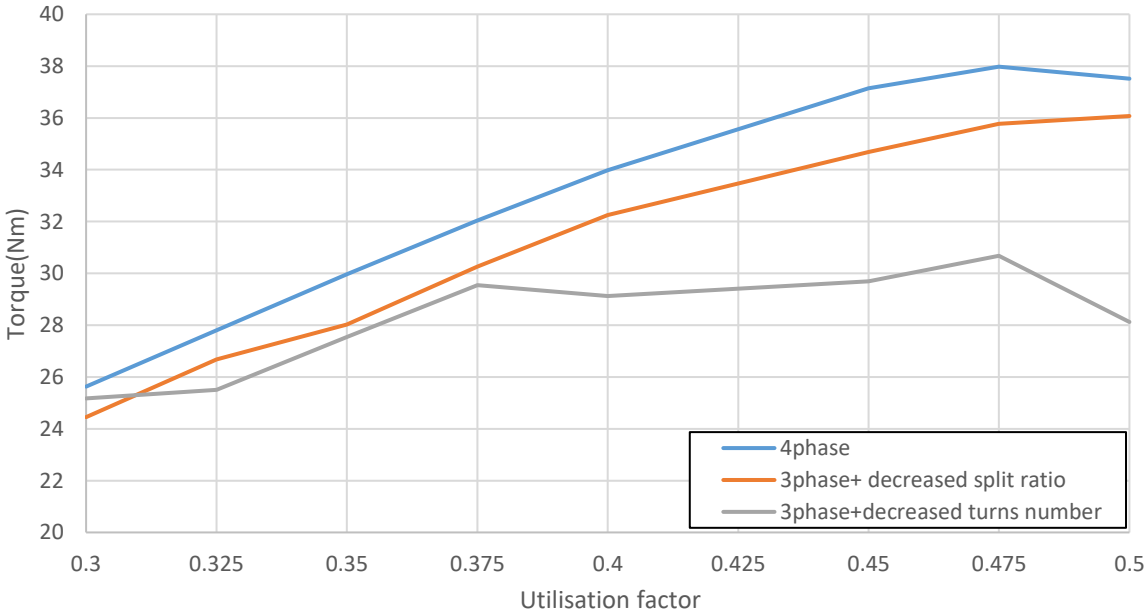

Figure 3-24 2D FEM results for torque against different utilisation factors

Based on the above results, the four-phase SRM had already proven its potential for offering higher torque capability and lower copper loss consumption than the three-phase SRM. Also, from the perspective of machine design, it indicated that the four-phase SRM required a larger split ratio than the three-phase SRM.

3.3 Conclusion

In conclusion, the work presented in this chapter can be divided into several steps.

1. The torque equation was developed as a tool to analyse the airgap torque of a conventional SRM. Also, the analysis showed that the SRM with a higher phase number produced less torque under this circumstance. The results were validated by 2D FEM.
2. Further analysis for considering linear permeability in lamination steel was completed using 2D FEM. The results revealed that the SRM with a higher phase number would have benefited from this condition, as its structure achieved better utilisation of the iron core. This conclusion could be proved by reducing the airgap or by letting the SRM operate in the saturated region.
3. A simplified flux linkage-current model was used to make a further comparison between the three-phase 6/4 and four-phase 8/6 SRMs. The analysis suggested that the 8/6 SRM would benefit from a larger inductance ratio and a high saturation condition. The 2D FEM results showed that this condition could be achieved effectively by increasing the split ratio. Moreover, it illustrated the fact that the 8/6 provided higher torque capability than the 6/4 SRM with the same copper loss.

These findings made contributions to knowledge as follows:

- The effect of SRM phase number upon torque capability is apparent: the SRM with lower phase number would take advantage at torque production when the airgap dominates the aligned flux path. On the other hand, the SRM with higher phase number has better utilisation of iron core.

- Further analysis at 6/4 and 8/6 SRM reveals that the 4 Phase SRM could produce higher torque with the same copper loss limit. This advantage will become prominent when the machine is operating at the saturated condition or has a large split ratio.

Chapter 4. The Development of Four-Phase SRM Design

Chapter 3 provided numerous comparisons between three-phase and four-phase SRMs. The conclusion revealed that the four-phase SRM has advantages of higher torque capability and lower copper loss. It also suggested that its design tended to require a larger split ratio, which could offer more design freedom in the rotor and could, therefore, be implemented in several novel structures, such as those with higher rotor pole numbers and double stators. The aim of Chapter 4 is to analyse those potential structures with 4 Phase SRMs.

Firstly, it should be noticed that the 4 Phase SRM has an issue with conventional coil configurations because there cannot be symmetry between phase polarities. Opposing coil configurations are introduced in the MCSRM and compared alongside the conventional coil with same core geometry using 2D FEM. The results suggests opposing coils could produce higher average torque. Moreover, by modifying the core geometry, it is suggested that the unique flux path from opposing coil has better usage of the stator core, which provides motivation for a larger split ratio and higher saturation level. It should be noticed that this motivation is in line with the 4 Phase SRM design.

Secondly, an investigation of cases where the rotor number exceeds that of the stator is considered for the opposing coil 4 Phase SRM. By using 2DFEM, the result reveals that the higher rotor number concept only produces higher torque during the linear condition due to the larger unaligned inductance. Based on this inference, a modified stator pole is then designed, and is shown to enhance the torque capability.

Thirdly, the double stator structure is studied using an analytical model. The study starts from a linear SRM (LSRM) geometry and linear magnetic conditions and then extends to a rotational SRM and saturated conditions. The study indicates that to utilise the advantage of the double stator structure, the SRM should have larger split ratio and operate at higher saturation level. It should be noticed that this design suggestion is in line with the 4 Phase SRM.and opposing coil arrangement.

Finally, to verify the design suggestion which is produced in this chapter, a 4 Phase16/12 SRM and a 16/12 DSSRM is designed and compared with a world-leading 3 Phase 18/12 SRM using 2D FEM.

.

4.1 Conventional Four-Phase Switched Reluctance Machine

The three-phase design is a standard option for most electric machine categories. As a consequence, research on the four-phase SRM is relatively limited – notably, studies that focus on more specific aspects, such as optimisation for higher torque output and lower copper loss. This section summarises the works and discoveries made whilst seeking to enhance the performance of the conventional four-phase SRM.

.

4.1.1 Mutual Coupling Effect and Opposing Coil Arrangement

As briefly mentioned in section 3.1.3, the mutual coupling effect is a phase interaction effect – and, unlike the other phase interaction effects, such as cross-saturation, mutual coupling is able to deliver positive assistance for torque output.

The Mutual Coupled SRM (MCSRM), which is developed from the fully pitched SRM, could generate torque from mutual coupling effects[98-100]. The major difference between the conventional SRM and MCSRM is the coil arrangement. Unlike the conventional coil arrangement in which the coils in the same phase generate flux in the same direction, the case with the MCSRM is the opposite. Under this opposing coil arrangement, the coil within the same phase generates flux in opposite direction The example in Figure 4-1 shows the specific coil arrangement and excitation pattern for a three-phase MCSRM.

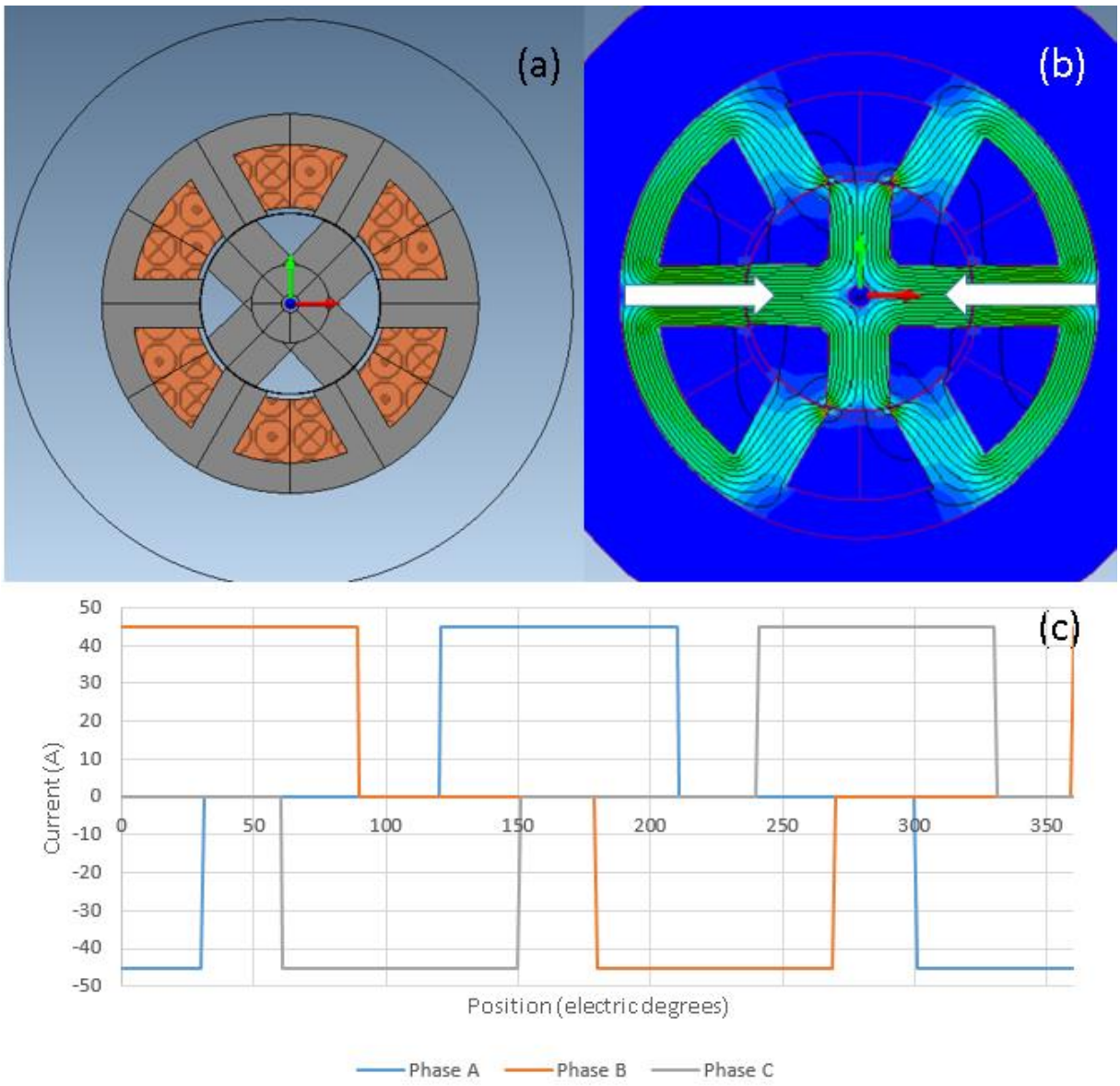

Figure 4-1 3 A three-phase MCSRM: (a) 2D model with coil distribution pattern, (b) flux path (the direction is indicated in white arrows)and flux density plots for a single-phase conducting and (c) the excitation current for each phase.

It can be noticed that it is impossible to achieve the desired flux path in a three-phase MCSRM without the more expensive bipolar drive. However, the opposing coil arrangement is suitable for an even phase condition [95, 101], since the opposing coil arrangement is symmetrical when the SRM has an even number of phases. It should also be noted that the four-phase SRM will always excite two phases at any given moment (assuming the excitation period is 180 electrical degrees for each phase). This provides sufficient opportunity for taking the mutual coupling benefits of the opposing coil arrangement.

In contrast, the conventional coil arrangement in the even phase number SRM introduces an asymmetric flux pattern, which leads to an unexpected torque drop at certain phase interaction

positions. A detailed comparison between the opposing coil and ordinary reinforced coil arrangements for the four-phase SRM are presented in this section. As can be seen from Figure 4-2, the geometry is identical in both models, the only difference being the coil polarity.

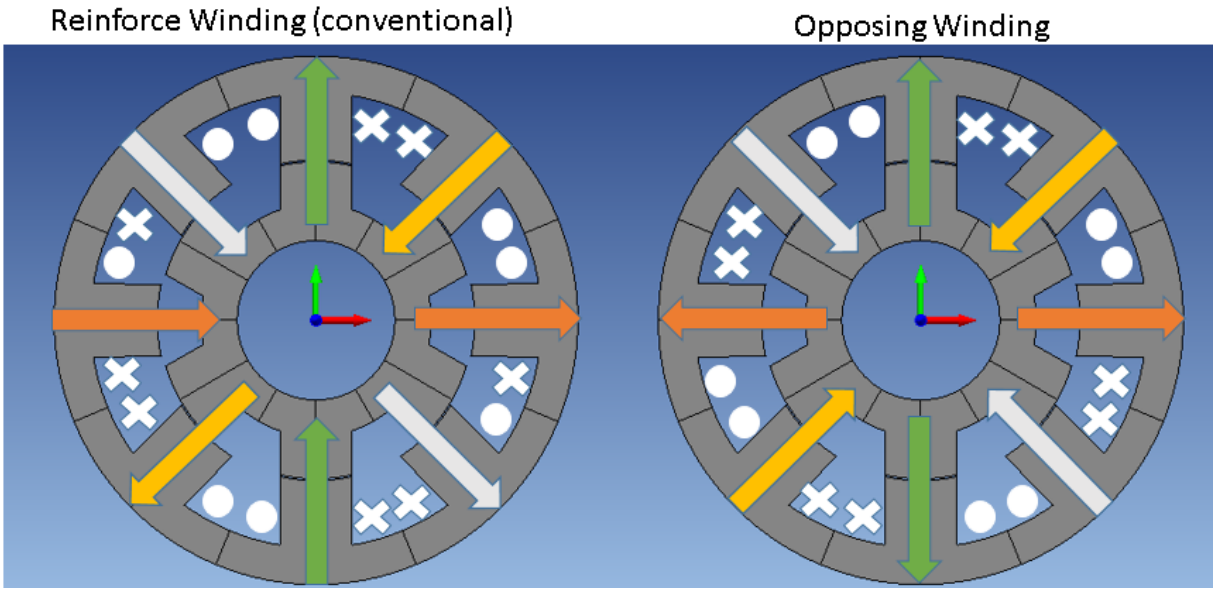

Figure 4-2 Coil distribution patterns. Left: reinforce coil. Right: opposing coil

It should be noted that the model using the reinforced coil does not have a continuous coil pattern around the entire circle [95, 101]; thus a torque disturbance can be expected when phase interaction happens at this position. The effects are presented in Figure 4-3.

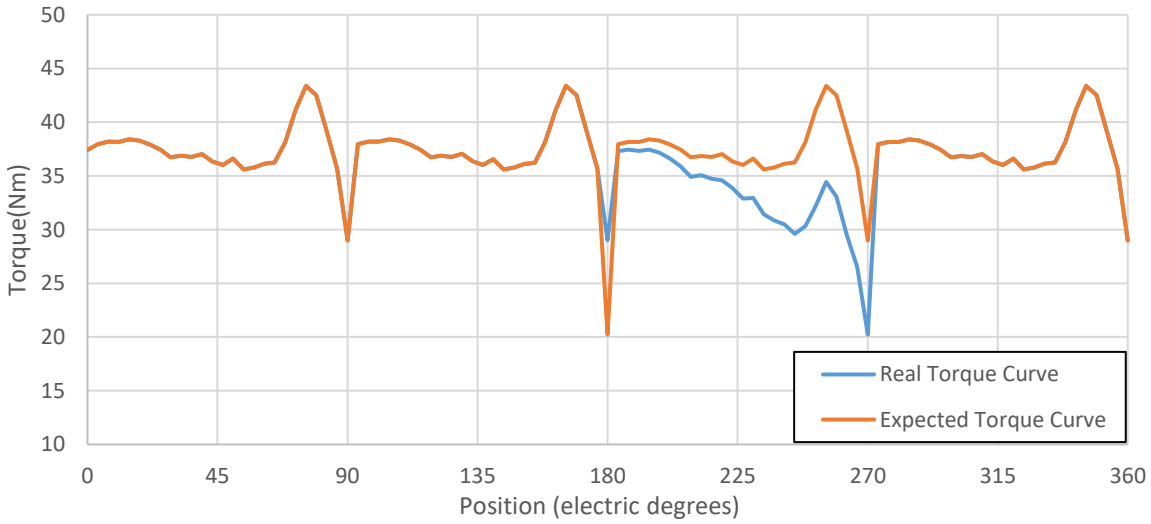

Figure 4-3 2D FEM Torque curve for a full electric cycle, showing a torque drop due to the discontinuous coil pattern in the 8/6 SRM with a conventional “reinforce” coil arrangement

This torque loss is considerable and inevitable, just as with a three-phase MCSRM using opposing coils. The results indicated that the reinforced coil arrangement could not be suitable for a four-phase conventional SRM, as it would create extra complexity for the controller. Moreover, this reinforced arrangement could also lead to lower torque output, compared to the opposing coil arrangement. To compare the torque capability between these two coil arrangement, 2D FE models have been built with identical geometries. By using a range of pole utilisation factors as a variable and adjusting the width of the entire magnetic circuit accordingly, the result is shown in Figure 4-4

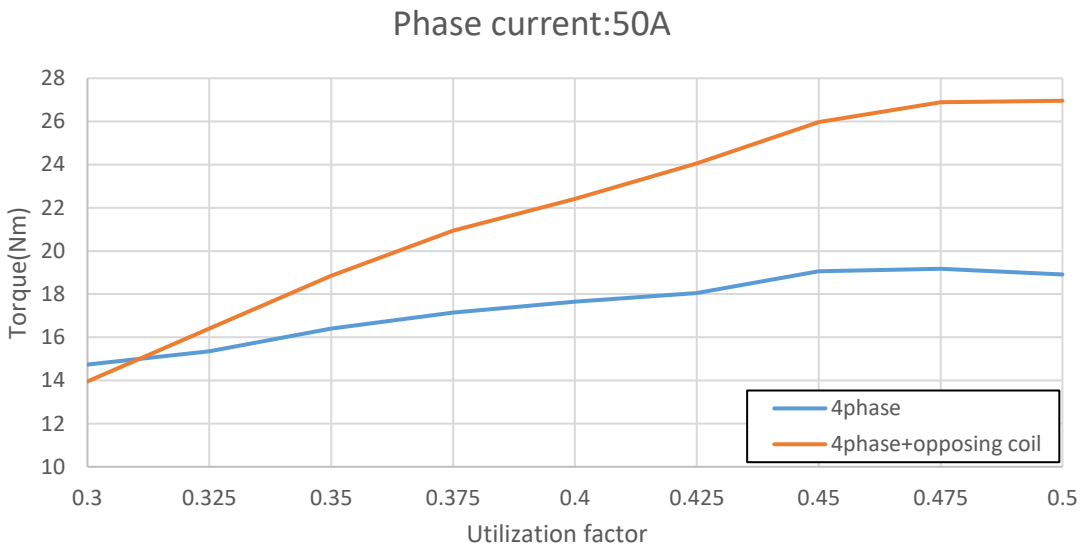

Figure 4-4 Average torque comparison between opposing coil and conventional coil arrangements with a range of pole utilisation factors

From the results in Figure 4-4, the four-phase SRM with the opposing coil appears to deliver more torque than the conventional reinforced coil in most cases (especially when the magnetic loop becomes wider). Examples of two extreme utilisation factors are shown in Figure 4-5 (note that the width of the entire magnetic circuit has been adjusted to fit the utilisation factor according to the previous assumption). This is because the SRM with opposing coil has less flux-density at stator yoke due to its unique flux pattern; while in a SRM with reinforced coil, the stator yoke will tend to suffer the local saturation. Further analysis is presented later in this section.

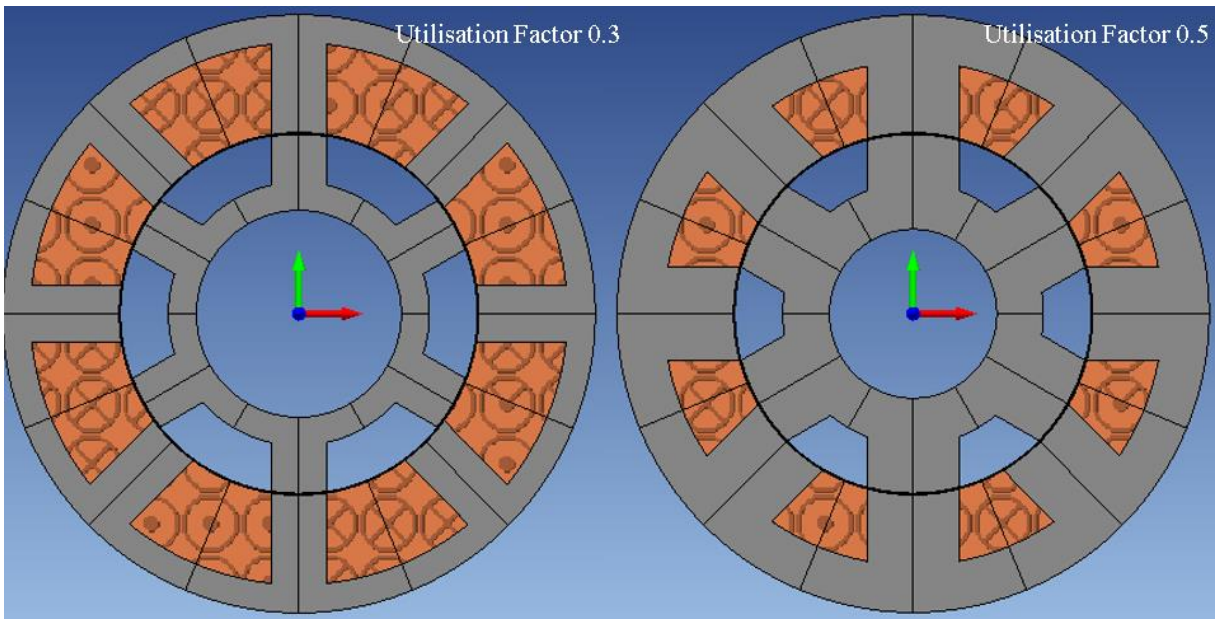

Figure 4-5 The example of the machine core design of different utilisation factors

From the result, it can be assumed that an opposing coil would make better use of the iron core part of the machine (since the iron core only dominates the magnetic circuit during saturated conditions and a wider magnetic loop will insure a higher flux density when the MMF is unchanged). This assumption was briefly verified by selecting different phase currents, the results of which are presented in Figure 4-6.

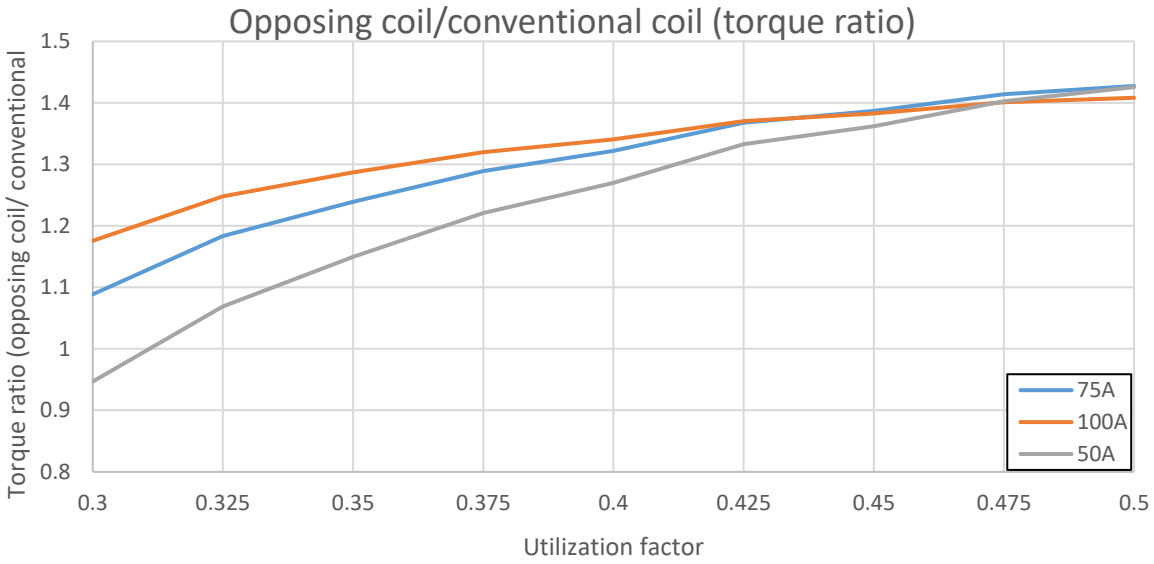

Figure 4-6 The advantages of the opposing coil method regarding torque output variation with pole utilisation factor and phase current.

In Figure 4-6, the vertical axis does not represent the absolute torque value. Instead, the value is a ratio that compares the torque from the opposing coil method to that from the reinforced coil method. If the torque ratio is larger than 1, it indicates that the opposing coil method delivers more torque than the reinforce method, in this scenario. There are three curves in this figure, representing three different excitation currents. Since a higher excitation current would undoubtedly lead to higher flux density, the values for the orange curve (100 A) and the blue curve (75 A) are higher than the grey curve (50 A) at low utilisation factors.

The reason why an opposing coil in the four-phase SRM demonstrates an advantage at this stage is due to its unique flux pattern. A comparison of flux patterns for different coil arrangements can be seen in Figure 4-7.

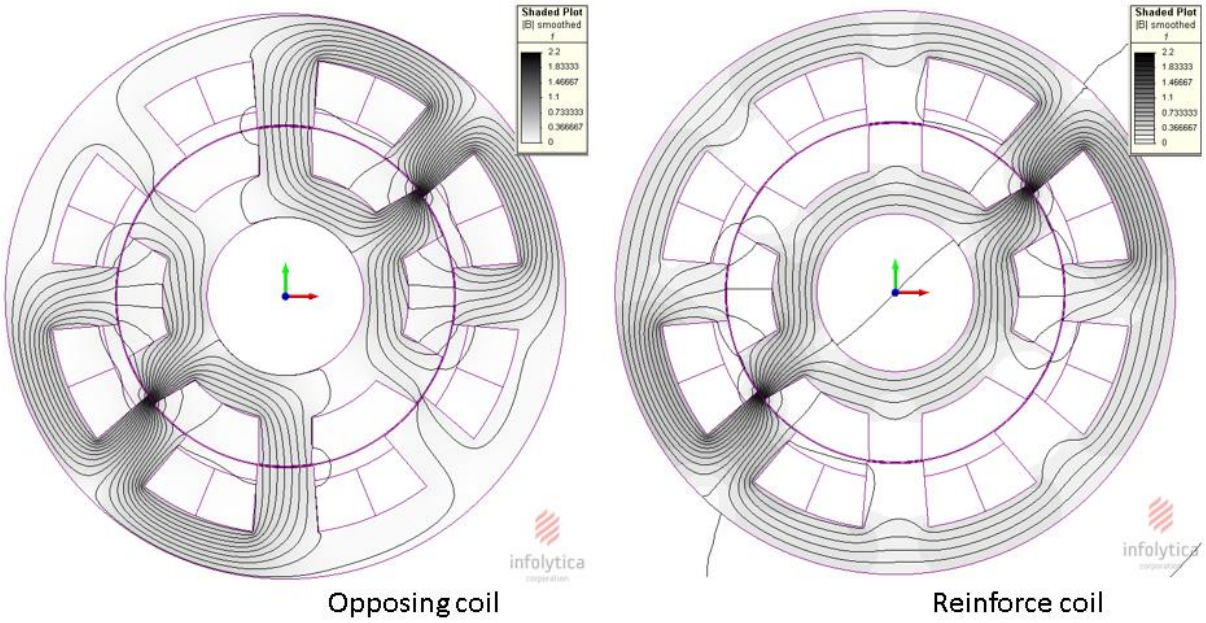

Figure 4-7 The different flux distribution patterns for opposing coil and reinforced coil

As can be seen from Figure 4-7, two phases are conducting simultaneously – one is at the unaligned position and the other is at an intermediate position. In both models, a portion of flux is flowing directly between these two conducting stator poles. The difference occurs in the remaining flux path. For the conventional coil on the right-hand side, a large proportion of flux is going between the two poles in the same phase and therefore needs to pass both the rotor and stator yokes. However, for the opposing coil, on the left-hand side, the remaining flux is going through the nearest poles and penetrates the airgap to eventually return to the coil. Moreover, it

appears that the conventional coil method suffers local saturation at its stator yoke between the two adjacent conducting phases.

Therefore, compared to the conventional path, the flux path of the opposing coil has larger airgap reluctance but lower iron reluctance. Because the iron core reluctance is affected by the flux density, it will increase rapidly in the saturated region. This is the reason why opposing coil could perform better with a higher exciting current and larger utilisation factor. Moreover, lower flux density in the iron core could also contribute to reducing iron loss.

As such, to further optimise the design for the opposing coil, a wider pole and narrower stator yoke could be used in contrast to the original reinforced coil design. Also, as mentioned in Chapter 3, the undesirable inductance rise at the unaligned position would prevent an increase in the utilisation factor. Then, a wider pole design could be achieved by expansion of the split ratio rather than by only increasing the utilisation factor.

4.1.2 The Development of a Static Torque Analysis Method for the Opposing Coil SRM

In a conventional-winding SRM, the average torque could be calculated using the static flux linkage-vs-current data at the unaligned and aligned positions[36]. This is a concise and effective method for estimating the performance of a new SRM model at the outset. But the precondition for this method is that the average torque should be similar to the superposition of the torque in each phase. This is not the case for the opposing-coil-winding SRM. Figure 4-8 shows the 2D transient FEM torque data (current control) for a four-phase opposing-coil SRM.

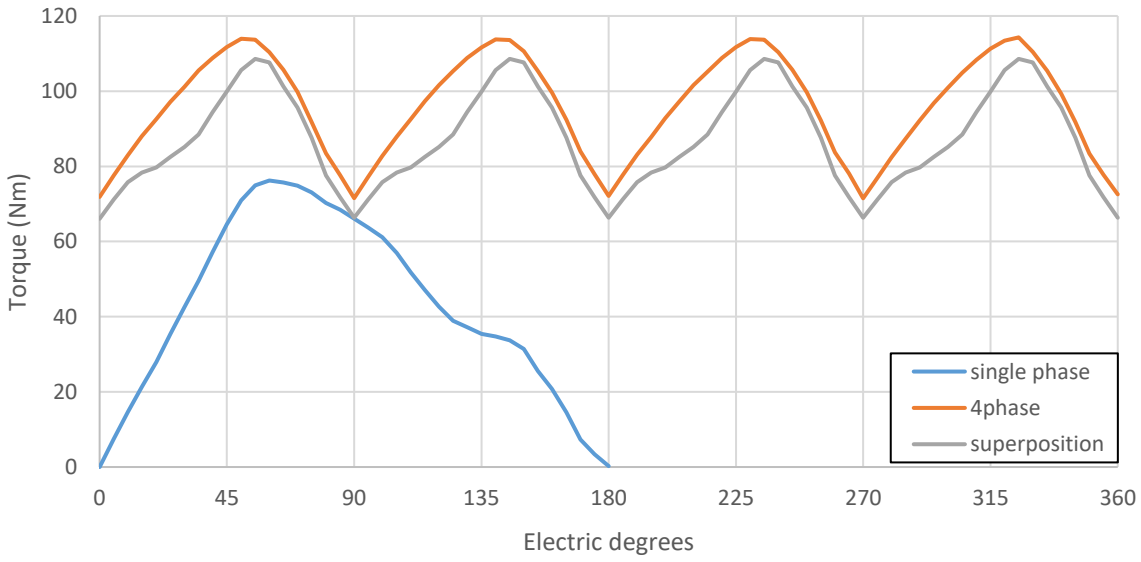

Figure 4-8 2D FEM torque curve in a full electric cycle (current control)

The superposition value of the single phase represents the torque value when only conducting a single phase. It is clear that the real average torque curve for the 4 phase machine is higher than the superposition curve and this difference is too significant to be ignored. Moreover, if the machine is operating at light load, where the magnetic circuit is unsaturated, the difference is likely to be greater. By setting the permeability value of the lamination steel to a constant, the situation for the linear region was simulated and is presented in Figure 4-9

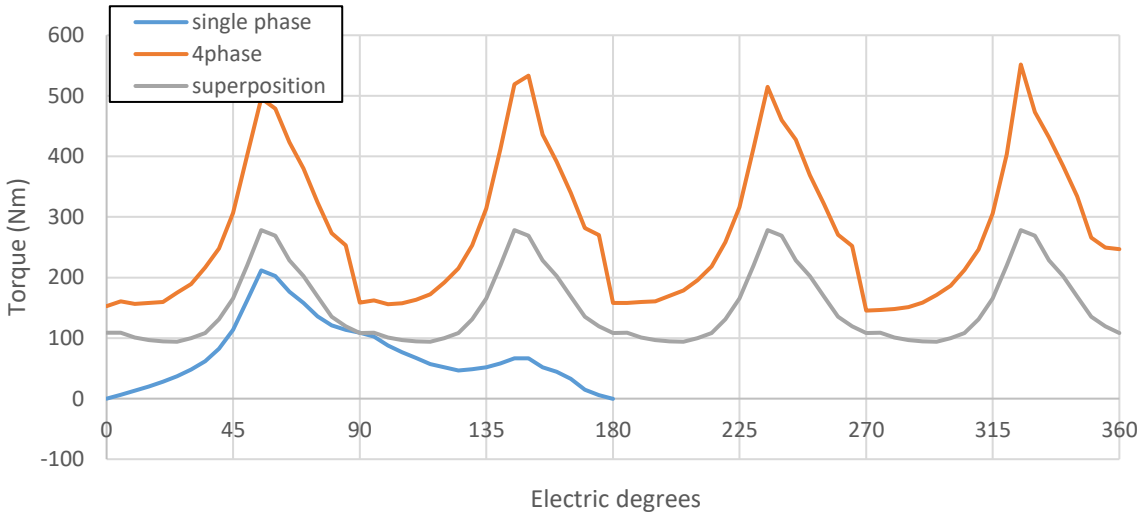

Figure 4-9 2D FEM torque curve in a full electric cycle under constant permeability

The cause of the significant difference is the interaction between phases, resulting from mutual coupling. In a conventional-winding SRM, as with a three-phase SRM, the phase interaction will only cause some cross-saturation issues which usually can be ignored(as can be seen from Section 3.1.2). However, for the opposing-coil-winding four-phase SRM, phase interaction will produce mutual coupling effects which enhance the torque capability.

Although it is not accurate to use a conventional one-phase static Psi-I curve for torque performance prediction, a full- cycle transient 2D FEM solution is still not necessary. As can be seen from Figure 4-10, the torque curve for a full mechanical cycle can be evenly divided into four repeat curves. Thus, only a quarter of the entire cycle needs to be solved.

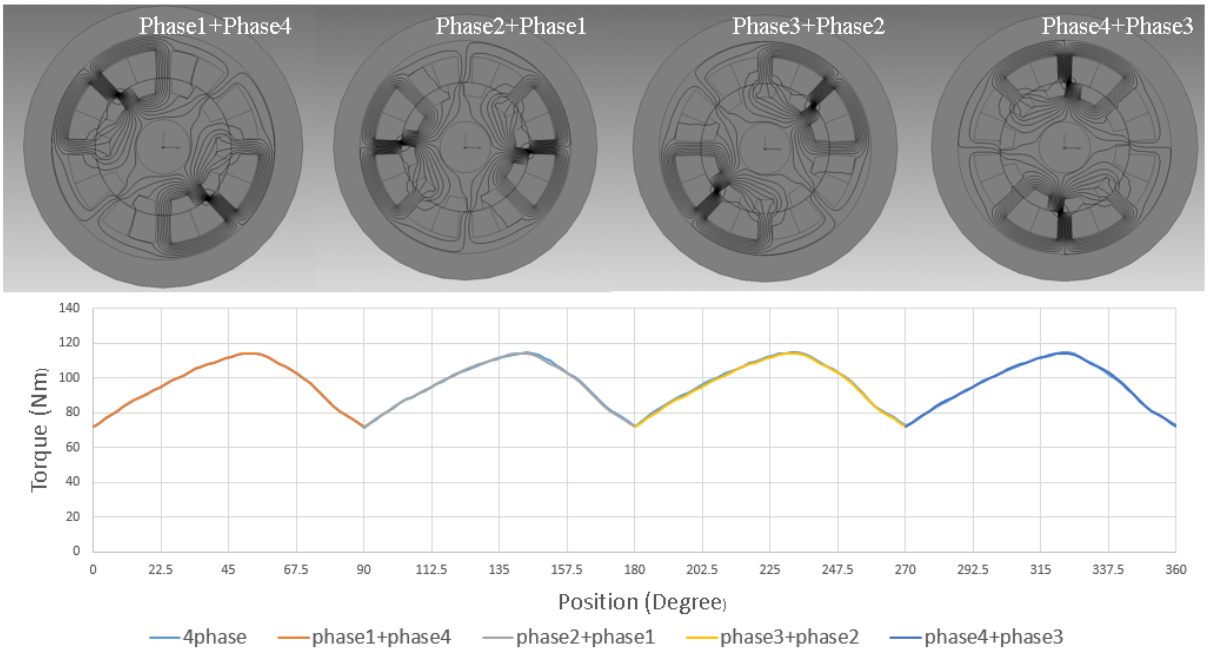

Figure 4-10 2D FEM-torque results in a full electric cycle under current control

Taking the first quarter (phase1+phase4 curve) as an example: during this period, phases 1 and 4 will conduct. As can be seen from Figure 4-11, the phase-1 period starts at the unaligned position and terminates at an intermediate position. In phase 4, its starting point is an intermediate position and ends at the aligned position.

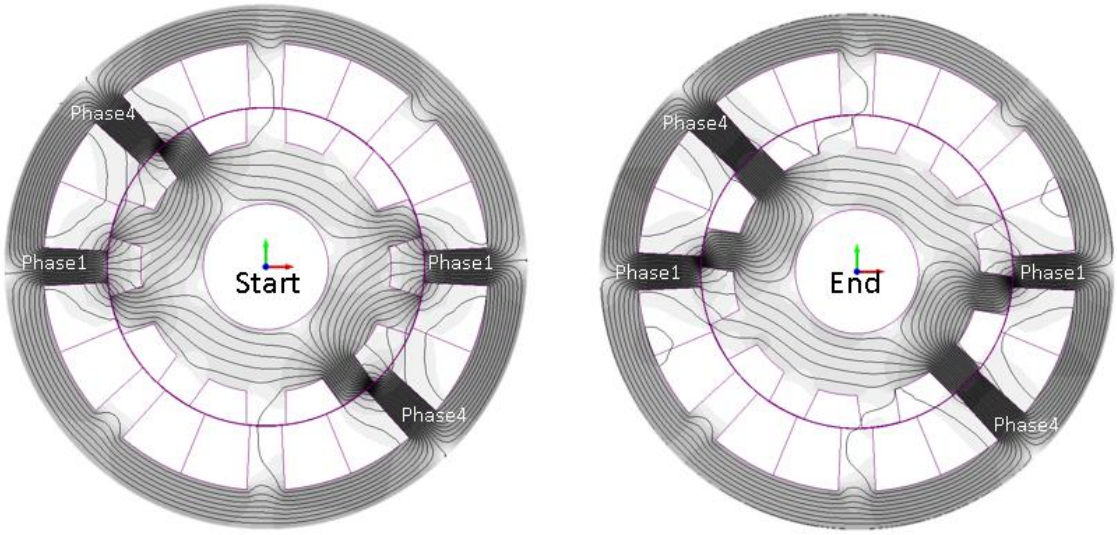

Figure 4-11 The period of a quarter of full-electric cycle when two adjacent phases are conducting together (rotation direction anticlockwise).

During this period, the inductance in these two phases should experience a monotonous increase (As this is the positive torque period for both phase1 and phase4). This could be verified by the 2D FEM:

When only conducting phase 1, the flux linkage in those two phases is shown in Figure 4-12. In this condition, the flux linkage wholly emanates from self-inductance, while the flux in phase 4 is completely due to mutual coupling effects. Both the self-inductance in phase 1 and mutual-inductance in phase 4 rise monotonously.

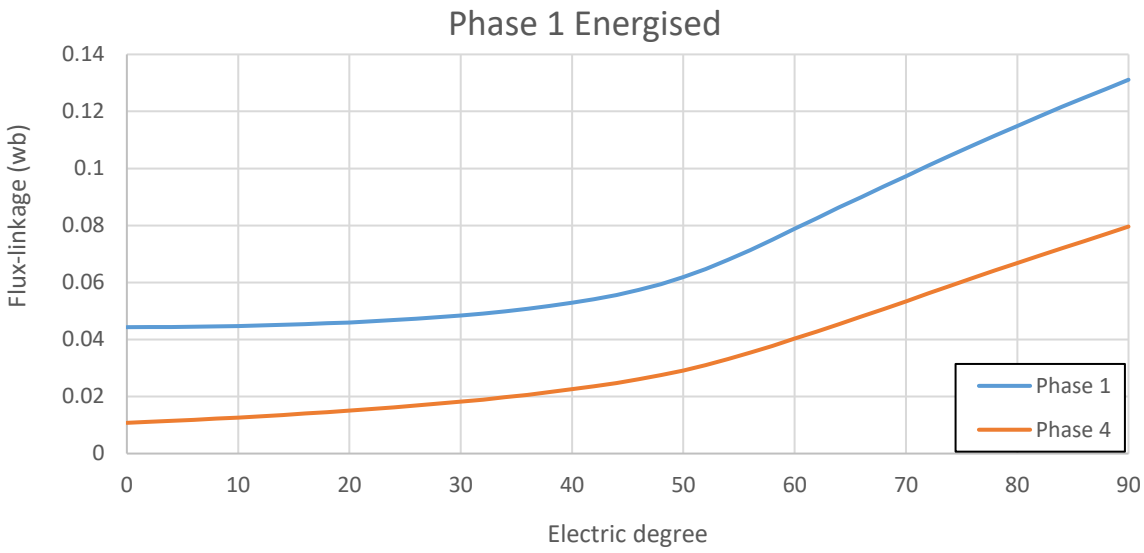

Figure 4-12 Flux linkage data for phases 1 and 4

A similar situation can also be seen when only conducting phase 4. (see Figure 4-13).

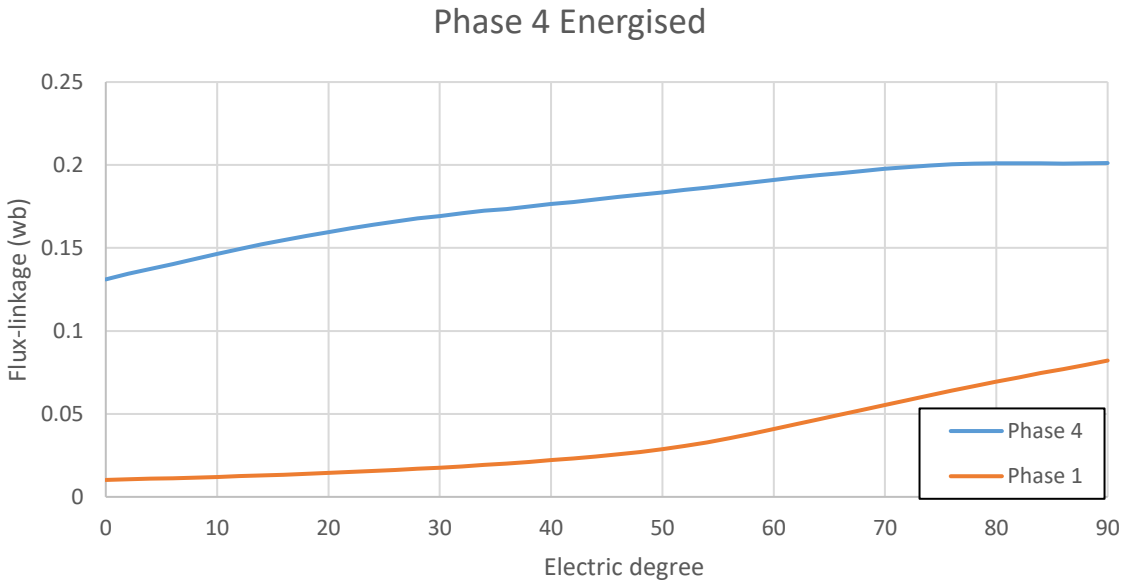

Figure 4-13 Flux linkage data for phases 1 and 4

Since the flux linkage in both phases is rising constantly during this period, the average torque for ideal current control can be easily estimated using the static flux linkage-vs-current data during a quarter of the full electric cycle.

The method is to conduct the two phases simultaneously and to collect the flux linkage-vs-current data at the beginning and ending positions for each phase, calculating the energy conversion during this period.

The energy conversion loop for phase 1 is shown in Figure 4-14, as an example. Just like a regular static method, the area between these two curves represents the co-energy that is converted into mechanical power. However, the difference is the energy conversion that is being investigated is from 0 to 90 electric degrees (rather than the 0 to 180 electric degree in a regular static method).

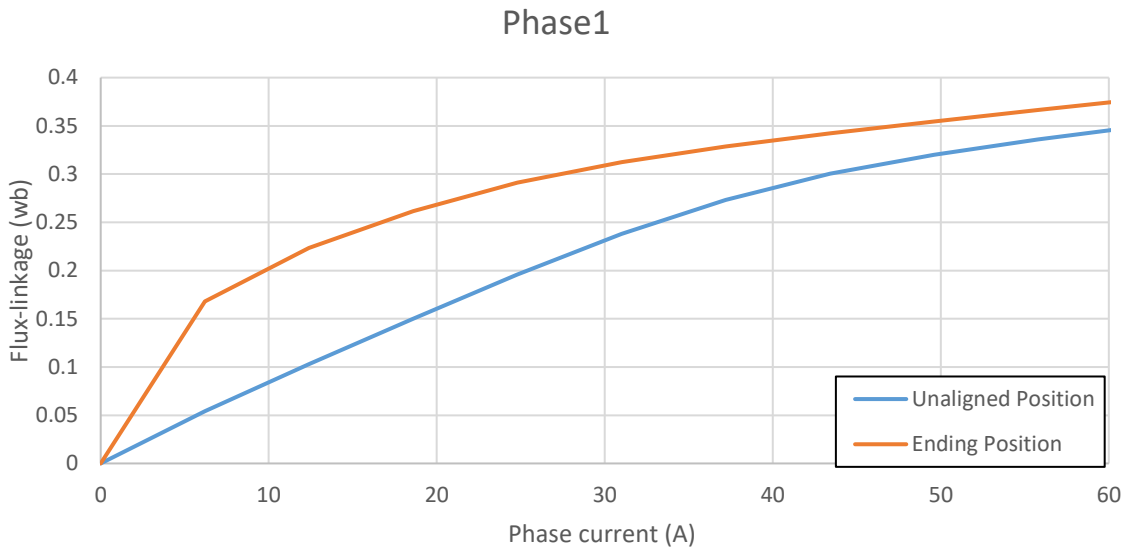

Figure 4-14 The flux linkage-vs-current curve for phase 1

A similar process can be repeated for phase 4 and, as can be seen from Figure 4-15, the energy conversion loop ends at the aligned position. Its starting position is at the mid-point, which happens to be the end position for phase 1.

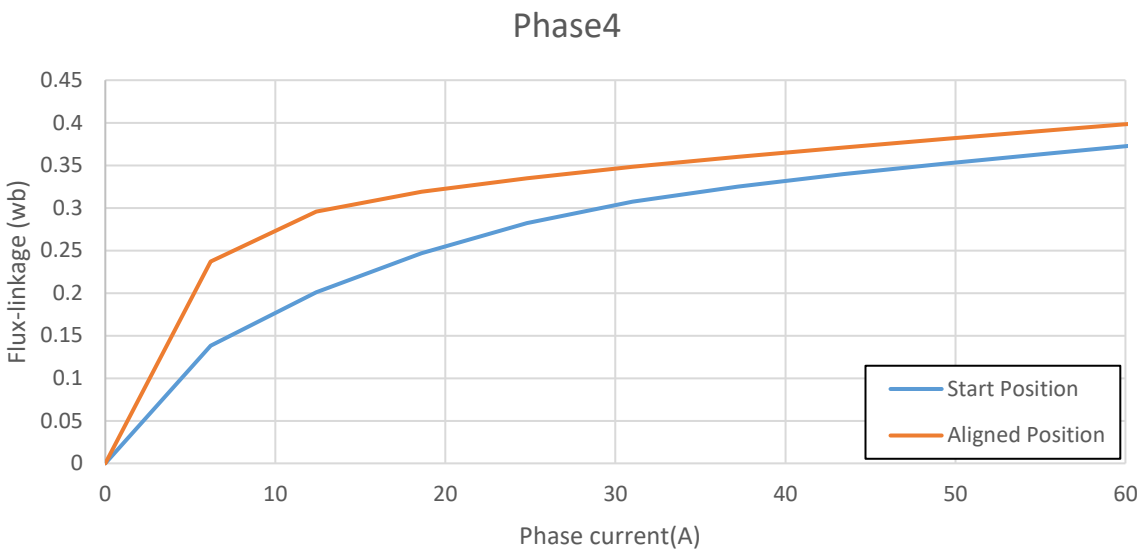

Figure 4-15 The flux linkage-vs-current curve for phase 4

The sum of the co-energy from these two phases can be used to calculate the average torque, just like the classic static method:

$$T = \frac{\mathrm{m}N_r W}{2\pi} \qquad (4\text{-}1)$$

Where m is the phase number, N_r is the rotor pole number, and W is the co-energy. The calculated torque T is compared to the results from the 2D transient FEM solution (current control) in Figure 4-16

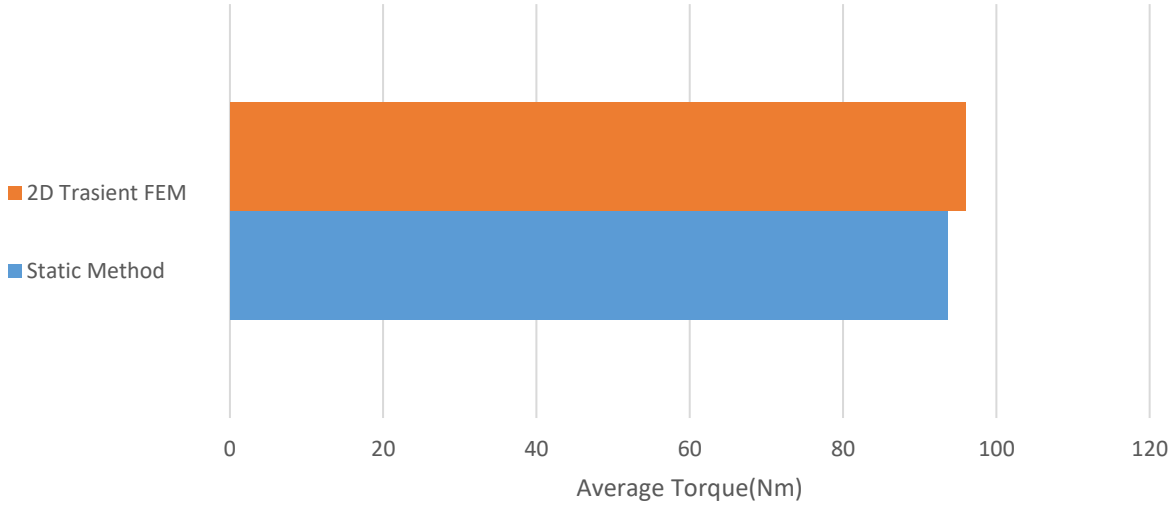

Figure 4-16 The difference between the 2D transient FEM (current control) and the static method results for the four-phase opposing-winding SRM

The difference between these two results is less than 2.4%. In fact, the classical single-phase static torque estimation for the conventional-winding SRM was unable to achieve a similar level of accuracy. Moreover, this method could be applied to other even-phase number SRMs

that use opposing winding. For example, the results comparison of a six-phase 12/10 SRM is shown in Figure 4-17, and is also relatively close.

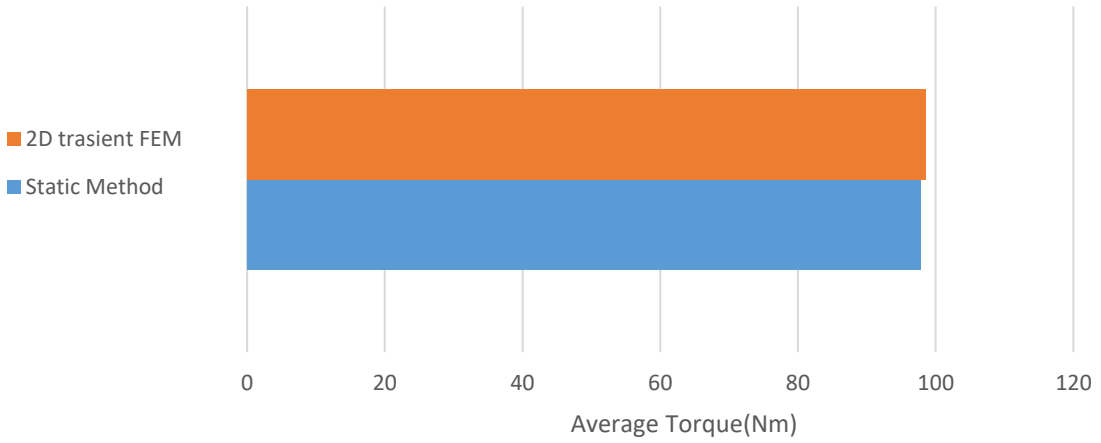

Figure 4-17 The difference between the 2D transient FEM (current control) and static method results for the six-phase opposing-winding SRM

Overall, the static method for SRMs with even-phase numbers and opposing windings was proven to be effective and efficient and could, therefore, be a useful tool for quick comparison of the different candidate designs during optimisation

4.1.3 Discussion of Higher Rotor Pole Number

A higher rotor pole number than stator pole number is not a novel concept for the SRM design and a discussion and analysis of this concept was carried out in the 1990s [36]. However, in some recent journals articles, such as [67] and [66], the higher-rotor-pole-number design has been discussed again, with experimental results for the small-scale prototypes claiming to provide better performance for static torque and torque ripple.

Because of the above work, in this project the higher-rotor-pole-number design was not excluded from the potential options for investigation.

However, a comparison of the 8/6 and 8/10 SRMs using a static 2D FEM did not reveal the obvious benefits of a higher-rotor pole-number design. The static flux linkage-vs-current curve is shown in Figure 4-18

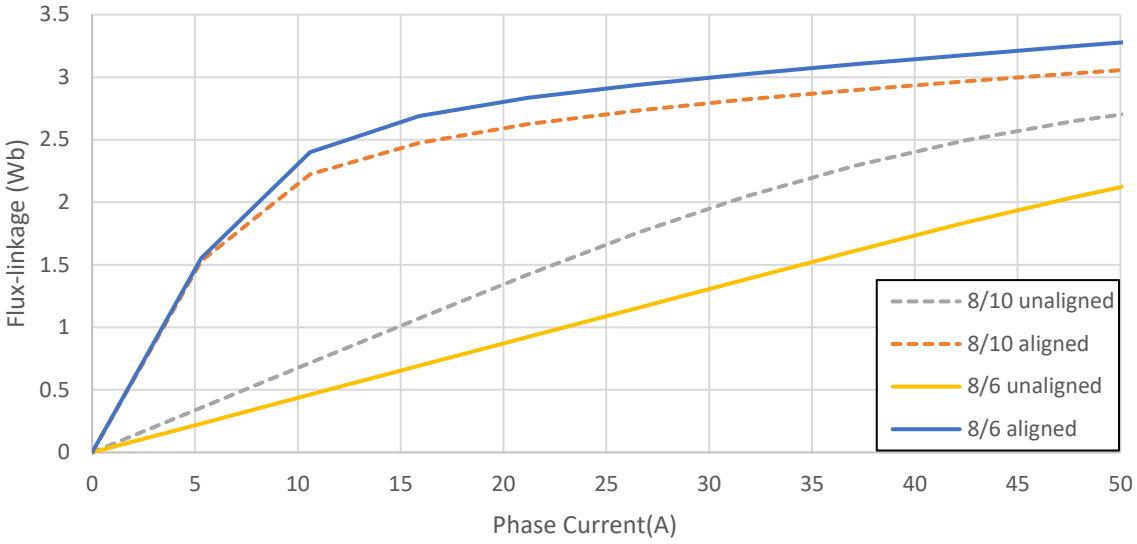

Figure 4-18 The 2D FEM flux linkage-vs-current curve for the 8/10 and 8/6 SRMs

As can be derived from Figure 4-18, the 8/10 SRM does have better static torque capability in the linear region. To be specific, the 8/10 model produces 40% higher torque than the 8/6 model if the phase current is limited to 10 A. However, when the phase current is 50 A, the torque from the 8/10 model is 5% less than that from the 8/6 SRM.

The narrow poles of the 8/10 SRM are one of the reasons it will become saturated earlier than the 8/6 SRM, but it is not the primary issue. Instead, the larger unaligned position inductance is mostly responsible for the inferior performance. Figure 4-19 shows a plot of the flux density distribution of the 8/10 SRM in the unaligned position, illustrating high flux densities.

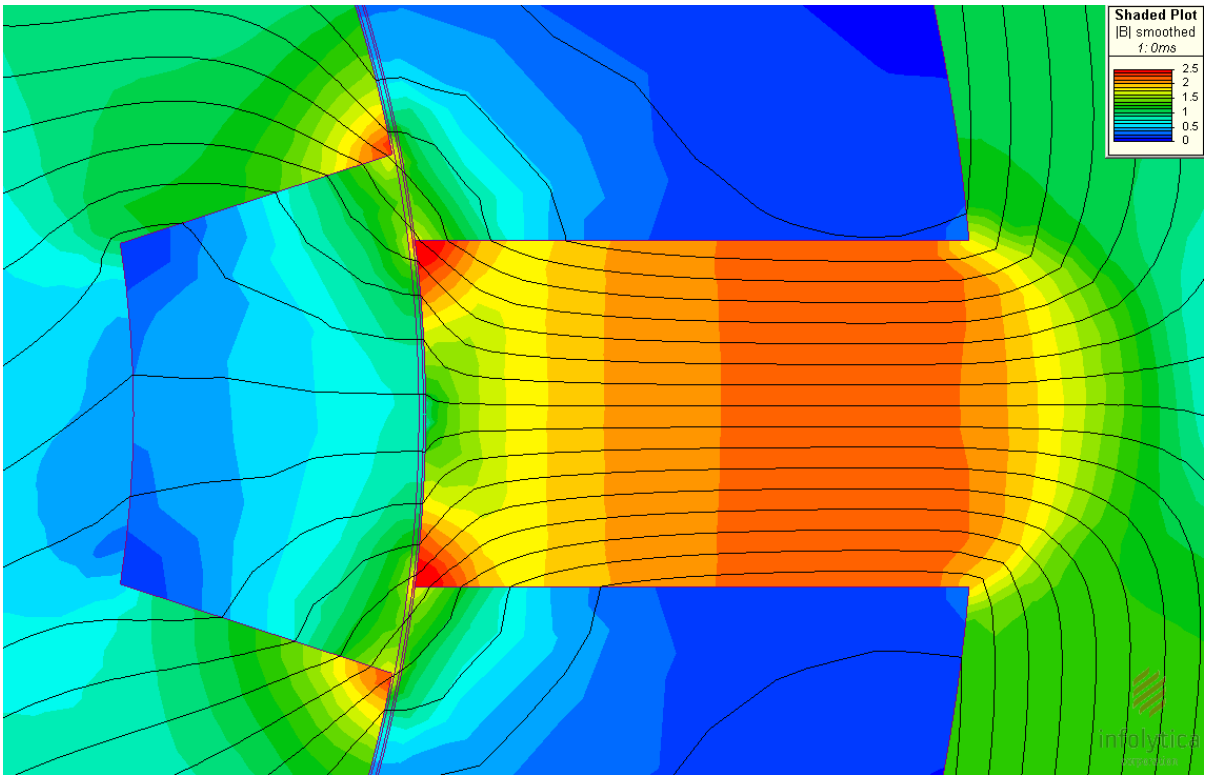

Figure 4-19 The flux density plot at the unaligned position for the 8/10 SRM

To solve this issue, the shape of the pole was redesigned to taper near the tip. The flux distribution plot for these uniquely tapered poles is presented in Figure 4-20. Compared to the plot in Figure 4-19, the novel pole design evidently relieves the inductance in the unaligned position while not losing too much inductance at aligned position.

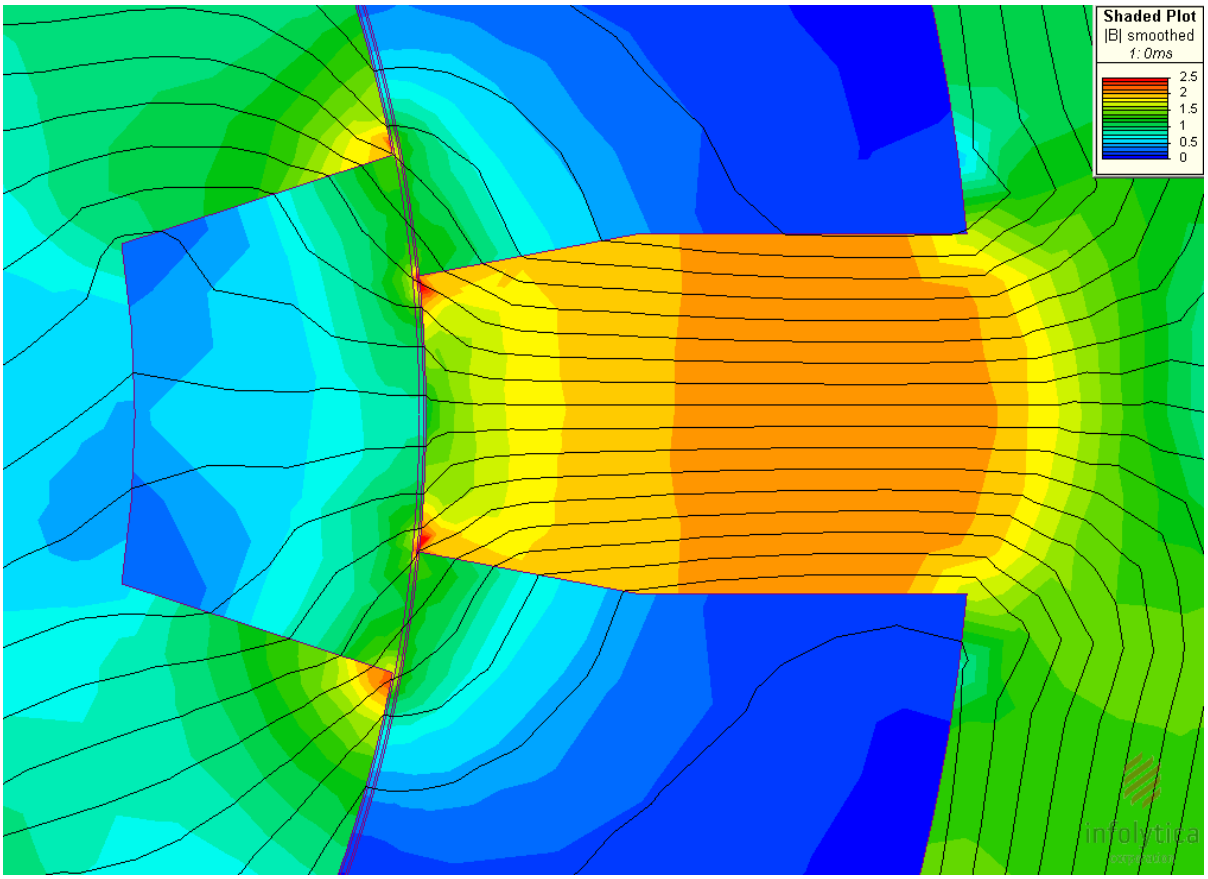

Figure 4-20 The flux density plot at the unaligned position for the 8/10 SRM with the redesigned stator pole

With the novel pole design, the static torque performance of the 8/10 model was effectively improved, even in the saturated condition. In Figure 4-21, the torque comparison between the novel-taper model and the original is presented.

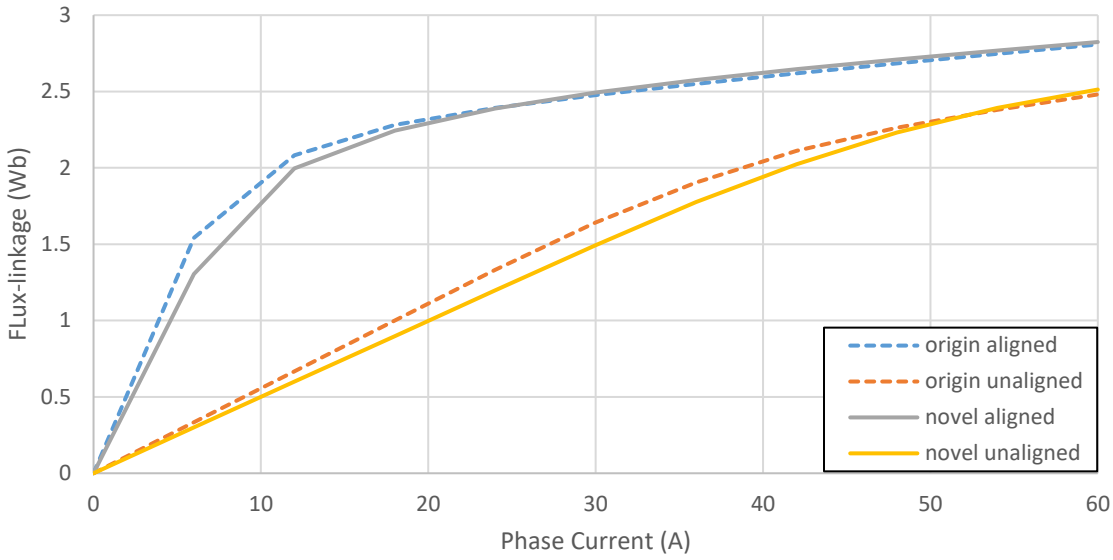

Figure 4-21 the 2D FEM-Psi-I curve for the conventional and novel stator poles

The 2D FEM result reveals that the co-energy from the novel taper model is 5.85% higher than that for the original model while phase current is kept identical (copper loss is 10.01% lower due to the larger slot area).

Although the higher-rotor-pole-number concept could potentially offer better static performance, especially in the linear region, its high commutation frequency (due to many more strokes per revolution than the conventional SRM) will significantly increase the requirement for volt-amperes and generate higher core loss. Thus, the specific output power would be difficult to achieve. The characteristics of the higher-rotor-pole-number design are more suitable for particular applications where efficiency at low speed and light load is critical.

4.1.4 Pole Number Combinations and Design Optimisation

The selection of the pole combination depends on the particular design requirement. Thus, a specific design objective needed to be settled at this stage. Meanwhile, an ideal method for evaluating the concept for a four-phase-opposing-coil SRM was to select a target SRM that had already been well optimised to make a fair comparison. For the conventional SRM structure, the SRM developed by Chiba et al. in [60, 103] is considered to be an outstanding design in this category [26]. Chiba's SRM was a three-phase 18/12 SRM, designed to be compatible with the PMSM currently used in the second-generation Toyota Prius hybrid vehicle. Then the objective of this stage was to develop a four-phase-opposing-coil SRM that was at least as competitive as Chiba's SRM.

The essential parameters for the objective SRM are shown in TABLE 4-1, Most parameters of the proposed four-phase SRM needed to be similar to Chiba's 18/12 SRM; the only difference being the phase current, which was reduced to compensate for the increased number of phases, thereby balancing the overall volt-ampere for a higher phase number.

TABLE 4-1 THE PARAMETERS FOR THE OBJECTIVE DESIGN

	18/12 SRM	4 Phase SRM
Stator Outer Diameter	269mm	269mm
Airgap Length	0.5mm	0.5mm
Stator Axis length	135mm	135mm
Maximum Speed	6000RPM	6000RPM
Torque Density	45Nm/L	>45Nm/L
Phase Current (RMS)	206A	155A
DC Voltage	500V	500V
Power	50kW	>50kW

According to [36], the selection of pole numbers is limited and for the regular SRM, the relation between the rotor pole number N_r and the stator pole number N_s is thus: $N_s = N_r \pm 2$ [36]. As such, for a four-phase SRM, the selection could contain the 8/6 and 8/10 options. In the interests of multiplicity[36], 16/12 and 16/20 could also be included. Moreover, in [67], a novel pole design formula was introduced: $N_r = 2N_s \pm 2$. This indicated that 8/14 and 8/18 could also be options.

However, as discussed in section 4.1.3, the higher-rotor-pole-number method could possess an advantage in static torque performance, especially in the linear region, but would also likely suffer a poor specific power output due to the high demand for controller volt-ampere (because the fluxlinkage is very high compared to a conventional design with same torque capability). Therefore, the higher-rotor-number design was merely used as a backup method for this project and the pole combination gave priority to the conventional options, such as 8/6 and 16/12.

Comparing the 8/6 and 16/12 methods, the 8/6 was deemed suitable for high-speed application, since the lower number of strokes per revolution reduces the commutation frequency and, therefore, effectively decreases the iron loss and volt-ampere requirement.

The 16/12 method, on the other hand, was deemed more suitable for the high-torque application. Comparing to the 8/6, the multiplicity structure could reduce the flux path length for each coil

and copper loss as well[36]. Moreover, due to the pole width being narrower than the 8/6 design, the stator yoke width could be thereby reduced and potentially contribute to increasing the airgap radius.

To achieve the design objective, the torque density achieved should be more than 45 Nm/L, a relatively high number for the conventional SRM. Compared to the torque requirement, the maximum speed of 6,000 rpm was more than acceptable. Therefore, the 16/12 pole combination was chosen for this project.

In Chiba's design, the lamination is made of high-silicon steel known as 10JNEX900. It is a very thin lamination material with a thickness of only 0.1 mm. According to [60], the B-H curve for this material is relatively poor and the main purpose of using this material is to reduce the iron loss. However, detailed data for this material is unachievable in the infolytica MagNet; therefore, Chiba's SRM needed to be remodelled using more conventional material, such as M270-35A in order to make a fair comparison.. The geometric details of Chiba's machine are presented in Figure 4-22, which was obtained from the 'SRM2' detailed in [103].

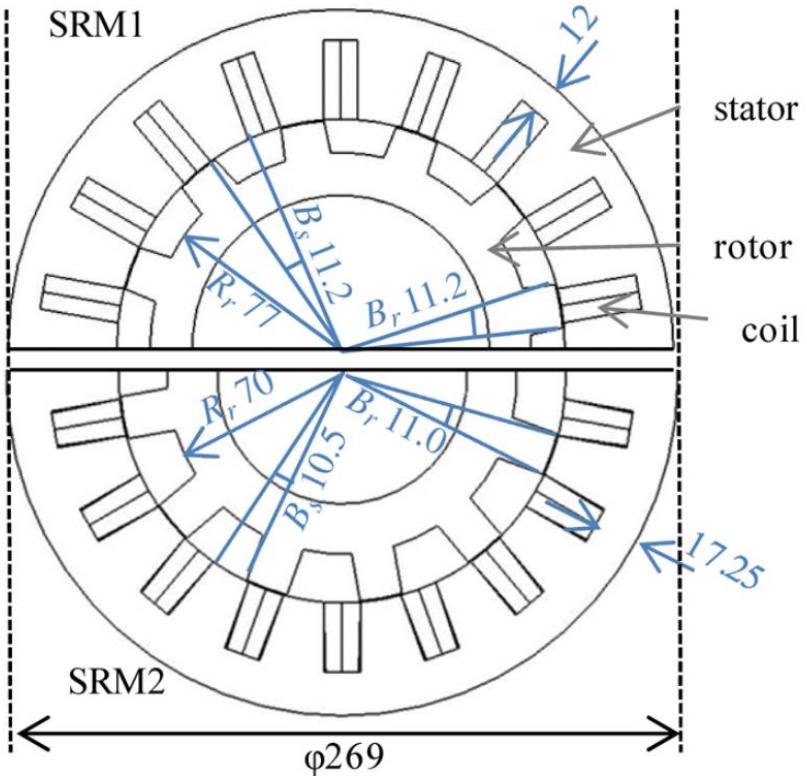

Figure 4-22 The iron core design of Chiba's SRM2 [103]

The first model of the 16/12 SRM was named SRM-1 and the half cross section of the SRM-1 in the MagNet is shown in Figure 4-23.

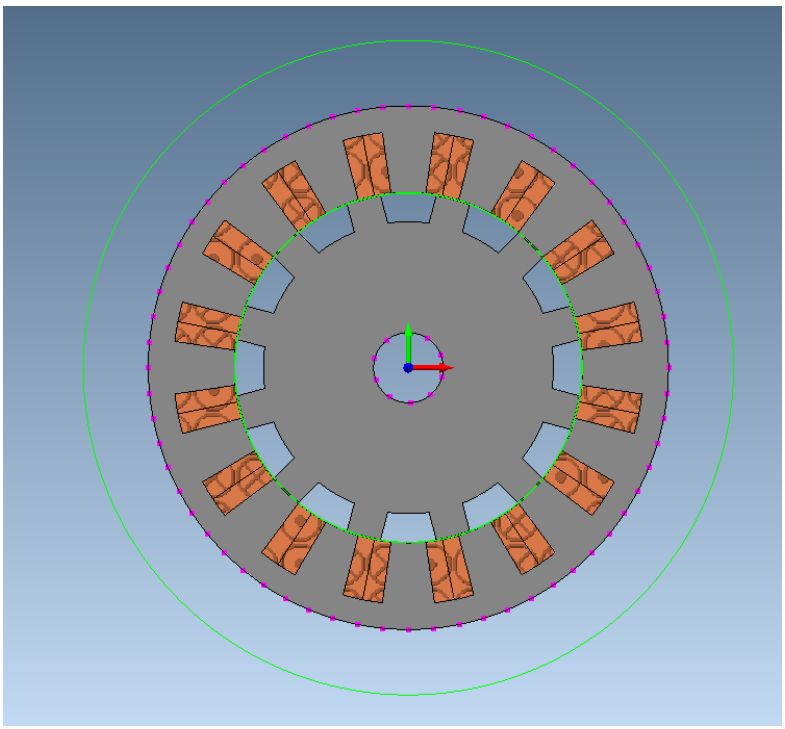

Figure 4-23 2D cross-section of 16/12 SRM developed in this section

The 2D FEMtorque comparison (under current control) between the two models at the same current density is shown in Figure 4-24. The current density for this condition is circa 34 A/mm^2, which is high, even for liquid cooling, and the average torque for the 16/12 and 18/12 SRMs is 593.5 Nm and 522.4 Nm, respectively. It can be observed that the torque from the 18/12 is higher than in [103], which is 400 Nm at a similar current density. There are two reasons behind this difference: first, the measured value is always lower than a 2D FEM result (about 10% for this machine); second, the lamination material M270-35A performed better magnetically than the 10JNEX900 in the original design.

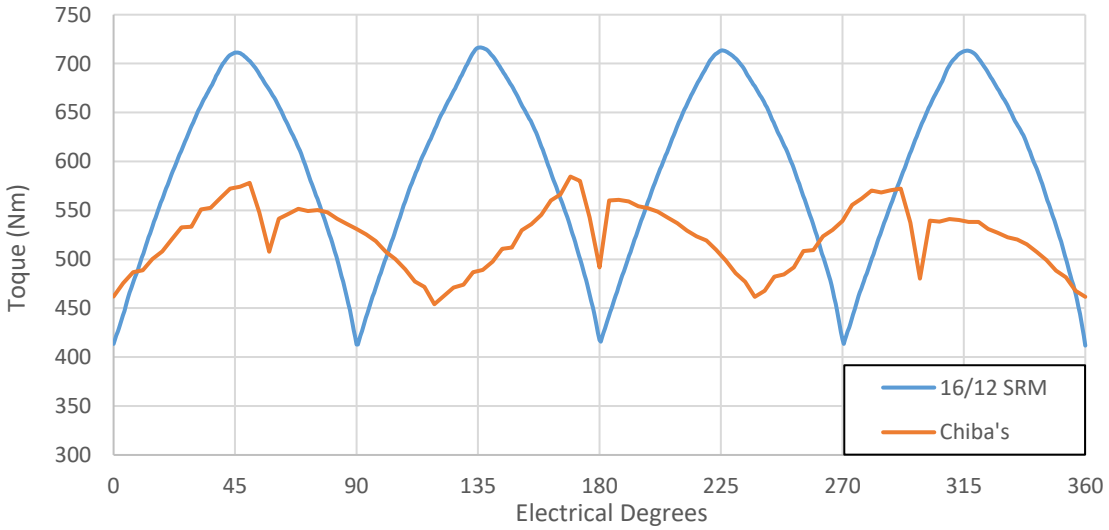

Figure 4-24 The static test comparision at a current density of 34A/mm^2

For a more reasonable comparison, the current of the 16/12 SRM was reduced to 155 A in rms. Under this condition, the two models were predicted to be driven with similar volt-amperes from the drive if the DC were limited to the same value of 500 V. The results reveal that these two models happened to produce a similar average torque at a very low speed (50 rpm). Since the fill factor was only 0.5, the copper loss was relatively high. But the copper loss in the 16/12 SRM was still 21.7% lower than in the 18/12 SRM.

TABLE 4-2 2D FEM RESULTS FOR LOW-SPEED

50rpm	**18/12 SRM**	**SRM-1 (16/12)**
Torque	521.7NM	520.4NM
Phase Current (RMS)	206.5A	155.0A
Copper loss	14.0KW	11.0KW
current density (assuming 50% fill factor)	34.4A/mm^2	27.0A/mm^2

However, although the 16/12 model performed better at a very low speed, the conditions for dynamic performance could be rather complicated. Figure 4-25 shows the 2D transient FEM results for the torque at 1,000 rpm. In this condition, the conducting angle for each phase is 180 electric degrees, without any advance angle. As can be seen from the results, the16/12 SRM failed to produce a competitive torque waveform compared with the 18/12 SRM

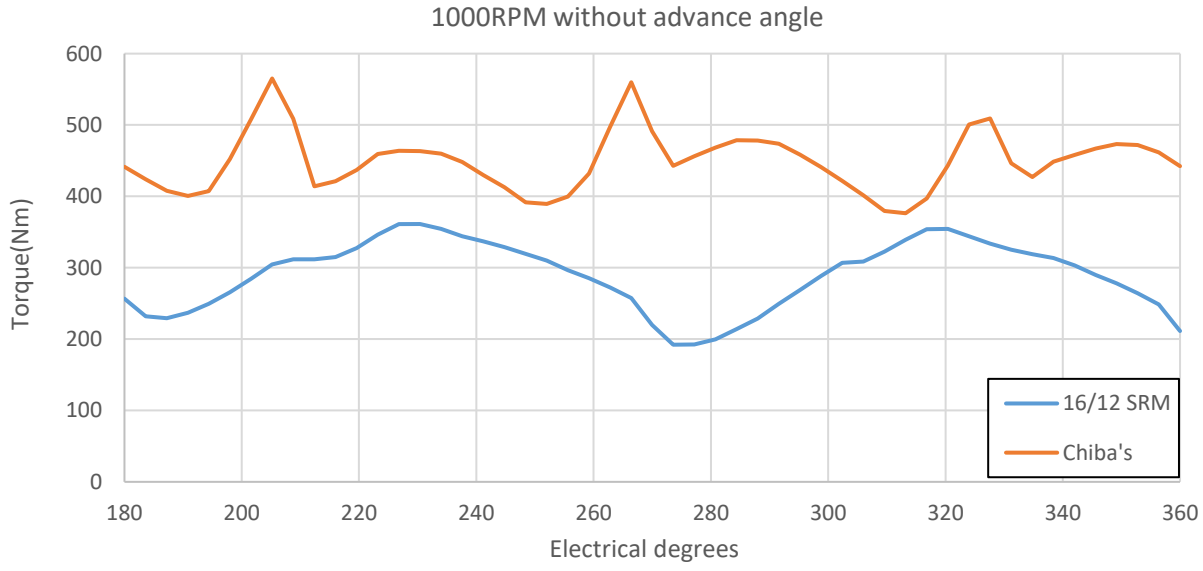

Figure 4-25 The 2D FEM torque waveform comparison at 1,000 rpm

The specific current waveform for this 1,000 rpm operation situation is shown in Figure 4-26. Clearly, it indicates that the 16/12 SRM requires more volt-amperes to offer a comparable output. As such, the design of the 16/12 SRM needed to be adjusted.

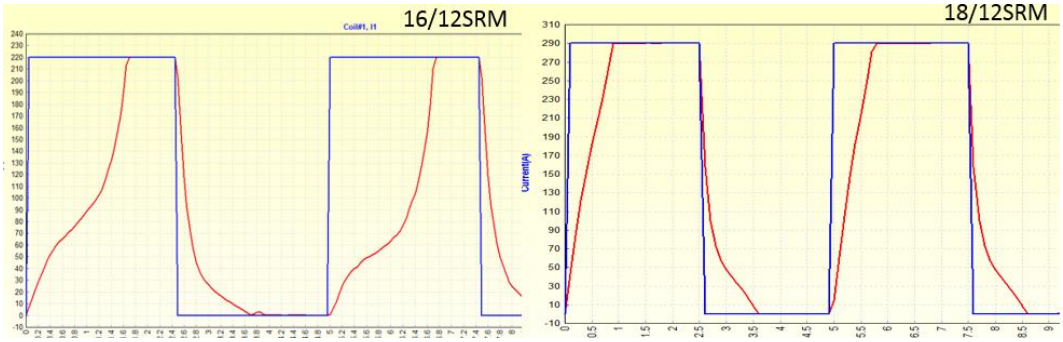

Figure 4-26 current waveform comparison at 1000 rpm

The phase voltage and current obey the following relation:

$$V = Ri + \frac{d\psi}{dt} = Ri + L\frac{di}{dt} + i\frac{dL}{d\theta}\omega \quad (4\text{-}2)$$

To improve the dynamic performance of the 16/12 SRM, the $\frac{di}{dt}$ needed to be increased.

$$\frac{di}{dt} \approx \frac{\Delta i}{\Delta t} = \frac{V - i(R + \frac{\Delta L}{\Delta \theta}\omega)}{L} \quad (4\text{-}3)$$

Since the Ri is relatively small compared to the $i\frac{dL}{d\theta}\omega$ (motional EMF), for a fixed DC voltage and peak current, the increase of $\frac{di}{dt}$ could be ensured by a decrease in L. Note that L here is the inductance at the aligned position for the peak-phase current. For convenience, it could also be marked as L_a^s.

However, a decrease in L_a^s would directly reduce the maximum flux-density at the aligned position and therefore could affect the torque capability and efficiency. To maintain the energy conversion loop in this situation, there were two possible methods:

1. Decrease the inductance for the unaligned position (also known as L_u). For an iron-core geometric design, this target could be achieved by enlarging the airgap between the stator and rotor poles at the unaligned position; specifically, either reducing the pole arc or increasing the split ratio could achieve this effect. In addition, decreasing the turn number-per-phase would also be a feasible choice, but this method has an adverse effect of lowering the inductance at the aligned position.
2. Saturate the machine earlier, at the aligned position. In fact, this method would require increasing the inductance for the unsaturated condition at the aligned position (L_a^u).

From the point of geometry design, a shorter flux path and wider poles (while yoke width remain unchanged) could be possible solutions. Increasing the turn number would also effectively increase theL_a^u but it would increase theL_u, as well. In theory, it is also possible to replace the iron core with a new material which saturates earlier while has a high permeability.

By increasing the split ratio and decreasing the pole arc, a revised model was developed. This new model was named SRM-2 and the 2D sector is shown in Figure 4-27. Although the model looks like a combination of several segments, in fact, the iron core portion is completely solid. The segmental appearance is due to the model having been drawn from the segment section created by Visual Basic Script.

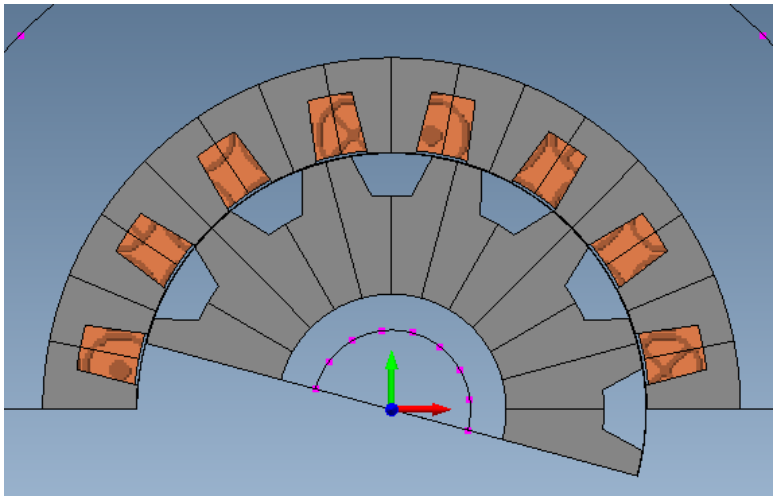

Figure 4-27 2D half cross-section of the revised 16/12 SRM (SRM-2)

The dynamic performance of the SRM-2 was verified by transient 2D FEM and the results are presented in Figure 4-28. This indicates that the SRM-2 could deliver the same torque as the 18/12 SRM under the given controller volt-amperes.

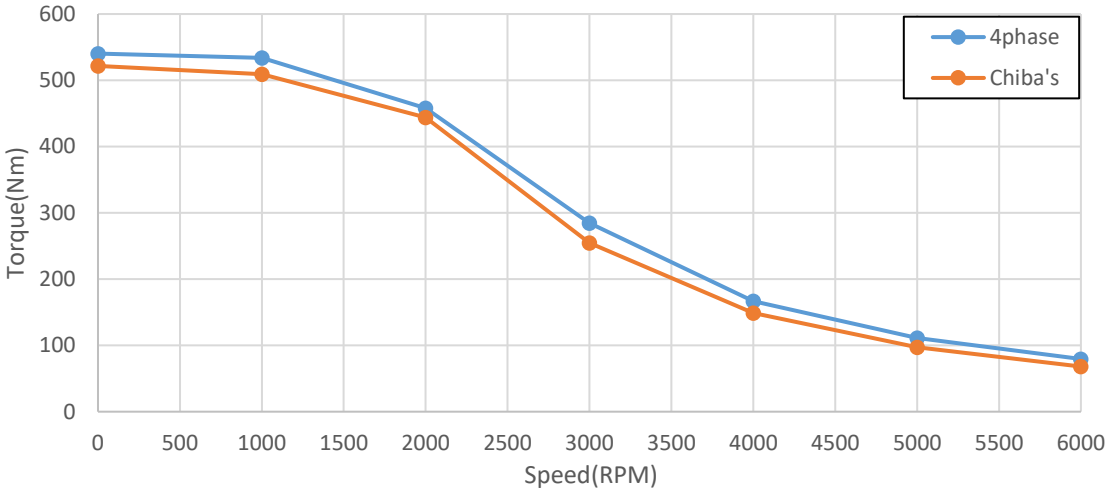

Figure 4-28 Torque-speed envelop comparison between SRM-2 and 18/12 SRM

The copper loss comparison can be seen from Figure 4-29, which shows that SRM-2 has a significant advantage at a lower speed. But as the speed increases, SRM-2 tends to follow a larger advance angle so as to maintain the torque output which finally reduces the efficiency. However, as can be seen from Figure 4-30, the iron loss of the SRM-2 is lower than the 18/12 SRM at this stage. Although the iron loss calculated in the 2D FEM would certainly be smaller than the real measured value, these results give a useful guide for comparing iron loss between two different models.

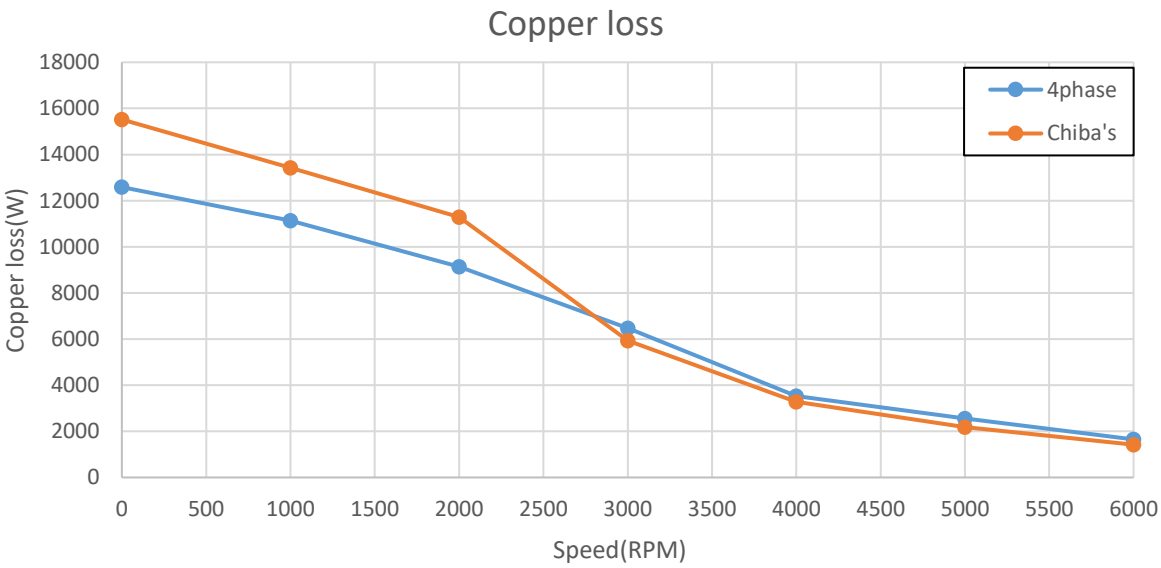

Figure 4-29 Copper loss comparison between SRM-2 and 18/12 SRM

Figure 4-30 Iron loss comparison between SRM-2 and 18/12 SRM

4.2 4 Phase Double Stator Switched Reluctance Machine

In section 4.1.4, a 16/12 SRM was developed to match the performance of Chiba's 18/12 [103] so as to verify the basic concept of the four-phase opposing-winding SRM. The results indicated that the 16/12 SRM would be able to offer similar performance to that of a well-designed three-phase SRM and would hold an apparent advantage with regard to copper loss at low speeds.

During the previous analysis and design process, the design of this machine was revealed to prefer a relatively large split ratio compared to the conventional three-phase and four-phase SRMs with a conventional winding. However, this design trend could prove to be a waste of space in the rotor since the unnecessarily large rotor yoke would not contribute to the torque capability. On the other hand, the large split ratio would provide an opportunity to implement a double-stator structure. In this section, the verification and analysis of the four-phase opposing-winding DSSRM will be described.

4.2.1 Analytical Analysis of Basic Concept

To analyse the electromagnetic performance of the DSSRM, simplified models of the conventional and double-stator SRMs are shown in Figure 4-31. As can be seen from the figure, the magnetic flux path in the SRM was simplified into that of a linearised segment, as in a linear SRM (LSRM) and several assumptions were made:

1. The LSRM and the double-stator LSRM (DSLSRM) models would both have a uniform cross section in the flux path.

2. The stator and rotor poles in the LSRM model as well as the inner and outer stator poles in the DSLSRM model would have the same length, marked as l_1.
3. The sum of the stator and rotor yoke lengths in the LSRM model would be equal to the sum of the outer- and inner-stator yoke lengths in the DSLSRM model, with a value l_2.
4. The airgap lengths in these two models would each be equal to l (the DSLSRM had two airgaps of this size).
5. The LSRM and DSLSRM models would be excited by the same level of current.

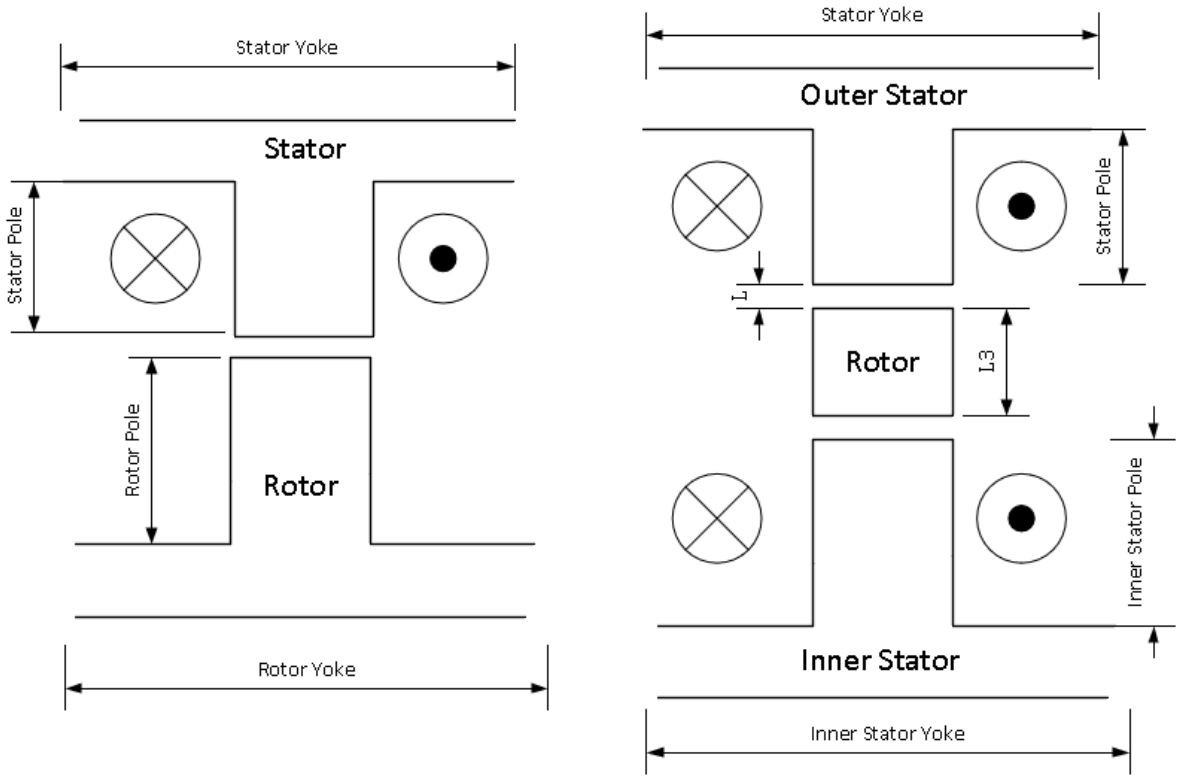

Figure 4-31 A simplified model of magnetic flux path. Left side : conventional SRM. Right side: double-stator SRM

When only taking into account the reluctance in the airgap, then there was no doubt that the reluctance of the DSLSRM would be twice that of the LSRM. To achieve the same inductance in both models, the following relation needed to be fulfilled:

$$L = \frac{{N_1}^2}{\mathcal{R}} = \frac{(N_2)^2}{2\mathcal{R}} \qquad (4\text{-}4)$$

Where $\mathcal{R}$ represents the reluctance of the LSRM, N_1 is the turn number in the LSRM model and N_2 is the turn number in the DSLSRM. It could be deduced that N_2 should be equal to

$\sqrt{2}N_1$. For this simplified model, the slot area of the DSLSRM was twice as large as that of the LSRM. As a result, these two models would have the same winding resistance:

$$R = \frac{lN_1}{\mu\frac{A}{N_1}} = \frac{lN_2}{\mu\frac{2A}{N_2}} \quad (4\text{-}5)$$

Thus, the above analysis suggested that there would be an equilibrium point between the double-stator and conventional single-stator structures in this condition. However, in reality, the majority of the reluctance in a magnetic circuit will be provided by the iron core of the machine. In this condition, the double-stator configuration would begin to gain the advantage. Since the flux path in these simplified models was assumed to have a uniform cross section, so the reluctance in the iron core would be proportional to the length of the flux path. If the analysis sets the μ_r as the permeability of the iron core, μ_0 as the permeability of air, and A as the cross section of the flux path, then the reluctance of the LSRM would be equal to $\frac{l_1+l_2}{\mu_r A} + \frac{l}{\mu_0 A}$, and the reluctance of the DSLSRM would be equal to $\frac{l_1+l_2+l_3}{\mu_r A} + \frac{2l}{\mu_0 A}$. The ratio between these two reluctances could be defined as k_r:

$$\frac{\frac{l_1+l_2+l_3}{\mu_r A}+\frac{2l}{\mu_0 A}}{\frac{l_1+l_2}{\mu_r A}+\frac{l}{\mu_0 A}} = 1 + \frac{\mu_0 l_3+\mu_r l}{\mu_0(l_1+l_2)+\mu_r l} = k_r \quad (4\text{-}6)$$

As discussed earlier in this section, k_r would be equal to 2 if only the airgap reluctance is being considered. This is, in fact, assumes the iron core has infinite permeability:

$$\lim_{\mu_r\to\infty} 1 + \frac{\mu_0 l_3+\mu_r l}{\mu_0(l_1+l_2)+\mu_r l} = 2 \quad (4\text{-}7)$$

Another limiting case is when μ_r approaches 0; this is a condition approximate to where the iron core is heavily saturated. The calculation is as follows:

$$\lim_{\mu_r\to 0} 1 + \frac{\mu_0 l_3+\mu_r l}{\mu_0(l_1+l_2)+\mu_r l} = 1 + \frac{l_3}{l_1+l_2} \quad (4\text{-}8)$$

Moreover, the rotor pole length l_3 was much shorter than the sum of the stator pole (l_1) and stator yoke (l_2) lengths, so the value of k_r in this condition would approximate to 1. Therefore, the value of k_r under real conditions would be between 1 and 2,

From equations $L=\frac{{N_1}^2}{\mathcal{R}} = \frac{(N_2)^2}{2\mathcal{R}}$ (4-4) and $R=\frac{lN_1}{\mu\frac{A}{N_1}} = \frac{lN_2}{\mu\frac{2A}{N_2}}$ (4-5), for $k_r = 2$, the DSLSRM will provide the same flux-linkage as the LSRM with the same copper loss. And with

smaller k_r, the DSLSRM would offer higher inductance than the LSRM. That means the DSLSRM would provide higher torque than LSRM. This is because the aligned inductance is significantly larger than the unaligned inductance.

In reality, k_r tends towards 2 in the unaligned position and towards 1 in the aligned position. This means that the advantage for the aligned position when normally saturated would be larger than that for the unaligned position. For example, assuming k_r to be 1.8 at the unaligned position and 1.5 at the aligned position, then the inductance ratios between the DSLSRM and LSRM would be 1.11 at the unaligned position and 1.33 at the aligned position and, obviously, a larger inductance ratio between the aligned and unaligned positions would increase the advantages of the DSLSRM. As mentioned in Chapter 3. the requirements of the inductance ratio could be fulfilled by increasing the split ratio in the iron core design.
Compared to the LSRM, the inductance increase is also contributed by the increase in the number of turns from the inner stator. Thus, the DSLSRM will have lower flux-density at the same torque output. This means that the DSLSRM also have advantages of lower iron loss and better overload potential.

Although the analysis in this section clearly reveals that the DSLSRM would offer higher torque capability than the LSRM within the same copper loss limit, the conditions for the rotational machine could be more complicated. For example, in the DSSRM, the inner-stator pole is narrower than the outer-stator pole to ensure sufficient slot area. Also, the slot area in the inner stator is smaller than in the outer stator. These problems will weaken the advantage of a double-stator structure in the rotational SRM. Thus, further analysis was required.

A quarter cross-section of a typical DSSRM is shown in Figure 4-32. The inner stator region, rotor region and outer stator region form three concentric annuli. The area of the inner stator region and outer stator region are $\pi\left({R_1}^2 - {R_0}^2\right)$ and $\pi\left({R_3}^2 - {R_2}^2\right)$ respectively. The difference between these two areas could be marked as e. For the DSLSRM, the structure is equivalent to the DSSRM with $e = 0$. When the DSSRM has a small e, its structure will be more closer to the structure of DSLSRM, and can take more advantage of the double stator configuration.

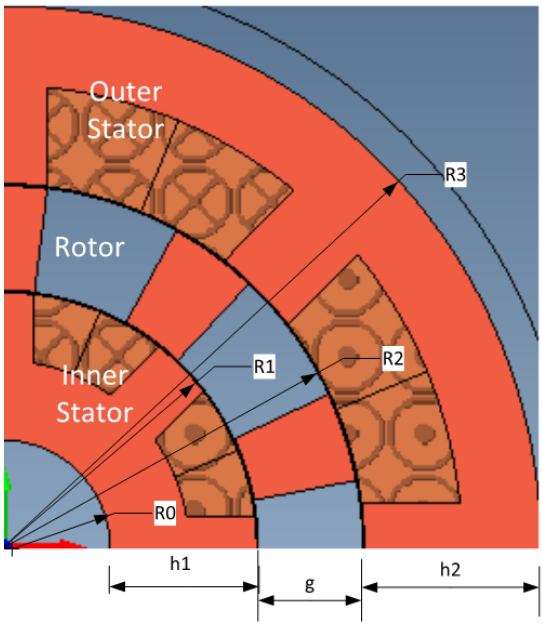

Figure 4-32 Quarter cross section of the DSSRM

Define h_1 to be the radial depth of the inner stator, h_2 the radial depth of the outer stator and g the radial depth of the rotor.

Since $R_1 = R_0 + h_1$, $R_2 = R_1 + g$, $R_3 = R_2 + h_2$, then e is calculated as follows:

$$\pi\left((R_0 + h_1)^2 - {R_0}^2\right) + e = \pi((R_0 + h_1 + g + h_2)^2 - (R_0 + h_1 + g)^2)$$

Assuming $h_1 \approx h_2 \approx h$, then e is approximated by:

$$e = 2\pi h(g + h)$$

This indicates that the values of g and h should be small for the DSSRM design. i.e. the machine works best when the inner and outer diameters are similar, making it similar to a linear machine.

In a conventional SRM, the unaligned inductance mainly depends on the clearance between the rotor pole and stator pole (which is related to the pole width). However, in the DSSRM, the unaligned inductance should also consider the clearance between the outer stator and inner stator (which is related to the rotor pole length: g). For instance, if the rotor pole length is too small compared to its width, the flux path at the unaligned position will directly connect between the inner stator and outer stator and significantly increase the inductance at this condition. There are two methods to reduce g:

- Simply reduce the radial length of the rotor, maintaining the same inside and outside diameter, thereby increasing h. The gap between the inner and outer stator reduces, so that a large unaligned inductance is inevitable, resulting in a poor magnetic design.
- Increase the stator-pole number so that the width of each pole reduces. This can be obtained by increasing the phase number or using the multiplicity of structure.

There are also two methods to reduce h:

- Increase the split ratio: a machine with more poles will tend to have a large split ratio.
- Reduce the stator-yoke width. This method could be fulfilled by using opposing-coil-winding and a higher phase number.

Thus, it was concluded that a four-phase design with opposing winding would be the ideal configuration for the DSSRM.

As can be seen from Figure 4-33, an 8/10 DSSRM was developed from the 8/10 SRM. It should be noted that the outer stator of the 8/10 DSSRM has exactly the same dimensions as the stator of the 8/10 SRM. The results of the static psi-I curve are shown in Figure 4-34. Compared to the 8/10 SRM, the 8/10 DSSRM increases the aligned position inductance by about 32 %, while less favourably the unaligned inductance also increases by approximately 23%. Moreover, for the same flux linkage, the flux density in the DSSRM is apparently lower, which will also contribute to reducing iron loss.

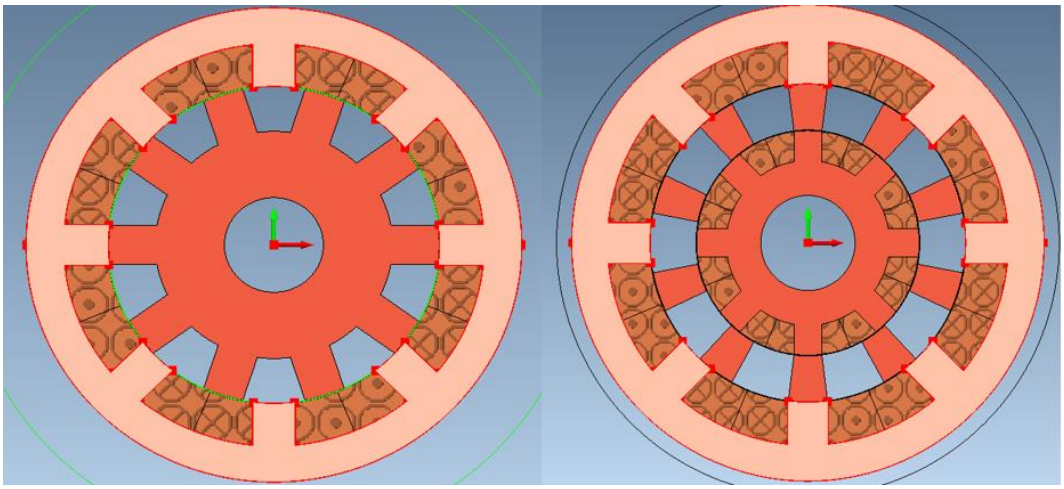

Figure 4-33 Cross-section of 8/10 SRM (left) and 8/10 DSSRM (right)

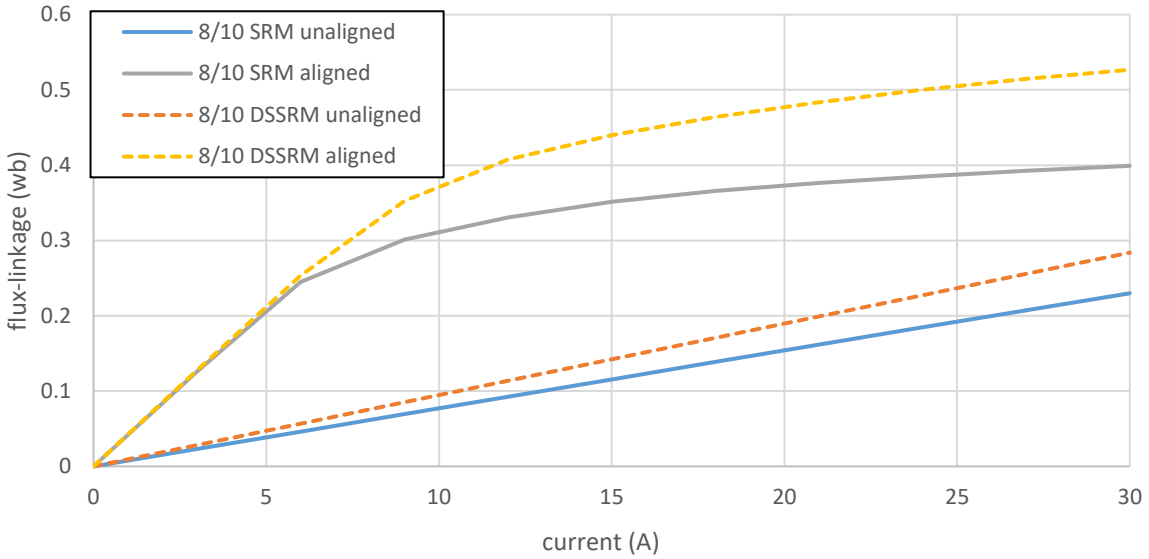

Figure 4-34 The flux-linkage vs current curve for 8/10 SRM and 8/10 DSSRM

With the assistance of the inner stator, the DSSRM will apparently be able to achieve higher torque density. As can be seen from TABLE 4-3, the 8/10 DSSRM would deliver 34.2 % higher torque than the single-stator SRM with the same current value.

Although the inner stator would also increase the copper loss by about 70 %, if the average torque of the 8/10 SRM were to be increased to a similar level, the 8/10 DSSRM would actually produce 24.6 % less copper loss.

TABLE 4-3 THE AVERAGE TORQUE AND CORRESPONDING COPPER LOSS OF 8/10 SRM AND 8/10 DSSM

	Single Stator SRM	**Double Stator SRM**	**Single Stator SRM (higher phase current)**
Average torque	79.86Nm	107.16Nm	109.61Nm
Copper losses	888W	1503.45W	1994.13W

4.2.2 Potential Design Developments and Simulation Results

To further verify the four-phase opposing-winding DSSRM concept, a design was developed to compare with the 18/12 and 16/12 models in section 4.1.4.

According to [87], the DSSRM is a machine type that potentially offers high torque capability, whilst maintaining low inductance. This is because the DSSRM has a relatively large airgap at the unaligned position. As a result, a lower controller volt-ampere could be expected.

In section 4.1.3, the higher-rotor-pole-number configuration of the four-phase SRM was discussed and several 8/10 SRMs were verified with the 2D FEM. The major issue for this design was the large volt-ampere requirement due to the small airgap at the unaligned position. Therefore, the double-stator structure represented a potential solution for improving the performance of the 8/10-pole configuration. The first attempted design, which will be introduced in this section, was an 8/10 DSSRM and the cross section of that machine is shown in Figure 4-35.

The machine was modelled with the same dimensions (269-mm outer diameter, 135-mm active length and 0.5-mm airgaps) that were used in section 4.1.4. The performance of this design was verified by the 2D FEM. The static results are shown in TABLE 4-4, and revealed that this model could provide a very high torque density with a 20 A/mm^2 current density.

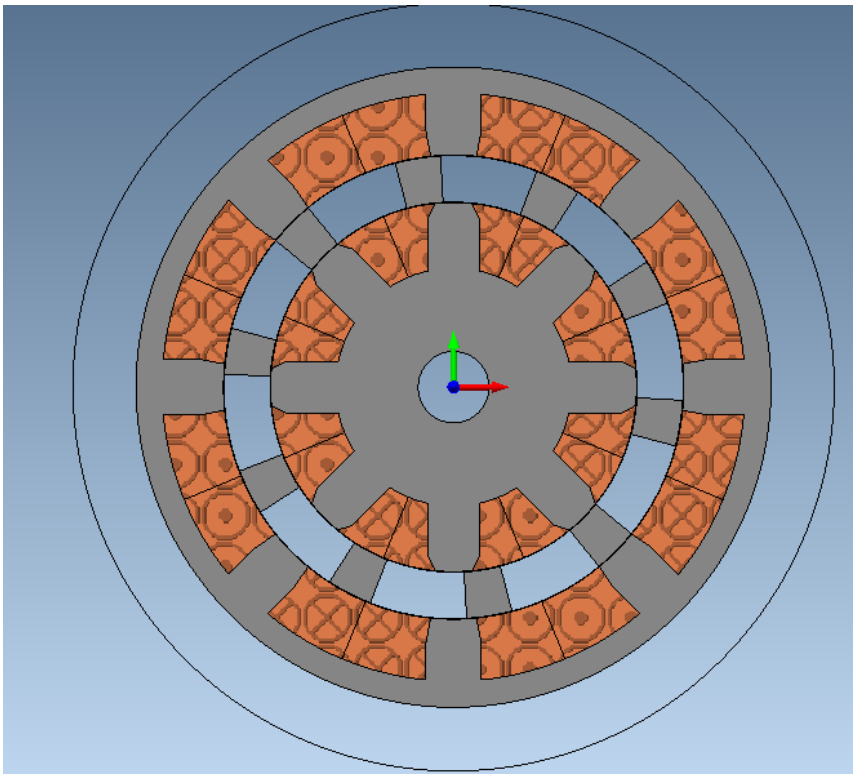

Figure 4-35 Cross section of the 8/10 DSSRM (269-mm stator diameter)

TABLE 4-4 STATIC PERFORMANCE OF 8/10 DSSRM

8/10DSSRM

Average torque	534.79NM
Torque density	69.64 Nm/L
Current density	20.36 A/mm^2

However, the dynamic performance of this machine would drop relatively quickly as the speed increases. As can be seen from TABLE 4-5, even with an advance angle of 30 degrees, the torque output at 1,000 rpm still reduced by about 24% from its static value. This situation was not observed during optimisation of the 16/12 SRM. This meant that the 8/10 DSSRM might not be suitable for this specific application.

Moreover, the eight-stator pole in this model could only offer limited freedom for design optimisation and might not adequately utilise the advantage of the double stator. This design was, therefore, abandoned.

TABLE 4-5 DYNAMIC PERFORMANCE OF 8/10 DSSRM

500V DC	30 degrees at 1000 rpm	45 degrees at 2000 rpm
torque	406.74Nm	131.69Nm
power	42.60KW	27.58KW

As the multiplicity of the basic four-phase design had already presented its effectiveness in the conventional single-stator SRM, as described in section 4.1.4. the second attempt described in this section is that of a DSSRM with 16 stator poles.

Under this condition, the feasible pole combinations would be limited to 16/12 and 16/20. However, as discussed in section 4.1.3, the higher rotor pole number configuration does not ensure better torque production, especially when the machine operates at saturated condition. Moreover, a higher rotor pole number will undoubtedly increase the commutation frequency, thus substantially increasing the iron loss. At this condition, it is the 16/12 rather than 16/20 which should be considered (the cross section is shown in Figure 4-36).

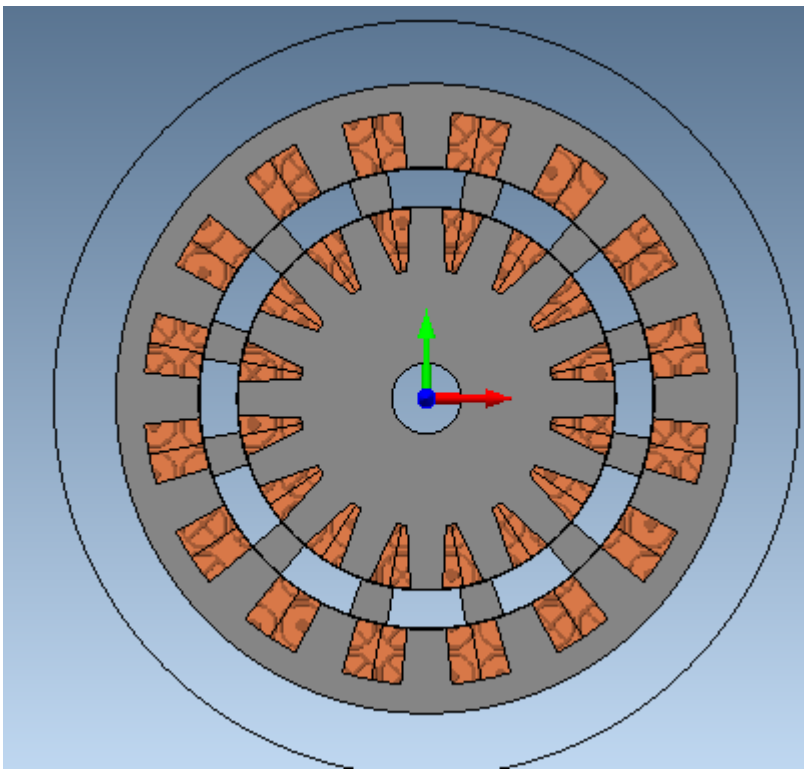

Figure 4-36 Cross-section of 16/12 DSSRM

The design of the 16/12 DSSRM is an upgrade from the 16/12 SRM whose development was outlined in section 4.1.4. Its torque-speed curve, copper loss data and iron loss result are shown in Figure 4-37, Figure 4-38, and Figure 4-39 respectively. The comparison reveals that although the 16/12 DSSRM does not enhance torque capability, both copper and iron loss are reduced efficiently.

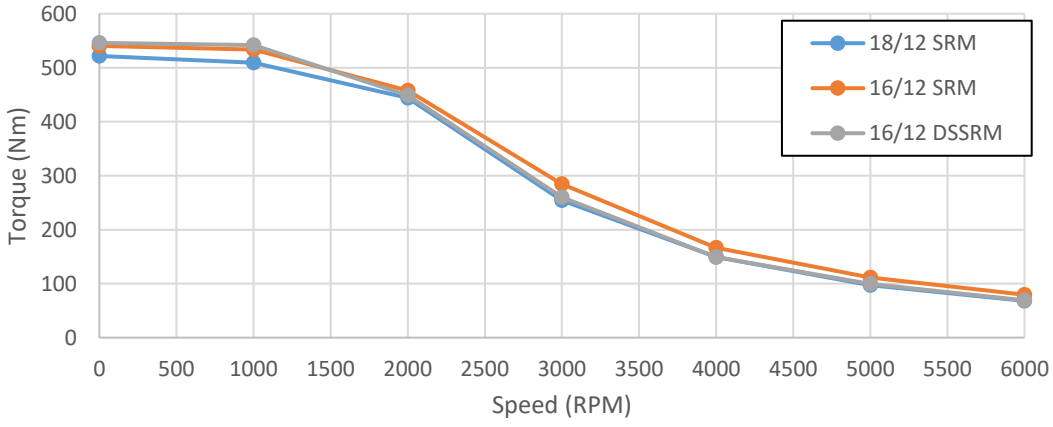

Figure 4-37 Torque-speed-curve comparison of the 16/12 DSSRM and the 18/12 SRM

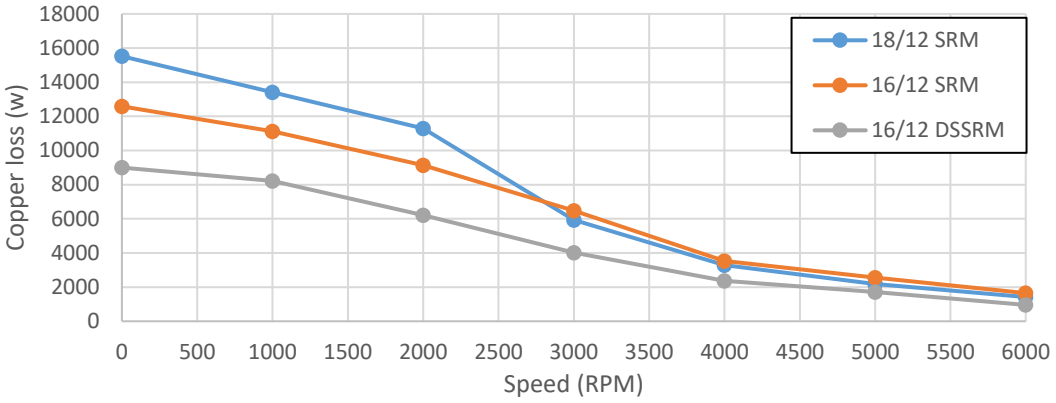

Figure 4-38 Copper-loss comparison of the 16/12 DSSRM and the 18/12 SRM

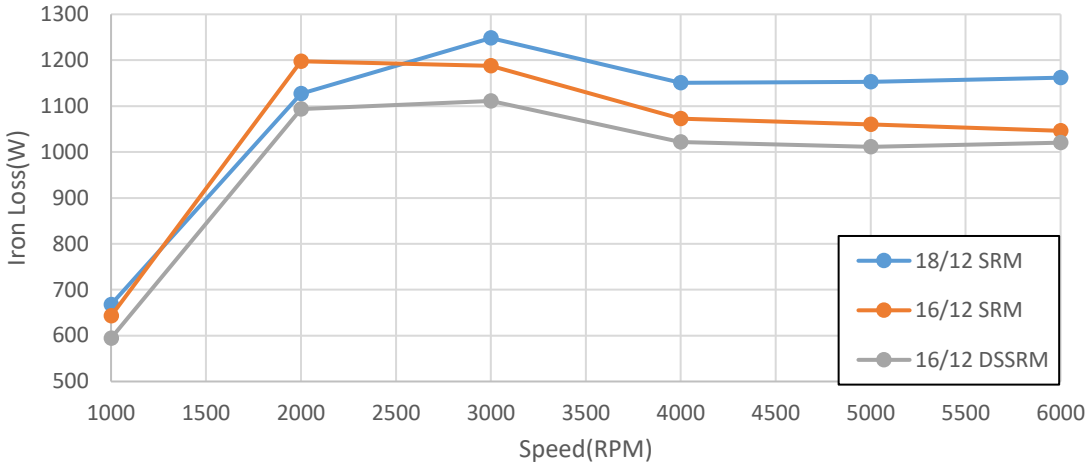

Figure 4-39 Iron-loss comparison of the 16/12 DSSRM and the 18/12 SRM

4.3 Conclusion

Several conclusions resulted from this chapter:

- Opposing windings were deemed suitable for four-phase SRMs. They have a symmetric flux distribution, better torque capability and lower iron loss in a saturated condition. Regarding the design rule, opposing winding would also allow for a narrower stator yoke and larger split ratio than in the conventional winding method.
- The 8/10 SRM was discussed briefly: with a higher number of rotor than stator poles, this machine could offer better torque performance before saturation. However, this machine type would also consume a larger number of volt-amperes, reducing its dynamic performance.
- To show the advantages of a four-phase opposing coil configuration, a 16/12 opposing-winding SRM was developed and compared with Chiba's 18/12 SRM. The results from 2D FEM showed the 16/12 SRM could provide the same torque as Chiba's SRM with lower copper loss.

- Analytical analysis of the DSLSRM revealed the advantages of the double-stator structure: better torque capability and lower loss can be expected. Additionally, further study suggested that for the rotational DSSRM, the four-phase opposing-winding configuration should be recommended.
- To verify the conclusion from the analytical analysis of DSSRM, a 16/12 opposing-winding DSSRM was developed; the 2D FEM results showed that this machine could efficiently reduce copper and iron loss compared with the previous 16/12 SRM.

This chapter made several contributions to knowledge:

- 2D FEM results have confirmed the opposing coil can produce higher torque than a traditional reinforced coil at 4 Phase SRM. Moreover, from a design perspective, opposing coil would require thinner stator core back and therefore leave the possibility of a larger split ratio.

- An analysis of higher rotor pole number configuration reveals that this concept only provides better torque capability at the linear region, which is a rare operating condition for most SRMs. Furthermore, a novel stator pole design is developed and shown to improve the performance of this configuration, with a higher rotor pole number.

- Analytical analysis demonstrates that a conventional SRM can benefit from a double stator structure (it should be noted that previous double stator SRM studies were based on a segmental rotor SRM). Moreover, this benefit will become evident with a higher split ratio.

- A 16/12 SRM and a 16/12 DSSRM is developed to compare with a world-leading three phase SRM design, and the result illustrates that the above analysis is reasonable.

Chapter 5. Multi-Physical Challenges and Prototype Development

Chapter 4 discussed the development of the proposed SRM topology which combines features from mutual coupled SRMs and double stator SRMs. An optimised design is generated to compare with Chiba's 18/12 SRM, which is considered to be one of the best ever published. The design had a very similar size and overall VA rating to that of Chiba's SRM, but results in 30% less copper loss whilst delivering same torque performance.

This chapter develops a prototype that will eventually be tested in Newcastle University. Firstly, the size of the prototype machine is selected by considering the limitations and accessibility for both benchmark equipment and the target machine. Since mechanical aspects of design could be a critical obstacle to building a double stator SRM, several rotor structures and a range of materials will be analysed in detail to ensure satisfactory mechanical and electromagnetic performance. Based on the selected rotor structure, the prototype design is generated and optimised. Finally, as a part of feasibility check, thermal properties of the prototype machine have also been simulated and analysed.

5.1 Volume Selection and Design Objective

In Chapter 4. the four-phase, opposing-coil, double-stator SRM was shown to be a capable and potential machine type for this project through comparison with a machine built and tested by Chiba. Chiba's machine was funded by the Toyota Motor Corporation to develop an electric machine that is capable of providing similar performance to an IPMSM that is being used in automotive traction. There are difficulties from both budget and bench equipment availability to build and test a SRM on that scale within this project. A reasonable alternative option is to build a smaller prototype and compare it with other SRMs which have the same volume.

Newcastle University has built a large number of electric machines in the past. The majority of the SRMs were constructed using the D100L frame size (150 mm active length and 150mm active diameter). As a result, using the D100L frame size also allows for direct comparisons with a recently built machine of a similar size.

Moreover, there is a 12/16 segmental rotor SRM in Newcastle University that can be used to make comparative analysis with the prototype machine[80, 104]: Not only because that 12/16 machine was built in D100L frame size, but also because it was a successful design that was developed for the same objective of providing higher torque per unit copper loss.

Considering the points mentioned above, the prototype machine needed to be built with the same frame size; however, the double-stator structure is relatively complicated compared to the conventional SRM, which is eased by a larger diameter. Thus, the final decision of prototype design was one with short axial length and a large diameter. In order to make comparisons with existing machines, the volume of the prototype needed to match that of the D100 frame size. The final dimensions were chosen to be a 210-mm outer diameter and a 75-mm active length.

Performance of the prototype was verified by comparing it with an SRM which had been previously constructed at Newcastle University [80, 104]. The cross section for the prototype and this rival machine are presented in Figure 5-1. The selected machine was a fully-pitched 12/16 segmental-rotor SRM, designed to provide high torque per unit copper-loss at low speeds. The requirements for the prototype are shown in TABLE 5-1

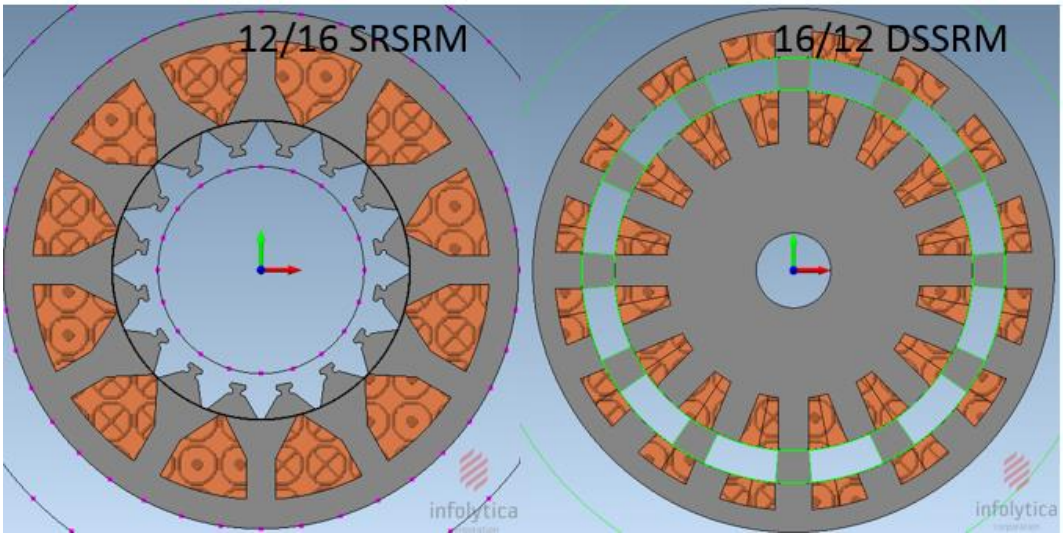

Figure 5-1 Full 2D cross section of the 12/16SRSRM (constructed at Newcastle University in the past[80, 104] and the 16/12 DSSRM (the prototype whose development was outlined in this chapter)

TABLE 5-1 BASIC PARAMETERS AND PERFORMANCE COMPARISON BETWEEN THE 12/16 SRSRM AND PROTOTYPE REQUIREMENT

	12/16 segmental	Prototype requirement
Outer Diameter	150mm	210mm
Axial Length	150mm	75mm
Airgap Length	0.3mm	0.3mm(each)
Average Torque at 10A/mm^2	45Nm	>45Nm
Copper Loss at 10A/mm^2	850W	<850W

The objectives of this prototype were to produce the following:

- Good torque per unit copper loss.
- Good torque density
- Can be constructed in the mechanical workshop within the university.

The preliminary design for this prototype selected the 16/12 configuration verified in section 4.2.2 and its parameters are shown in TABLE 5-2.

TABLE 5-2 THE NECESSARY GEOMETRIC PARAMETERS FOR THE PRELIMINARY DESIGN OF THE PROTOTYPE

	16/12 DSSRM
Inner Stator Angle	5
Outer Stator Angle	5
Inner Stator Radius	72.5mm
Rotor Depth	10mm
Stator Yoke	8mm

5.2 Mechanical Challenges for the Rotor Support Structure

Before optimising the preliminary design of the prototype, the specific rotor-structure needed to be determined, since it could significantly affect the eventual electromagnetic capability.

Due to the unique segmental structure of the rotor in this four-phase DSSRM, there were several potential mechanical problems which needed careful consideration:

- The rotor in this DSSRM consisted of a series of independent segments located between the inner and outer stators; therefore, a support structure should be developed to connect these rotor segments and to assemble them to a shaft.
- The segmental rotor is not naturally as strong as the rotor in the conventional SRM. As such, the rotor support structure should be strong and rigid to guarantee its survival during high-speed operation; its specific requirement was that it must be capable of enduring the centrifugal force created at 3,500 rpm.

- The iron core design needed to be modified to implement the support structure; thus, the performance of the prototype would be affected.
- The material in the rotor support structure should be both affordable and easily machined by conventional methods.

The basic idea of how to construct and insert the rotor is presented in Figure 5-2. The inner stator is fixed on a shallow, stationary shaft with bearings on either side. The rotor segments is then be connected to the two rotor caps, which are mounted on these bearings. Several methods that could potentially secure the connection between the rotor segments and caps were subsequently investigated and are discussed in this section. Mechanical modelling used 2D/3D FEM in the JMAG.

The rotor segments are made of 0.35 mm M270-35A silicon-steel sheets. Thus it gives weak mechanical strength in the axial direction and needs to be considered during the investigation. Based on the data in [105], the mechanical property of this orthotropic material are shown in TABLE 5-3.

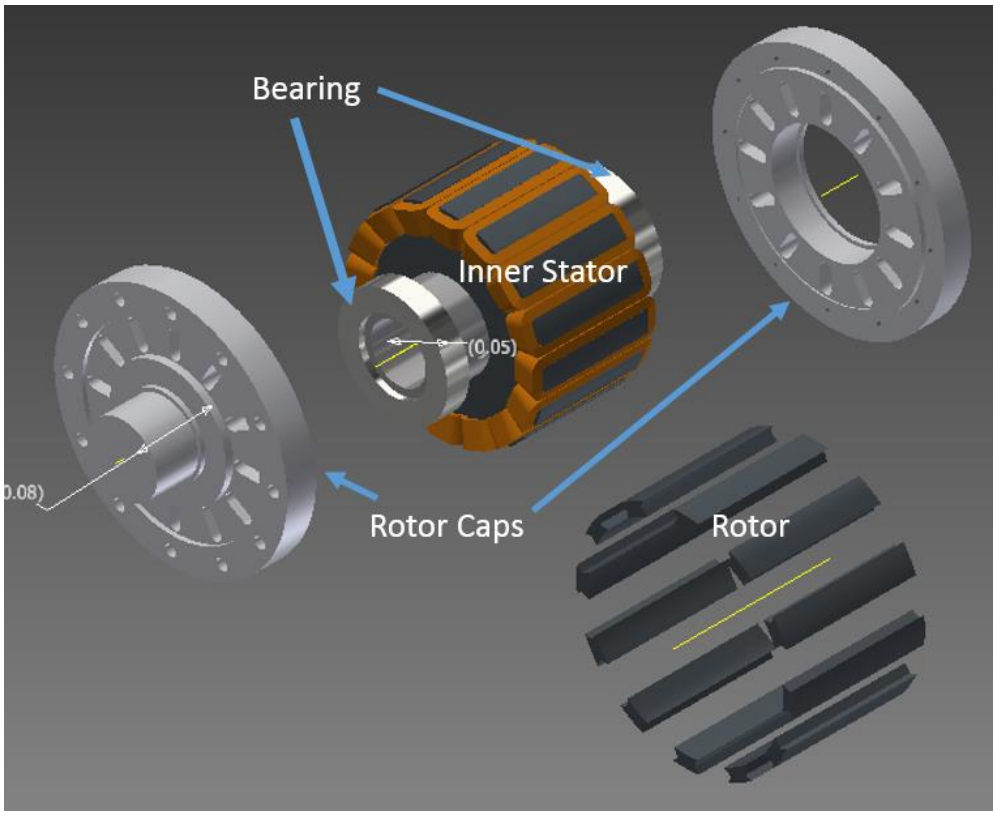

Figure 5-2 An assembly view of how the rotor mounts onto the inner stator

TABLE 5-3 A MECHANICAL-CHARACTERISTICS COMPARISON BETWEEN LAMINATION STEEL AND SOLID STEEL [105, 106]

	lamination	Solid Steel
Mass Density	7461kg/m^3	7840 kg/m^3
Steel fraction	0.97	1
Young's Modulus	187.2 GPa (in-plane)	207 GPa
	75.73 GPa (z-axial)	207 GPa
Poisson's Ratio	0.3(in-plane)	0.3
	0.121 (z-axial)	0.3
Material Type	Orthotropy	Isotropy

5.2.1 The Stainless-Steel Bolt and Eddy Currents

The first potential method was to use non-magnetic stainless steel or aluminium to link the rotor segments together and to fit them into the corresponding keyhole in the rotor caps. The advantage of this method is straight forward, for the metal – especially the stainless steel – offers the required stiffness and strength.

However, as can be seen from Figure 5-3, the solid metal structures between the rotor segments would induce a significantly large eddy current (the eddy current loss almost equal to 38% of the copper loss from winding). This would severely hinder efficiency and performance due to the extra loss.

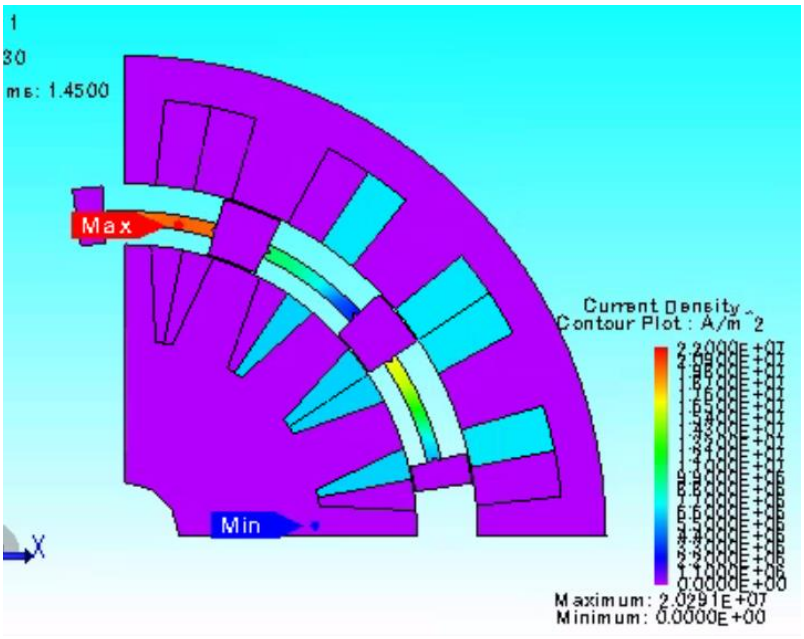

Figure 5-3 The current density distribution in a quarter-cross section view when a very high current density is induced in the stainless-steel link

A more developed solution to reduce the eddy current would be to insert a bolt into the rotor segments, as it would be surrounded by the high-permeability iron core and not directly exposed to the flux. The effects can be seen from Figure 5-4; comparing the current density plot at the same position as in **Error! Reference source not found.**. A significant reduction in eddy current losses is predicted, at 13% of the copper loss from the winding.

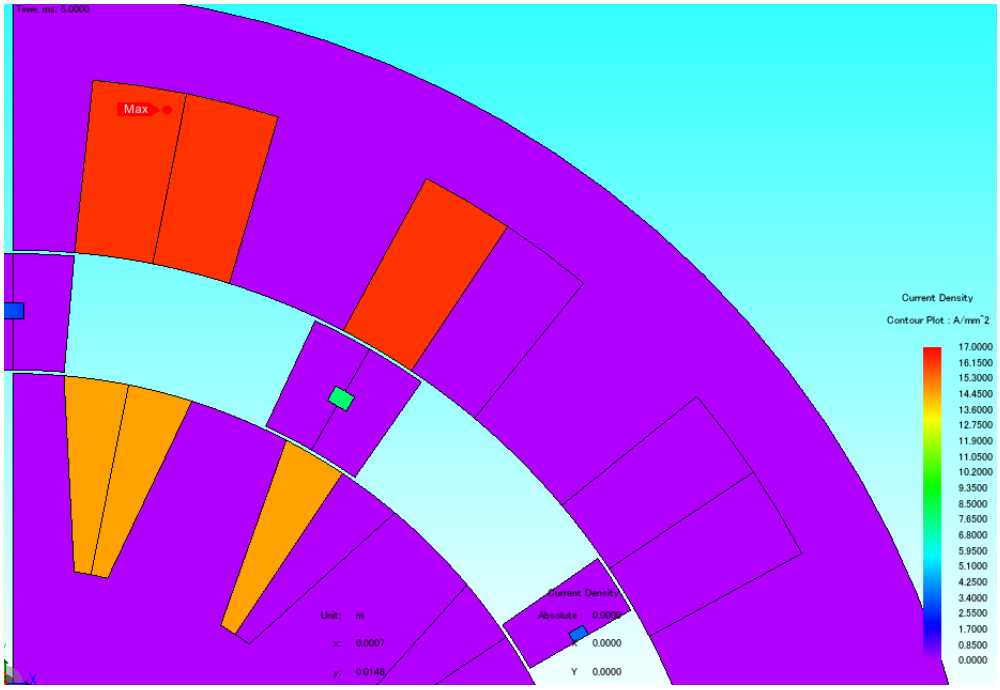

Figure 5-4 The current density distribution in a quarter cross-section view: the bolt within the middle of a rotor segment has very low current density comparing to conducting winding

As mentioned at the beginning of section 5.2, the primary mechanical issue that needs to be solved is whether the rotor structure can withstand the centrifugal force during operation. Thus, to verify the mechanical performance of the new rotor design, a 3D FEA model is developed in JMAG(Structural Study- Static Analysis). In this model, the structures are made up of rotor segments, bolt, and endplates. Their material properties are linked to orthotropic silicon steel, stainless steel and aluminium, respectively. A solution is obtained at 4000rpm. The deformation and stress condition of the bolt is shown in Figure 5-5 with a scaling factor of 200 to highlight the displacement, indicating that the maximum principal stress in this scenario is around 63 MPa. Considering the typical tensile strength (yield) of type 304-stainless steel is 215 MPa, this mechanical design is considered suitable. However, the bolt will still have small eddy current losses during operation. For this specific design, it is predicted to increase the overall loss from 564 W to 636 W; therefore, other structure types made of non-metallic materials needed to be considered.

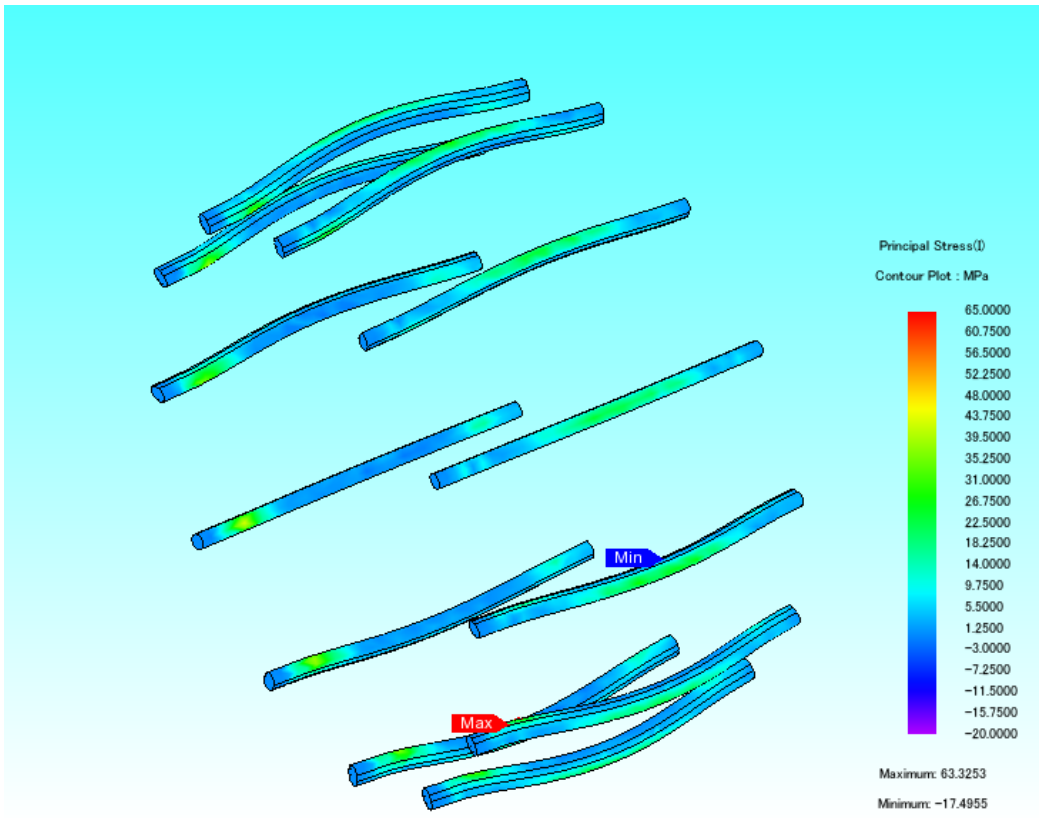

Figure 5-5 The principal stress distribution from the 3D FEM. Maximum stress occurs at the connection between the bolt and rotor cap.

5.2.2 Study of Potential Rotor Structures using Engineering Plastic

Since any metal material will have induced eddy currents during operation, thereby reducing efficiency, a non-metal material rotor support would be advantageous. One option is engineering plastic. By considering the Young's modulus, tensile strength, temperature and accessibility, polyether ether ketone (PEEK) was found to be a good choice. The physical properties of PEEK are presented below in comparison to aluminium. It transpired that the mechanical properties of PEEK are poorer than aluminium, especially when considering the Young's Modulus.

TABLE 5-4 MECHANICAL PROPERTIES COMPARISON BETWEEN PEEK AND ALUMINIUM

	PEEK	Aluminium
Mass Density	1320 kg/m^3	2700kg/m^3
Young's Modulus	3.6 GPa	68.9GPa
Tensile Strength	100 MPa	290MPa

Young's modulus (also known as the elastic modulus) is a means of measuring the stiffness of a solid. A material with a lower Young's modulus value will have more significant deformation under stress. Therefore, to prevent the rotor eventually impacting into the outer stator at high speed, a rotor support made from PEEK would need to have less stress than its metallic rivals. To achieve this requirement, a PEEK support component needed to be significantly thicker than a metal component. Four potential designs for the PEEK supporting structure were proposed, as shown in Figure 5-6. In these designs, the rotor lamination is represented by the colour red, while the white component represents the PEEK.

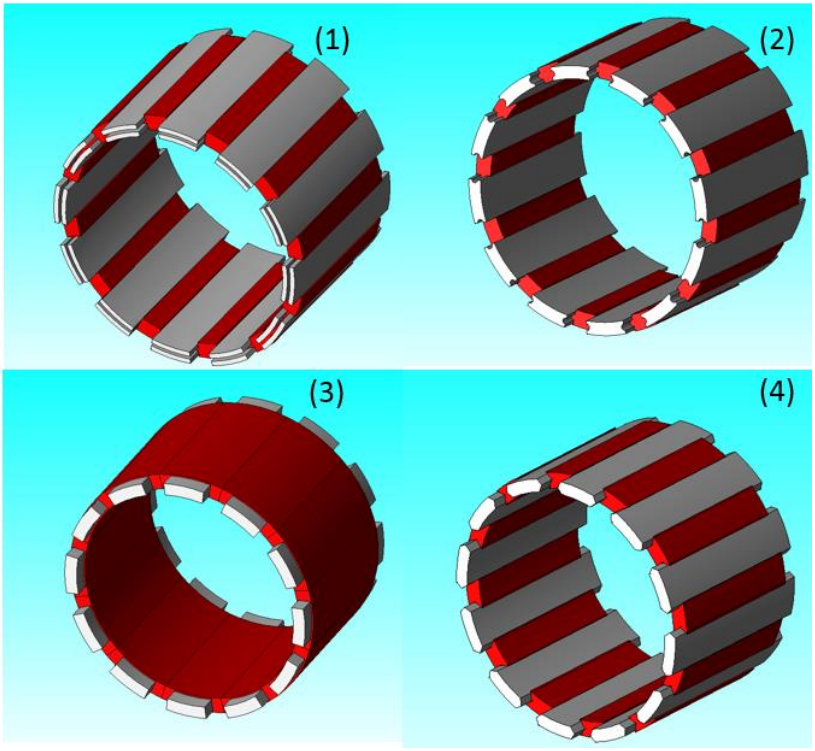

Figure 5-6 The 3D models of four different rotor structure candidates

The features and structures of each design can be described in turn:

(1) In this design, the rotor lamination is linked by a thin bridge in the middle and PEEK sheets secure the position from both sides of the bridge.

(2) In this design, the rotor segments have round wedges on each side that insert into the PEEK sheets.

(3) This method is a modification of the first design but the bridge, which links the segments together, is no longer in the middle. Instead, the PEEK sheet is fitted into the middle and surrounded by the bridge.

(4) The last method is a modification of the second design. Here, the rotor segments have a groove on both sides to allow the PEEK sheet to be fitted.

It should be noted that the rotor segments in the fourth design are wider than the original segments at the edges near the airgap. The entire design, including the stator cores, is shown in Figure 5-7. This shows that the stator poles have small tips extruded which would match the arc of the rotor segments at the airgap. The purpose of these small tips is to enhance electromagnetic performance:

In Figure 5-8, the torque data (from 2D FEM under current control) of the preliminary prototype with different pole widths is presented. It suggests the torque performance would be enhanced, even if the stator arc-to-pitch ratio reaches 0.6. On the other hand, wider poles would lead to narrower slot areas which would increase the copper loss at the same phase current. But increasing the width of the stator pole solely at the airgap would not cause significant sacrifice of the slot area and would still enhance electromagnetic performance at the airgap. Moreover, combined with the rotor segments design of the fourth method, the unaligned inductance would not increase much compared to directly increasing the pole width. Thus, a decent inductance ratio between the aligned and unaligned positions is maintained. As a result, the electromagnetic characteristics of this method are equivalent to a reduced airgap. As discussed in Chapter 3. lower airgap reluctance is highly advantageous and will enhance the torque capability.

The torque capability and copper loss for these four different rotor structures is shown in TABLE 5-5 which indicates that the third method would exhibit the worst torque performance and the fourth the best, as expected. The copper loss of the fourth method is slightly higher than that of the other three candidates because the slot area is occupied partially by the stator-pole tip. But this trade-off would be entirely worthwhile, since the copper loss only rises by around 4.2 % while the torque capability increases by 32.5 % compared to the first method.

TABLE 5-5 TORQUE CAPABILITY AND COPPER LOSS COMPARISON BETWEEN THESE FOUR ROTOR STRUCTURE CANDIDATES

Structural Design	(1)	(2)	(3)	(4)
average torque (Nm)	34.1	33.2	28.3	45.2
Copper loss(W)	564	564	564	588

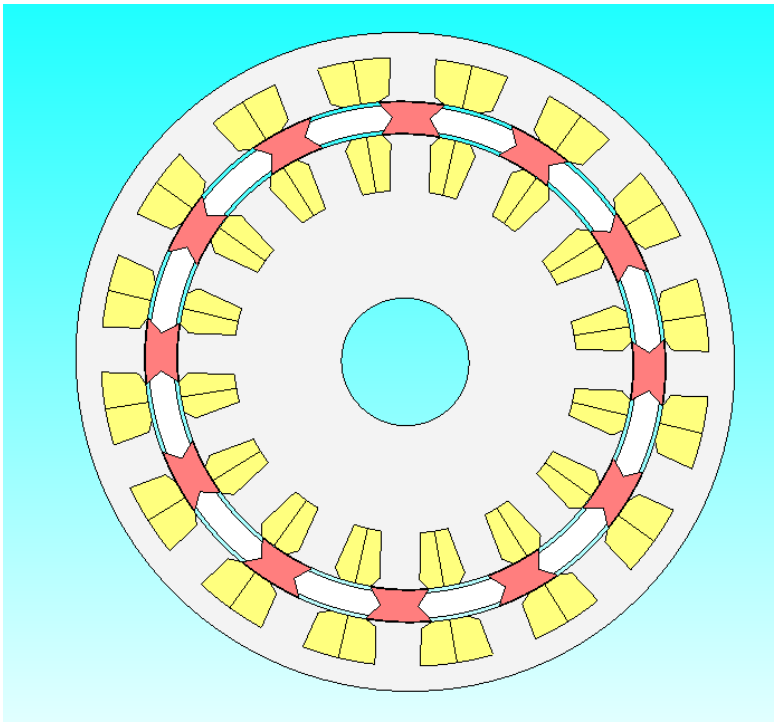

Figure 5-7 2D cross-section of the rotor structure Number 4

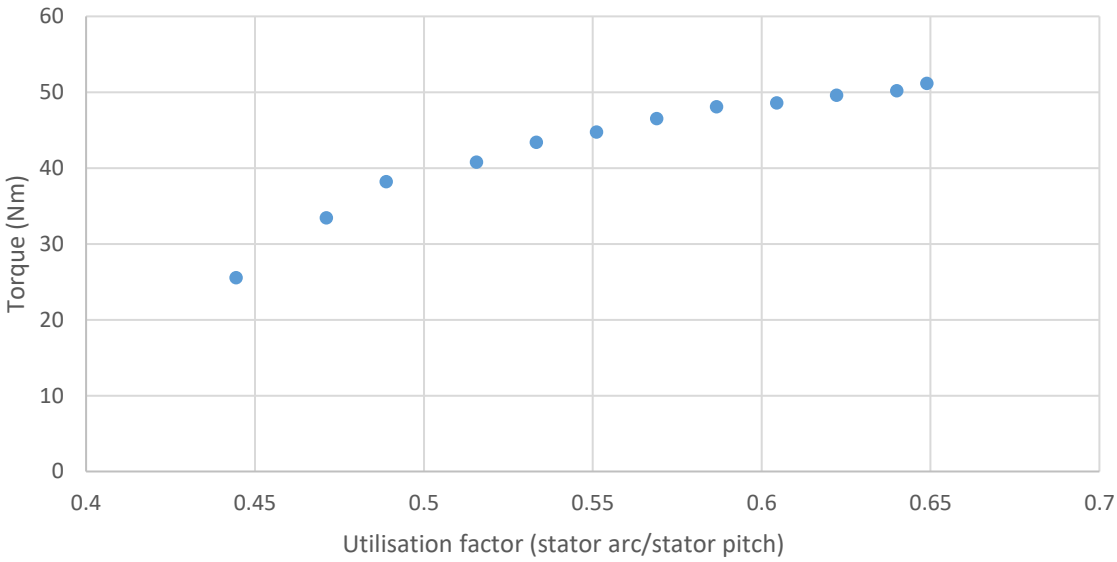

Figure 5-8 The relation between the average torque and the stator arc-to-pitch ratio

The mechanical performance of these four different designs was verified by 3D FEM with the condition of centrifugal force being under 4000rpm, and the plots of principal stress are shown in Figure 5-9, Figure 5-10, Figure 5-11, and Figure 5-12 respectively. The results indicate that the tensile strength of PEEK (which is 100MPa) is strong enough for those four designs.

The fourth method was assumed to be the best choice due to its outstanding torque capability. Further analysis was undertaken for this design.

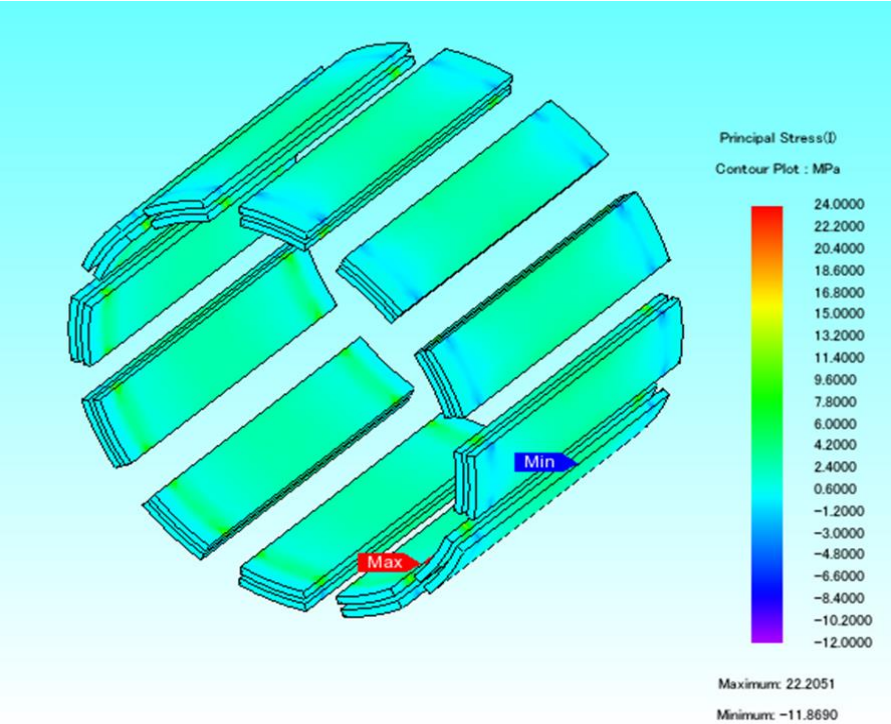

Figure 5-9 principal stress-distribution for rotor structure number 1(22MPa at maximum)

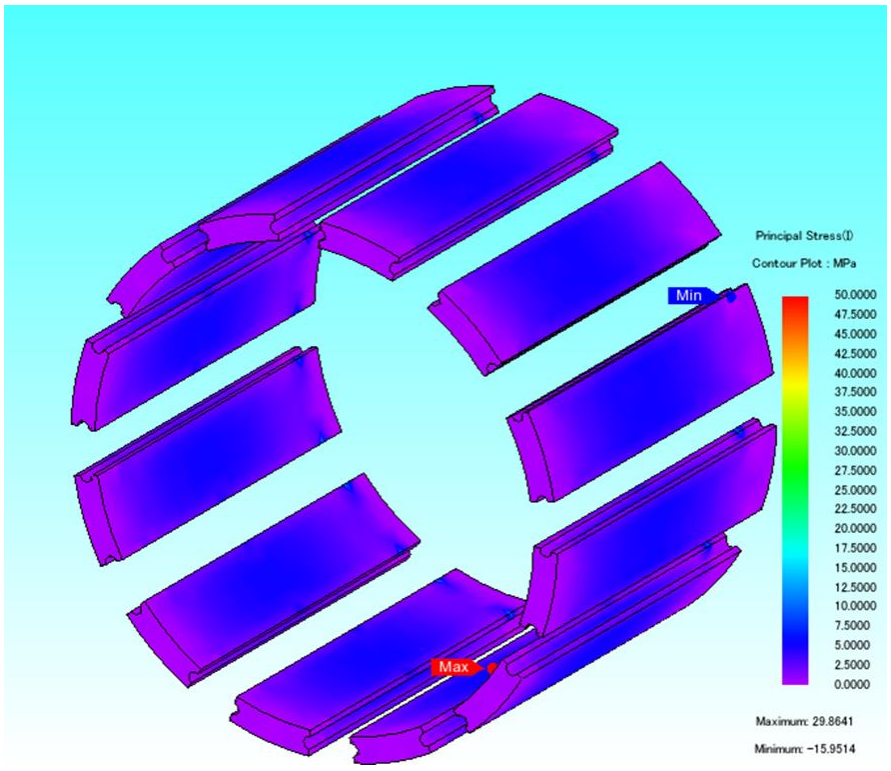

Figure 5-10 principal stress-distribution for rotor structure number 2(29MPa at maximum)

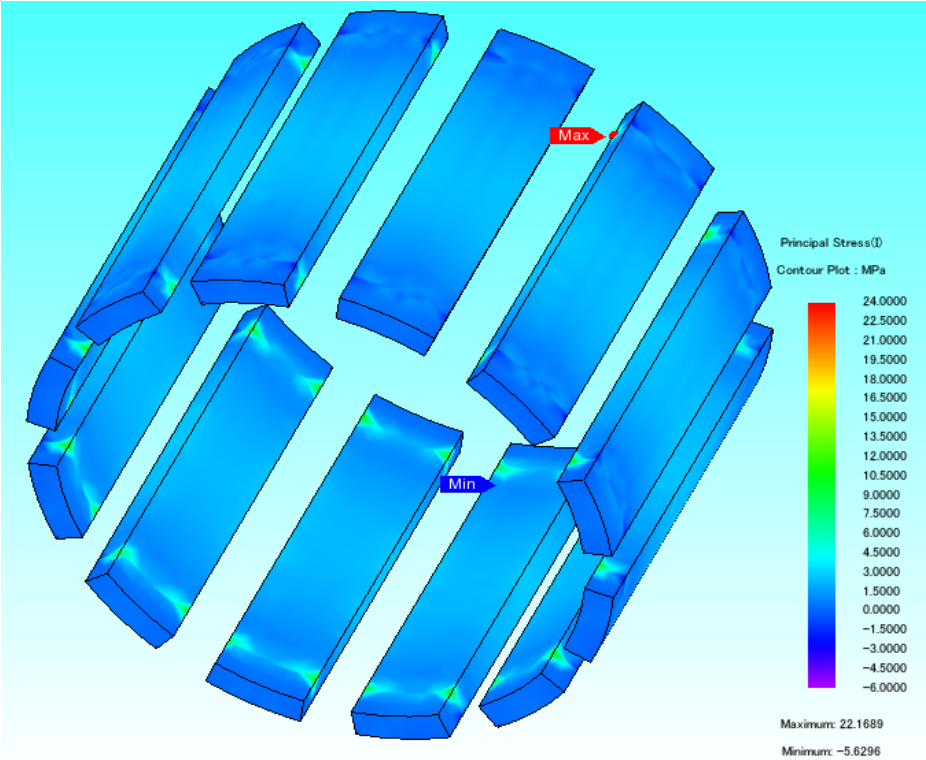

Figure 5-11 principal-stress-distribution for rotor structure Number 3(22MPa at maximum)

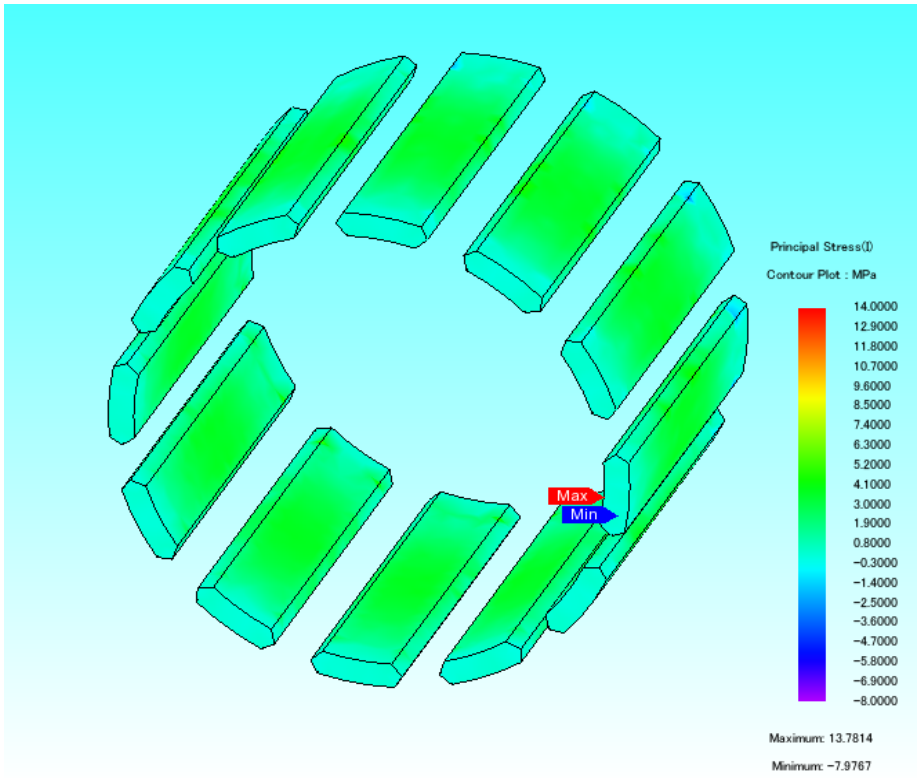

Figure 5-12 principal stress-distribution for rotor structure number 4(13MPa at maximum)

5.2.3 Discussion of Potential Alternative Materials

The relatively low Young's modulus of PEEK was the most significant uncertainty of this rotor design. The 3D FEM results showed that the maximum radial direction displacement would be circa 0.1 mm at 4,000 rpm. This would be feasible since the airgap would be 0.3-mm long. However, the simulation could not absolutely preclude a potential hazard during high-speed operation. As such, other stronger non-metal materials with higher Young's modulus values were taken into consideration. The mechanical properties of several potential candidates are shown in TABLE 5-6

TABLE 5-6 THE MECHANICAL PROPERTIES COMPARISON BETWEEN PEEK, ALUMINA CERAMIC, GLASS, AND BAMBOO

	PEEK	Alumina Ceramic	Glass	Bamboo(1)
Young's modulus	3700Mpa	330000Mpa	70000Mpa	20000Mpa
tensile strength	96.5Mpa	172Mpa	40Mpa	160Mpa

Note: 1) Material properties of Bamboo based on the references [107-109]

One of the stiffest non-metal materials widely used in engineering is alumina ceramic. Its Young's modulus is more than 50 % higher than typical steel. As can be seen from Figure 5-13, alumina ceramic could provide more than enough strength and stiffness in this application. However, it can be extremely expensive and is extremely difficult to be machined by traditional equipment. Thus, it was excluded from the options.

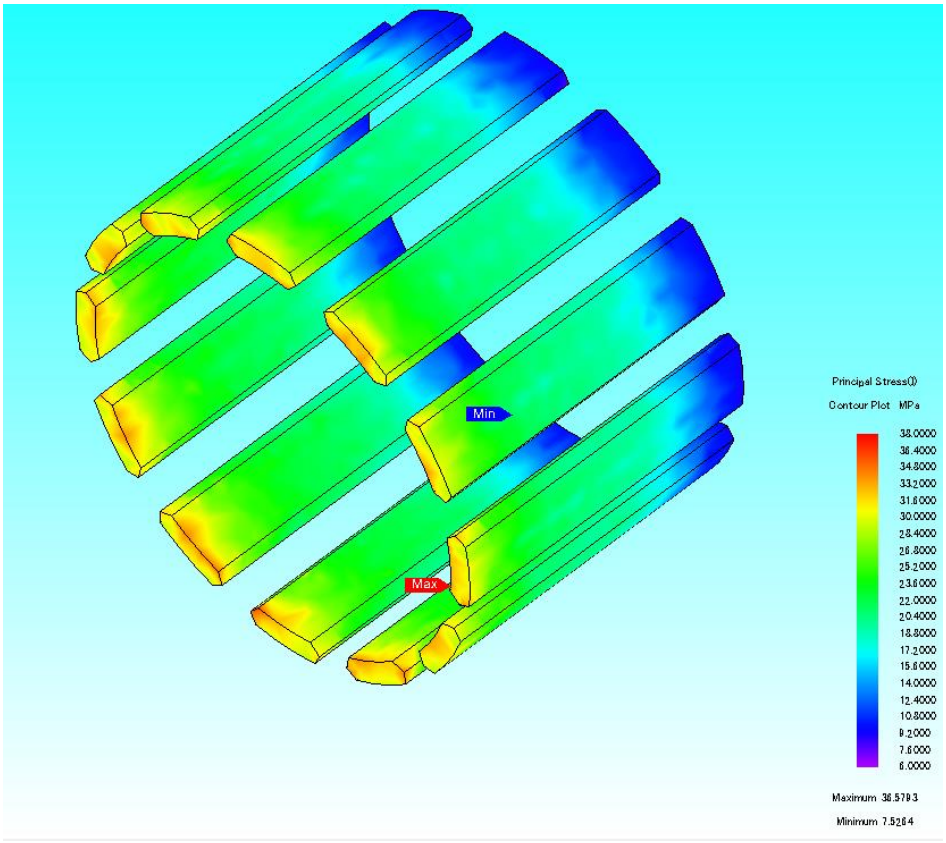

Figure 5-13 The 3D principal stress-distribution graph for an alumina ceramic rotor support

Glass was another candidate with a Young's modulus similar to aluminium and its price affordable compared to alumina ceramic. This material could offer enough stiffness to restrict the axial displacement; however, it is also relatively fragile with a typical tensile strength of around 40 MPa. The results in Figure 5-14 indicate the stiffness of glass could limit the strain of the rotor to the expected value, but the principle strength at this condition would break the glass itself.

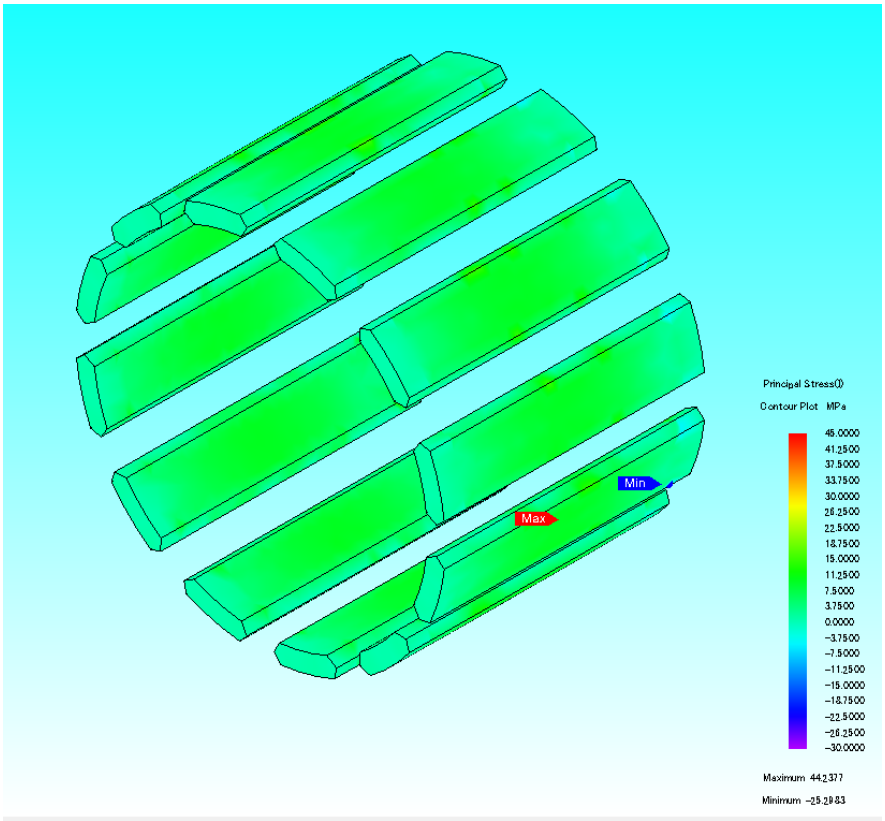

Figure 5-14 The 3D principal stress-distribution graph for a glass rotor support

The third option was bamboo. This is not usually used in electrical and electronic engineering but, according to [107-109], it has long been used as a construction material and is being investigated as an alternative to glass fibre in the mass production of wind turbine blades. The Young's modulus of bamboo is around 20,000 MPa, which is five times higher than PEEK. Although its stiffness would not be comparable to alumina ceramic or glass, the tensile strength of bamboo is high. As can be seen from Figure 5-15, the maximum tensile stress on the bamboo bar is less than 40 MPa, which is low compared to its capability of 160 MPa tensile strength. Consequently, bamboo could fulfil the mechanical requests for this application; but there were still some issues that could prevent its use in this project:

- Accessibility: it is difficult to find a vendor that can offer natural bamboo of a suitable size and with reliable mechanical property information. Although solid bamboo products could be supplied in appropriate sizes, these products are made by gluing together processed bamboo strips and have a relatively low Young's modulus.
- Reliability: since most research about bamboo is carried out for the construction industry, its mechanical properties are mainly investigated under moderate temperatures. However, for electric machine applications, the maximum temperature inside the case could reach 120 ˚C so more research for this condition is required.

Therefore, although bamboo is a readily available material for this application and has several advantages, such as low cost and being environmentally friendly, because of issues surrounding reliability and accessibility, it was decided not to use it in the construction of the prototype machine, but only as a study option in future work.

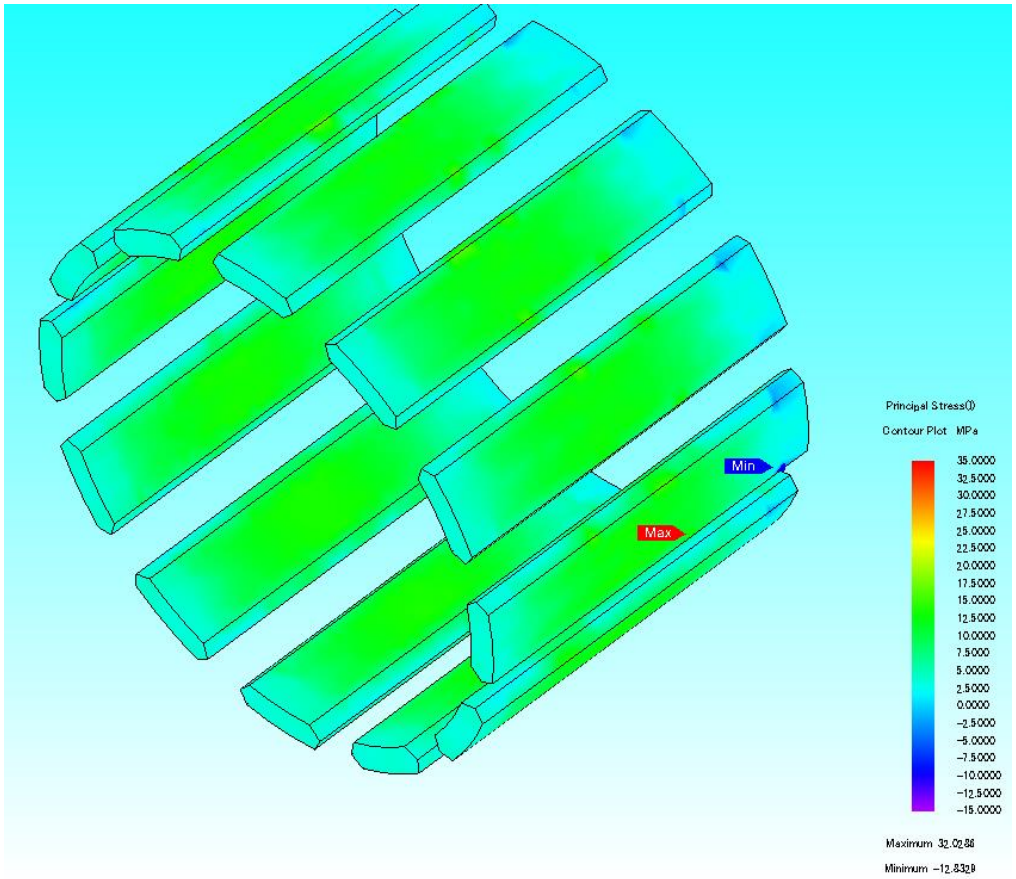

Figure 5-15 The 3D principal stress-distribution graph for a bamboo rotor support

5.2.4 Electromagnetic Force and Resonant Analysis

Other than the centrifugal force, the electromagnetic force might also challenge the robustness of the rotor. However, due to the unique airgap distribution, the electromagnetic force in a radial would almost achieve balance on the rotor segments. As can be seen from Figure 5-16, the radial force would slightly bias towards the inner stator and, therefore, might even neutralise a small portion of the centrifugal force – and since the rotor support structure would be relatively solid and thick in the tangential direction, it is unnecessary to discuss tangential force more specifically in this section. The effect of the electromagnetic force on the rotor structure for 45

Nm average torque is shown in Figure 5-17. The results revealed that the principal stress for the electromagnetic force would be lower than that for the centrifugal force.

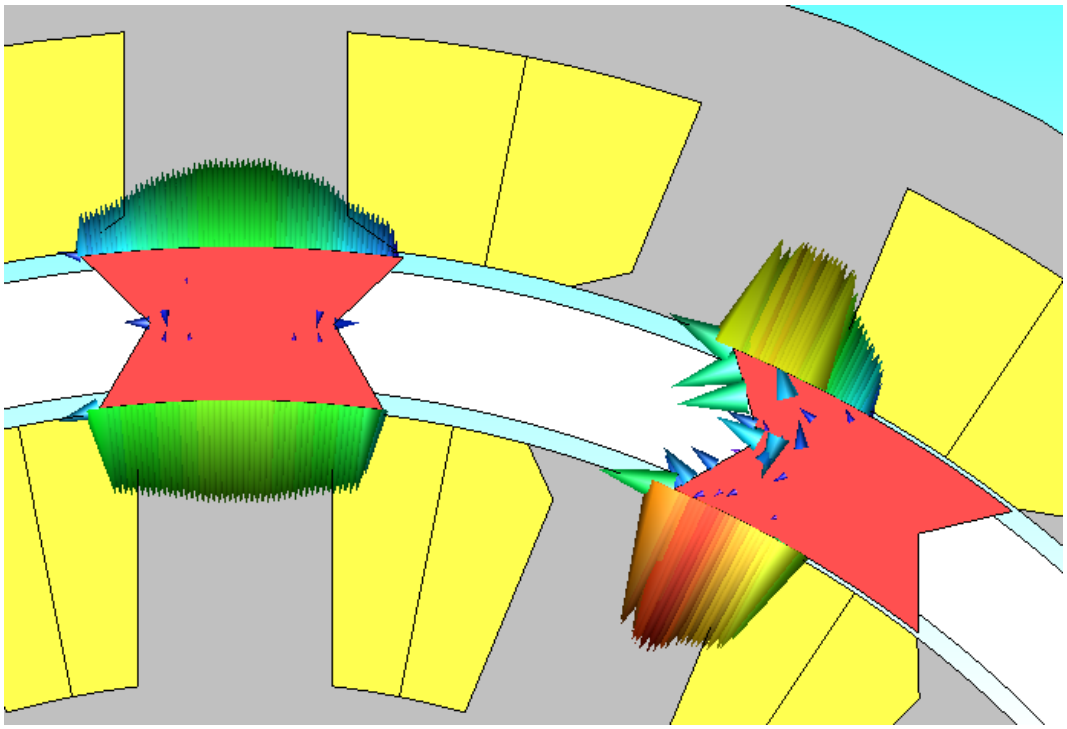

Figure 5-16 Vector graph showing the electromagnetic force on the rotor segment

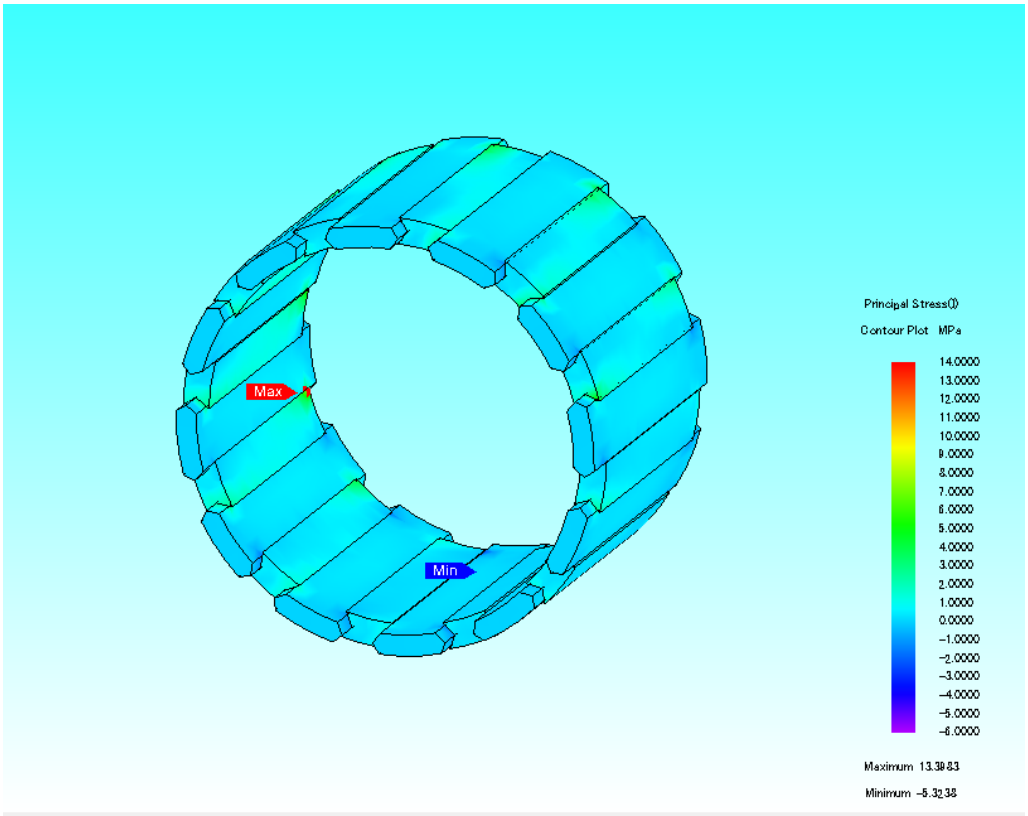

Figure 5-17 The 3D principal stress-distribution graph for the electromagnetic force on the rotor

However, vibration would still exist in the rotor, since the electromagnetic force in the radial direction would not achieve complete balance. Resonance is an extremely harmful phenomenon for any structure as it can significantly magnify the vibration at a particular frequency. For the conventional SRM with a relatively robust rotor, resonance investigation is usually focused on the stator to prevent excessive vibration and noise. In this project, as the prototype machine has a fragile rotor, so the resonance study concentrates on the rotor.

In this prototype, the electromagnetic force on the rotor would emanate from four directions, evenly distributed in a full circle. Under these conditions, the resonance should mainly occur at eigenmode 4.

The results of the vibration analysis are presented in Figure 5-18, revealing that the frequency of eigenmode 4 is 4,244 Hz. For the 16/12-pole combination, the rotational speed at this conducting frequency would be in excess of 20,000 rpm. As discussed in section 5.2.2, the rotor structure needed to be designed to survive at a maximum speed of 4,000 rpm. Consequently, it would be meaningless to investigate any potential resonance hazard over 20,000 rpm, since the centrifugal force would already have destroyed the rotor at a far lower speed.

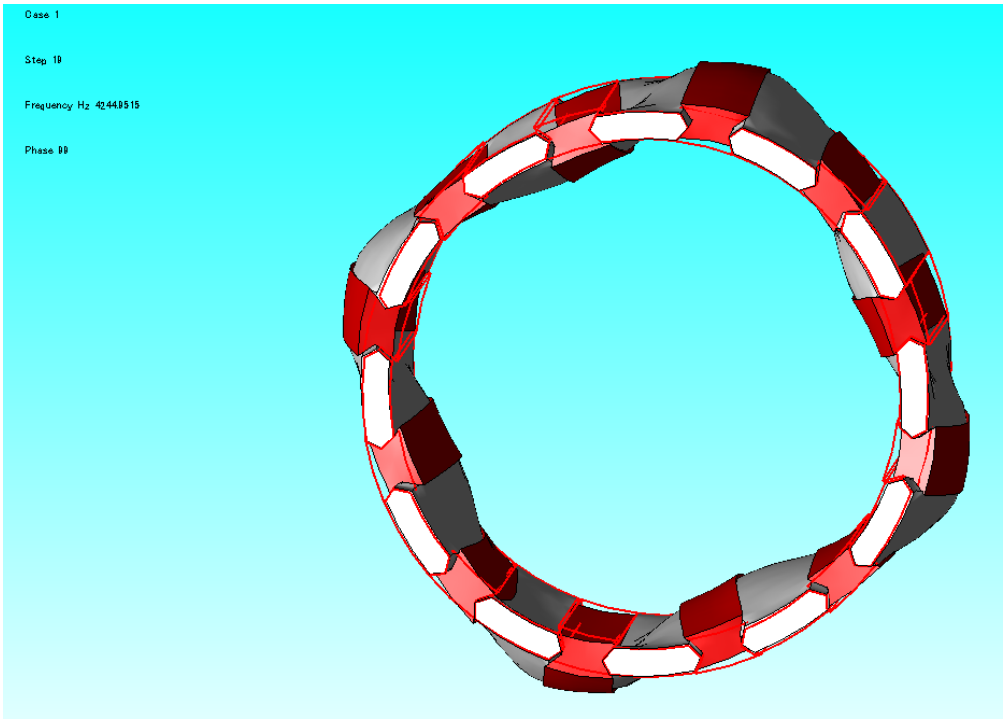

Figure 5-18 The eigonmode for the four-pole conducting condition

5.3 Design Optimisation and Simulation Results

Once the design of the rotor structure had been chosen, the primary iron core geometry of the prototype was confirmed. Subsequent work optimised the design to further enhance performance. For the PC-based automatic optimisation process, two types of algorithm are commonly used: annealing and genetic algorithms.

JMAG software offers a built-in optimisation function based on a genetic algorithm. The genetic algorithm, known as the 'revolution algorithm', is an optimisation method developed using the well-known concepts of genetic endowment, evolution, and natural selection in biology. The algorithm consists of several steps:

1. It initially establishes a set of possible solutions, at random. This set represents the population of the first generation. The design parameters for each individual are in the 'genes'. These genes are combined in the 'chromosomes' which contain the entire design details of an individual.
2. After solving the entire population, all the individuals are given a fitness score from the fitness function: there are three different methods for generating the population of the next generation ion:
    - Some of those individuals with the best fitness score are directly promoted to the next generation.
    - Crossover: some individuals in the current population with better fitness scores are selected as parents, as if those animals in the real world who adapted to the environment and are more likely to propagate; then, their children (i.e. the next generation) would have a mixture of 'chromosomes' from the parents.
    - Mutation: some of the individuals are also promoted to the next generation if a random change in their chromosome occurs. In reality, this mechanism is a critical driving force for biological evolution.
3. The new generation repeats the process in step two and continually evolves until the termination condition is achieved. This condition would include, but is not restricted to the following:
    - Generation number limit: This is a method of terminating the process after the generation number reaches a pre-set value.
    - Tolerance limit: Because the diversity of such a population would be relatively low compared to in real biological evolution, the fitness score of the population would eventually converge to a certain number after several generations. Thus, the algorithm should terminate after the fitness score drops to the tolerance.

Since this optimisation mechanism is a simulation of the biological evolutionary process, the result would not necessarily be the best among the entire set of possibilities, but the algorithm can be relied upon to consistently function reliably, no matter how complicated the problem. It is, therefore, suitable for solving issues in which the objective function is relatively nonlinear and random.

For this specific task, the dimensions that were involved in the optimisation process are shown in Figure 5-19. The limit of range can be seen in TABLE 5-7.

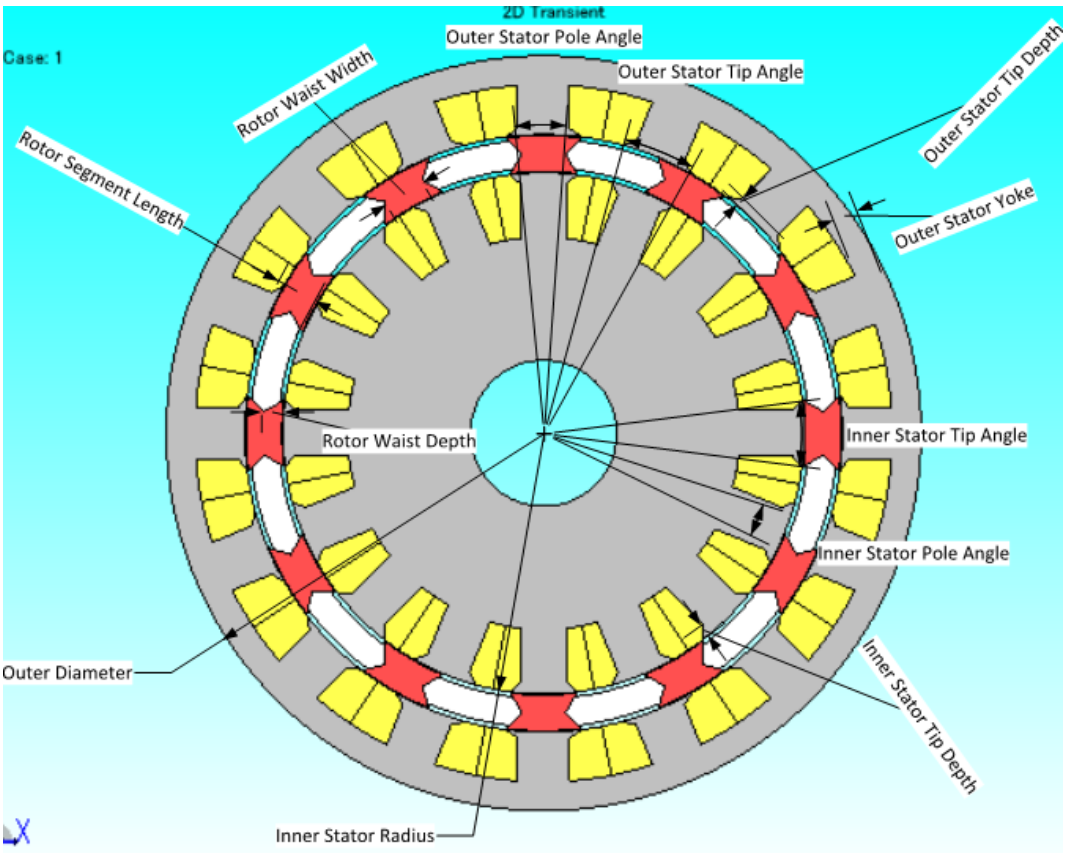

Figure 5-19 The dimensions that were involved in optimisation

TABLE 5-7 THE DIMENSION RANGES USED IN OPTIMISATION

Dimensions	Minimum	Maximum
Outer Diameter	210mm (fixed)	
Active Length	75mm (fixed)	
Airgap Length	0.3mm (fixed)	
Inner Stator Radius	64.5mm	78.5mm
Inner Stator Pole Angle	4.5˚	6˚
Inner Stator Tip Angle	6.3˚	7.1˚
Inner Stator Tip Depth	1mm	3mm
Outer Stator Pole Angle	4.5˚	6˚
Outer Stator Tip Angle	6.3˚	7.1˚
Outer Stator Yoke	6mm	12mm
Outer Stator Tip Depth	1mm	3mm
Rotor Segment Length	8mm	12mm
Rotor Waist Depth	4mm	7mm
Rotor Waist Width	3mm	10mm

Several constraints were set in JMAG to prevent any invalid design accidentally appearing in the population. Examples of these constraints are shown in Figure 5-20 and included the following cases:

- The stator tip angle should always be larger than the stator pole angle. This would guarantee that the tip of the stator pole is wider than other parts of the poles.
- The rotor waist width should be smaller than the arc length at the airgap. This is because the rotor segment is designed to be narrow in the middle and wider near the airgap, as if two trapezoidal shapes were combined, end-to-end – otherwise, the PEEK bar structure will not remain fixed to constrain the location between the rotor segments.
- The rotor waist depth should always be smaller than its length. Since the waist is expected to be in the middle of the rotor, if the rotor waist depth is larger than the length, an error would occur in the iron core geometry.
- The sum of the airgaps, rotor length, inner stator radius, and outer stator yoke should total less than 95 mm. This would allow at least 10 mm of leeway for allocating the outer stator pole.

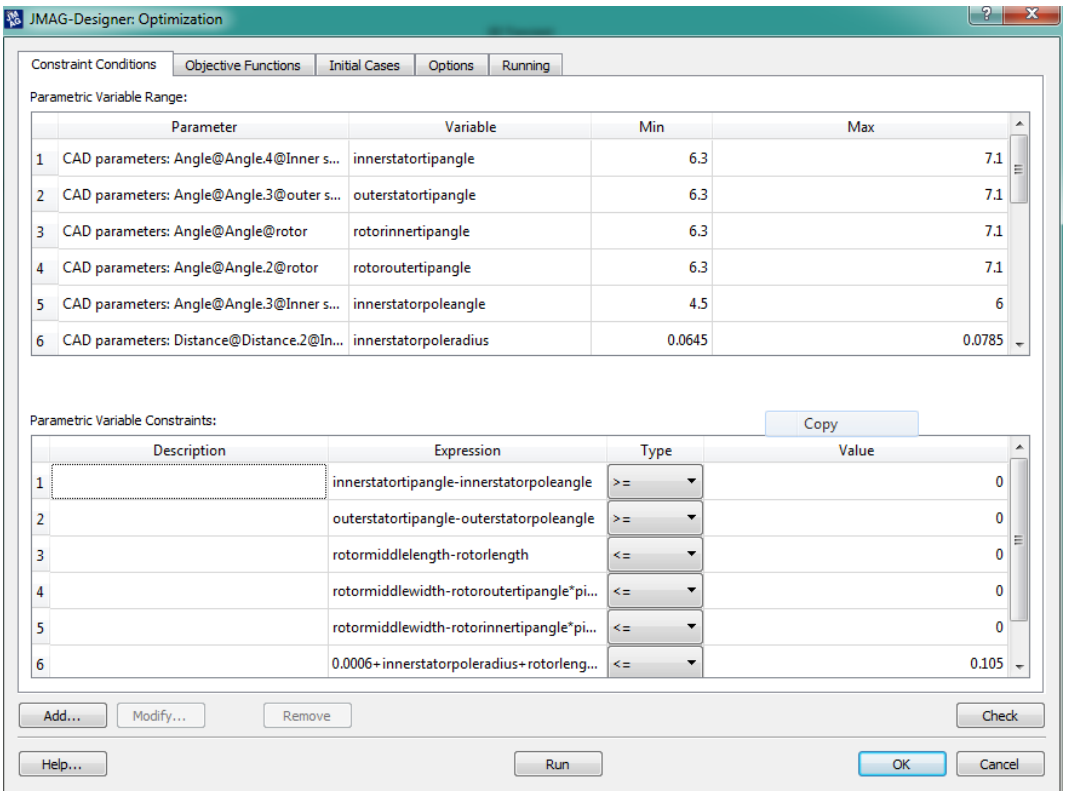

Figure 5-20 The constraints set for optimisation

The winding was assumed to be solid conductor, filling the slot area, while the current density of 10 A/mm^2 would be fixed for each individual in the optimisation, since this is a typical value for an air-cooled SRM at this volume. In addition, the optimisation process would focus on three objectives:

- The average torque should be no less than 45 Nm. This is because the competitor SRM with which it was to be compared could offer 45-Nm torque at 10-A/mm^2 current density. The prototype should be capable of providing better torque capacity under the same conditions, even though the current density limit could vary between different SRMs.
- The maximum average torque should be sought. In conjunction with the first objective, this would guarantee an optimised result with obvious advantage regarding torque capability.
- The highest torque-to-copper loss value should be sought. This objective was the most important of the three; moreover, since the current density would be fixed at 10 A/mm^2, the copper loss would be directly proportional to the section area of the slot. Thus, this objective was equivalent to seeking those individuals with a higher torque-to-slot area ratio.

Eventually, the genes of the various individuals would converge to form a specific combination. Figure 5-21 shows the changes in the geometric design following optimisation. Compared to

the original design, the optimised DSSRM has a shorter rotor length, narrower stator pole tips, and a wider stator pole and yoke. The details of these modifications are presented in TABLE 5-8.

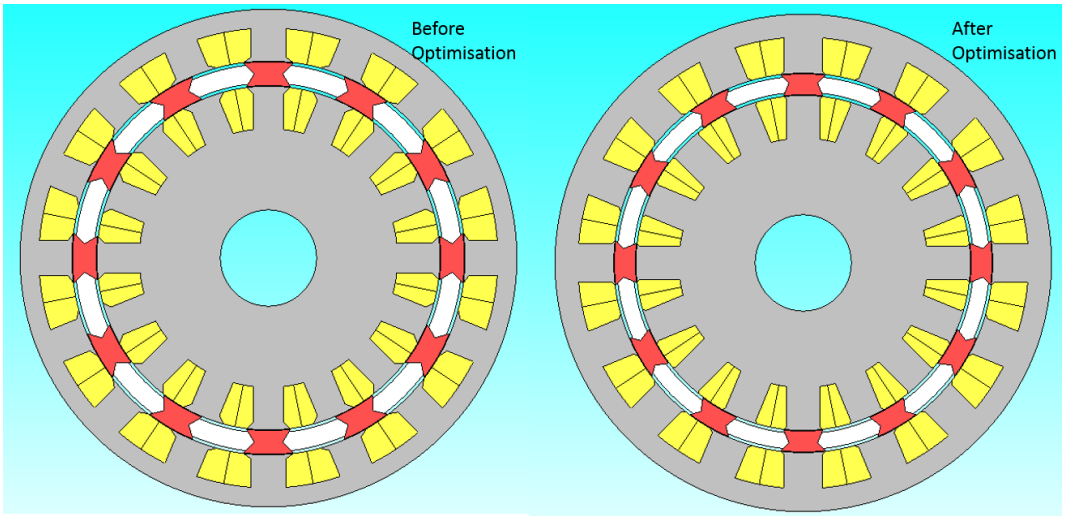

Figure 5-21 A comparison of the original and optimised geometric designs

TABLE 5-8 A COMPARISON OF THE DIMENSIONS BETWEEN THE ORIGINAL AND OPTIMISED DESIGNS

Dimensions	Before Optimisation	After Optimisation
Outer Diameter	210mm (fixed)	
Active Length	75mm (fixed)	
Airgap Length	0.3mm (fixed)	
Inner Stator Radius	64.5mm	78.5mm
Inner Stator Pole Angle	4.5˚	6˚
Inner Stator Tip Angle	6.3˚	7.1˚
Inner Stator Tip Depth	1mm	3mm
Outer Stator Pole Angle	4.5˚	6˚
Outer Stator Tip Angle	6.3˚	7.1˚
Outer Stator Yoke	6mm	12mm
Outer Stator Tip Depth	1mm	3mm
Rotor Segment Length	8mm	12mm
Rotor Waist Depth	4mm	7mm
Rotor Waist Width	3mm	10mm

In terms of performance enhancement, the average torque was increased by 13% from 45.19 Nm to 51.37 Nm at a current density of 10 A/mm^2, while the copper loss was reduced by 6.75 %. The optimisation process proved to be effective.

In comparing this model to its competitor, which is the 12/16 segmental-rotor SRM with similar volume, it was evident that the optimised DSSRM produced significantly higher torque-to-copper loss ratio, especially under high loading conditions. Figure 5-22 presents a comparison of torque-to-copper loss between these two SRMs with a current density of up to 20 A/mm^2. The prototype DSSRM provides 15% higher torque than the 12/16 segmental-rotor SRM with a 500W copper loss, and this advantage would increase to 25 % with a 1,000W copper loss, eventually reaching 65 % if a 2,000W copper loss were allowed. From these curves, it can be seen that both machines actually demonstrate a similar torque-to-copper loss performance, at low currents but, once the copper loss exceeds 500 W, the curve of the prototype machine continues to increase at a steady rate, while the curve of the 12/16 segmental SRM becomes saturated.

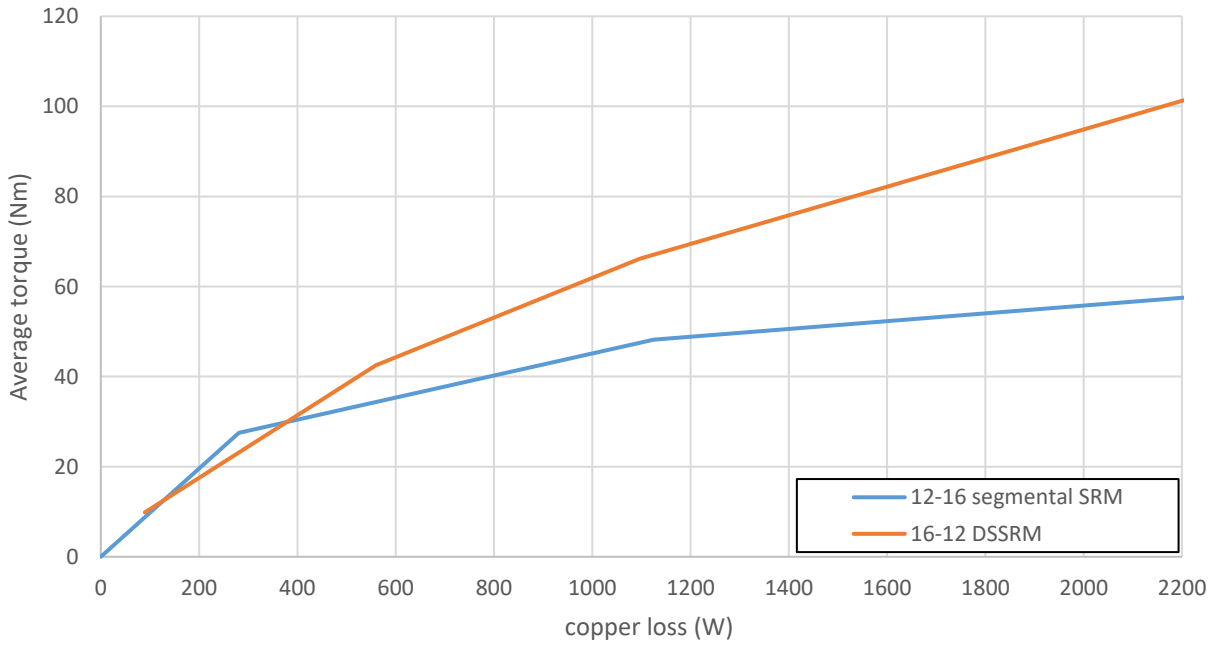

Figure 5-22 A torque-to-copper loss comparison between the prototype and the 12/16 segmental-rotor SRM

As can be seen from Figure 5-23, this phenomenon is more clearly reflected in the flux linkage-vs-current curve. These two machines would have a very similar flux linkage-vs-current curve at the aligned position, but the prototype machine maintains very low flux linkage at the unaligned position, which effectively enhances its energy-conversion loop. Consequently, this

indicates that the DSSRM would offer higher torque capability than its rival in the saturation region. Moreover, since the peak current and inductance of the DSSRM was lower than that of the segmental SRM, a lower volt-ampere requirement from the drive could be expected.

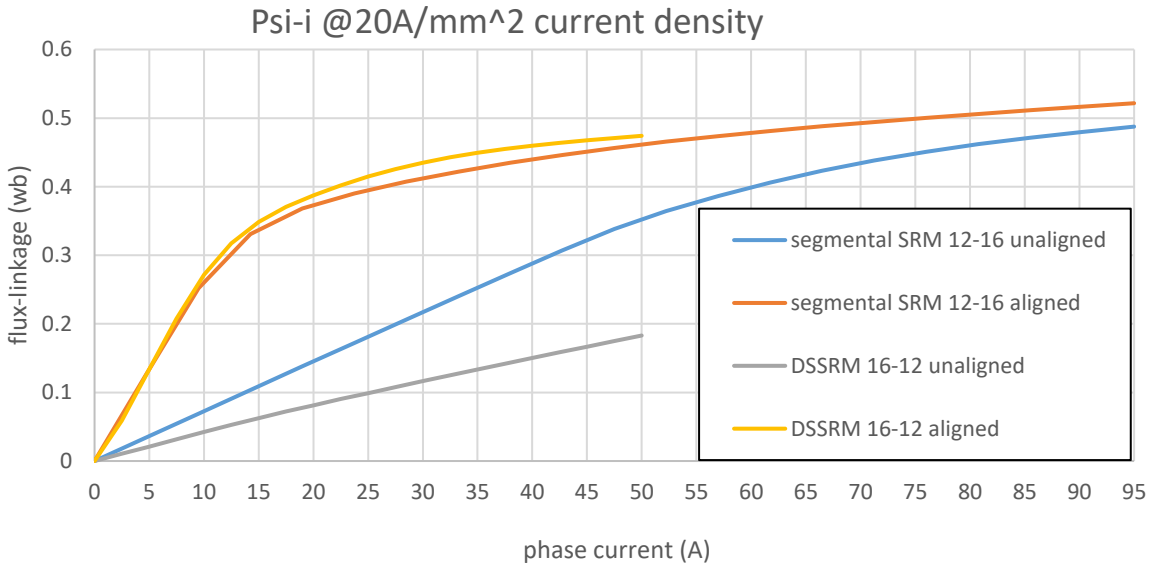

Figure 5-23 A flux linkage-vs-current comparision between the prototype and the 12/16 segmental-rotor SRM

Further comparison at 1500 rpm is delivered using 2D transient FEM, in which the two machines are under current control (with the limitation of same DC voltage at 500V while the advance angle is selected with the maximum average torque for each machine respectively.). The peak current of the 12/16 SRSRM is 35A, which is almost as twice that of the 16/12 DSSRM (18A). This indicates the 12/16 SRSRM should require a higher VA rating than the 16/12 DSSRM (even after considering the 1atter has one more phase). The comparison result is shown in TABLE 5-9, which indicates the 16/12 DSSRM has better efficiency with similar output.

TABLE 5-9 PERFORMANCE COMPARISON

1500rpm	12-16 segmental SRM	16-12 DSSRM
Resistance (Per Phase)	0.38ohms	0.78ohms
Torque (Average)	43.6Nm	43.7Nm
Copper Loss	1175.5W	477.7W
Iron Loss	144.6W	152.4W
Efficiency	83.8%	91.6%
DC Voltage	500V	500V
Peak Current	48A	18A

5.4 Thermal Analysis

Unlike conventional SRMs, the DSSRM would have another stator in the centre of the machine. Obviously, the heat generated by the inner winding could have difficulty transferring to the motor case. It was necessary to verify the heat transfer of the inner-stator winding in this project.

The experimental test of the prototype machine would be undertaken with a phase current density up to 10 A/mm^2. This level of current density is not unusual for an air-cooling SRM, but for a DSSRM, its inner-stator winding would possibly require additional investigation. To analyse the thermal problem, the half model of the machine was deveoped in JMAG. The thermal properties of the materials that comprised the machine are presented in TABLE 5-10.

TABLE 5-10 THE THERMAL PROPERTIES FOR DIFFERENT MATERIALS IN THE PROTOTYPE

property	Lamination	Coils	Slot Liner	Structure	Rotor Support
material	M270-35A	Copper	Nomex	Aluminium	PEEK
Heat Capacity J/(kg.K)	460	380	260	900	1050
Thermal Conductivity W/(m.K)	23	380	0.13	230	0.25

As can be seen from the lumped-parameter model in Figure 5-24, there are distinct differences between the prototype machine and the conventional SRM. For example, there are two air gaps connect to the rotor and the shaft in the middle of the device is a hollow and stationary structure which also provides a heat path to the ambient environment. Then, there are three heat-transfer paths to the ambient: the end cap, hallow shaft, and case. For modelling convenience, the heat transfer coefficient was set at the outer stator-to-case and inner stator-to-shaft conditions, by assuming the case to be a fluid and ignoring its heat capacity.

TABLE 5-11 THERMAL PROPERTY SETTING IN SIMULATION

	Case to Ambinet	End Cap to Ambient	Shaft to Ambient
Heat Capacity	NA	1230.2J/K	NA
Heat Transfer	1.35W/K	0.2945W/K	0.057W/K

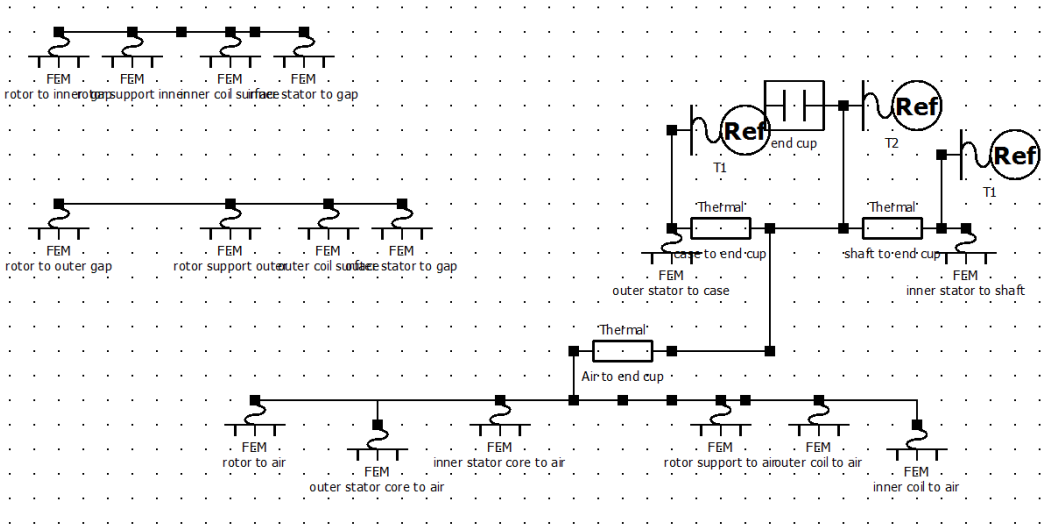

Figure 5-24 Lumped-parameter model for thermal analysis

In the simulation, the prototype DSSRM was defined to use a air-cooling method. Thus, the heat transfer coefficient of any surface to the ambient was set to 10 W/m^2 /°C. Regarding the heat source, the copper loss in the winding was circa 550 W, which corresponded to the average torque at 45 Nm or a current density of 10 A/mm^2. The simulation results in Figure 5-25 show that the final temperature rise could be limited to 120 K. If an ambient temperature of 20 °C is considered, then this rise could eventually reach 140 °C. Unlike a permanent magnet synchronous machine, the primary thermal limitation of the SRM would be the isolation of the windings, a temperature of 140 °C being entirely acceptable in this situation. Considering this result was modeled on a air-cooling senario, the prototype machine proved to be relatively effective in terms of cooling performance.

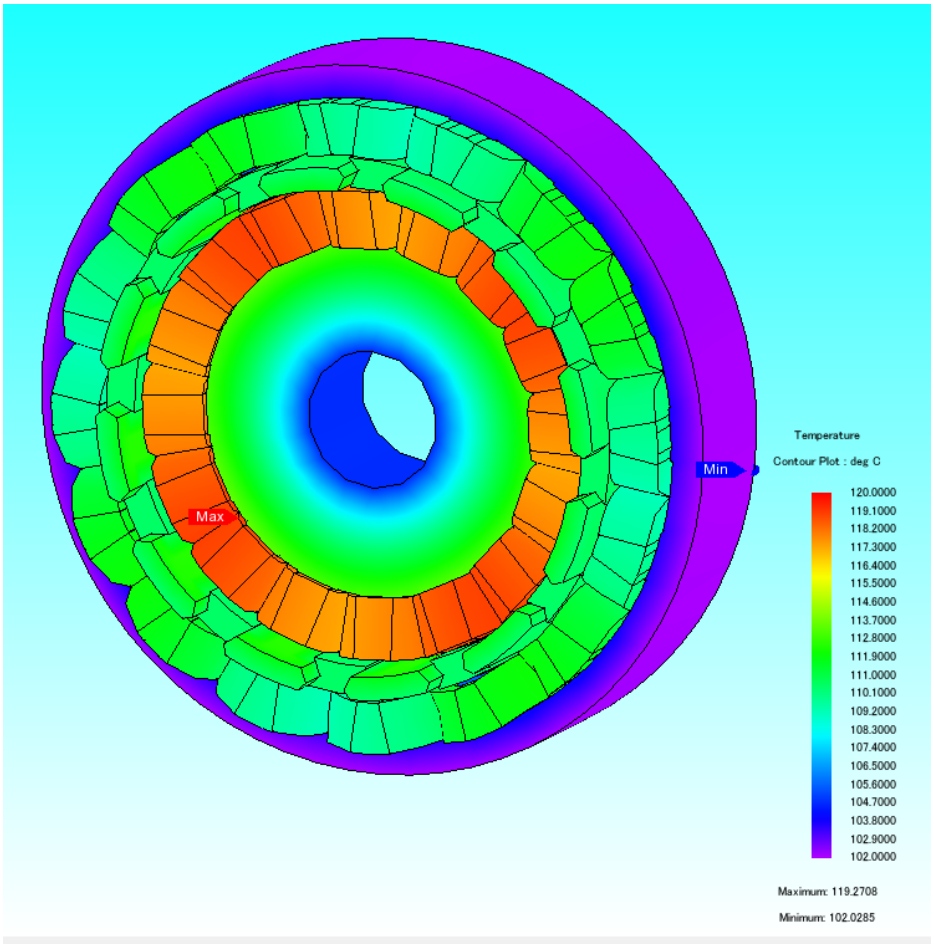

Figure 5-25 Temperature distribution in 3D model

Although the temperature distribution plot and results seem reasonable, the definition in the lumped-parameter model is subject to many assumptions and, therefore, needed to be verified. As such, a new lumped-parameter model was developed, assuming a small airgap between the case and the stator core, and so the heat-transfer coefficient would be calculated for this small airgap. The new lumped-parameter model and temperature-distribution plot can be seen in Figure 5-26 and Figure 5-27 respectively. Observing the new temperature-distribution plot, it is apparent that although a different modelling method was used, the eventual result is nevertheless close enough. Thus, this thermal analysis result could be considered reliable.

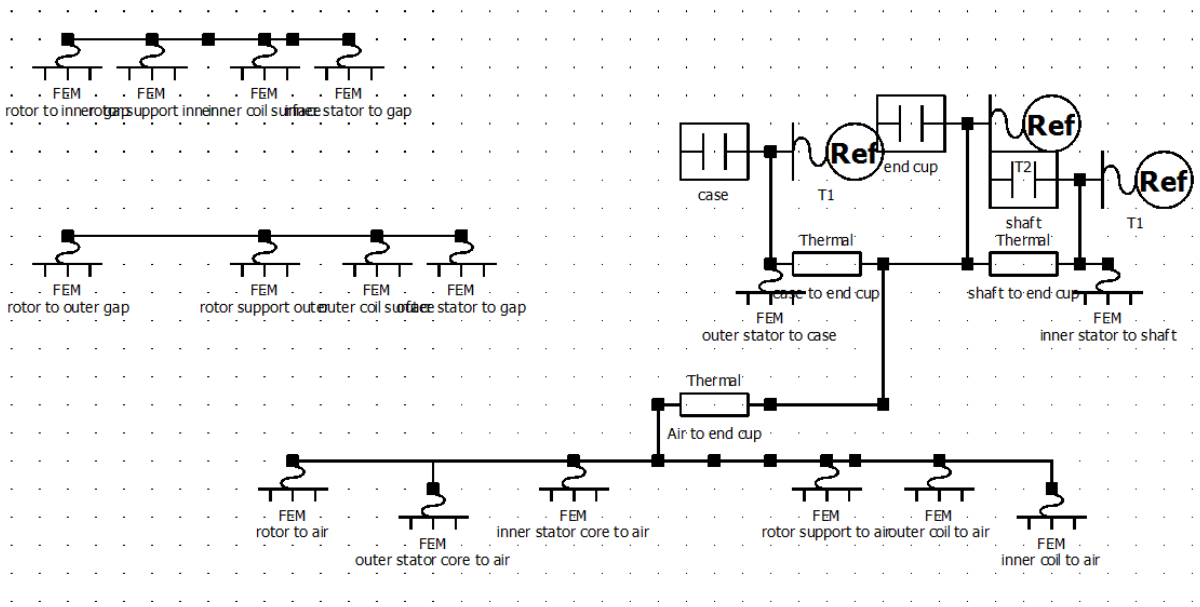

Figure 5-26 Lumped-parameter model for thermal analysis

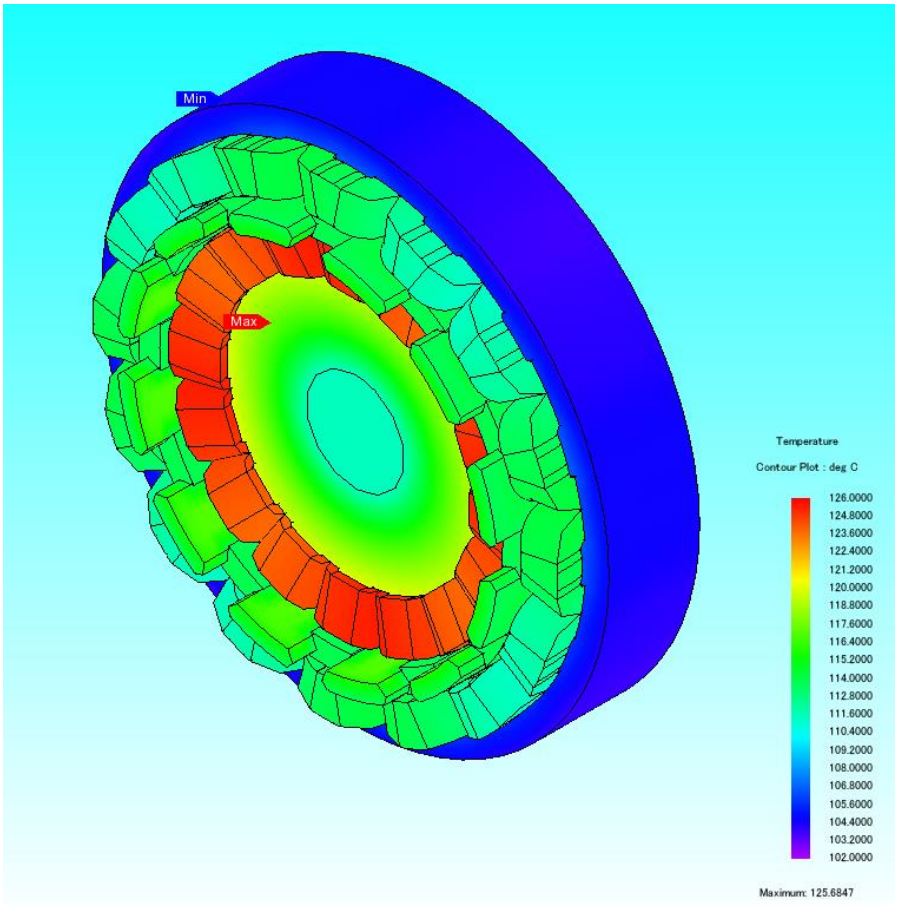

Figure 5-27 Temperature distribution in 3D model

5.5 Conclusion

In this chapter, several milestones for developing the final design of the prototype have been described:

- The frame size of the prototype machine was 210 mm in diameter and 75 mm in active length. There were two important reasons for choosing these dimensions: firstly, the structure of the DSSRM would be more complicated in the radial direction; therefore, it would be easier to construct it with a larger diameter; secondly, a segmental SRM with the same design purpose (high torque-to-copper loss ratio) was constructed in Newcastle University and the prototype machine would need to maintain a similar volume in order to make a fair comparison.
- The development for the novel rotor support structure has been presented. This section could be divided into four parts:
    (1) The conventional metal (stainless-steel) structure has been analysed. The 2D FEM revealed that the metal support would induce a large loss from the eddy current and the method with a bolt imbedded inside the rotor segment would create less losses compared to others.
    (2) An engineering plastic named Polyether Ether Ketone (PEEK) has been considered for use in the support structure to avoid an eddy current. Four different support structures were analysed by the 3D FEM for both mechanical robustness and electromagnetic performance. The centrifugal force at a maximum speed of 6,000 rpm was carried out to verify the mechanical properties. Finally, a structure for the prototype was chosen due to its outstanding electromagnetic performance.
    (3) Several potential alternative materials for PEEK have been discussed, including alumina ceramic, glass, and bamboo. This revealed bamboo to be a suitable material, in terms of both cost and processing; but its reliability within a harsh environment (a hot electric machine) would require further investigation.
    (4) The electromagnetic force on the rotor structure has also been analysed in this section. Since there are two airgaps in each side, the radial force on the rotor segment would be almost balanced with a slight bias towards the shaft. The principal stress from the electromagnetic force would be relatively small compare to the centrifugal force at maximum speed. A resonance analysis was implemented for the four-pole vibration model and revealed that the resonance

frequency would exceed 4,000 Hz, which is far beyond the conducting frequency at maximum speed.

- After the rotor-structure type was developed, optimisation of the prototype SRM could commence. The optimisation used a built-in genetic algorithm-optimisation tool in JMAG. The prototype achieved 13% torque enhancement and 6.75% copper loss reduction after optimisation. Further comparison between the prototype machine and a previously constructed segmental SRM was made by the 2D FEM. The results revealed that the prototype machine could provide relatively higher torque capability with the same copper loss limit.
- Thermal analysis is necessary for an unusual machine structure. In this machine, the heat in the inner stator could have difficulty transferring to the outer stator, causing these components to experience the highest temperature rise inside the machine. However, since there was a hollow stationary shaft within the middle of the prototype, there would be more areas, if required for cooling, compared to the conventional SRM. The thermal analysis by the 3D FEM revealed that the prototype machine could maintain the max temperature rise to 120 ℃ in a 10 A/mm^2 current density with only air-cooling method.

The work presented in this chapter has contributed to knowledge as follows:

To minimise the extra eddy current loss, several novel rotor structures have been developed, and several non-metal materials are discussed. The analysis indicates that the rotor support structure could fulfil the mechanical requirement and that non-metallic structures are feasible.

Chapter 6. Construction and Test Result

Chapter 5 analysed the prototype development and design details, using a variety of simulations covering mechanical robustness, thermal capability and optimisation of torque performance. The mechanical simulation included applying a centrifugal force at a maximum speed of 6,000 rpm, an electromagnetic force at a 45-Nm operating point and a vibration mode-verification for resonance effects. Consequently, this simulation confirmed the design of the rotor support structure. The optimisation focused on enhancing the torque-to-copper loss performance with a genetic algorithm. This optimised design was compared with the original design and a SR-SRM, proving it capable in terms of performance. Finally, the thermal properties were examined by assuming the prototype machine would operate at a 10 A/mm^2 current density while cooled by natural air convection. In this Chapter, the construction process, experimental test procedure and results will be presented in detail.

6.1 Rotor Design Revision for Construct Feasibility

Although the rotor structure was analysed in Chapter 5. concerns over installation accuracy and durability from mechanical experts led to several revisions of the motor design:

1. Firstly, to guarantee the robustness and accuracy of the rotor laminations, the rotor structure had to be linked together.
2. Secondly, as a single-tooth machine, the winding could be pre-wound on a bobbin to achieve a higher fill factor. However, to fit the winding on the stator, the tang design near the pole tip had to be eliminated.

The geometric design revisions can be seen in Figure 6-1. Comparing this to the original design in Chapter 5. the modified version has a thin bridge in the rotor lamination and the stator pole is completely straight, without any tang or taper. Thus, it could be expected that the torque performance might be affected and very likely deteriorate.

In TABLE 6-1, the effects of the geometric modification to the torque capability are presented. This shows that the presence of the bridge will decrease the torque capability by nearly 20 %. In terms of the stator-pole modification, there are two ways to achieve a straight pole from the previous overhang-tip design: either remove the overhang or fill in the slot behand it. Based on 2D FEM, the first option of directly redesigning the pole tips would offer the best result. When the bridge was introduced into the rotor core, the stator pole with the tang removed would provide almost the same average torque compared to the original design. In addition, with regard to enhancing the fill factor from the straight pole design, its torque capability would

increase under the same copper loss conditions. Since the fill factor could be improved from 0.4 to 0.5, the proposed design (removing the overhang from the stator tip and placing a bridge in the rotor) could offer 56.27 Nm in average torque, which would be as much as 9.5 % higher than the original design at the same current density.

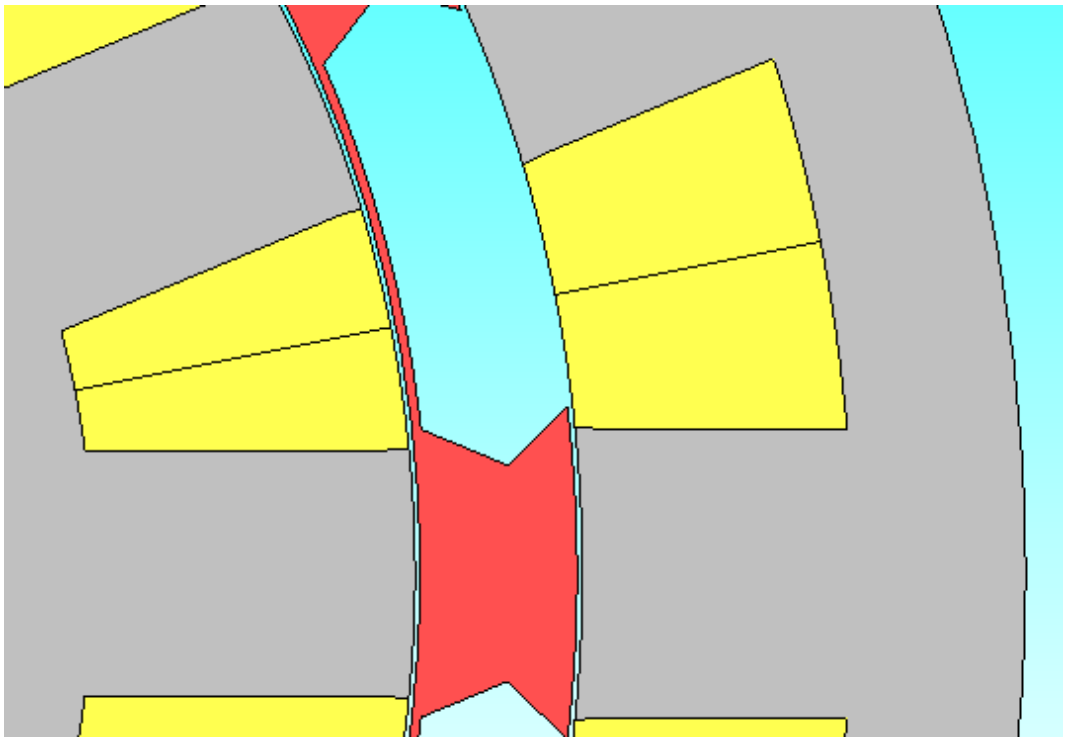

Figure 6-1 Cross section of the rotor with a thin bridge-link along the inner airgap

TABLE 6-1 THE CHANGES IN AVERAGE TORQUE FOR THE DIFFERENT GEOMETRIC MODIFICATIONS

		Fill Factor 0.4		Fill Factor 0.5	
Torque(NM)	original	remove tang	fill the slot	remove tang	fill the slot
without bridge	51.36	46.23	38.95	61.70	52.33
bridge	41.41	41.40	34.60	56.27	47.40

Another significant change in the rotor structure was the materials for the rotor support. In reality, the university's manufacturing team lack the experience in processing the solid plastic with high precision. Thus, an epoxy potting compound (834ATH) which would remain liquid before a full cure could be selected to fill in the hole between the rotor segments. However, the mechanical properties of the epoxy might not satisfy the requirements, as its tensile strength is

28 MPa, which is relatively low compared to PEEK. To guarantee sufficient strength, a number of carbon fibre rods would be inserted into the rotor support structure. The modified rotor structure is shown in Figure 6-2

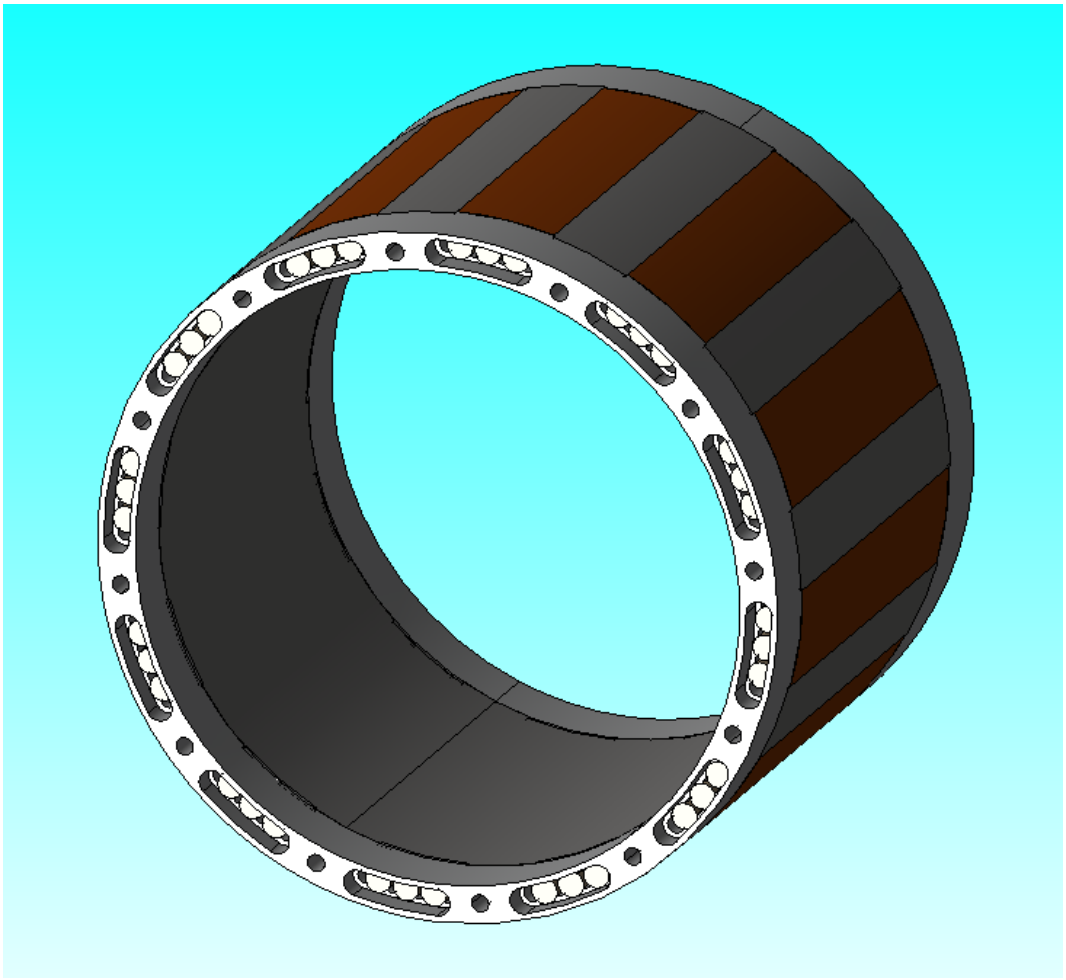

Figure 6-2 3D model of the revised rotor structure

The mechanical robustness of the modified structure was also verified by the 3D FEM. The simulation would run at under 4,200 rpm and the Young's modulus of the epoxy would be reduced to 50 % of its ideal value. The reason for adopting the above conditions was to introduce a safety factor.

The principal stress result is shown in Figure 6-3, and reveals that the stress on the epoxy parts is far below its tensile strength. As expected, the maximum stress is focused on the tip of the carbon fibre rods with a maximum value of 40 MPa. Considering the ultimate tensile strength of carbon fibre rods is claimed to be 1600 MPa to 2300 MPa by the vendor, the revised rotor support is shown to be sufficient for this design. Moreover, the displacement plot with a 1000X scale factor is presented in Figure 6-4. It shows that the maximum displacement occurs at the

middle of the rotor with a deformation in the radial direction. It is generally safe since the airgap is about 0.3mm long which is more than sufficient for the maximum 0.0075 mm displacement.

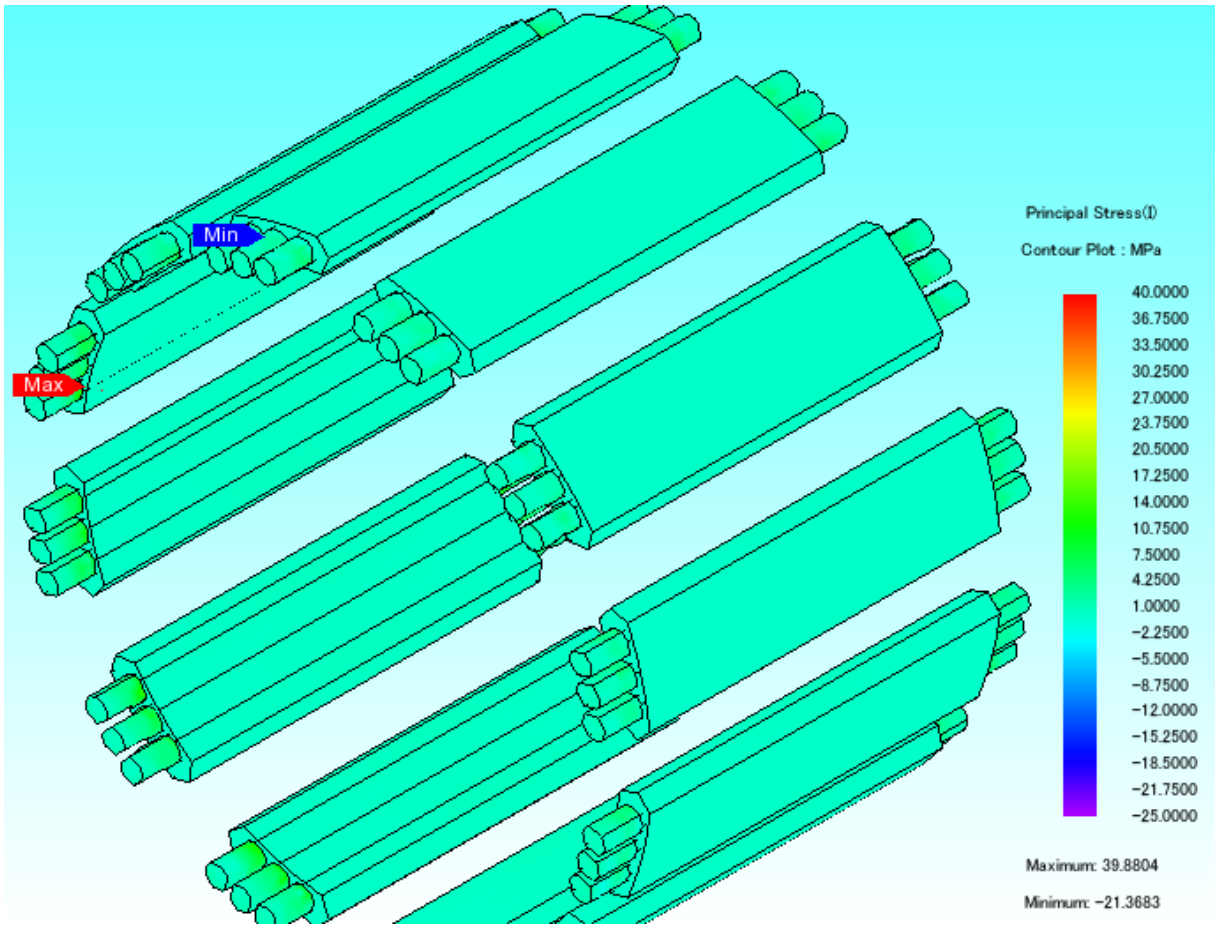

Figure 6-3 The principal stress distribution conditions of the revised rotor-support structure

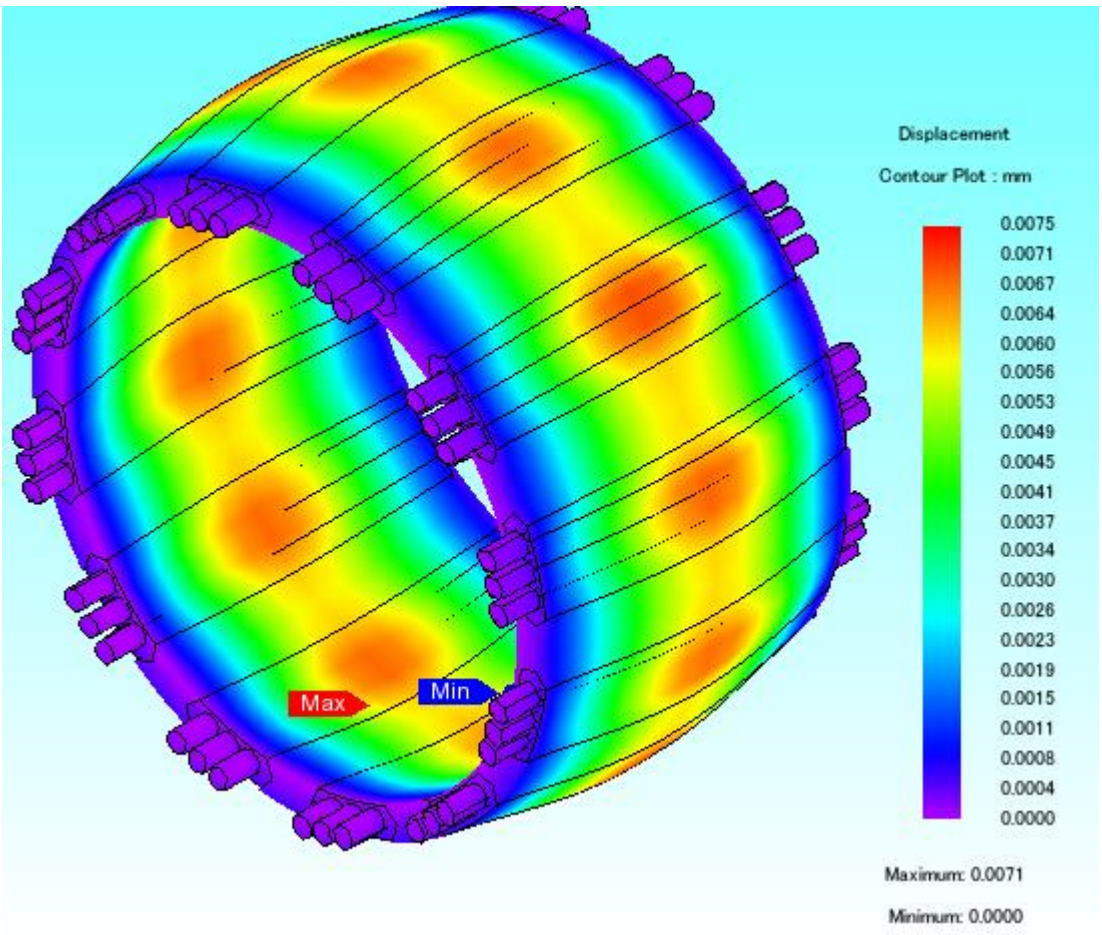

Figure 6-4 The displacment results and 1000X deformation view of the revised rotor

6.2 Construction Process

The construction process consisted of four steps:

- Firstly, the stator laminations were machined from steel sheets and compressed together to form the stator core.
- The coil bobbins were pre-wound and fitted into the stator slot.
- Next, the case and shaft were machined from aluminium to act as a holder for the stator core.
- Lastly, the rotor lamination and support structures were constructed, based on the design in section 6.1, and mounted on the bearing on the shaft.

6.2.1 Stator Lamination and Machining Method

M270-35A steel was selected as the lamination material, to provide direct comparison with existing machines. The stator lamination was designed to have a 75-mm stack length and it was

decided it would be glued into three 25-mm sub-stacks before being machined. It was believed this method would provide very good tolerance in the machining precision. As can be seen from Figure 6-5, the laminations were glued with epoxy resin and compressed to achieve a high stack factor of circa 98 %.

Figure 6-5 The laminations – glued, compressed and drilled

Holes on the lamination stack were drilled to offer an action point for the Electrical Discharge Machining (EDM). EDM offers high precision for machining metal components and, thus, was considered advantageous for the prototype manufacture. However, this technology also has one major drawback – a relatively slow cutting speed (9.8 mm/h during this task). Since the speed was not a critical consideration for a one-off manufacture, it was deemed acceptable for this task. A glimpse of the cutting process of the EDM is presented in Figure 6-6. As the workpiece was immersed in the dielectric fluid, the machining process will be near the ambient temperature. This is another advantage over laser cutting and conventional machining, both of which generate a considerable temperature rise.

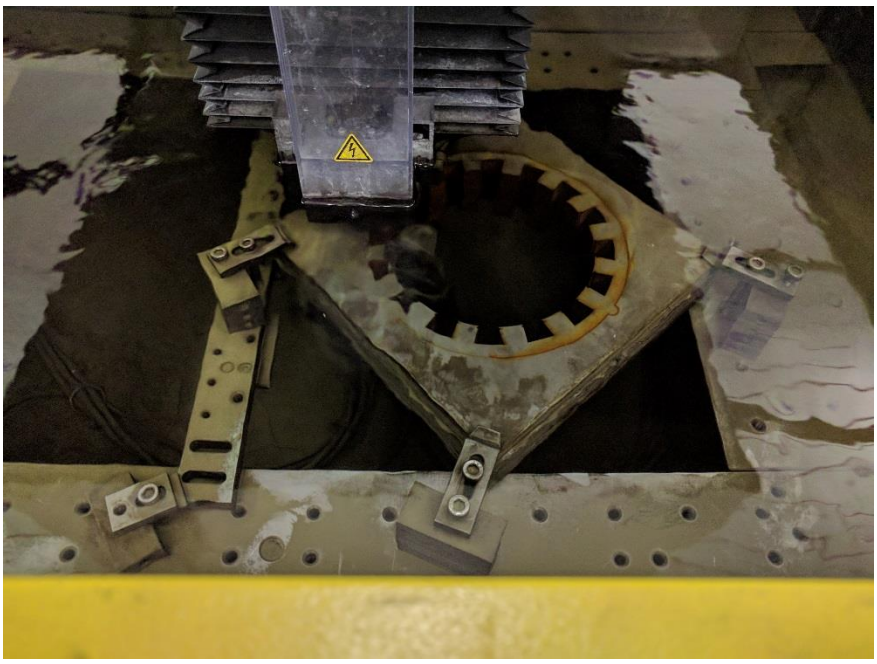

Figure 6-6 The outer stator lamination was created using EDM

The finished workpiece of the inner stator is shown in Figure 6-7. Two minor modifications from the 2D FEA model can be seen:

- A small groove has been cut near the pole tips to install the slot wedge, which could isolate the winding and prevent it from intruding into the airgap.
- A location feature has been created along the inner edge in the middle hole, which was designed to correctly position the inner stator onto the shaft.

Figure 6-7 The finished inner stator sub-stacks

6.2.2 Manufacture of the Shaft

The shaft was constructed from 6082 T6 Aluminium, a material which offers both adequate mechanical strength (a tensile strength of 260 MPa, Young's modulus of 70 GPa) and good machinability (a hardness of 75 HV), a conventional machining process (see Figure 6-8) was selected.

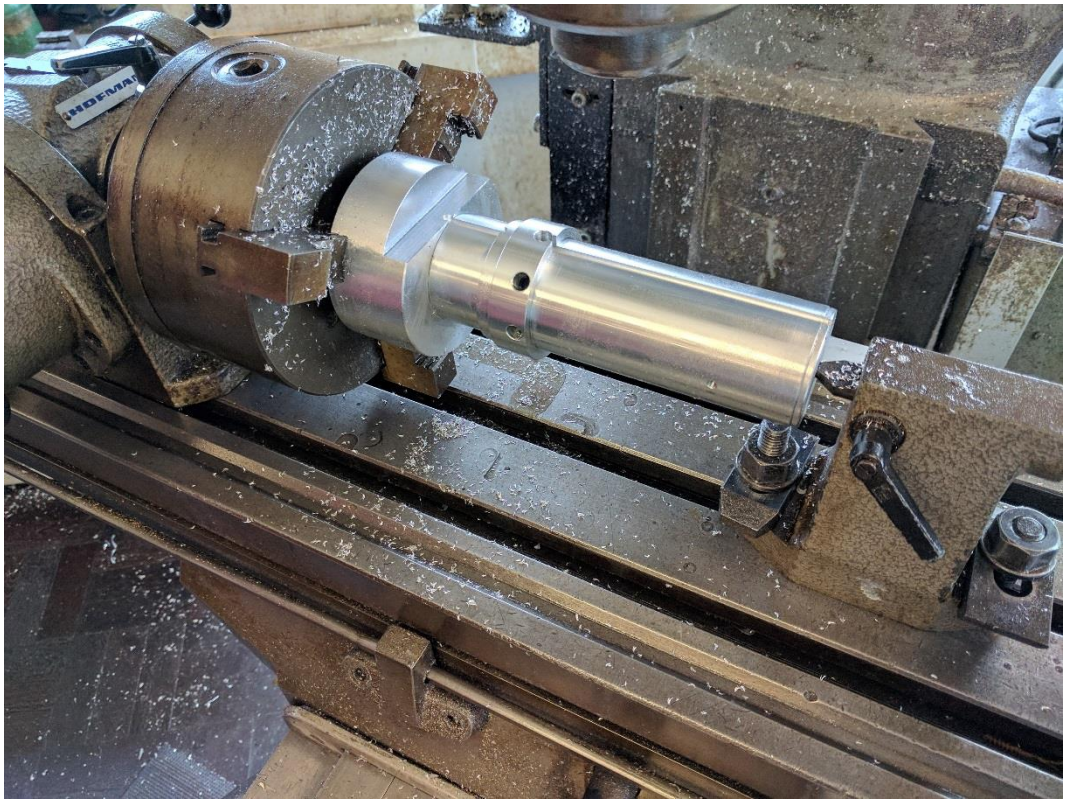

Figure 6-8 The stationary shaft during the machining process

As can be seen from the Figure 6-9, the shaft in the prototype differs from a conventional shaft in two aspects:

- The shaft is stationary and hollow, with eight holes of 3.8-mm radius distributed evenly around the shaft surface.
- The shaft was engineered to lock the position of the inner stator and to deliver pressure to compress the lamination in the axial direction. Moreover, the hollow structure and drill holes would offer a path for the inner stator coils to exit the machine.

The completed work is shown in Figure 6-10, where the inner stator is mounted on the shaft.

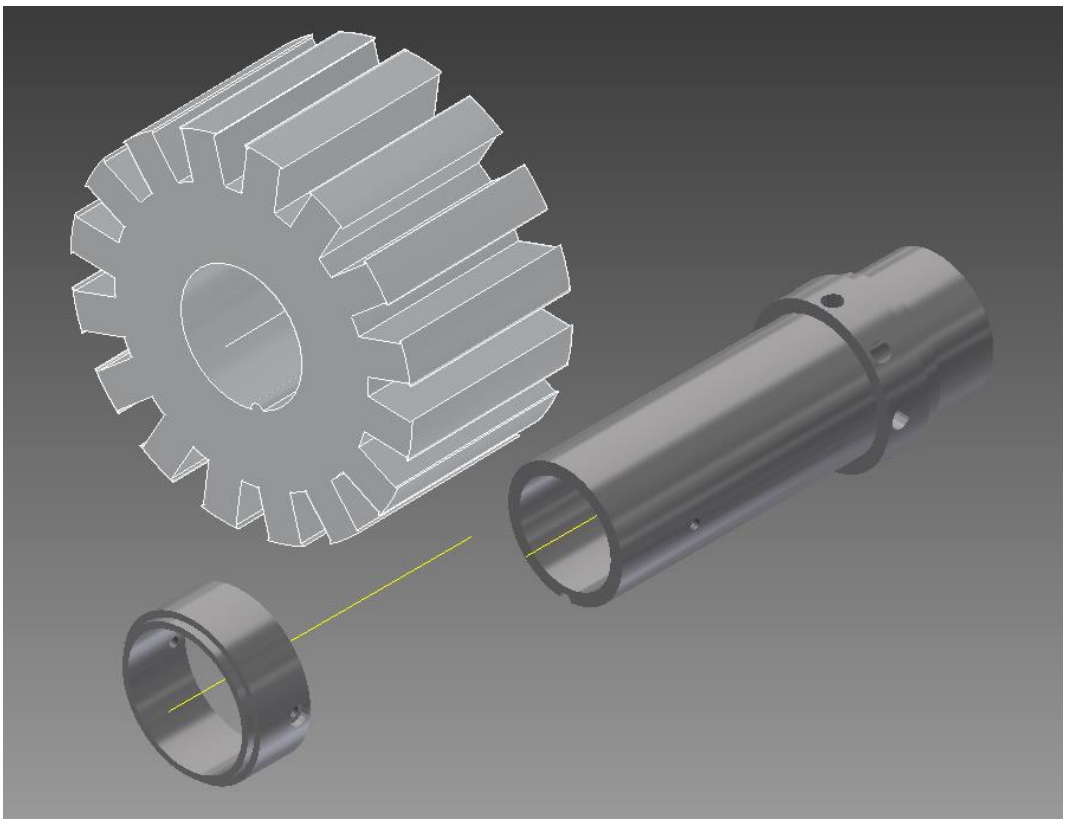

Figure 6-9 The assembly view of the inner stator and shaft in Autodesk Inventor

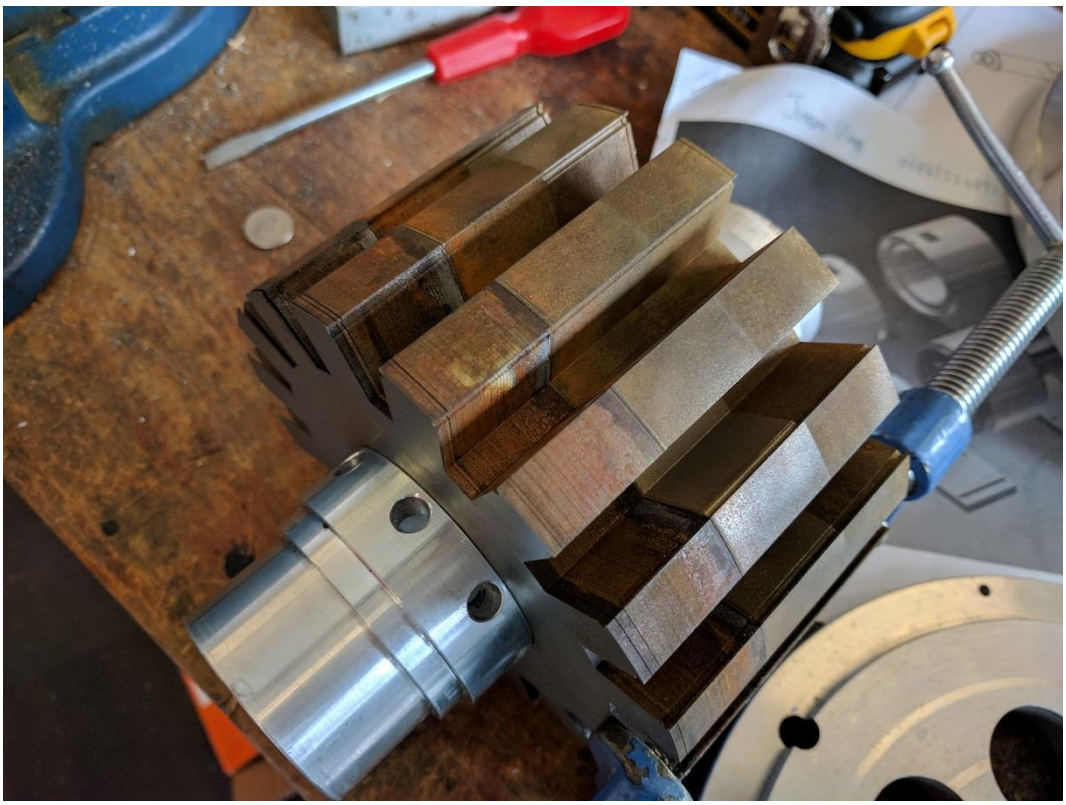

Figure 6-10 The inner stator, mounted on the shaft, being compressed to eliminate any gaps between laminations.

6.2.3 Motor Winding Production

The prototype machine used single-tooth windings which were pre-wound on bobbins.

The turn number for an SRM is determined by the dynamic performance requirement. In a DSSRM, there exists an extra constraint: the same current density shall be maintained in both the inner- and outer-stator windings.

Based on transient 2D FEM result in Chapter 5. 5.3, the turn number was selected as 30 for the inner stator and 44 for the outer to provide a torque-speed profile compatible with the previous 12/16 segmental SRM. With the appropriate turn number set, a diameter of 1.4 mm (a cross section area of approximately 1.5 mm^2) was decided for this machine.

The machine used pre-wound bobbins to achieve a 50%fill factor. As can be seen from Figure 6-11, the bobbin was wound on a turning lathe. The rotation of the lathe and the tension of the coils was based on manual force only. With a mechanical counter connected to the lathe shaft, the turn number could be precisely measured during the winding process. Although the coils would be pre-wound on bobbins, coil-pressing and gluing was not considered for this prototype. The complete winding was bound by electric tape to provide fundamental isolation for protection and to prevent the winding from coming loose.

In Figure 6-12, two windings have been installed on two adjacent inner-stator poles. The winding was insulated using a slot liner made from 0.5-mm Nomex sheet to prevent the coil touching the stator core, thus ensuring isolation even in the event of a flaw in the wire coating. A glass fibre slot wedge was also used to prevent anything in the slots from intruding into the airgap and impacting the rotor.

Figure 6-11 The procees of winding the coils onto the bobbin

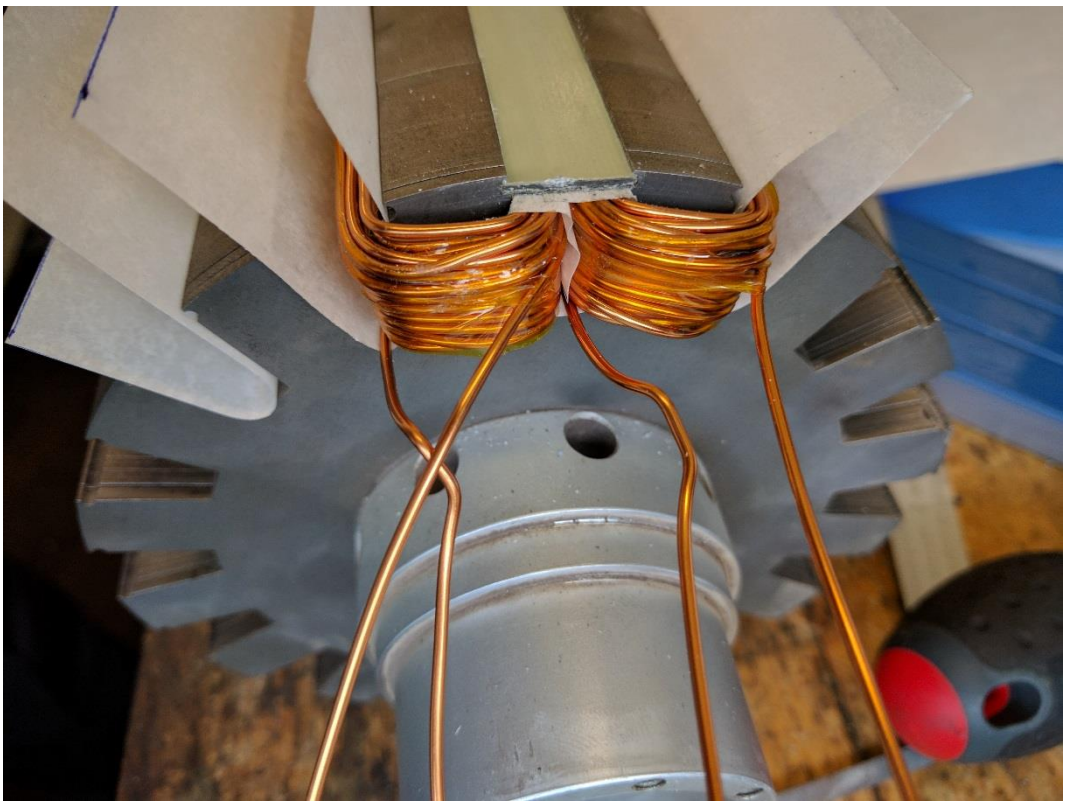

Figure 6-12 The process of fitting the pre-winding onto the inner stator

Since the slot in the outer stator was wider at the bottom and narrower at the tip, two pre-windings from adjacent poles would struggle to fit into the slot together. To solve this issue,

two different pre-winding shapes were produced. Bobbins manufactured to allow these coils to be wound are presented in Figure 6-13: half of the windings were completed prior to using the left bobbin and fitted to the eight non-adjacent poles; then another eight windings were made using the right bobbin and successfully fitted to the remaining poles. As can be seen from Figure 6-14, the windings were installed on the outer stator and the red lines drawn along the edges clearly demonstrate the difference in these two winding types. Eventually, the windings in both the inner and outer stators were tested with 2,000 V to confirm isolation for the phase-to-stator core or the phase-to-phase condition.

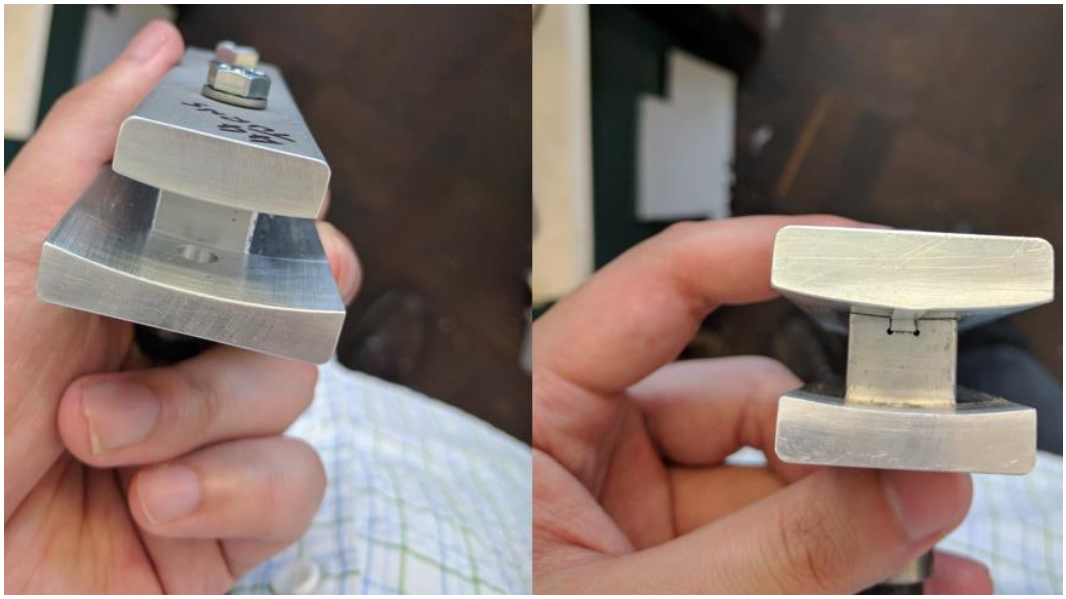

Figure 6-13 Two differenct bobbins for the outer-stator windings

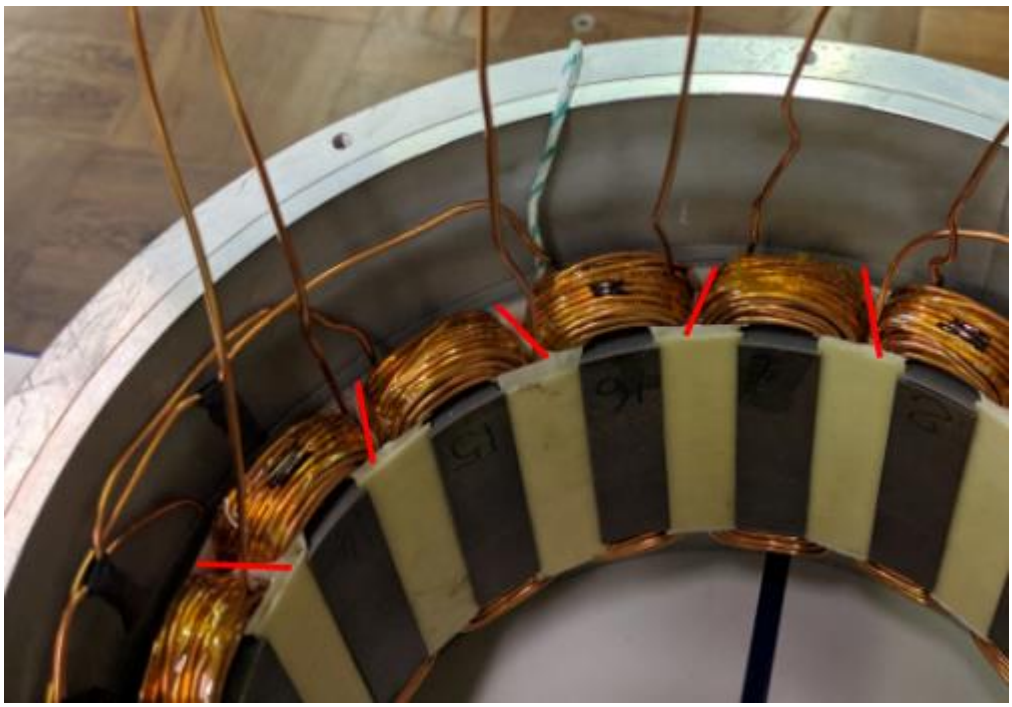

Figure 6-14 The winding assemblage in the outer stator

6.2.4 Rotor Lamination and Support Structure

The rotor lamination was cut with the same method as the stator lamination, as can be seen from Figure 6-15. Corrosion on the surface was due to immersion in the dielectric liquid during machining.

At this stage, the rotor segments were linked by bridges, which enclose several slots to allow for the further procession. As can be seen from the Figure 6-16, an epoxy potting compound has been filled into those slots. This compound was allowed 24 hours to cure at room temperature.

The terminal ring was made from 6082 T6 aluminium and its structure is presented in Figure 6-17. This was the adapter between the rotor laminations (filled with the carbon fibre reinforced epoxy support) and the rotor caps (mounted on the bearings). The connection between the rotor cups and rotor ring was based on a screw method; thus, it would offer detachability to some extent. However, the connection between the rotor ring and the rotor support became permanent once the epoxy filling had cured. The physical security of this connection was guaranteed by the fillings in the rotor support hole (see Figure 6-17). Specifically, three carbon fibre rods were locked within one rotor support hole to prevent displacement between the rotor and rotor ring in the radical or tangential directions (see Figure 6-18). Furthermore, as the support hole was filled with epoxy, these step shapes around the edges could provide stress through the rotor-support structure in the axial direction. As such, the rotor laminations could obtain stress from

the two rotor rings on both sides to maintain the tightness between the steel sheets unless the epoxy filling cracked.

Figure 6-15 Rotor lamination made using EDM

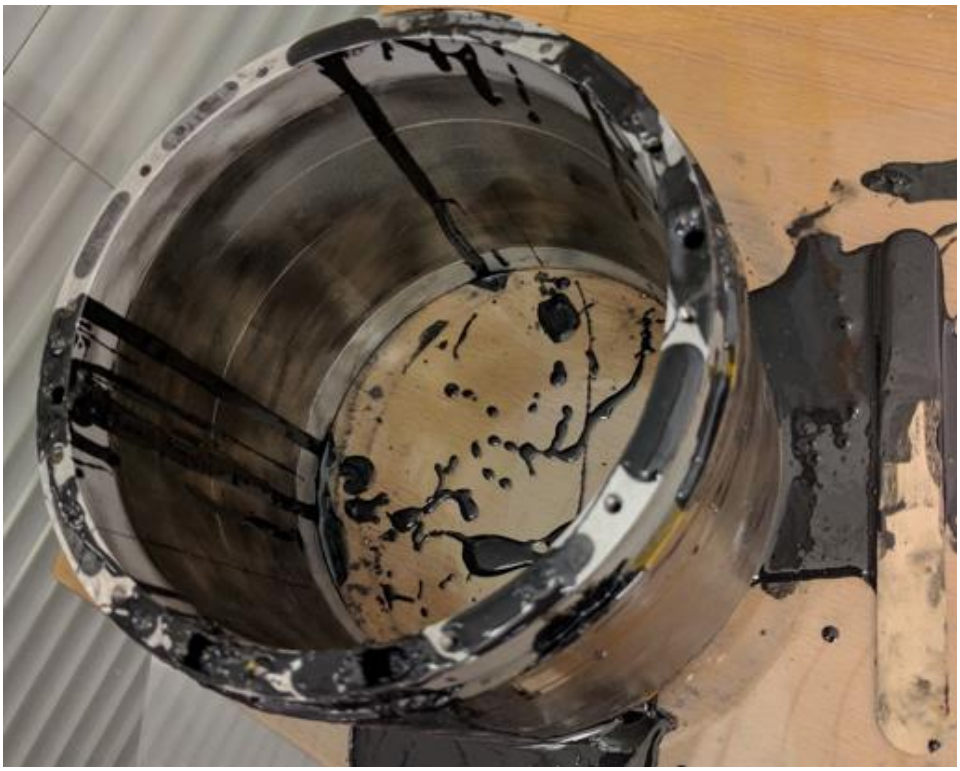

Figure 6-16 Pouring the epoxy plotting compound into the rotor lamination slot

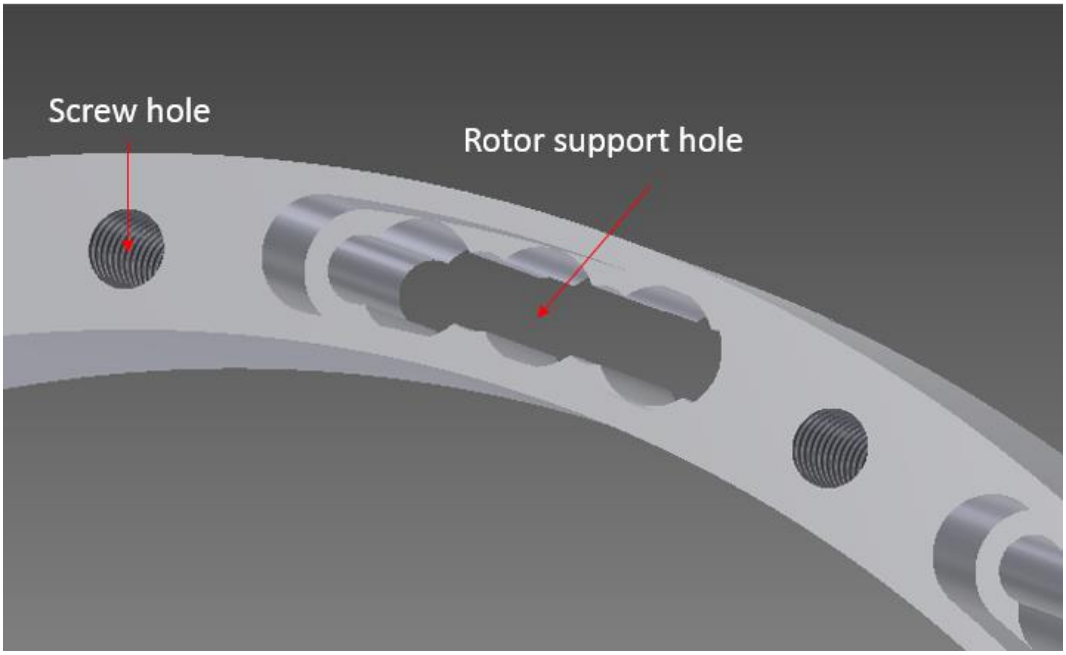

Figure 6-17 Model of the rotor terminal ring in Autodesk Inventor

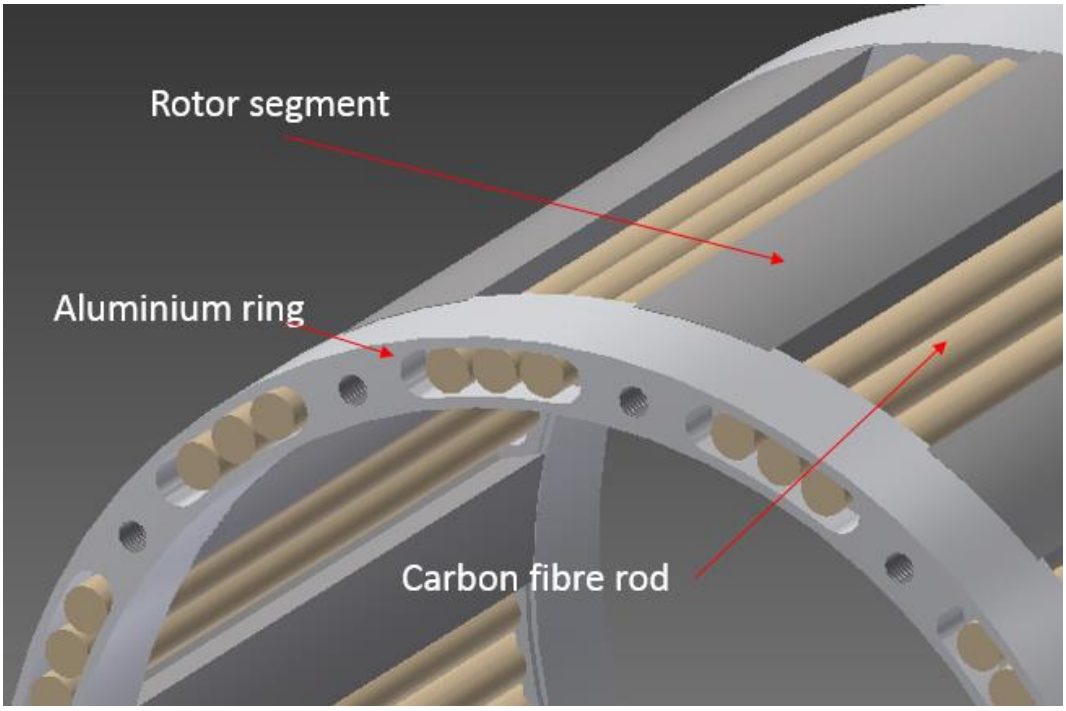

Figure 6-18 Connection between the rotor terminal ring and the rotor (only the rotor segments and carbon fibre rod are visible)

Left for 24 hours at room temperature and with the assistance of a heat gun, the viscous black fluid in Figure 6-16 was finally transformed into a rigid solid. Its hardness in Shore D durometer

was 85 D; as a comparison, hard hats used for head protection are made from a material of 80 D, as measured on the same hardness scale.

After the epoxy potting compound had cured, the outer redundant ring had also finished its task and needed to be cut off from the rotor lamination (see Figure 6-19). During the cutting process, some cavities were found on the surface of the epoxy, in part due to the imperfect filling method. Although the structure proved relatively stiff during cutting, it was decided to fill the cavity and repeat the cure process.

Figure 6-19 The process of post machining the redundant parts from the rotor lamination

6.3 Test Result

Experimental testing of the machine was based on the static method, since a four–phase drive was unavailable at the university; however, these tests should offer sufficient experimental data for performance analysis via the following steps:

- First, a pulse test was used to generate the details of the flux linkage-vs-current characteristics during an electric cycle.

- Static torque was obtained from a torque transducer to develop the torque-vs-electric degree curve.
- Mechanical performance was verified with a load machine by spinning at a speed up to 4,000 rpm.

These tests are presented in the following sections with technical details.

6.3.1 Static Pulse Test

As briefly mentioned above, the purpose of the pulse test was to obtain the motor's magnetisation characteristics. According to [36] and [42], the digital integration method is the most in common measurement in technology. To be specific, the rotor would be locked into a fixed position and the phase current and voltage trace would be obtained during the conduction period. Then, the flux linkage-vs-current data could be generated, based on the following equation:

$$[\Psi] = \int ([V] - R[I])\, dt \qquad (6\text{-}1)$$

Where the square bracket represents the value obtained from the discrete form and which is stored in arrays for digital computation. Thus, to calculate the flux linkage $[\Psi]$ at a certain position, the voltage and current trace need to be recorded during a current rising (or falling) process while the rotor is locked at this position.

As can be seen from Figure 6-20, the machine was mounted on a bench table in order to be tested. So as to ensure accurate measurement of the rotor angle, the machine shaft was connected to a torque transducer and a rotary table. The test process is briefly concluded in a flowchart (see Figure 6-21). The rotary table locked the position of the rotor during the test and allowed precise alteration of the rotor angle, by manually rotating the hand wheel. This test was taken between the unaligned and aligned positions. In reality, the rotor would tend to rotate to the aligned position while the winding is conducted. However, since the shaft could not freely rotate in this test, the start position had to be found with the aid of a torque transducer. Because the aligned and unaligned positions were in stable- and unstable-equilibrium positions, respectively, the static torque at these two position equalled 0 Nm. The prototype machine had 12 rotor segments, thus 360 electric degrees was equal to 30 mechanical degrees. The rotor angles were accumulated in half-degree increments from the starting point (either the aligned or unaligned position) and completed 30 increments, in total. In each angle, the programmable DC power supply provided a five-second current pulse with the maximum allowable current for this machine, which was 46 A (peak)/32.5 A (RMS) and equivalent to an RMS current density of 20 A/mm^2.

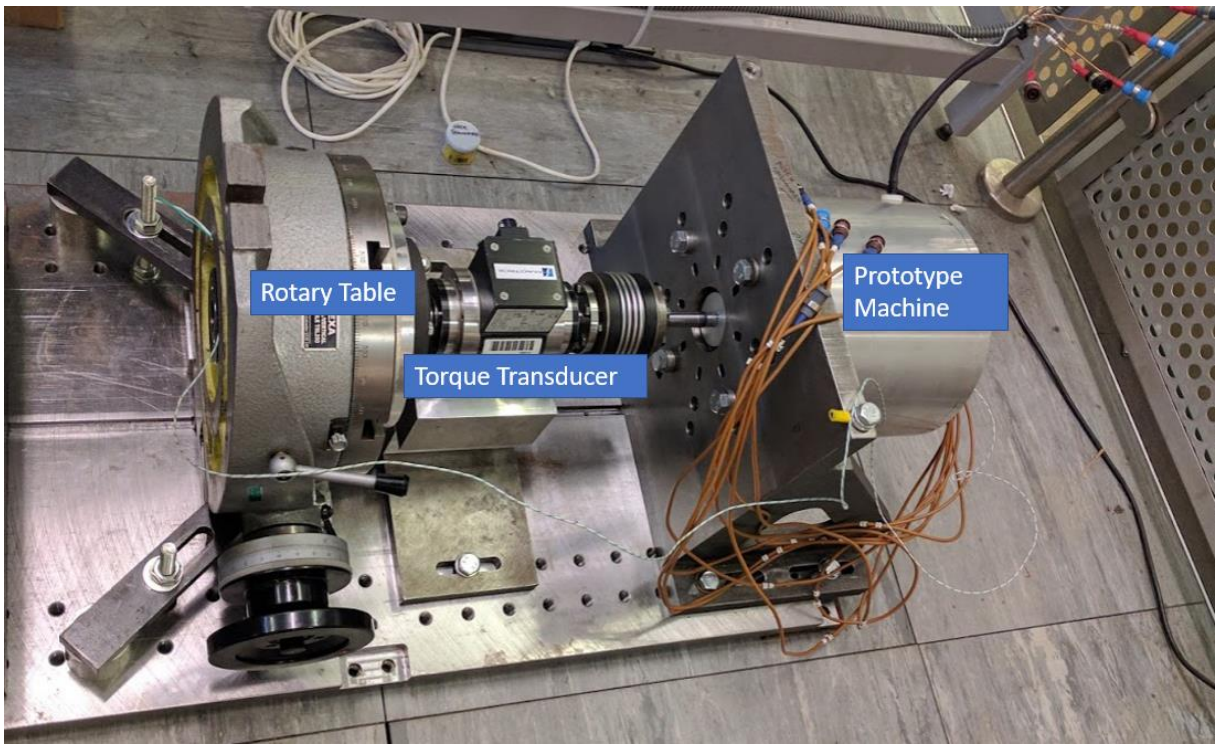

Figure 6-20 The benchmark table and prototype machine

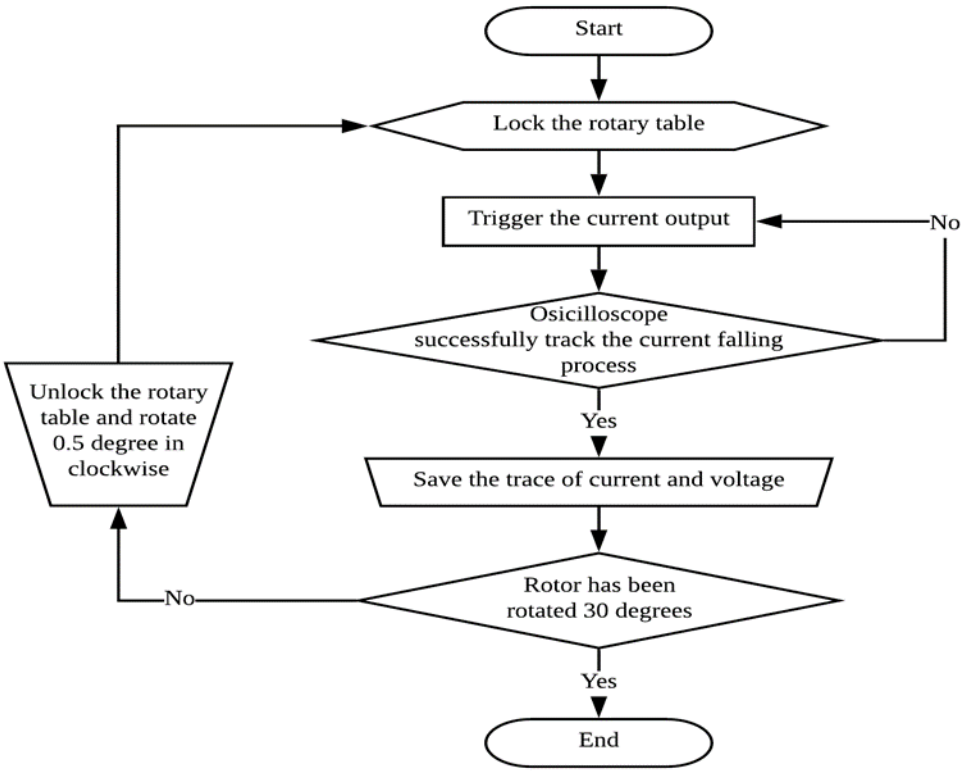

Figure 6-21 the flowchart of the static pulse test process

The voltage and current probes were mounted to the current carrying winding. Their signals were obtained using an oscilloscope and then stored in .csv format to allow for further analysis. One of the current and voltage traces at the aligned position is shown in Figure 6-22.

In order to consider the effects of temperature rise on the winding resistance during the conducting period, the winding resistance was calculated, based on the static value of the voltage and current trace during the excitation periods: its value was 0.76Ω, according to ohm' law. The calculation of the instantaneous flux linkage was done using the equation $[\Psi] = \int([V] - R[I])\,dt$ (6-1) within Matlab, and specific code is shown in Appendix 3 Script for Pulse Test

The script from Matlab is responsible for calculate the magnetisation curve from the current and voltage data which collected during pulse test

```
cd('D:\OneDrive\static test\23A')
filename = ('T0001all.csv');

voltage=xlsread(filename,'D17:D90000')
current=xlsread(filename,'B17:B90000')
time=xlsread(filename,'A17:A90000')


%filter the source data
b = fir1(100,0.0001); % design a FIR filter
filtvoltage=filter(b,1,voltage);
filtcurrent=filter(b,1,current);

maxcurrent=max(filtcurrent);
mincurrent=min(filtcurrent);
maxvolts=max(filtvoltage);
minvoltage=min(filtvoltage);

%find rise start point

for n = 1:length(filtvoltage)
    if(filtvoltage(n) > minvoltage*1.05)
        start_point = n;
        break
    end
end

%find rise end point

for n = 1:length(filtcurrent)
    if filtcurrent(n) > maxcurrent*(0.995)
        settling_point = n;
        break
```

```
    end
end




%find fall start point

for n = settling_point:length(filtvoltage)

    if(filtvoltage(n) < 0.9*maxvolts)  %the voltage goes negative on switch
off and we need to detect when the current begins to decay
        fall_start_point = n-1;
        break
    end
end



%find fall end point
for n = settling_point:length(filtcurrent)
    if (filtcurrent(n) < mincurrent*1.2)&(filtvoltage(n) > 0.5*minvoltage)
        fall_settling_point = n;
        break
   end
end

%Now find the value of resistance just after the end of the rise
%v= sum(filtvoltage(settling_point-5:settling_point+5))/10;
%i= sum(filtcurrent(settling_point-5:settling_point+5))/10;
v= sum(filtvoltage(34000:34110))/110;
i= sum(filtcurrent(34000:34110))/110;
coil_resistance_rise=v/i;

Psi=zeros(1,length(filtcurrent));
for i=start_point:settling_point;
deltaT = time(i+1)-time(i);
%Psi(i+1)=(deltaT*((filtvoltage(i)+filtvoltage(i+1))/2-(filtcurrent(i)-
filtcurrent(i+1))/2*coil_resistance_rise))+Psi(i);
Psi(i+1)=(deltaT*(((filtvoltage(i)-
filtcurrent(i)*coil_resistance_rise)+(filtvoltage(i+1)-
filtcurrent(i+1)*coil_resistance_rise))/2))+Psi(i);
end
hold on
plot
(filtcurrent(start_point:settling_point),Psi(start_point:settling_point),'r
');

risecurrent=filtcurrent(start_point:settling_point)
risefluxlinkage=Psi(start_point:settling_point)

xi=0:2:60
yi=interp1(risecurrent,risefluxlinkage,xi,'linear','extrap').
```

During the test, noise and oscillation in the voltage and current trace should be avoided; otherwise, a significant accumulative error would be generated during the digital integration process. As such, the data collected from the oscilloscope was smoothed by using a filter technique to eliminate the

In order to consider the effects of temperature rise on the winding resistance during the conducting period, the winding resistance was calculated, based on the static value of the voltage and current trace during the excitation periods: its value was 0.76

sampling noise. Moreover, only the falling periods of winding-current data were taken into consideration in the integration calculation. There were two reasons for not considering the data of the rising period:

- The temperature would rise rapidly once the winding was excited which would lead to an inaccurate winding resistance value in the integration calculation.
- Although the programmable DC power supply used in this test was equipped with a dedicated controller, overshoot and oscillations were still inevitable during the current-rising period and would potentially give rise to an accumulative error.

In order to consider the effects of temperature rise on the winding resistance during the conducting period, the winding resistance was calculated, based on the static value of the voltage and current trace during the excitation periods: its value was 0.76

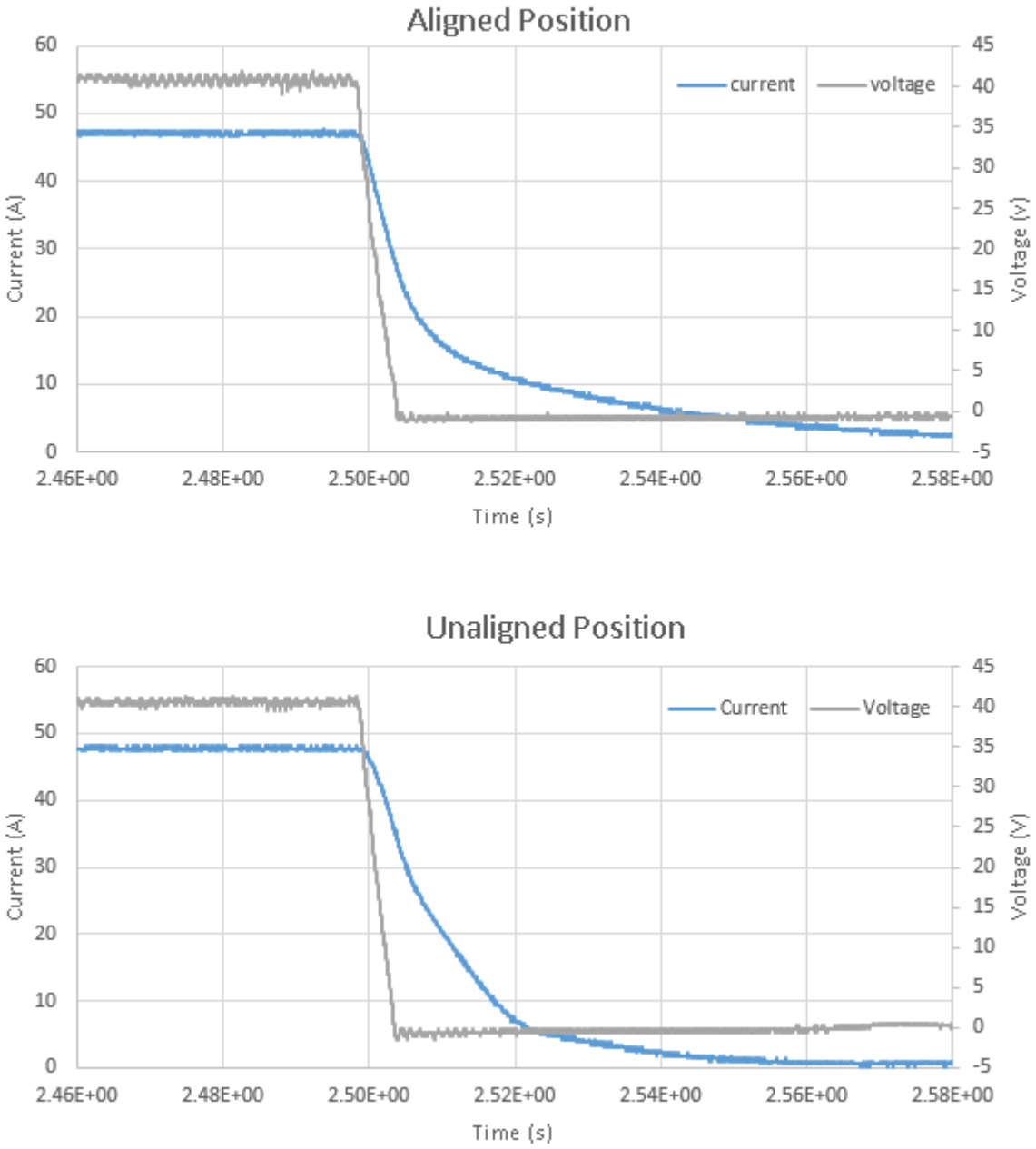

Figure 6-22 Current and voltage traces collected during the pulse period

The flux linkage-vs-current curve at the aligned and unaligned positions are presented in Figure 0-23 to make a comparison between the simulation and test results. It appears there are several differences between the 2D FEM and reality:

- At the unaligned position, the flux linkage is higher in the experimental test.

In order to consider the effects of temperature rise on the winding resistance during the conducting period, the winding resistance was calculated, based on the static value of the voltage and current trace during the excitation periods: its value was 0.76

- At the aligned position, the flux linkage is higher in the experimental test at the beginning, but then the two curves converge soon after.

This situation is relatively common and typical in almost every SRMs and is widely recognised as the absence of 3D effects in 2D FEA. In addition, according to [47, 49, 110], the 3D effects would include end-winding flux and axial fringing; however, it should be noted that the axial fringing effects were minimal in the unaligned position (because the airgap between stator and rotor pole is at a maximum at this point). The flux linkage difference of the unaligned position in Figure 0-23 was mainly caused by the extra flux from the end-winding. In terms of the aligned position, the 3D effects should depend on both end-winding flux and axial fringing effects; but this extra flux would be suppressed in the saturation condition (this phenomenon is indicated in Figure 0-23).

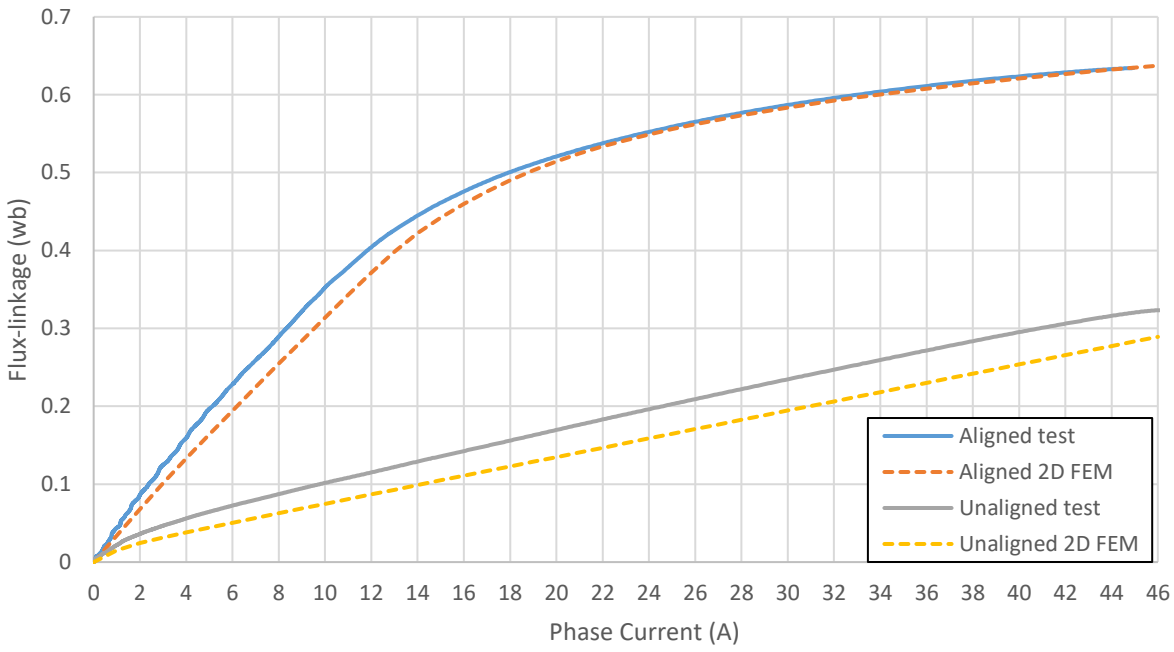

Figure 0-23 Flux linkage-vs-current result comparison between the experimental test and the 2D FEM

As the energy-conversion loop of the measured result was slightly smaller than that of the 2D FEM result, there is no doubt that the measured torque would be lower than in the simulation data. In Figure 0-24, the average torque curve at different phase currents is presented. It reveals that the measured torque and 2D FEM results are relatively close when the phase current is below 23A (equal to a current density of 10 A/mm^2). However, when the phase current exceeds 23 A, the gap between the measured data and the 2D simulation result increasingly expands, and a circa 10% drop can be witnessed at peak current.

In order to consider the effects of temperature rise on the winding resistance during the conducting period, the winding resistance was calculated, based on the static value of the voltage and current trace during the excitation periods: its value was 0.76

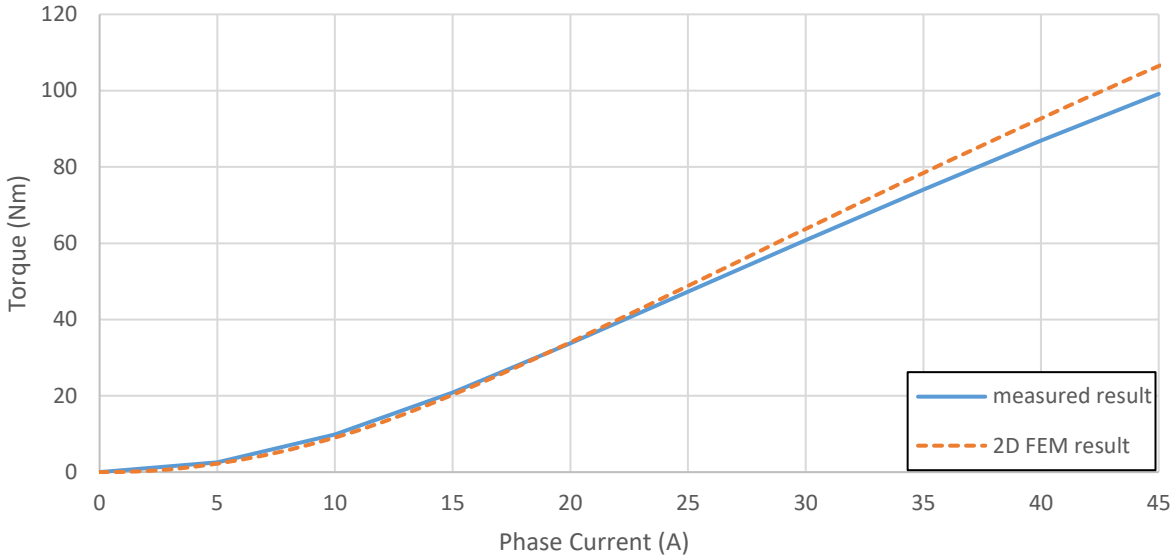

Figure 0-24 The average torque comparison between the measured result and 2D FEM result

Moreover, the unaligned flux linkage curve in this machine was slightly different to that of a conventional SRM. As can be seen, the unaligned curve for both the test and 2D FEM results reveal evidence of saturation at the very beginning. The explanation of this phenomenon relates to the geometrical design revision in section 6.1. In Figure 0-25, the flux density plot at the unaligned position is presented. Here, it can be noted that the thin rotor bridge along the inner airgap would be deeply saturated at this position.

In order to consider the effects of temperature rise on the winding resistance during the conducting period, the winding resistance was calculated, based on the static value of the voltage and current trace during the excitation periods: its value was 0.76

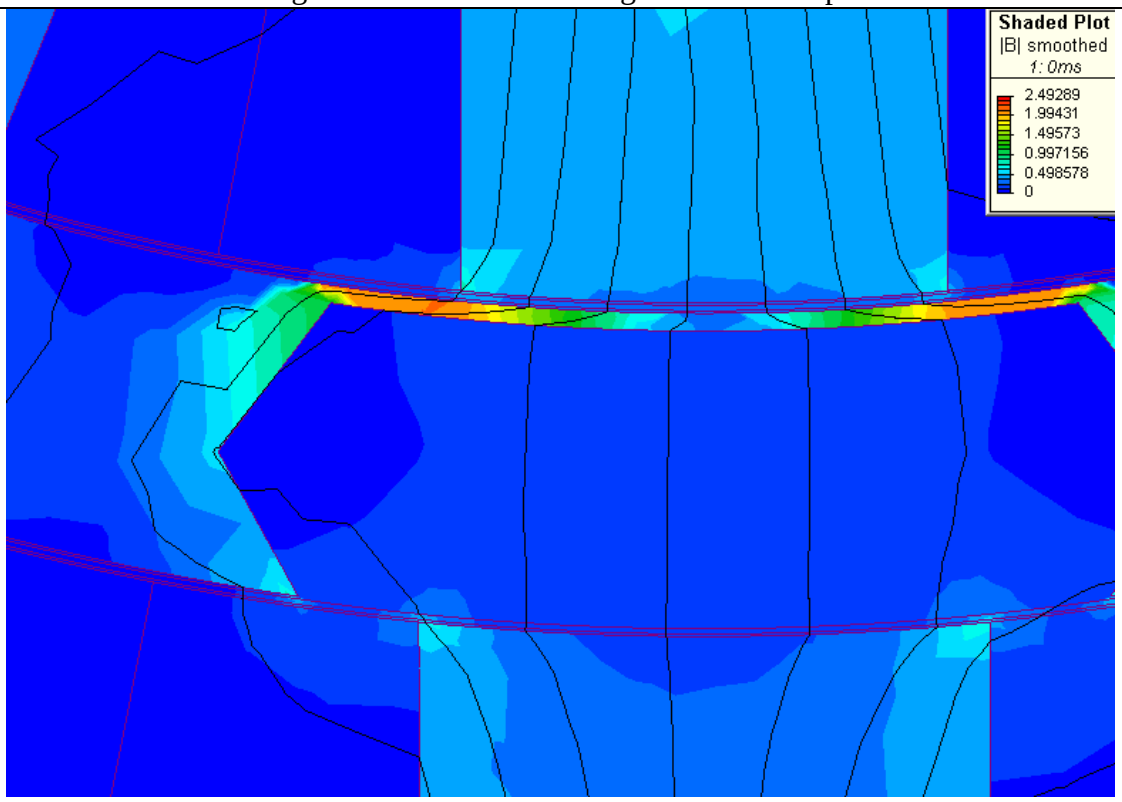

Figure 0-25 The flux density plot of the prototype machine at the unaligned position (2D FEM)

6.3.2 Static Torque Test

As the torque transducer was installed on the bench table, the torque-position data could be obtained and a comparison with the 2D FEM made.

The torque was measured simultaneously during the static pulse test and its values in different rotor positions were collected. In Figure 0-26, both the measured- and 2D FEM-torques for an entire electric cycle are presented and the average values are 19.58 Nm and 20.83 Nm, respectively. However, compared to the 2D FEM results, the curve of the measured torque experiences distortion in the horizontal direction.

Since Figure 0-23 and Figure 0-24 indicates that the magnetisation characteristic of the prototype machine performed as expected, this indicates that the construction tolerance of the iron core geometry was maintained properly.

Subsequently, excluding the core geometry issue, there were two possible reasons that could have led to this distortion in the torque-angle curve:

- Since there was a small flexure between gears in the rotary table, the accuracy of angular tolerance was about 0.1 mechanical degrees during the static test. Therefore, the

In order to consider the effects of temperature rise on the winding resistance during the conducting period, the winding resistance was calculated, based on the static value of the voltage and current trace during the excitation periods: its value was 0.76

measured-torque curve could have suffered an error of approximately 1.2 electric degrees.

- The rotor cap of the machine was connected with a stainless-steel extender. As can be seen from Figure 0-27, this connection shaft was relatively thin, thus a twist under the torque was inevitable.

Nevertheless, the rotor-position error is unlikely to have occurred at the aligned position and the unaligned position (which are the equilibrium positions in the static torque test). Thus, the data in Figure 0-23 and Figure 0-24 should be reliable.

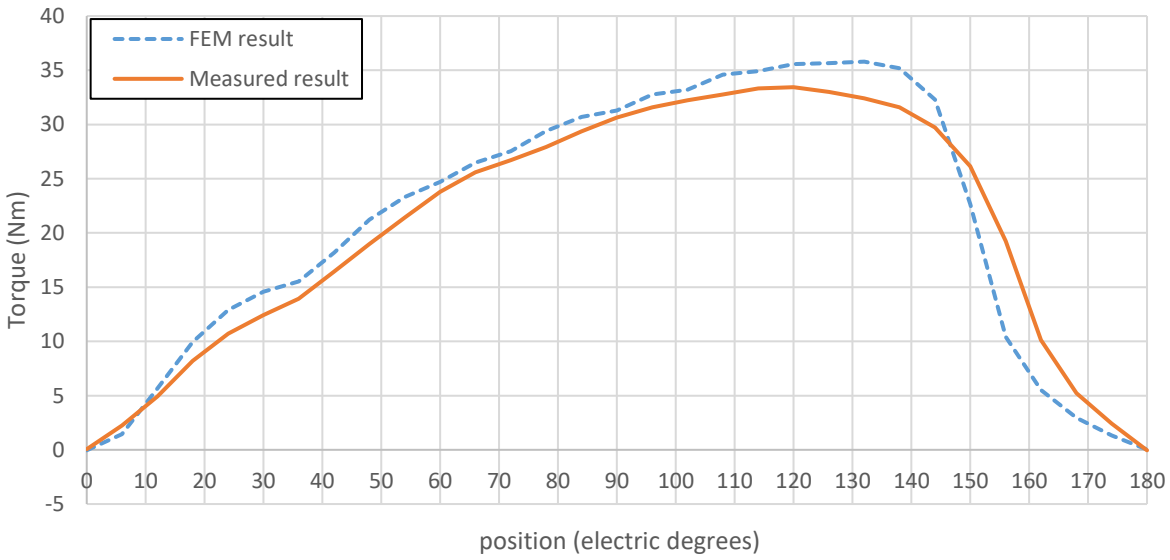

Figure 0-26 Static torque comparison between experimental test and 2D FEM

In order to consider the effects of temperature rise on the winding resistance during the conducting period, the winding resistance was calculated, based on the static value of the voltage and current trace during the excitation periods: its value was 0.76

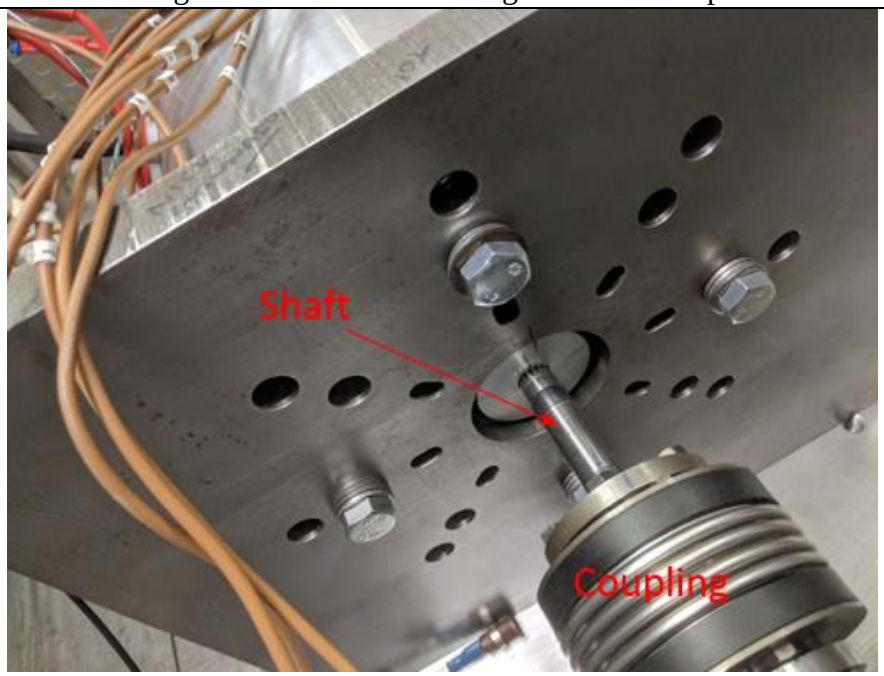

Figure 0-27 The connection between the extended shaft and the coupling

6.3.3 Rotation Test

The mechanical test was intended to exam the robustness of the rotor structure during operation. According to Section 5.2, the major challenge for the rotor structure was the centrifugal force under high-speed spinning. To counter this, the prototype was connected to a load machine with a maximum speed of 3,500 rpm, while a torque transducer was used to provide early warning if any abnormality occurred (see Figure 0-28).

Figure 0-28 The prototype machine was connected to a load machine and a torque transducer

In order to consider the effects of temperature rise on the winding resistance during the conducting period, the winding resistance was calculated, based on the static value of the voltage and current trace during the excitation periods: its value was 0.76

For safety reasons, the bench was covered by a stainless-steel guard to offer basic protection, in case of rotor-structure failure and its subsequent adverse effects (see Figure 0-29).

Figure 0-29 The bench table is covered with a stainless-steel protective guard

During the test, noise and vibration was observed to be significant once the rotational speed rose above 2,000 rpm. However, the reading on the torque transducer did not reveal any mechanical contact between the rotor and stator. As can be seen from Figure 0-30, the power measured by the torque transducer almost linearly increases with the rotational speed, while the torque value is distributed around 0.25 Nm during the full-speed range.

In order to consider the effects of temperature rise on the winding resistance during the conducting period, the winding resistance was calculated, based on the static value of the voltage and current trace during the excitation periods: its value was 0.76

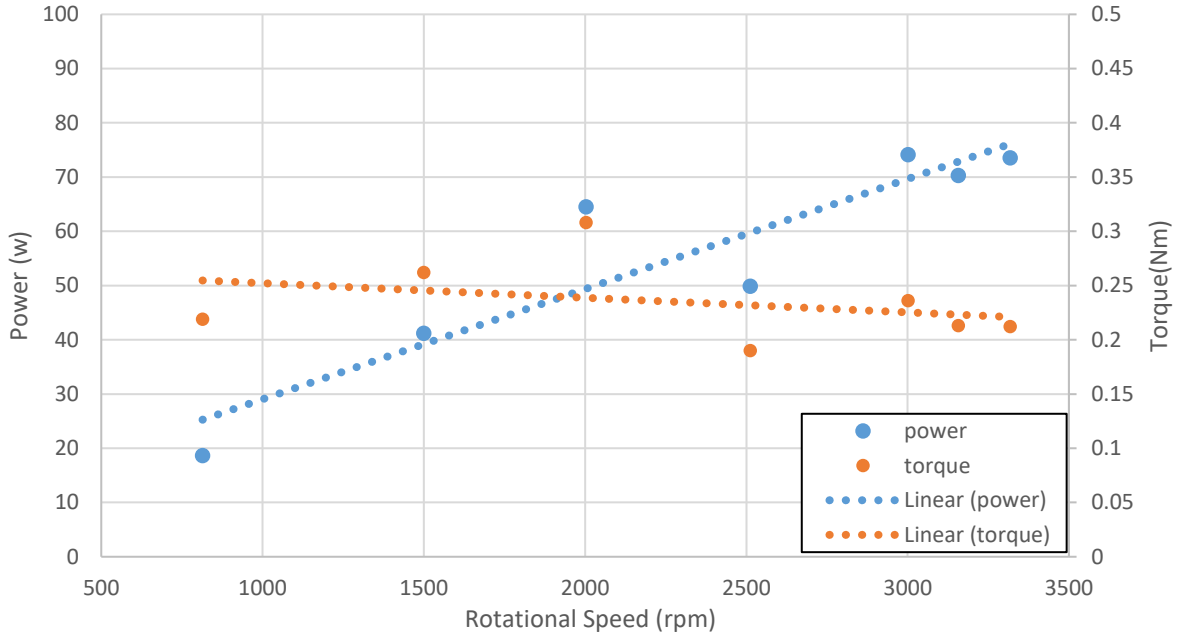

Figure 0-30 Torque and power readings taken from the torque transducer indicates no catching between rotor and stator during the accelaration process

After discussion with the mechanical technicians in the University, it was believed that the vibration might be attributed to the absence of a balancing process and voids in the epoxy (see Figure 0-31). Consequently, there was no indication that the rotor structure would not be robust enough under the centrifugal force in this condition.

In order to consider the effects of temperature rise on the winding resistance during the conducting period, the winding resistance was calculated, based on the static value of the voltage and current trace during the excitation periods: its value was 0.76

Figure 0-31 The void is randomly distributed in the epoxy parts as a manufacturing faliure; this could lead to an unbalanced force being imposed on the shaft and bearings

6.4 Conclusion

In this Chapter, the manufacturing process and experimental test of the prototype machine have been described in detail:

- Considering the equipment from the university's mechanical workshop, several revisions of the prototype design were made for construction convenience:
    1. To enhance the assembly precision and mechanical robustness, it was decided that the rotor segments would be connected by very thin bridges along the inner airgap.
    2. Due to the limited machining accuracy of the PEEK sheet, the rotor support structure was to be replaced by epoxy potting compound and reinforced carbon fibre rod.
    3. A trade-off was made in the stator-pole design by eliminating the overhang near the airgap to allow for a higher fill factor in the winding technique.

In order to consider the effects of temperature rise on the winding resistance during the conducting period, the winding resistance was calculated, based on the static value of the voltage and current trace during the excitation periods: its value was 0.76

- The prototype machine was a double-stator SRM, and its structure was relatively complicated compared to a conventional SRM. These differences in the construction process have been described in detail in this chapter:
    1. The inner stator was a unique structure, only existing in double-stator SRMs. The geometry of its lamination core was similar to the rotor lamination in a conventional rotor. However, the inner stator was mounted and fixed to a stationary hollow shaft, which not only locked the lamination in both the axial and tangential directions but also provided a path for the stator winding and heat flux.
    2. This machine initially consisted of pre-wound bobbins prior to installation of the stator slot. There were three different bobbins used during this stage (one for the inner and another two for the outer stator), and a fill factor of 50% was obtained.
    3. The slot for the support structure in the rotor lamination was enclosed by a redundant bridge at the beginning to allow for the filling process of the epoxy compound. Once the epoxy was cured, this redundant bridge was removed by a lathe. This process would guarantee a precise rotor-diameter tolerance.
- The prototype machine was experimentally tested in the lab; a process which can be divided into three steps:
    1. Static pulse test: during this test, the machine was fixed on the bench table while the rotor was connected to the rotary table. The electromagnetic characteristics were derived from the current and voltage data at every 0.1 mechanical degrees. The test results were compared to the 2D FEM data and considered to be close to expectations (the gap is less than 10% at a peak current density of 20A/mm^2).
    2. Static torque test: the static torque data was collected at a current density of 20 A/mm^2 during a full electric cycle. Due to the shaft being very thin, a distortion of the torque-angle curve was found between the test and simulation results.
    3. Mechanical test: during this test, the prototype machine was connected to a load machine to verify the robustness of the rotor structure under centrifugal force.

Chapter 7. Conclusion and Future Work

This thesis has described the development of a four-phase double-stator SRM with a mutually coupled-winding configuration and a straight stator-pole configuration. The work comprised a number of steps:

- Firstly, the background literature relating to SRM torque-capability enhancement was reviewed in Chapter 2. Compared with the SRSRM, which is considered a successful novel SRM in terms of torque capability, the conventional SRM was proven to have its own advantages. Methods to improve the torque production of a conventional SRM include increasing the number of strokes per revolution and the energy conversion per stroke. The former indicates that higher phase numbers may give better torque capability and thus requires further analysis; meanwhile the latter suggests that modification of the flux-path in the iron-core could be considered. Clues to a proper solution were inspired by mutually coupled and double-stator SRMs.

- The phase number of a conventional SRM was investigated in Chapter 3. An analytical torque equation was introduced to compare the torque capability for 6/4, 8/6, 10/8, 12/10 SRMs with a condition in which the iron-core is assumed to have infinite permeability. After comparing the analytical results with the results of the 2D FEA, it was demonstrated that the higher phase number will benefit higher torque production when the iron core-reluctance tended to dominant the flux path. Further analysis was carried out between 6/4 and 8/6 SRMs using a semi-linear psi-I model. The results were subsequently verified by 2D FEA, which confirmed that an 8/6 SRM would provide a higher torque-per-unit copper loss than a 6/4 SRM, especially when operating in a saturated condition. It also suggested that the four-phase machine should have a relatively large split ratio.

- Based on the four-phase SRM, the proposed SRM design achieved clarity in Chapter 4. The mutually coupled winding configuration was proven capable of enhancing the torque production of the four-phase SRM. The higher-rotor pole-number concept was found to potentially contradict the four-phase SRM, as it did not prefer a saturated condition. Then, a 16/12 MCSRM was designed and compared with Chiba's 18/12 SRM which is widely considered a successful example of SRM design for automotive traction. The results showed that the 16/12 MCSRM could provide torque capability comparable

to that of the 18/12 SRM, while generating significantly lower copper loss and slightly lower iron loss. Moreover, the double-stator structure was analysed using a simplified linear model, revealing this structure would benefit from a similar design and operating condition to the four-phase MCSRM. Results of the transient 2D FEM confirmed that the 16/12 DSSRM with a mutually coupled-winding configuration had a significant advantage regarding the torque-to-copper loss ratio when compared with the previous 16/12 MCSRM.

- A specific prototype design has been developed (Chapter 5). The size of the prototype machine was selected to provide a fair comparison with an SRSRM constructed at Newcastle University. To avoid eddy current loss in the rotor support construction, several novel structures and materials were investigated. The final decision on the rotor shape was taken by considering both mechanical and electromagnetic performance. Once the basic design was confirmed, further optimisation processes were carried out using a genetic algorithm, which was briefly described. The simulation results revealed that the optimised design could provide comparable torque production to that of the SRSRM and had a significantly smaller copper loss and VA requirement. In addition, thermal analysis was conducted using FEM and demonstrated that the DSSRM had adequate cooling performance due to the extra-heat-dissipation path at the inner stator. Thus, the thermal issue was not a concern.

- For convenience and feasibility of manufacturing, the final design of the prototype was modified (Chapter 6). The rotor structure was enhanced by reserving a slender bridge linking the rotor poles together and the rotor support was reinforced with carbon-fibre rods. Moreover, the stator-pole tip was trimmed to fit the pre-wound coil technique. It is certain that these modifications caused negative effects on the electromagnetic performance to a certain extent, but with a higher fill factor achieved than in the original design, the overall performance of the prototype was still be able to meet expectations. The electromagnetic performance of the completed prototype was verified by a static-pulse test and, finally, it was possible to determine that its performance was relatively close to expectations (with nearly no difference in the linear condition and 10% lower at a current density of 20 A/mm^2). Finally, a mechanical test examined the rotor robustness under centrifugal force at 3,500 rpm, proving that the novel rotor support was able to provide the containment required.

In overall conclusion, this project consisted of a series of investigations and developments of a four-phase mutually coupled DSSRM. Based on analysis and test, it was proven that this machine is able to offer a relatively high torque-to-loss ratio under heavy load conditions, while not consuming a large number of volt-amperes compared with other novel SRMs of similar torque density. Consequently, this machine type has the potential to become a magnet-free solution in the large-scale electrification of automotive traction in the future.

Several challenges remain to be addressed, including the investigation of the use of bamboo as a more eco-friendly and affordable material in the rotor support; further analysis and optimisation of this particular machine concept over the full-speed range and under a variety of load conditions; and a study to expand the design into a six-phase model, which could be driven by a novel converter developed from a standard three-phase full-bridge inverter[111].

Appendix 1 Script File for Machine Design and Optimisation

This appendix provides the Visual Basic script that were used to build SRM models and calculate critical parameter in Infolytica software (MagNet and OptiNet)

A1.1 Script File for Conventional SRM

```
' MagNet 64-bit Version 7.4.1.4 (2012/11/16 03:06 R2012-4)
' Computer: EEEJWPG01, User: b3015239
' Time: 28/11/2014 16:31:26
Call SetLocale("en-us")
Dim Name, Control(0)
Dim xr0(30), yr0(30), xr1(30), yr1(30), xs2(30), ys2(30), xs3(30), ys3(30) , xc(30), yc(30) , xc2(30), yc2(30)
Dim stator, statslotr, betaS, betaR, statorpolepitch, gap, rotorpolepitch
Dim r0, r1, r2, r3, r4, r5, s, AMP, Length, alphar, alphas, theta
Dim lcore, lpole, halfpole, statpole, statarc2, statarc3, halfwidth, polewidth, ext
Dim I, ns, nr, Nt
Dim z0, L, a, b, d, position
Dim CoilMaterial, CoilName, I1, I2, I3, I4, I5, turns, IPEAK
Dim Errorflag
Dim MN6, Doc, Con, Cur, Sol
Dim Dir, File, Material, Unit
Dim x0, y0, X1, Y1, Z1, X2, Y2, Z2, X3, Y3, Z3
Dim Pi, rad
Dim transX0, transY0, transR


nr=4
ns=6
r1=4.5 'rotor radius(bore)
gap=0.025
stator=7.5 'stator radius (outer)
betar=36 '(rotor pole arc in degrees)
r0=3 'radius of rotor core
rotorpolepitch=360/nr
rc=r1+gap
statorpolearc=0.418
  Pi = 3.14159265358979
```

```
  rad = Pi / 180       'Converts degrees to radians
alphar = betaR / rotorpolepitch      'Ratio of rotor pole arc to pole pitch

  alphas = statorpolearc/ (pi/3)
theta = 0         'Angular position
'calculate stator pole length and stator core depth
lcore = 1.03 'back iron sickness
lpole = stator-lcore - r1 - gap 'rotor pole length

'Construct stator
r2 = r1 + gap
r3 = r2 + lpole
r4 = r3 + lcore
halfpole = Pi / ns
statpole = 2 * halfpole
statarc2 = alphas * halfpole
halfwidth = Sin(statarc2) * r2
polewidth = 2 * halfwidth
s = halfwidth / r3
statarc3 = Atn(s / Sqr(1 - s * s))
For I = 0 To ns
    beta1 = -statarc2 + I * statpole
    beta2 = statarc2 + I * statpole
    xs2(2 * I + 1) = r2 * Cos(beta1)
    ys2(2 * I + 1) = r2 * Sin(beta1)
    xs2(2 * I + 2) = r2 * Cos(beta2)
    ys2(2 * I + 2) = r2 * Sin(beta2)
Next
For I = 0 To ns + 1
    beta1 = -statarc3 + I * statpole
    beta2 = statarc3 + I * statpole
    xs3(2 * I + 1) = r3 * Cos(beta1)
    ys3(2 * I + 1) = r3 * Sin(beta1)
    xs3(2 * I + 2) = r3 * Cos(beta2)
    ys3(2 * I + 2) = r3 * Sin(beta2)
Next
For I = 0 To ns
```

```
    Call getDocument().getView().newArc(0, 0, xs2(2 * I + 1), ys2(2 * I + 1),
xs2(2 * I + 2), ys2(2 * I + 2))

Next

For I = 0 To ns

    Call getDocument().getView().newArc(0, 0, xs3(2 * I + 2), ys3(2 * I + 2),
xs3(2 * I + 3), ys3(2 * I + 3))

Next

For I = 1 To 2 * ns + 1

    Call getDocument().getView().newLine(xs2(I), ys2(I), xs3(I), ys3(I))

Next

Call getDocument().getView().newCircle(0, 0, r4)


ReDim ArrayOfValues(0)

    ArrayOfValues(0) = infoSliceSurface

   Call  getDocument().getView().selectAt(0,  r4  *  0.99,  infoSetSelection,
ArrayOfValues)

    ArrayOfValues(0) = "Stator"

Call     getDocument().getView().makeComponentInALine(0,     ArrayOfValues,
"Name=M270-35A")


'Construct rotor

halfpole = Pi / nr

rotpole = 2 * halfpole

rotarc1 = alphar * halfpole

s = Sin(rotarc1) * r1 / r0

rotarc0 = Atn(s / Sqr(1 - s * s))

For I = 0 To nr

    beta1 = rad * theta - rotarc1 + I * rotpole

    beta2 = rad * theta + rotarc1 + I * rotpole

    xr1(2 * I + 1) = r1 * Cos(beta1)

    yr1(2 * I + 1) = r1 * Sin(beta1)

    xr1(2 * I + 2) = r1 * Cos(beta2)

    yr1(2 * I + 2) = r1 * Sin(beta2)

Next

For I = 0 To nr + 1

    beta1 = rad * theta - rotarc0 + I * rotpole

    beta2 = rad * theta + rotarc0 + I * rotpole

    xr0(2 * I + 1) = r0 * Cos(beta1)

    yr0(2 * I + 1) = r0 * Sin(beta1)
```

```
    xr0(2 * I + 2) = r0 * Cos(beta2)

    yr0(2 * I + 2) = r0 * Sin(beta2)

Next

For I = 0 To nr

    Call getDocument().getView().newArc(0, 0, xr1(2 * I + 1), yr1(2 * I + 1),
xr1(2 * I + 2), yr1(2 * I + 2))

Next

For I = 0 To nr

    Call getDocument().getView().newArc(0, 0, xr0(2 * I + 2), yr0(2 * I + 2),
xr0(2 * I + 3), yr0(2 * I + 3))

Next

Call getDocument().getView().newCircle(0, 0, 1.4)

For I = 1 To 2 * nr + 1

    Call getDocument().getView().newLine(xr1(I), yr1(I), xr0(I), yr0(I))

      next

ReDim ArrayOfValues(0)

    ArrayOfValues(0) = infoSliceSurface

    Call  getDocument().getView().selectAt(0,  0.99*r0,  infoSetSelection,
ArrayOfValues)

    ArrayOfValues(0) = "Rotor"

    Call   getDocument().getView().makeComponentInALine(0,   ArrayOfValues,
"Name=M270-35A")


'construct coils

For I = 0 To ns

    beta1 = 0.5*statpole + I * statpole

xc(i) = r3 * Cos(beta1)

    yc(i) = r3 * Sin(beta1)

next

For I = 0 To ns

    Call getDocument().getView().newLine(0, 0, xc(I), yc(I))

Next

Call getDocument().getView().newCircle(0, 0, rc)


For I = 0 To ns

    beta1 = 0.4*statpole + I * statpole

    beta2 = 0.6*statpole + I * statpole

    xc2(2 * I + 1) = 0.9*r3 * Cos(beta1)

    yc2(2 * I + 1) = 0.9*r3 * Sin(beta1)
```

```
    xc2(2 * I + 2) = 0.9*r3 * Cos(beta2)

    yc2(2 * I + 2) = 0.9*r3 * Sin(beta2)

Next

for i=1 to 2*ns

ReDim ArrayOfValues(0)

    ArrayOfValues(0) = infoSliceSurface

   Call getDocument().getView().selectAt(xc2(i) , yc2(i) , infoSetSelection,
ArrayOfValues)

  segmentname="conductor"&i

    ArrayOfValues(0) = segmentname

Call     getDocument().getView().makeComponentInALine(0,     ArrayOfValues,
"Name=Copper: 5.77e7 Siemens/meter")

next


'air

Call getDocument().getView().selectAll(infoSetSelection, Array(infoSliceLine,
infoSliceArc))

Call getDocument().getView().deleteSelection()

rrotorair=r1+0.5*gap

rrotorvirtualair=r1+0.25*gap

rstatorair=r1+0.75*gap

routerair=1.25*stator

Call getDocument().getView().newCircle(0, 0, rrotorair)

Call getDocument().getView().newCircle(0, 0, rrotorvirtualair)

Call getDocument().getView().newCircle(0, 0, rstatorair)

Call getDocument().getView().newCircle(0, 0, routerair)

ReDim ArrayOfValues(0)

    ArrayOfValues(0) = infoSliceSurface

   Call    getDocument().getView().selectAt(0,rrotorvirtualair-0.1*gap    ,
infoSetSelection, ArrayOfValues)

    ArrayOfValues(0) =  "rotor virtual air"

Call     getDocument().getView().makeComponentInALine(0,     ArrayOfValues,
"Name=Virtual Air")

ReDim ArrayOfValues(0)

    ArrayOfValues(0) = infoSliceSurface

   Call        getDocument().getView().selectAt(0,rrotorair-0.1*gap       ,
infoSetSelection, ArrayOfValues)

    ArrayOfValues(0) =  "rotor air"

Call     getDocument().getView().makeComponentInALine(0,     ArrayOfValues,
"Name=AIR")
```

```
ReDim ArrayOfValues(0)

    ArrayOfValues(0) = infoSliceSurface

   Call       getDocument().getView().selectAt(0,rstatorair-0.1*gap       ,
infoSetSelection, ArrayOfValues)

    ArrayOfValues(0) =  "stator air"

Call     getDocument().getView().makeComponentInALine(0,     ArrayOfValues,
"Name=AIR")

ReDim ArrayOfValues(0)

    ArrayOfValues(0) = infoSliceSurface

   Call  getDocument().getView().selectAt(0,rs-0.1*gap  ,  infoSetSelection,
ArrayOfValues)

    ArrayOfValues(0) =  "stator virtual air"

Call   getDocument().getView().makeComponentInALine(0,   ArrayOfValues,   "
Name=Virtual Air")


' rotor

Call getDocument().getView().selectObject("Rotor", infoToggleInSelection)

Call     getDocument().getView().selectObject("rotor     virtual     air",
infoToggleInSelection)

Call getDocument().getView().selectObject("rotor air", infoToggleInSelection)

REDIM ArrayOfValues(2)

ArrayOfValues(0)= "Rotor"

ArrayOfValues(1)= "rotor virtual air"

ArrayOfValues(2)= "rotor air"

Call getDocument().makeMotionComponent(ArrayOfValues)

Call getDocument().setMotionSourceType("Motion#1", infoVelocityDriven)

Call getDocument().beginUndoGroup("Set Motion Component", true)

Call getDocument().setMotionRotaryCenter("Motion#1", Array(0, 0, 0))

Call getDocument().setMotionRotaryAxis("Motion#1", Array(0, 0, 1))

Call getDocument().endUndoGroup()


'coils

n=2*ns

Call getDocument().getView().selectObject("conductor1", infoSetSelection)

Call                    getDocument().getView().selectObject("conductor"&n,
infoToggleInSelection)

 ReDim ArrayofValues(1)

    ArrayofValues(0) = "conductor1"

    ArrayofValues(1) = "conductor"&n

Call getDocument().makeSimpleCoil(1, ArrayOfValues)
```

```
    i = 2
    Do While i < n
        ArrayofValues(0) = "conductor"&i
        ArrayofValues(1) = "conductor"&i + 1
        Call getDocument().makeSimpleCoil(1, ArrayofValues)
        i = i + 2
    Loop
      for i=1 to ns/2
      s=2*i+1
    Call getDocument().reverseCoilSide("Coil#"&s, 1)
    Call getDocument().reverseCoilSide("Coil#"&s, 2)
    next


    'For i = 1 To ns / 2
       '  Call  getDocument().setParameter("Coil#"  &  i,  "NumberOfTurns",
"%n_turns", Con.infoNumberParameter)
    'Next i
```

A1.2 Script File for DSSRM

```
' MagNet 64-bit Version 7.4.1.4 (2012/11/16 03:06 R2012-4)
' Computer: EEEJWPG01, User: b3015239
' Time: 28/11/2014 16:31:26
Call SetLocale("en-us")
Dim Name, Control(0)
Dim xr0(60), yr0(60), xsi1(60), ysi1(60), xs2(60), ys2(60), xs3(60),
ys3(60)    ,xs4(60),    ys4(60)    ,    xc(60),    yc(60)    ,    xc2(60),
yc2(60),xr1(60),xr2(60),yr1(60),yr2(60),xc3(60),yc3(60),xr05(60),yr05(60)
Dim stator, statslotr, betaS, betaR, statorpolepitch, gap,
innerstatorpolepitch
Dim r0, si1, r2, r3, r4, r5, s, AMP, Length, alphar, alphas,
theta ,rro,rri,airgap,rotorpole,rotorinnerarc,rotorouterarc
Dim lcore, lpole, halfpole, statpole, statarc2, statarc3, halfwidth,
polewidth, ext
Dim I, ns, nsi, Nt
Dim z0, L, a, b, d, position
Dim CoilMaterial, CoilName, I1, I2, I3, I4, I5, turns, IPEAK
Dim Errorflag
Dim MN6, Doc, Con, Cur, Sol
Dim Dir, File, Material, Unit
```

```
Dim x0, y0, X1, Y1, Z1, X2, Y2, Z2, X3, Y3, Z3
Dim Pi, rad
Dim transX0, transY0, transR
nr=12
nsi=16
ns=16
spilt=0.813236321065956
gap=0.017/(269/210) ' the space for air-gap and rotor
airgap=0.0003
stator=0.105 'stator radius (outer)
StatorToothArctoPitchinner=0.438380087625864
si1=stator*spilt-gap 'inner stator radius(bore)without air gap
betar=360/ns*StatorToothArctoPitchinner'(inner stator pole arc in degrees)

isp=0.02662/(269*1/210) 'inner stator pole length
r0=si1-isp      'radius of inner stator core
innerstatorpolepitch=360/nsi
rc=si1+gap
Pi = 3.14159265358979
statorpolearc=(2*pi/ns)*StatorToothArctoPitchinner
  rad = Pi / 180       'Converts degrees to radians
alphar = betaR / innerstatorpolepitch       'Ratio of inner stator pole arc
to pole pitch
  alphas = statorpolearc/ (pi/(ns/2))
theta = 0         'Angular position

'calculate stator pole length and stator core depth
lcore = 0.012*0.95/(269/210) 'back iron sickness

lpole = stator-lcore -si1-gap 'outer stator pole length
 msgbox lpole

'Construct stator
r2 = si1+gap  'stator inner radius
r3 = r2 + lpole'statorpole outer radius
r4 = stator
halfpole = Pi / ns
statpole = 2 * halfpole
```

```
statarc2 = alphas * halfpole
halfwidth = Sin(statarc2) * r2
polewidth = 2 * halfwidth
s = halfwidth *1.3/1.3/ r3
'r25=(0.6*r2+0.4*r3)
's1= halfwidth*1.2/r25
statarc3 = Atn(s / Sqr(1 - s * s))
statarc4 = Atn(s1 / Sqr(1 - s1 * s1))
For I = 0 To ns
    beta1 = -statarc2 + I * statpole
    beta2 = statarc2 + I * statpole
    xs2(2 * I + 1) = r2 * Cos(beta1)
    ys2(2 * I + 1) = r2 * Sin(beta1)
    xs2(2 * I + 2) = r2 * Cos(beta2)
    ys2(2 * I + 2) = r2 * Sin(beta2)
Next
For I = 0 To ns + 1
    beta1 = -statarc3 + I * statpole
    beta2 = statarc3 + I * statpole
    xs3(2 * I + 1) = r3 * Cos(beta1)
    ys3(2 * I + 1) = r3 * Sin(beta1)
    xs3(2 * I + 2) = r3 * Cos(beta2)
    ys3(2 * I + 2) = r3 * Sin(beta2)
Next
For I = 0 To ns
    beta1 = -statarc4 + I * statpole
    beta2 = statarc4 + I * statpole
    xs4(2 * I + 1) = r25 * Cos(beta1)
    ys4(2 * I + 1) = r25 * Sin(beta1)
    xs4(2 * I + 2) = r25 * Cos(beta2)
    ys4(2 * I + 2) = r25 * Sin(beta2)
Next
For I = 0 To ns
    Call getDocument().getView().newArc(0, 0, xs2(2 * I + 1), ys2(2 * I + 1),
xs2(2 * I + 2), ys2(2 * I + 2))
Next
For I = 0 To ns
```

```
    Call getDocument().getView().newArc(0, 0, xs3(2 * I + 2), ys3(2 * I + 2),
xs3(2 * I + 3), ys3(2 * I + 3))

Next

For I = 1 To 2 * ns + 1

    Call getDocument().getView().newLine(xs2(I), ys2(I), xs3(I), ys3(I))

Next

'For I = 1 To 2 * ns + 1

  '  Call getDocument().getView().newLine(xs4(I), ys4(I), xs3(I), ys3(I))

'Next

Call getDocument().getView().newCircle(0, 0, r4)


ReDim ArrayOfValues(0)

    ArrayOfValues(0) = infoSliceSurface

   Call  getDocument().getView().selectAt(0,  r4  *  0.99,  infoSetSelection,
ArrayOfValues)

    ArrayOfValues(0) = "Stator"

Call     getDocument().getView().makeComponentInALine(0,     ArrayOfValues,
"Name=M270-35A")


'Construct inner stator

halfpole = Pi / nsi

rotpole = 2 * halfpole

rotarc1 = alphar * halfpole

s = Sin(rotarc1) * si1*1.2*(1/1.2) / r0

r05=(0.2*r0+0.8*si1)

's1=Sin(rotarc1) * si1*1.4 /r05

rotarc0 = Atn(s / Sqr(1 - s * s))

'rotarc05 = Atn(s1 / Sqr(1 - s1 * s1))

For I = 0 To nsi

    beta1 = rad * theta - rotarc1 + I * rotpole

    beta2 = rad * theta + rotarc1 + I * rotpole

    xsi1(2 * I + 1) = si1 * Cos(beta1)

    ysi1(2 * I + 1) = si1 * Sin(beta1)

    xsi1(2 * I + 2) = si1 * Cos(beta2)

    ysi1(2 * I + 2) = si1 * Sin(beta2)

Next

For I = 0 To nsi + 1

    beta1 = rad * theta - rotarc0 + I * rotpole
```

```
    beta2 = rad * theta + rotarc0 + I * rotpole

    xr0(2 * I + 1) = r0 * Cos(beta1)

    yr0(2 * I + 1) = r0 * Sin(beta1)

    xr0(2 * I + 2) = r0 * Cos(beta2)

    yr0(2 * I + 2) = r0 * Sin(beta2)

Next

'For I = 0 To nsi

  '  beta1 = rad * theta - rotarc05 + I * rotpole

   ' beta2 = rad * theta + rotarc05 + I * rotpole

   ' xr05(2 * I + 1) = r05 * Cos(beta1)

   ' yr05(2 * I + 1) = r05 * Sin(beta1)

   ' xr05(2 * I + 2) = r05 * Cos(beta2)

   ' yr05(2 * I + 2) = r05 * Sin(beta2)

'Next

For I = 0 To nsi

    Call getDocument().getView().newArc(0, 0, xsi1(2 * I + 1), ysi1(2 * I +
1), xsi1(2 * I + 2), ysi1(2 * I + 2))

Next

For I = 0 To nsi

    Call getDocument().getView().newArc(0, 0, xr0(2 * I + 2), yr0(2 * I + 2),
xr0(2 * I + 3), yr0(2 * I + 3))

Next


Call getDocument().getView().newCircle(0, 0, 0.015)

For I = 1 To 2 * nsi + 1

    Call getDocument().getView().newLine(xsi1(I), ysi1(I), xr0(I), yr0(I))

      next

'For I = 1 To 2 * nsi + 1

  '  Call getDocument().getView().newLine(xr05(I), yr05(I), xr0(I), yr0(I))

      'next

ReDim ArrayOfValues(0)

    ArrayOfValues(0) = infoSliceSurface

    Call  getDocument().getView().selectAt(0,  0.99*r0,  infoSetSelection,
ArrayOfValues)

    ArrayOfValues(0) = "inner stator"

    Call   getDocument().getView().makeComponentInALine(0,   ArrayOfValues,
"Name=M270-35A")


'construct coils
```

```
For I = 0 To ns
    beta1 = 0.5*statpole + I * statpole
xc(i) = r3 * Cos(beta1)
    yc(i) = r3 * Sin(beta1)
next
For I = 0 To ns
    Call getDocument().getView().newLine(0, 0, xc(I), yc(I))
Next
Call getDocument().getView().newCircle(0, 0, rc)
Call getDocument().getView().newCircle(0, 0, si1)
For I = 0 To ns
    beta1 = 0.4*statpole + I * statpole
    beta2 = 0.6*statpole + I * statpole
    xc2(2 * I + 1) = 0.95*r3 * Cos(beta1)
    yc2(2 * I + 1) = 0.95*r3 * Sin(beta1)
    xc2(2 * I + 2) = 0.95*r3 * Cos(beta2)
    yc2(2 * I + 2) = 0.95*r3 * Sin(beta2)
Next
For I = 0 To ns
    beta1 = 0.4*statpole + I * statpole
    beta2 = 0.6*statpole + I * statpole
    xc3(2 * I + 1) = 0.95*si1 * Cos(beta1)
    yc3(2 * I + 1) = 0.95*si1 * Sin(beta1)
    xc3(2 * I + 2) = 0.95*si1* Cos(beta2)
    yc3(2 * I + 2) = 0.95*si1 * Sin(beta2)
Next
for i=1 to 2*ns
ReDim ArrayOfValues(0)
    ArrayOfValues(0) = infoSliceSurface


   Call getDocument().getView().selectAt(xc2(i) , yc2(i) , infoSetSelection,
ArrayOfValues)
  segmentname="conductor"&i
    ArrayOfValues(0) = segmentname
Call     getDocument().getView().makeComponentInALine(0,     ArrayOfValues,
"Name=Ideal Copper")
next
```

```
for i=1 to 2*ns

ReDim ArrayOfValues(0)

    ArrayOfValues(0) = infoSliceSurface


   Call getDocument().getView().selectAt(xc3(i) , yc3(i) , infoSetSelection,
ArrayOfValues)

  segmentname="conductorinner"&i

    ArrayOfValues(0) = segmentname

Call     getDocument().getView().makeComponentInALine(0,     ArrayOfValues,
"Name=Ideal Copper")

next

'coils

n=2*ns

Call getDocument().getView().selectObject("conductor1", infoSetSelection)

Call                    getDocument().getView().selectObject("conductor"&n,
infoToggleInSelection)

 ReDim ArrayofValues(1)

    ArrayofValues(0) = "conductor1"

    ArrayofValues(1) = "conductor"&n

Call getDocument().makeSimpleCoil(1, ArrayOfValues)

    i = 2

    Do While i < n

        ArrayofValues(0) = "conductor"&i

        ArrayofValues(1) = "conductor"&i + 1

        Call getDocument().makeSimpleCoil(1, ArrayofValues)

        i = i + 2

    Loop

      for i=1 to ns/2

      s=2*i-1

    Call getDocument().reverseCoilSide("Coil#"&s, 1)

    Call getDocument().reverseCoilSide("Coil#"&s, 2)

    next


      O_turns=1

    For i = 1 To ns

       Call   getDocument().setParameter("Coil#"   &   i,   "NumberOfTurns",
"%O_turns", infoNumberParameter)

         'i=i+1

    Next
```

```
n=2*ns

Call                 getDocument().getView().selectObject("conductorinner1",
infoSetSelection)

Call                getDocument().getView().selectObject("conductorinner"&n,
infoToggleInSelection)

 ReDim ArrayofValues(1)

    ArrayofValues(0) = "conductorinner1"

    ArrayofValues(1) = "conductorinner"&n

Call getDocument().makeSimpleCoil(1, ArrayOfValues)


    i = 2

    Do While i < n

        ArrayofValues(0) = "conductorinner"&i

        ArrayofValues(1) = "conductorinner"&i + 1

        Call getDocument().makeSimpleCoil(1, ArrayofValues)

        i = i + 2

    Loop

      for i=9 to ns

      s=2*i-1

    Call getDocument().reverseCoilSide("Coil#"&s, 1)

    Call getDocument().reverseCoilSide("Coil#"&s, 2)

   next

   I_turns=1

   For i = 17 To 2*ns

       Call   getDocument().setParameter("Coil#"   &   i,   "NumberOfTurns",
"%I_turns", infoNumberParameter)

         'i=i+1

    Next

 ' delete lines

Call getDocument().getView().selectAll(infoSetSelection, Array(infoSliceLine,
infoSliceArc))

Call getDocument().getView().deleteSelection

' construct rotor

rro=r2-airgap

rri=si1+airgap

rotorouterarc=statorpolearc

rotorinnerarc=betaR*2*pi/360

rotorpole=2*3.14159265358979/nr

For i= 0 to nr
```

```
      beta1= -rotorinnerarc/2+i*rotorpole
      beta2= rotorinnerarc/2+i*rotorpole
       xr1(2 * I + 1) = rri * Cos(beta1)
    yr1(2 * I + 1) = rri * Sin(beta1)
    xr1(2 * I + 2) = rri * Cos(beta2)
    yr1(2 * I + 2) = rri * Sin(beta2)
Next
For i= 0 to nr
      beta1= -rotorouterarc/2+i*rotorpole
      beta2= rotorouterarc/2+i*rotorpole
       xr2(2 * I + 1) = rro * Cos(beta1)
    yr2(2 * I + 1) = rro * Sin(beta1)
    xr2(2 * I + 2) = rro * Cos(beta2)
    yr2(2 * I + 2) = rro * Sin(beta2)
next
For I = 0 To nr
    Call getDocument().getView().newArc(0, 0, xr1(2 * I + 1), yr1(2 * I + 1),
xr1(2 * I + 2), yr1(2 * I + 2))
Next
For I = 0 To nr
    Call getDocument().getView().newArc(0, 0, xr2(2 * I + 1), yr2(2 * I + 1),
xr2(2 * I + 2), yr2(2 * I + 2))
Next
For I = 1 To 2 * nr + 1
    Call getDocument().getView().newLine(xr1(I), yr1(I), xr2(I), yr2(I))
Next
   'air
Call getDocument().getView().newCircle(0, 0, (r2+rro)/2)
Call getDocument().getView().newCircle(0, 0, (rri+si1)/2)
Call getDocument().getView().newCircle(0, 0, (r2+(r2+rro)/2)/2)
Call getDocument().getView().newCircle(0, 0, (si1+(rri+si1)/2)/2)
Call getDocument().getView().newCircle(0, 0, (rro+(r2+rro)/2)/2)
Call getDocument().getView().newCircle(0, 0, (rri+(rri+si1)/2)/2)
'Call getDocument().getView().newCircle(0, 0, si1)
Call getDocument().getView().newCircle(0, 0, 1.2*stator)
ReDim ArrayOfValues(0)
    ArrayOfValues(0) = infoSliceSurface
```

```
   Call    getDocument().getView().selectAt(0,((r2+(r2+rro)/2)/2+r2)/2    ,
infoSetSelection, ArrayOfValues)

    ArrayOfValues(0) =  "outer stator  virtual air"

      Call  getDocument().getView().makeComponentInALine(0,  ArrayOfValues,
"Name=Virtual Air")

ReDim ArrayOfValues(0)

    ArrayOfValues(0) = infoSliceSurface

   Call getDocument().getView().selectAt(0,((r2+(r2+rro)/2)/2+(r2+rro)/2)/2 ,
infoSetSelection, ArrayOfValues)

    ArrayOfValues(0) =  "outer stator  air"

      Call  getDocument().getView().makeComponentInALine(0,  ArrayOfValues,
"Name=AIR")

ReDim ArrayOfValues(0)

    ArrayOfValues(0) = infoSliceSurface

   Call
getDocument().getView().selectAt(0,((r2+rro)/2+(rro+(r2+rro)/2)/2)/2      ,
infoSetSelection, ArrayOfValues)

    ArrayOfValues(0) =  "outer rotor  air"

      Call  getDocument().getView().makeComponentInALine(0,  ArrayOfValues,
"Name=AIR")

ReDim ArrayOfValues(0)

    ArrayOfValues(0) = infoSliceSurface

   Call
getDocument().getView().selectAt(0,((rri+si1)/2+(rri+(rri+si1)/2)/2)/2    ,
infoSetSelection, ArrayOfValues)

    ArrayOfValues(0) =  "inner rotor  air"

      Call  getDocument().getView().makeComponentInALine(0,  ArrayOfValues,
"Name=AIR")

ReDim ArrayOfValues(0)

    ArrayOfValues(0) = infoSliceSurface

   Call
getDocument().getView().selectAt(0,((rri+si1)/2+(si1+(rri+si1)/2)/2)/2    ,
infoSetSelection, ArrayOfValues)

    ArrayOfValues(0) =  "inner stator  air"

Call     getDocument().getView().makeComponentInALine(0,     ArrayOfValues,
"Name=AIR")

ReDim ArrayOfValues(0)

    ArrayOfValues(0) = infoSliceSurface

   Call   getDocument().getView().selectAt(0,(si1+(si1+(rri+si1)/2)/2)/2   ,
infoSetSelection, ArrayOfValues)

    ArrayOfValues(0) =  "inner stator virtual air"

Call     getDocument().getView().makeComponentInALine(0,     ArrayOfValues,
"Name=Virtual Air")
```

A1.3 Script File for Average Torque Calculation

```
const CATEGORY_OPTINET="OptiNet"

const VARIANT_RESULTS= 2

Call SetLocale ("en-us")

Call setVariant(VARIANT_RESULTS, Torque(), CATEGORY_OPTINET)

Function Torque()

      CALL getDocument().getProblem(1).getParameter("","cycles", cycles)

      CALL       getDocument().getProblem(1).getParameter("","steps_cycle",
steps_cycle)

      CALL getDocument().getProblem(1).getParameter("","t_step", t_step)

      CALL getDocument().getProblem(1).getParameter("","t_elec", t_elec)

      CALL getDocument().getProblem(1).getParameter("","fraction", fraction)

      t_start = 0

      t_end = 5

      for i = 0 to (5/0.1)

            t_i = t_start + (0.1*i)

            CALL
getDocument().getSolution().getTorqueAboutOriginOnBody(Array(1,t_i),     1,
torque_x, torque_y, torque_z)

            T_sum=T_sum+abs(torque_z)

      Next

      Torque=T_sum/i/fraction

      'MsgBox Torque

End Function


const CATEGORY_OPTINET="OptiNet"

const VARIANT_RESULTS= 2

Call SetLocale ("en-us")

Call setVariant(VARIANT_RESULTS, Resistance(), CATEGORY_OPTINET)
```

```
Function Resistance()

      CALL getDocument().getProblem(1).getParameter("","split", split)

      CALL getDocument().getProblem(1).getParameter("","t_sc", t_sc)

      CALL getDocument().getProblem(1).getParameter("","k_si", k_si)

      CALL getDocument().getProblem(1).getParameter("","k_so", k_so)

      CALL getDocument().getProblem(1).getParameter("","l_z", l_z)

      CALL getDocument().getProblem(1).getParameter("","n_turns", n_turns)

      statorinnerR=269*split/2

      statorouterR=269/2-t_sc

      statortoothW=(statorinnerR*k_si+statorouterR*k_so)/2

      statorpitch=2*3.1415926/16

      CoilslotW=((statorpitch-k_si)*statorinnerR+(statorpitch-
k_so)*statorouterR)/2

      endwindingD=(statortoothW+CoilslotW)

      statortoothL=statorouterR-statorinnerR

      CoilsectionA=statortoothL*CoilslotW

      fillfactor=0.5

      Resistance=(1.6/100000)*n_turns*4*(3.1415926*endwindingD+2*l_z)/(Coil
sectionA*fillfactor/n_turns)

End Function
```

Appendix 2 16/12 DSSRM Drawing

This appendix describe the drawing of the critical component of the prototype machine which constructed in Chapter 6.

A2.1 Shaft

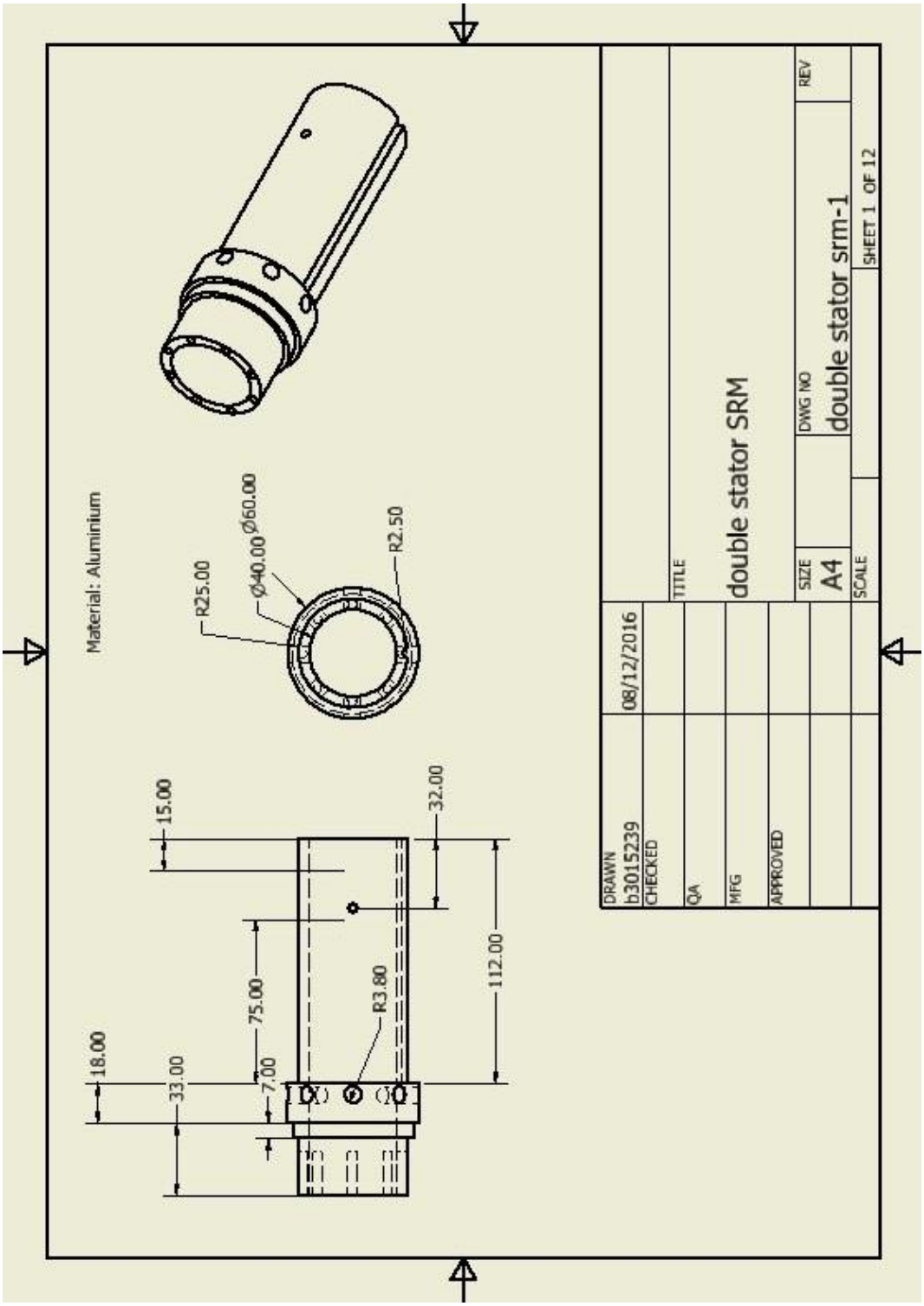

A2.2 Inner Stator Lamination

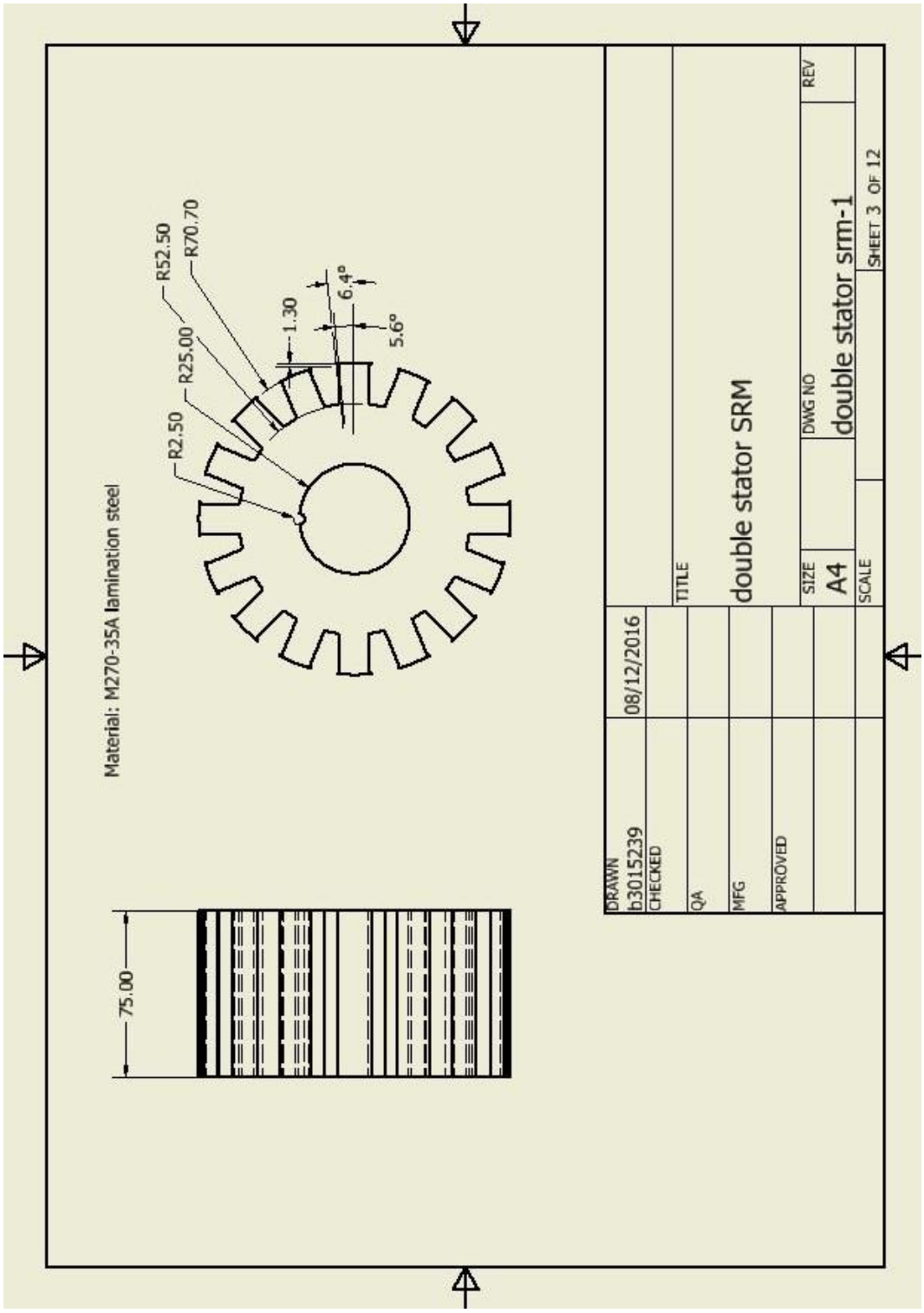

A2.3 Rotor Assembly

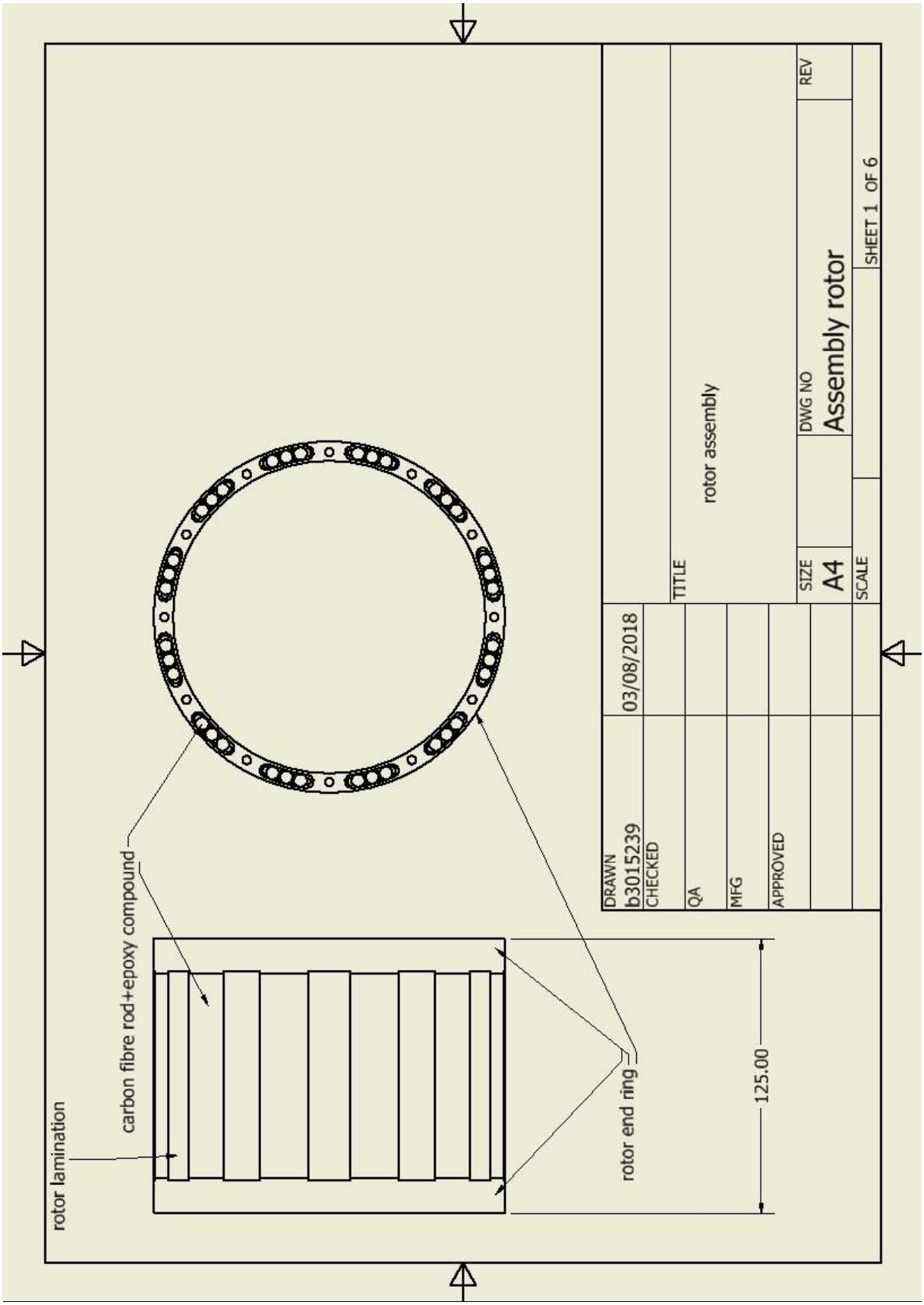

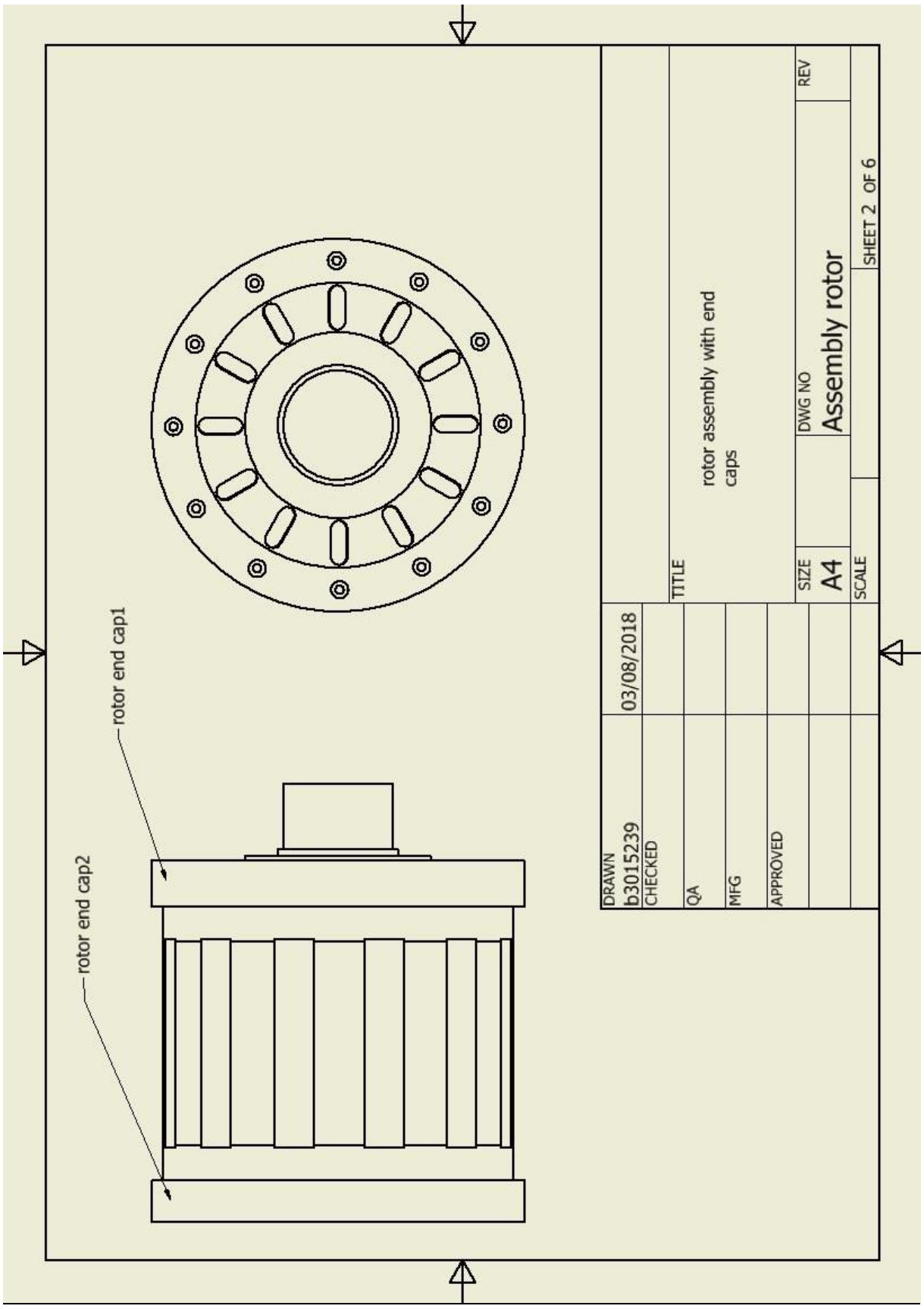
rotor end cap1
rotor end cap2
DRAWN
b3015239
03/08/2018
CHECKED
QA
MFG
APPROVED
TITLE
rotor assembly with end caps
SIZE
A4
DWG NO
Assembly rotor
REV
SCALE
SHEET 2 OF 6

A2.4 Rotor Lamination

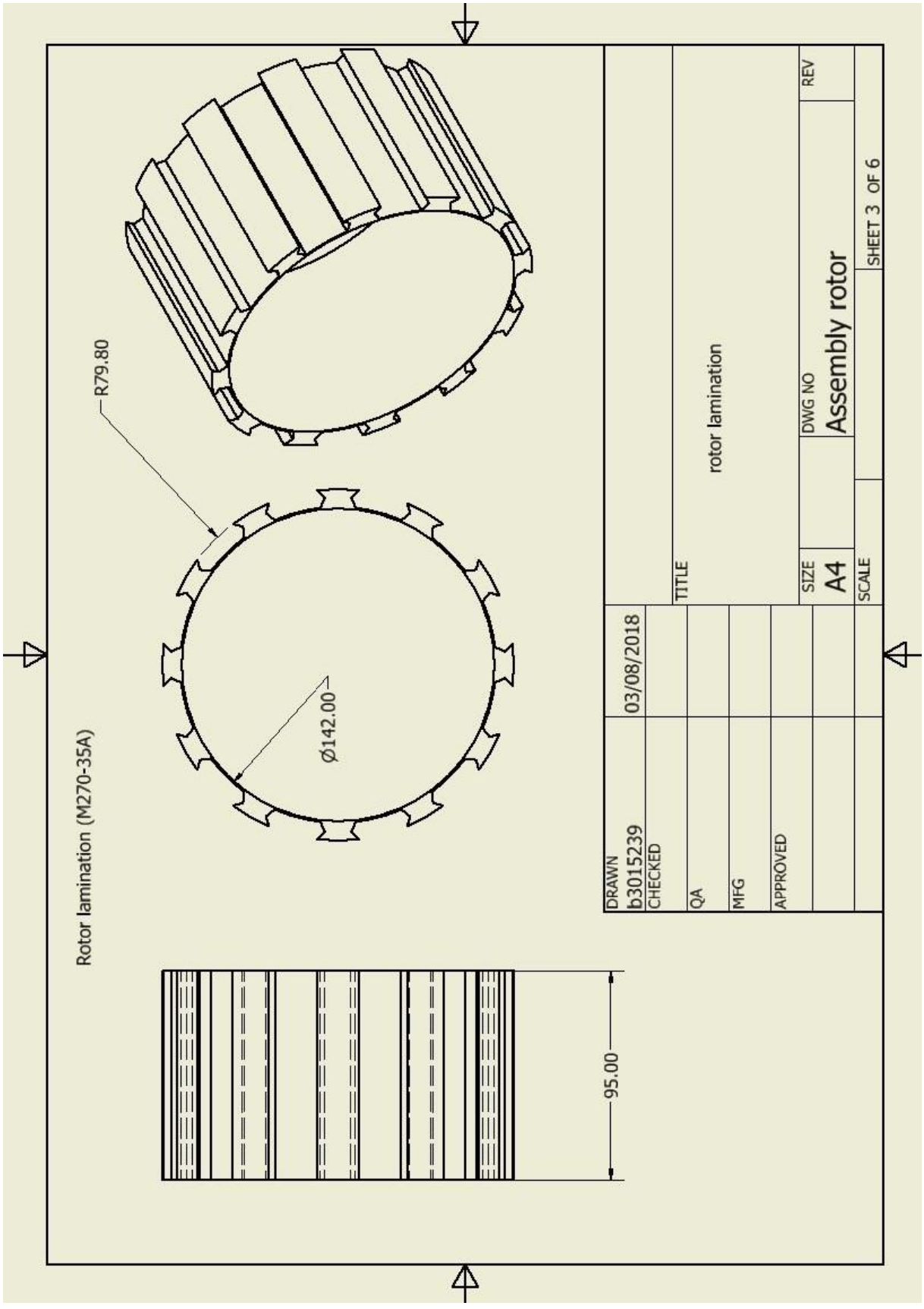

A2.5 Rotor Ring

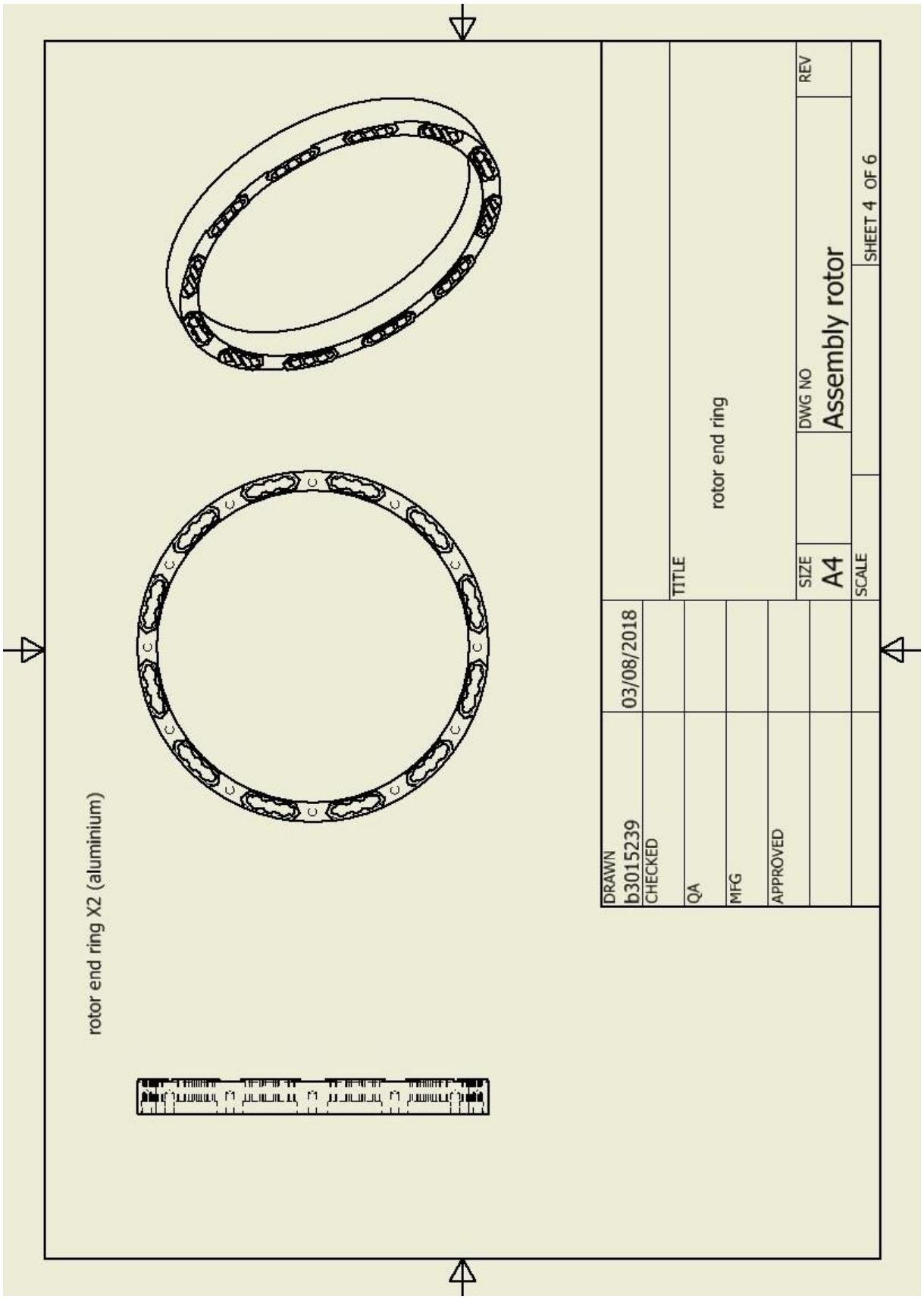

A2.6 Rotor Caps

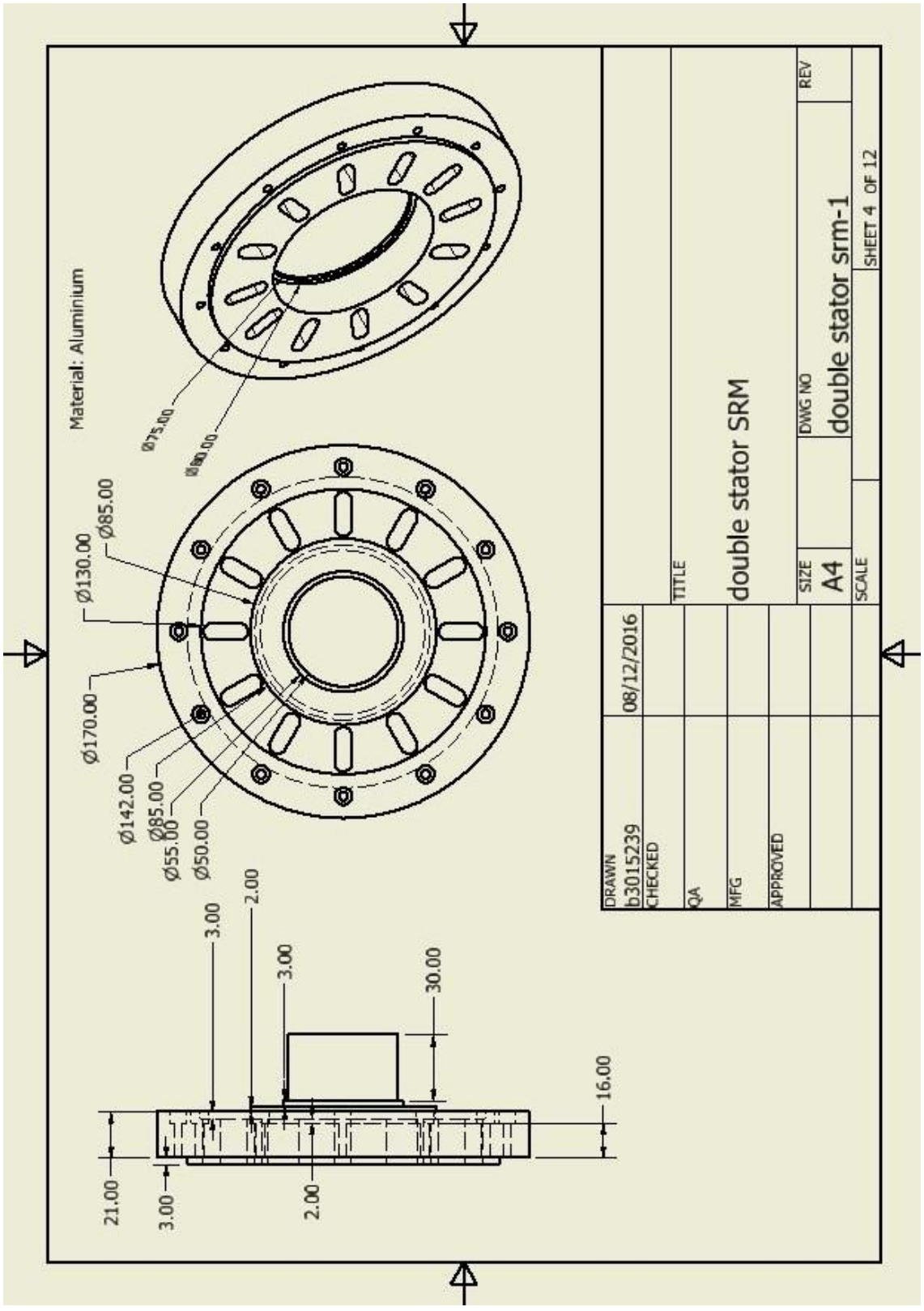

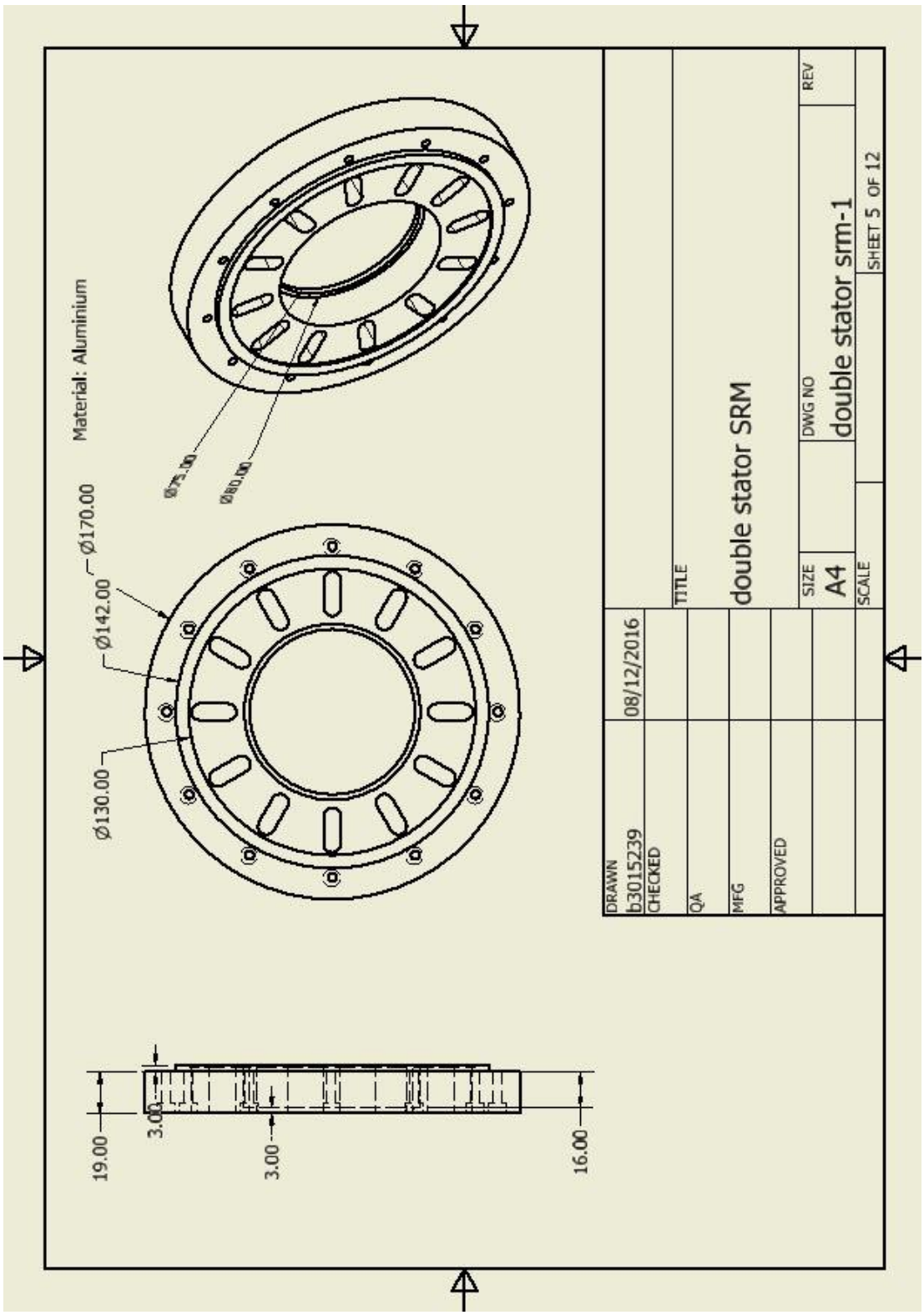
Material: Aluminium
Ø170.00
Ø142.00
Ø130.00
Ø75.00
Ø80.00
19.00
3.00
3.00
16.00
DRAWN
b3015239
08/12/2016
CHECKED
QA
MFG
APPROVED
TITLE
double stator SRM
SIZE
A4
DWG NO
double stator srm-1
REV
SCALE
SHEET 5 OF 12

A2.7 Outer Stator Lamination

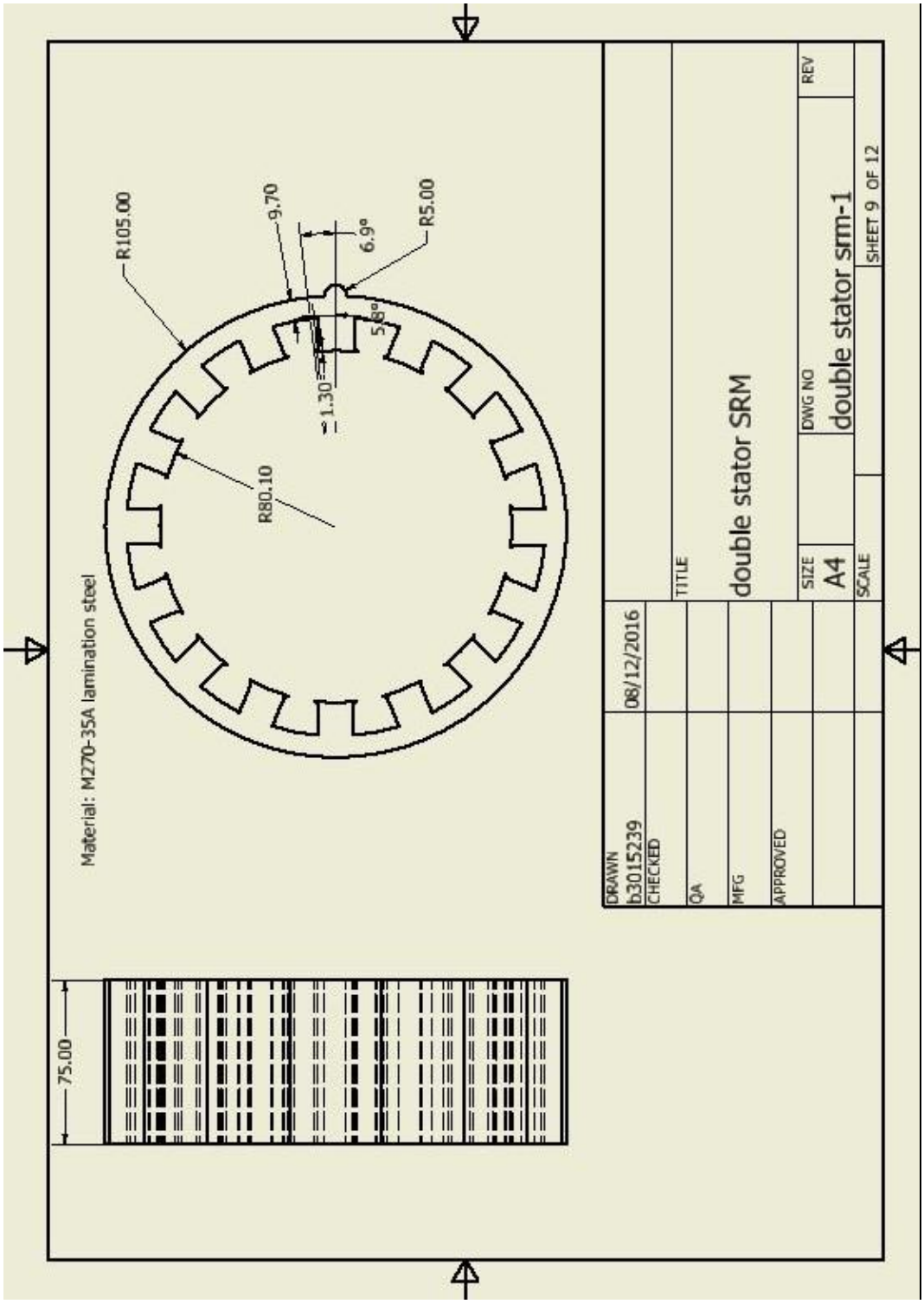

Appendix 3 Script for Pulse Test

The script from Matlab is responsible for calculate the magnetisation curve from the current and voltage data which collected during pulse test

```
cd('D:\OneDrive\static test\23A')
filename = ('T0001all.csv');

voltage=xlsread(filename,'D17:D90000')
current=xlsread(filename,'B17:B90000')
time=xlsread(filename,'A17:A90000')


%filter the source data
b = fir1(100,0.0001); % design a FIR filter
filtvoltage=filter(b,1,voltage);
filtcurrent=filter(b,1,current);

maxcurrent=max(filtcurrent);
mincurrent=min(filtcurrent);
maxvolts=max(filtvoltage);
minvoltage=min(filtvoltage);

%find rise start point

for n = 1:length(filtvoltage)
    if(filtvoltage(n) > minvoltage*1.05)
        start_point = n;
        break
    end
end

%find rise end point

for n = 1:length(filtcurrent)
    if filtcurrent(n) > maxcurrent*(0.995)
        settling_point = n;
        break
    end
end




%find fall start point

for n = settling_point:length(filtvoltage)

    if(filtvoltage(n) < 0.9*maxvolts)  %the voltage goes negative on switch
off and we need to detect when the current begins to decay
        fall_start_point = n-1;
        break
    end
end
```

```
%find fall end point
for n = settling_point:length(filtcurrent)
    if (filtcurrent(n) < mincurrent*1.2)&(filtvoltage(n) > 0.5*minvoltage)
        fall_settling_point = n;
        break
   end
end

%Now find the value of resistance just after the end of the rise
%v= sum(filtvoltage(settling_point-5:settling_point+5))/10;
%i= sum(filtcurrent(settling_point-5:settling_point+5))/10;
v= sum(filtvoltage(34000:34110))/110;
i= sum(filtcurrent(34000:34110))/110;
coil_resistance_rise=v/i;

Psi=zeros(1,length(filtcurrent));
for i=start_point:settling_point;
deltaT = time(i+1)-time(i);
%Psi(i+1)=(deltaT*((filtvoltage(i)+filtvoltage(i+1))/2-(filtcurrent(i)-
filtcurrent(i+1))/2*coil_resistance_rise))+Psi(i);
Psi(i+1)=(deltaT*(((filtvoltage(i)-
filtcurrent(i)*coil_resistance_rise)+(filtvoltage(i+1)-
filtcurrent(i+1)*coil_resistance_rise))/2))+Psi(i);
end
hold on
plot
(filtcurrent(start_point:settling_point),Psi(start_point:settling_point),'r
');

risecurrent=filtcurrent(start_point:settling_point)
risefluxlinkage=Psi(start_point:settling_point)

xi=0:2:60
yi=interp1(risecurrent,risefluxlinkage,xi,'linear','extrap')
```

Reference

[1] J. Zhang, X. Lu, J. Lu, Q. Kang, and X. Dong, "Study of the New Permanent Magnet switched reluctance motor," in *2011 International Conference on Advanced Power System Automation and Protection*, 16-20 Oct. 2011 2011, vol. 3, pp. 1684-1687, doi: 10.1109/APAP.2011.6180757. [Online]. Available: https://ieeexplore.ieee.org/ielx5/6175562/6180616/06180757.pdf?tp=&arnumber=6180757&isnumber=6180616

[2] "Reducing CO2 emissions from passenger cars." https://ec.europa.eu/clima/policies/transport/vehicles/cars_en (accessed.

[3] "Jaguar Land Rover to make only electric or hybrid cars from 2020 ", ed, 2017.

[4] A. Tovey. "Volvo becomes the first major car manufacturer to go all electric." http://www.telegraph.co.uk/business/2017/07/05/volvo-becomes-first-major-car-manufacturer-go-electric/ (accessed 2017).

[5] D. Tracy. "Everything You Need To Know About The Upcoming 48-Volt Electrical Revolution In Cars." http://jalopnik.com/everything-you-need-to-know-about-the-upcoming-48-volt-1790364465 (accessed 2017).

[6] "Mild Hybrid Electric Vehicle (MHEV) – architectures." https://x-engineer.org/automotive-engineering/vehicle/hybrid/mild-hybrid-electric-vehicle-mhev-architectures/ (accessed.

[7] "The official U.S. government source for fuel economy information." https://www.fueleconomy.gov/feg/findacar.shtml (accessed 2018).

[8] D. Scutt. "Global electric vehicle sales are booming." https://www.businessinsider.com.au/the-rapid-growth-in-global-electric-vehicle-sales-in-4-charts-2018-1 (accessed.

[9] "Large luxury vehicle sales by model in the United States 2017." https://www.statista.com/statistics/287753/large-luxury-vehicles-sales-by-make-in-the-united-states/ (accessed 2018).

[10] M. Chediak. "The Latest Bull Case for Electric Cars: the Cheapest Batteries Ever." https://www.bloomberg.com/news/articles/2017-12-05/latest-bull-case-for-electric-cars-the-cheapest-batteries-ever (accessed 2018).

[11] "Electric Vehicle Battery: Materials, Cost, Lifespan." Electric Vehicle Battery: Materials, Cost, Lifespan (accessed 2018).

[12] "Fuel cell vehicle." https://en.wikipedia.org/wiki/Fuel_cell_vehicle (accessed 2018).

[13] F. Ognissanto, T. Landen, A. Stevens, M. Emre, and D. Naberezhnykh, "Evaluation of the CO_2 emissions pathway from hydrogen production to fuel cell car utilisation," *IET Intelligent Transport Systems*, vol. 11, no. 7, pp. 360-367, 2017, doi: 10.1049/iet-its.2016.0210.

[14] H. Oman, "Performance, life-cycle cost, and emissions of fuel cells," *IEEE Aerospace and Electronic Systems Magazine*, vol. 17, no. 9, pp. 33-37, 2002, doi: 10.1109/MAES.2002.1039792.

[15] "Number of cars sold worldwide from 1990 to 2018 (in million units)." https://www.statista.com/statistics/200002/international-car-sales-since-1990/ (accessed 2018).

[16] "List of countries banning fossil fuel vehicles." https://en.wikipedia.org/wiki/List_of_countries_banning_fossil_fuel_vehicles (accessed 2018).

[17] Y. Sato, S. Ishikawa, T. Okubo, M. Abe, and K. Tamai, *Development of High Response Motor and Inverter System for the Nissan LEAF Electric Vehicle*. 2011.

[18] F. Momen, K. Rahman, Y. Son, and P. Savagian, "Electrical propulsion system design of Chevrolet Bolt battery electric vehicle," in *2016 IEEE Energy Conversion Congress*

and Exposition (ECCE), 18-22 Sept. 2016 2016, pp. 1-8, doi: 10.1109/ECCE.2016.7855076. [Online]. Available: https://ieeexplore.ieee.org/ielx7/7835398/7854636/07855076.pdf?tp=&arnumber=7855076&isnumber=7854636

[19] "Forecast of rare earth oxide prices worldwide from 2014 to 2025." https://www.statista.com/statistics/449838/forecast-average-rare-earth-oxide-prices-globally/ (accessed 2018).

[20] "Neodymium oxide price worldwide from 2009 to 2025 (in U.S. dollars per metric ton)." https://www.statista.com/statistics/450152/global-reo-neodymium-oxide-price-forecast/ (accessed 2018).

[21] D. G. Dorrell, A. M. Knight, M. Popescu, L. Evans, and D. A. Staton, "Comparison of different motor design drives for hybrid electric vehicles," in *2010 IEEE Energy Conversion Congress and Exposition*, 12-16 Sept. 2010 2010, pp. 3352-3359, doi: 10.1109/ECCE.2010.5618318. [Online]. Available: https://ieeexplore.ieee.org/ielx5/5606065/5617696/05618318.pdf?tp=&arnumber=5618318&isnumber=5617696

[22] J. D. Widmer, R. Martin, and M. Kimiabeigi, "Electric vehicle traction motors without rare earth magnets," *Sustainable Materials and Technologies*, vol. 3, pp. 7-13, 2015/04/01/ 2015, doi: https://doi.org/10.1016/j.susmat.2015.02.001.

[23] C. Bontron. "Rare-earth mining in China comes at a heavy cost for local villages." https://www.theguardian.com/environment/2012/aug/07/china-rare-earth-village-pollution (accessed 2018).

[24] S. PARRY and E. DOUGLAS. "In China, the true cost of Britain's clean, green wind power experiment: Pollution on a disastrous scale." http://www.dailymail.co.uk/home/moslive/article-1350811/In-China-true-cost-Britains-clean-green-wind-power-experiment-Pollution-disastrous-scale.html (accessed 2018).

[25] "Global Hybrid Cooperation." https://en.wikipedia.org/wiki/Global_Hybrid_Cooperation (accessed.

[26] I. Boldea, L. N. Tutelea, L. Parsa, and D. Dorrell, "Automotive Electric Propulsion Systems With Reduced or No Permanent Magnets: An Overview," *Industrial Electronics, IEEE Transactions on*, vol. 61, no. 10, pp. 5696-5711, 2014, doi: 10.1109/TIE.2014.2301754.

[27] J.-R. Riba, C. López-Torres, L. Romeral, and A. Garcia, "Rare-earth-free propulsion motors for electric vehicles: A technology review," *Renewable and Sustainable Energy Reviews*, vol. 57, pp. 367-379, 2016/05/01/ 2016, doi: https://doi.org/10.1016/j.rser.2015.12.121.

[28] "Tesla, Inc." https://en.wikipedia.org/wiki/Tesla,_Inc. (accessed.

[29] "Global Plug-in Vehicle Sales for 2017 – Final Results." http://www.ev-volumes.com/news/global-plug-in-vehicle-sales-for-2017-final-results/ (accessed.

[30] E. Musk. https://twitter.com/elonmusk/status/998015873167208448?s=21 (accessed.

[31] N. Zabihi and R. Gouws, "A review on switched reluctance machines for electric vehicles," in *2016 IEEE 25th International Symposium on Industrial Electronics (ISIE)*, 8-10 June 2016 2016, pp. 799-804, doi: 10.1109/ISIE.2016.7744992. [Online]. Available: https://ieeexplore.ieee.org/ielx7/7740453/7744853/07744992.pdf?tp=&arnumber=7744992&isnumber=7744853

[32] B. C. Mecrow, E. A. El-Kharashi, J. W. Finch, and A. G. Jack, "Performance evaluation of switched reluctance motors with segmental rotors," in *Electric Machines and Drives Conference, 2003. IEMDC'03. IEEE International*, 1-4 June 2003 2003, vol. 1, pp. 568-574 vol.1, doi: 10.1109/IEMDC.2003.1211319. [Online]. Available:

http://ieeexplore.ieee.org/ielx5/8600/27264/01211319.pdf?tp=&arnumber=1211319&isnumber=27264

[33] M. Abbasian, M. Moallem, and B. Fahimi, "Double-Stator Switched Reluctance Machines (DSSRM): Fundamentals and Magnetic Force Analysis," *Energy Conversion, IEEE Transactions on,* vol. 25, no. 3, pp. 589-597, 2010, doi: 10.1109/TEC.2010.2051547.

[34] M. Asgar and E. Afjei, "Radial Force Reduction in a New Flat-Type Double-Stator Switched Reluctance Motor," *Energy Conversion, IEEE Transactions on,* vol. PP, no. 99, pp. 1-9, 2015, doi: 10.1109/TEC.2015.2465833.

[35] L. Guangjin, J. Ojeda, S. Hlioui, E. Hoang, M. Lecrivain, and M. Gabsi, "Modification in Rotor Pole Geometry of Mutually Coupled Switched Reluctance Machine for Torque Ripple Mitigating," *Magnetics, IEEE Transactions on,* vol. 48, no. 6, pp. 2025-2034, 2012, doi: 10.1109/TMAG.2011.2179307.

[36] T. J. E. Miller, *Switched Reluctance Motors and their Control*. Oxford University Press, 1993.

[37] T. J. E. Miller, *Electronic Control of Switched Reluctance Machines*. Newnes, 2001.

[38] P. Lawrenson, "Switched-reluctance motor drives," *Electronics and Power,* vol. 29, no. 2, pp. 144-147, 1983, doi: 10.1049/ep.1983.0071.

[39] P. Materu and R. Krishnan, "Analytical prediction of SRM inductance profile and steady-state average torque," in *Industry Applications Society Annual Meeting, 1990., Conference Record of the 1990 IEEE*, 7-12 Oct. 1990 1990, pp. 214-223 vol.1, doi: 10.1109/IAS.1990.152189. [Online]. Available: http://ieeexplore.ieee.org/ielx2/497/3988/00152189.pdf?tp=&arnumber=152189&isnumber=3988

[40] P. J. Lawrenson, J. M. Stephenson, P. T. Blenkinsop, J. Corda, and N. N. Futon, "Variable-speed switched reluctance motors," *Electric Power Applications, IEE Proceedings B,* vol. 127, no. 4, pp. 253-265, 1980, doi: 10.1049/ip-b:19800034.

[41] Y. C. Wu, S. J. Song, S. Chen, H. C. Liu, and Z. H. Zhang, "Analytic calculation of electromagnetic characteristics of switched reluctance machine," in *Industrial Electronics and Applications (ICIEA), 2013 8th IEEE Conference on*, 19-21 June 2013 2013, pp. 1005-1010, doi: 10.1109/ICIEA.2013.6566514. [Online]. Available: http://ieeexplore.ieee.org/ielx7/6559347/6566328/06566514.pdf?tp=&arnumber=6566514&isnumber=6566328

[42] A. D. Cheok and N. Ertugrul, "Computer-based automated test measurement system for determining magnetization characteristics of switched reluctance motors," *IEEE Transactions on Instrumentation and Measurement,* vol. 50, no. 3, pp. 690-696, 2001, doi: 10.1109/19.930441.

[43] V. N. Walivadekar, S. K. Pillai, S. S. Sadistap, and R. Bhandhari, "PC based data acquisition system for measurement of switched reluctance motor (SRM)," in *Power Electronics, Drives and Energy Systems for Industrial Growth, 1996., Proceedings of the 1996 International Conference on*, 8-11 Jan 1996 1996, vol. 2, pp. 957-963 vol.2, doi: 10.1109/PEDES.1996.536401. [Online]. Available: http://ieeexplore.ieee.org/ielx3/3837/11204/00536401.pdf?tp=&arnumber=536401&isnumber=11204

[44] R. Krishnan and P. Materu, "Measurement and instrumentation of a switched reluctance motor," in *Industry Applications Society Annual Meeting, 1989., Conference Record of the 1989 IEEE,* 1-5 Oct. 1989 1989, pp. 116-121 vol.1, doi: 10.1109/IAS.1989.96639. [Online]. Available: http://ieeexplore.ieee.org/ielx2/858/3081/00096639.pdf?tp=&arnumber=96639&isnumber=3081

[45] Z. Jinhui and A. V. Radun, "A New Method to Measure the Switched Reluctance Motor's Flux," *Industry Applications, IEEE Transactions on,* vol. 42, no. 5, pp. 1171-1176, 2006, doi: 10.1109/TIA.2006.880876.

[46] L. Kaiyuan, P. O. Rasmussen, and A. E. Ritchie, "Investigation of Flux-Linkage Profile Measurement Methods for Switched-Reluctance Motors and Permanent-Magnet Motors," *Instrumentation and Measurement, IEEE Transactions on,* vol. 58, no. 9, pp. 3191-3198, 2009, doi: 10.1109/TIM.2009.2017154.

[47] T. J. E. Miller, M. I. McGilp, and M. Olaru, "Finite elements applied to synchronous and switched reluctance motors," in *Current Trends in the Use of Finite Elements (FE) in Electromechanical Design and Analysis (Ref. No. 2000/013), IEE Seminar on*, 2000 2000, pp. 3/1-3/4, doi: 10.1049/ic:20000050. [Online]. Available: http://ieeexplore.ieee.org/ielx5/6817/18283/00843240.pdf?tp=&arnumber=843240&isnumber=18283

[48] A. B. J. Reece, *Finite element methods in electrical power engineering*. Oxford, [England]: Oxford, England : Oxford University Press, 2000.

[49] A. M. Michaelides and C. Pollock, "Effect of end core flux on the performance of the switched reluctance motor," *Electric Power Applications, IEE Proceedings* -, vol. 141, no. 6, pp. 308-316, 1994, doi: 10.1049/ip-epa:19941476.

[50] R. Krishnan, *Switched Reluctance Motor Drives : modeling, simulation, analysis, design, and applications*

CRC Press, 2001.

[51] J. M. Kokernak and D. A. Torrey, "Magnetic circuit model for the mutually coupled switched-reluctance machine," *Magnetics, IEEE Transactions on,* vol. 36, no. 2, pp. 500-507, 2000, doi: 10.1109/20.825824.

[52] S. Li, S. Zhang, T. G. Habetler, and R. G. Harley, "Modeling, Design Optimization, and Applications of Switched Reluctance Machines—A Review," *IEEE Transactions on Industry Applications,* vol. 55, no. 3, pp. 2660-2681, 2019, doi: 10.1109/TIA.2019.2897965.

[53] J. Faiz and J. W. Finch, "Aspects of design optimisation for switched reluctance motors," *Energy Conversion, IEEE Transactions on,* vol. 8, no. 4, pp. 704-713, 1993, doi: 10.1109/60.260984.

[54] A. M. Michaelides and C. Pollock, "A new magnetic flux pattern to improve the efficiency of the switched reluctance motor," in *Conference Record of the 1992 IEEE Industry Applications Society Annual Meeting*, 4-9 Oct. 1992 1992, pp. 226-233 vol.1, doi: 10.1109/IAS.1992.244290. [Online]. Available: https://ieeexplore.ieee.org/ielx2/650/6279/00244290.pdf?tp=&arnumber=244290&isnumber=6279

[55] A. M. Michaelides and C. Pollock, "Modelling and design of switched reluctance motors with two phases simultaneously excited," *Electric Power Applications, IEE Proceedings* -, vol. 143, no. 5, pp. 361-370, 1996, doi: 10.1049/ip-epa:19960483.

[56] J. R. Hendershot, "Polyphase electronically commutated reluctance motor," European Patent WO 90/01823 Patent Appl. WO 90/01823, 1990.

[57] C. Lee, R. Krishnan, and N. S. Lobo, "Novel Two-Phase Switched Reluctance Machine Using Common-Pole E-Core Structure: Concept, Analysis, and Experimental Verification," *IEEE Transactions on Industry Applications,* vol. 45, no. 2, pp. 703-711, 2009, doi: 10.1109/TIA.2009.2013592.

[58] C. Lee and R. Krishnan, "New Designs of a Two-Phase E-Core Switched Reluctance Machine by Optimizing the Magnetic Structure for a Specific Application: Concept, Design, and Analysis," *IEEE Transactions on Industry Applications,* vol. 45, no. 5, pp. 1804-1814, 2009, doi: 10.1109/TIA.2009.2027570.

[59] J. W. Jiang, B. Bilgin, and A. Emadi, "Three-Phase 24/16 Switched Reluctance Machine for a Hybrid Electric Powertrain," *IEEE Transactions on Transportation Electrification,* vol. 3, no. 1, pp. 76-85, 2017, doi: 10.1109/TTE.2017.2664778.

[60] A. Chiba, K. Kiyota, N. Hoshi, M. Takemoto, and S. Ogasawara, "Development of a Rare-Earth-Free SR Motor With High Torque Density for Hybrid Vehicles," *Energy Conversion, IEEE Transactions on,* vol. 30, no. 1, pp. 175-182, 2015, doi: 10.1109/TEC.2014.2343962.

[61] Y. Takano *et al.*, "Design and analysis of a switched reluctance motor for next generation hybrid vehicle without PM materials," in *The 2010 International Power Electronics Conference - ECCE ASIA -*, 21-24 June 2010 2010, pp. 1801-1806, doi: 10.1109/IPEC.2010.5543565. [Online]. Available: https://ieeexplore.ieee.org/ielx5/5523765/5542000/05543565.pdf?tp=&arnumber=5543565&isnumber=5542000

[62] Y. Takano *et al.*, "Torque density and efficiency improvements of a Switched Reluctance Motor without rare earth material for hybrid vehicles," in *Energy Conversion Congress and Exposition (ECCE), 2010 IEEE*, 12-16 Sept. 2010 2010, pp. 2653-2659, doi: 10.1109/ECCE.2010.5618025. [Online]. Available: http://ieeexplore.ieee.org/ielx5/5606065/5617696/05618025.pdf?tp=&arnumber=5618025&isnumber=5617696

[63] A. Chiba, M. Takeno, N. Hoshi, M. Takemoto, S. Ogasawara, and M. A. Rahman, "Consideration of Number of Series Turns in Switched-Reluctance Traction Motor Competitive to HEV IPMSM," *IEEE Transactions on Industry Applications,* vol. 48, no. 6, pp. 2333-2340, 2012, doi: 10.1109/TIA.2012.2227093.

[64] A. Chiba *et al.*, "Torque Density and Efficiency Improvements of a Switched Reluctance Motor Without Rare-Earth Material for Hybrid Vehicles," *IEEE Transactions on Industry Applications,* vol. 47, no. 3, pp. 1240-1246, 2011, doi: 10.1109/TIA.2011.2125770.

[65] K. Kiyota and A. Chiba, "Design of Switched Reluctance Motor Competitive to 60-kW IPMSM in Third-Generation Hybrid Electric Vehicle," *IEEE Transactions on Industry Applications,* vol. 48, no. 6, pp. 2303-2309, 2012, doi: 10.1109/TIA.2012.2227091.

[66] B. Bilgin, A. Emadi, and M. Krishnamurthy, "Comprehensive Evaluation of the Dynamic Performance of a 6/10 SRM for Traction Application in PHEVs," *IEEE Transactions on Industrial Electronics,* vol. 60, no. 7, pp. 2564-2575, 2013, doi: 10.1109/TIE.2012.2196015.

[67] P. C. Desai, M. Krishnamurthy, N. Schofield, and A. Emadi, "Novel Switched Reluctance Machine Configuration With Higher Number of Rotor Poles Than Stator Poles: Concept to Implementation," *IEEE Transactions on Industrial Electronics,* vol. 57, no. 2, pp. 649-659, 2010, doi: 10.1109/TIE.2009.2034678.

[68] M. Ćosović, S. Smaka, I. Salihbegović, and M. Š, "Design optimization of 8/14 switched reluctance machine for electric vehicle," in *2012 XXth International Conference on Electrical Machines*, 2-5 Sept. 2012 2012, pp. 2654-2659, doi: 10.1109/ICElMach.2012.6350260. [Online]. Available: http://ieeexplore.ieee.org/document/6350260/

https://ieeexplore.ieee.org/ielx5/6330482/6349821/06350260.pdf?tp=&arnumber=6350260&isnumber=6349821

[69] J. B. Bartolo, M. Degano, J. Espina, and C. Gerada, "Design and Initial Testing of a High-Speed 45-kW Switched Reluctance Drive for Aerospace Application," *IEEE Transactions on Industrial Electronics,* vol. 64, no. 2, pp. 988-997, 2017, doi: 10.1109/TIE.2016.2618342.

[70] M. Besharati, J. Widmer, G. Atkinson, V. Pickert, and J. Washington, "Super-high-speed switched reluctance motor for automotive traction," in *2015 IEEE Energy*

Conversion Congress and Exposition (ECCE), 20-24 Sept. 2015 2015, pp. 5241-5248, doi: 10.1109/ECCE.2015.7310397. [Online]. Available: https://ieeexplore.ieee.org/ielx7/7298093/7309651/07310397.pdf?tp=&arnumber=7310397&isnumber=7309651

[71] G. A. HORST, "Isolated segmental switched reluctance motor," United States, 1992.

[72] B. C. Mecrow, J. W. Finch, E. A. El-Kharashi, and A. G. Jack, "Switched reluctance motors with segmental rotors," *IEE Proceedings - Electric Power Applications*, vol. 149, no. 4, pp. 245-254, 2002, doi: 10.1049/ip-epa:20020345.

[73] B. C. Mecrow, E. A. El-Kharashi, J. W. Finch, and A. G. Jack, "Preliminary performance evaluation of switched reluctance motors with segmental rotors," *Energy Conversion, IEEE Transactions on*, vol. 19, no. 4, pp. 679-686, 2004, doi: 10.1109/TEC.2004.837290.

[74] B. C. Mecrow, E. A. El-Kharashi, J. W. Finch, and A. G. Jack, "Segmental rotor switched reluctance motors with single-tooth windings," *Electric Power Applications, IEE Proceedings -*, vol. 150, no. 5, pp. 591-599, 2003, doi: 10.1049/ip-epa:20030366.

[75] X. Chen, Z. Deng, X. Wang, J. Peng, and X. Li, "New designs of switched reluctance motors with segmental rotors," in *5th IET International Conference on Power Electronics, Machines and Drives (PEMD 2010)*, 19-21 April 2010 2010, pp. 1-6, doi: 10.1049/cp.2010.0179.

[76] T. Higuchi, K. Suenaga, and T. Abe, "Torque ripple reduction of novel segment type Switched reluctance motor by increasing phase number," in *2009 International Conference on Electrical Machines and Systems*, 15-18 Nov. 2009 2009, pp. 1-4, doi: 10.1109/ICEMS.2009.5382754.

[77] J. Oyama, T. Higuchi, T. Abe, and K. Tanaka, "The fundamental characteristics of novel switched reluctance motor with segment core embedded in aluminum rotor block," in *2005 International Conference on Electrical Machines and Systems*, 27-29 Sept. 2005 2005, vol. 1, pp. 515-519 Vol. 1, doi: 10.1109/ICEMS.2005.202582.

[78] R. Vandana, N. Vattikuti, and B. G. Fernandes, "A Novel High Power Density Segmented Switched Reluctance Machine," in *2008 IEEE Industry Applications Society Annual Meeting*, 5-9 Oct. 2008 2008, pp. 1-7, doi: 10.1109/08IAS.2008.66.

[79] J. D. Widmer, R. Martin, and B. C. Mecrow, "Optimisation of an 80kW Segmental Rotor Switched Reluctance Machine for automotive traction," in *Electric Machines & Drives Conference (IEMDC), 2013 IEEE International*, 12-15 May 2013 2013, pp. 427-433, doi: 10.1109/IEMDC.2013.6556132. [Online]. Available: http://ieeexplore.ieee.org/ielx7/6548947/6556119/06556132.pdf?tp=&arnumber=6556132&isnumber=6556119

[80] J. D. Widmer and B. C. Mecrow, "Optimized Segmental Rotor Switched Reluctance Machines With a Greater Number of Rotor Segments Than Stator Slots," *Industry Applications, IEEE Transactions on*, vol. 49, no. 4, pp. 1491-1498, 2013, doi: 10.1109/TIA.2013.2255574.

[81] N. Arbab, W. Wei, L. Chenjie, J. Hearron, and B. Fahimi, "Thermal Modeling and Analysis of a Double-Stator Switched Reluctance Motor," *Energy Conversion, IEEE Transactions on*, vol. 30, no. 3, pp. 1209-1217, 2015, doi: 10.1109/TEC.2015.2424400.

[82] A. H. Isfahani and B. Fahimi, "Comparison of Mechanical Vibration Between a Double-Stator Switched Reluctance Machine and a Conventional Switched Reluctance Machine," *Magnetics, IEEE Transactions on*, vol. 50, no. 2, pp. 293-296, 2014, doi: 10.1109/TMAG.2013.2286569.

[83] M. Abbasian, B. Fahimi, and M. Moallem, "High torque double-stator switched reluctance machine for electric vehicle propulsion," in *Vehicle Power and Propulsion Conference (VPPC), 2010 IEEE*, 1-3 Sept. 2010 2010, pp. 1-5, doi: 10.1109/VPPC.2010.5729077. [Online]. Available:

http://ieeexplore.ieee.org/ielx5/5720573/5728974/05729077.pdf?tp=&arnumber=5729077&isnumber=5728974

[84] W. Jiang, M. Moallem, B. Fahimi, and S. Pekarek, "Qualitative Investigation of Force Density Components in Electromechanical Energy Conversion Process," in *IECON 2006 - 32nd Annual Conference on IEEE Industrial Electronics*, 6-10 Nov. 2006 2006, pp. 1113-1118, doi: 10.1109/IECON.2006.347809. [Online]. Available: http://ieeexplore.ieee.org/document/4153697/

https://ieeexplore.ieee.org/ielx5/4152824/4152825/04153697.pdf?tp=&arnumber=4153697&isnumber=4152825

[85] W. Wang and B. Fahimi, "Comparative study of electric drives for EV/HEV propulsion system," in *Electrical Systems for Aircraft, Railway and Ship Propulsion (ESARS), 2012*, 16-18 Oct. 2012 2012, pp. 1-6, doi: 10.1109/ESARS.2012.6387497. [Online]. Available: http://ieeexplore.ieee.org/ielx5/6375603/6387375/06387497.pdf?tp=&arnumber=6387497&isnumber=6387375

[86] E. Bostanci, M. Moallem, A. Parsapour, and B. Fahimi, "Opportunities and Challenges of Switched Reluctance Motor Drives for Electric Propulsion: A Comparative Study," *IEEE Transactions on Transportation Electrification,* vol. 3, no. 1, pp. 58-75, 2017, doi: 10.1109/TTE.2017.2649883.

[87] M. Asgar, E. Afjei, and H. Torkaman, "A New Strategy to Design and Analysis of a Double-Stator Switched Reluctance Motor: Electromagnetics, FEM and Experiment," *Magnetics, IEEE Transactions on,* vol. PP, no. 99, pp. 1-1, 2015, doi: 10.1109/TMAG.2015.2465307.

[88] M. Asgar, E. Afjei, A. Behbahani, and A. Siadatan, "A 12/8 double-stator switched reluctance motor for washing machine application," in *Power Electronics, Drives Systems & Technologies Conference (PEDSTC), 2015 6th*, 3-4 Feb. 2015 2015, pp. 168-172, doi: 10.1109/PEDSTC.2015.7093268. [Online]. Available: http://ieeexplore.ieee.org/ielx7/7085977/7093233/07093268.pdf?tp=&arnumber=7093268&isnumber=7093233

[89] P. Luk and P. K. Jinupun, "Yokeless switched reluctance motors," in *2006 37th IEEE Power Electronics Specialists Conference*, 18-22 June 2006 2006, pp. 1-5, doi: 10.1109/pesc.2006.1712236. [Online]. Available: http://ieeexplore.ieee.org/ielx7/11209/36090/01712236.pdf?tp=&arnumber=1712236&isnumber=36090

[90] X. D. Xue, K. W. E. Cheng, Y. J. Bao, and J. Leung, "Design consideration of C-core switched reluctance generators for wind energy," in *2011 4th International Conference on Power Electronics Systems and Applications*, 8-10 June 2011 2011, pp. 1-6, doi: 10.1109/PESA.2011.5982957.

[91] N. Arbab, W. Wang, C. Lin, J. Hearron, and B. Fahimi, "Thermal Modeling and Analysis of a Double-Stator Switched Reluctance Motor," *Energy Conversion, IEEE Transactions on,* vol. 30, no. 3, pp. 1209-1217, 2015, doi: 10.1109/TEC.2015.2424400.

[92] B. C. Mecrow, "Fully pitched-winding switched-reluctance and stepping-motor arrangements," *Electric Power Applications, IEE Proceedings B,* vol. 140, no. 1, pp. 61-70, 1993.

[93] J. Sun, S. Wang, Z. Kuang, and H. Wu, "Torque ripple comparison of short-pitched and fully-pitched winding switched reluctance machine," in *2012 15th International Conference on Electrical Machines and Systems (ICEMS)*, 21-24 Oct. 2012 2012, pp. 1-6.

[94] M. A. Preston and J. P. Lyons, "A switched reluctance motor model with mutual coupling and multi-phase excitation," *IEEE Transactions on Magnetics,* vol. 27, no. 6, pp. 5423-5425, 1991, doi: 10.1109/20.278859.

[95] P. Debiprasad and V. Ramanarayanan, "Mutual Coupling and Its Effect on Steady-State Performance and Position Estimation of Even and Odd Number Phase Switched Reluctance Motor Drive," *Magnetics, IEEE Transactions on,* vol. 43, no. 8, pp. 3445-3456, 2007, doi: 10.1109/TMAG.2007.898101.

[96] Q. Bingni, S. Jiancheng, L. Tao, and Z. Hongda, "Mutual coupling and its effect on torque waveform of even number phase switched reluctance motor," in *Electrical Machines and Systems, 2008. ICEMS 2008. International Conference on*, 17-20 Oct. 2008 2008, pp. 3405-3410.

[97] D. Wen and L. Deliang, "Calculation of Flux Linkages of a 12/8 Dual-Channel SRM Including Mutual Coupling and Saturation: From Magnetic Circuit Model to FEM Analysis," in *Industry Applications Society Annual Meeting, 2008. IAS '08. IEEE*, 5-9 Oct. 2008 2008, pp. 1-8, doi: 10.1109/08IAS.2008.68. [Online]. Available: http://ieeexplore.ieee.org/ielx5/4658787/4658788/04658856.pdf?tp=&arnumber=4658856&isnumber=4658788

[98] A. Jin-Woo, O. Seok-Gyu, M. Jae-Won, and H. Young-Moon, "A three-phase switched reluctance motor with two-phase excitation," *Industry Applications, IEEE Transactions on,* vol. 35, no. 5, pp. 1067-1075, 1999, doi: 10.1109/28.793367.

[99] G. J. Li, X. Ojeda, S. Hlioui, E. Hoang, M. Gabsi, and C. Balpe, "Comparative study of Switched Reluctance Motors performances for two current distributions and excitation modes," in *Industrial Electronics, 2009. IECON '09. 35th Annual Conference of IEEE*, 3-5 Nov. 2009 2009, pp. 4047-4052, doi: 10.1109/IECON.2009.5415318. [Online]. Available: http://ieeexplore.ieee.org/ielx5/5405664/5414636/05415318.pdf?tp=&arnumber=5415318&isnumber=5414636

[100] L. Xiaobin, L. Guangjin, J. Ojeda, M. Gabsi, and R. Zhuoxiang, "Comparative Study of Classical and Mutually Coupled Switched Reluctance Motors Using Multiphysics Finite-Element Modeling," *Industrial Electronics, IEEE Transactions on,* vol. 61, no. 9, pp. 5066-5074, 2014, doi: 10.1109/TIE.2013.2282907.

[101] J. D. Widmer, R. Martin, C. M. Spargo, B. C. Mecrow, and T. Celik, "Winding configurations for a six phase switched reluctance machine," in *Electrical Machines (ICEM), 2012 XXth International Conference on*, 2-5 Sept. 2012 2012, pp. 532-538, doi: 10.1109/ICElMach.2012.6349921. [Online]. Available: http://ieeexplore.ieee.org/ielx5/6330482/6349821/06349921.pdf?tp=&arnumber=6349921&isnumber=6349821

[102] T. J. E. Miller, "Converter Volt-Ampere Requirements of the Switched Reluctance Motor Drive," *IEEE Transactions on Industry Applications,* vol. IA-21, no. 5, pp. 1136-1144, 1985, doi: 10.1109/TIA.1985.349516.

[103] M. Takeno, A. Chiba, N. Hoshi, S. Ogasawara, M. Takemoto, and M. A. Rahman, "Test Results and Torque Improvement of the 50-kW Switched Reluctance Motor Designed for Hybrid Electric Vehicles," *Industry Applications, IEEE Transactions on,* vol. 48, no. 4, pp. 1327-1334, 2012, doi: 10.1109/TIA.2012.2199952.

[104] J. D. Widmer and B. C. Mecrow, "Optimised Segmental Rotor Switched Reluctance Machines with a greater number of rotor segments than stator slots," in *Electric Machines & Drives Conference (IEMDC), 2011 IEEE International*, 15-18 May 2011 2011, pp. 1183-1188, doi: 10.1109/IEMDC.2011.5994770. [Online]. Available: http://ieeexplore.ieee.org/ielx5/5981421/5993850/05994770.pdf?tp=&arnumber=5994770&isnumber=5993850

[105] R. Pupadubsin, A. Steven, J. D. Widmer, and B. C. Mecrow, "Mechanical material properties for structural simulation model of switched reluctance machines," in *2016 XXII International Conference on Electrical Machines (ICEM)*, 4-7 Sept. 2016 2016, pp. 2293-2299, doi: 10.1109/ICELMACH.2016.7732841. [Online]. Available:

http://ieeexplore.ieee.org/ielx7/7592391/7732494/07732841.pdf?tp=&arnumber=7732841&isnumber=7732494

[106] M. v. d. Giet, K. Kasper, R. W. D. Doncker, and K. Hameyer, "Material parameters for the structural dynamic simulation of electrical machines," in *2012 XXth International Conference on Electrical Machines*, 2-5 Sept. 2012 2012, pp. 2994-3000, doi: 10.1109/ICElMach.2012.6350314.

[107] " Mechanical properties of bamboo." http://bambus.rwth-aachen.de/eng/reports/mechanical_properties/referat2.html (accessed.

[108] P. Michael James, "Strength, Fatigue Strength and Stiffness of High-Tech Bamboo/Epoxy Composites," *Agricultural Sciences*, vol. Vol.05No.13, p. 10, 2014, Art no. 51594, doi: 10.4236/as.2014.513136.

[109] S. Schröder. "What are the Mechanical Properties of Bamboo?" https://www.bambooimport.com/en/blog/about-bamboo/what-are-the-mechanical-properties-of-bamboo (accessed.

[110] Y. Sofiane, A. Tounzi, F. Piriou, and M. Liese, "Study of head winding effects in a switched reluctance machine," *Magnetics, IEEE Transactions on*, vol. 38, no. 2, pp. 989-992, 2002, doi: 10.1109/20.996254.

[111] J. D. Widmer, B. C. Mecrow, C. M. Spargo, R. Martin, and T. Celik, "Use of a 3 phase full bridge converter to drive a 6 phase switched reluctance machine," in *Power Electronics, Machines and Drives (PEMD 2012), 6th IET International Conference on*, 27-29 March 2012 2012, pp. 1-6, doi: 10.1049/cp.2012.0260. [Online]. Available: http://ieeexplore.ieee.org/ielx5/6235114/6241991/06242110.pdf?tp=&arnumber=6242110&isnumber=6241991